

CHEMIA

STUDIA UNIVERSITATIS BABEȘ-BOLYAI CHEMIA

4/2025

ISSN (print): 1224-7154;
ISSN (online): 2065-9520; ISSN-L: 1224-7154
© STUDIA UBB CHEMIA
Published by Babeș-Bolyai University

EDITORIAL BOARD OF STUDIA UNIVERSITATIS BABEȘ-BOLYAI CHEMIA

HONORARY EDITOR:

IONEL HAIDUC – Member of the Romanian Academy

EDITOR-IN-CHIEF:

LUMINIȚA SILAGHI-DUMITRESCU

EXECUTIVE EDITOR:

ALEXANDRU LUPAN

ASSOCIATE EDITOR:

CASTELIA CRISTEA

EDITORIAL BOARD:

PAUL ȘERBAN AGACHI, Babeș-Bolyai University, Cluj-Napoca, Romania

LIVAIN BREAU, UQAM University of Quebec, Montreal, Canada

HANS JOACHIM BREUNIG, Institute of Inorganic and Physical Chemistry,
University of Bremen, Bremen, Germany

JEAN ESCUDIE, HFA, Paul Sabatier University, Toulouse, France

ION GROSU, Babeș-Bolyai University, Cluj-Napoca, Romania

EVAMARIE HEY-HAWKINS, University of Leipzig, Leipzig, Germany

FLORIN DAN IRIMIE, Babeș-Bolyai University, Cluj-Napoca, Romania

FERENC KILAR, University of Pecs, Pecs, Hungary

BRUCE KING, University of Georgia, Athens, Georgia, USA

ANTONIO LAGUNA, Department of Inorganic Chemistry, ICMA, University
of Zaragoza, Zaragoza, Spain

JURGEN LIEBSCHER, Humboldt University, Berlin, Germany

KIERAN MOLLOY, University of Bath, Bath, UK

IONEL CĂTĂLIN POPESCU, Babeș-Bolyai University, Cluj-Napoca,
Romania

CRISTIAN SILVESTRU, Babeș-Bolyai University, Cluj-Napoca, Romania

S T U D I A

UNIVERSITATIS BABEȘ-BOLYAI

CHEMIA

4

CONTENT/ SOMMAIRE/ INHALT/ CUPRINS

Ioan PETEAN, Emanoil PRIPON, Marzena GROCHOWSKA-JASNOS, Simona Elena AVRAM, Lucian Barbu TUDORAN, Gheorghe BORODI, Nicoleta IGNAT, Corrosive Effect of Rolling Faults Induced by Microstructural Segregations in a Silver Coin Issued by Gabriel Bethlen in 1626.....	7
Gabriele-Mario BOGDAN, Sorin-Aurel DORNEANU, Electrochemical ph-stat as Acidity Monitoring System in High Ionic Strength Solutions. I. Design Challenges and Preliminary Results.....	23
Victor MALYSHEV, Angelina GAB, Ana-Maria POPESCU, Virgil CONSTANTIN, Study of Electrochemical Behavior of VI-B Group Metal Oxides in Tungstate Melt	41
Sebastian Ionuț OGNEAN, Emilia Valentina PANTEA, Valer MICLE, Daria-Maria-Ecaterina FENEȘAN, Efficiency Analysis of Some Zeolite Media in the Treatment of Technological Wastewater in Agro-zootechnical Units.....	57
Silvia BURCĂ, Cerasella INDOLEAN, Studies on the Adsorption of Congo Red Anionic Dye from Synthetic Aqueous Solutions Using Waste Eggshell Biomass	75

Nesimi ULUDAG, Alper SANLI, A New Reagent for Synthesis of Nitriles from Aldoximes Using Aluminium (III) Triflate.....	97
Daniel BOMBOȘ, Gabriel VASILIEVICI, Ana Maria MANTA, Loredana Irena NEGOIȚĂ, Ioan SAROSI, Andrei MOLDOVAN, Filip MIUTA, Andra-Ioana STĂNICĂ, Stanca CUC, Waste Grape Pomace for Food Packaging.....	107
Ana BALEA, Irina CIOTLĂUȘ, Rahela CARPA, Mihaela-Cecilia VLASSA, Sonia ANDRESI, Quality Assessment of Handmade Soaps, Plant-Based Oils, and Skincare Creams: Physicochemical and Microbiological Analysis	131
Hichem HAFFAR, Asma CHETOUANI, Souhir IZOUNTAR, Fatima Zohra BEZGHOUD, <i>Ex vivo</i> Experimental and Spectroscopic Analysis of Urinary Stone Dissolution by El-Maatya Spring Water: A Multi-analytical Approach	157
Zehra Ceren ERTEKİN, Erdal DİNÇ, Experimental Design-based Optimization Approaches in UPLC Method Development: Simultaneous Quantitative Estimation of Sulfadiazine and Trimethoprim in a Combined Veterinary Formulation	181
Denis MITOV, Stefan PETROVIĆ, Katarina MILENKOVIĆ, Jelena MRMOŠANIN, Biljana ARSIĆ, Aleksandra PAVLOVIĆ, Snežana TOŠIĆ, Effect of Elevated Concentrations of Cadmium on Heavy Metal(oid)s Content, Antioxidant Activity and Content of Rosmarinic Acid of Lemon Balm (<i>Melissa Officinalis</i> L.)	201
Nicoleta MATEI, Semaghiul BIRGHILA, Simona DOBRINAS, Elena Carmen LUPU, Antoanela POPESCU, HPLC/DAD Analysis of Vitamin C and Antioxidant Capacity Determination of <i>Vitis Vinifera</i> L. Grapes During Ripening	219
Aysun DİNÇEL, Murat KÜRŞAT, İbrahim Seyda URAS, Belma KONUKLUGİL, A New HPLC Method Approach for the Quantification of Quercetin in Seven Different Anatolian Plant Extracts.....	233
Ahmet BAKIR, Mehtap BAKIR, Suat EKİN, Mehmet FIRAT, Antioxidant, Anti-haemolytic Activity, Vitamin and Element Profile of <i>Rhamnus Cornifolius</i>	243
Selin KALENDER, Alper GÖKBULUT, Burçin ÖZÜPEK, Sultan PEKACAR, Didem Deliorman ORHAN, RP-HPLC and HPTLC-Based Phytochemical Studies of Endemic <i>Nepeta Cadmea</i> Boiss. and Its Effects on Carbohydrate Digestive Enzymes	263

Ourdia AMZAL, Ahmed Salah Eddine MEDDOUR, Farid SOUAS, Radia AKSOUH, Abdelhamid SAFRI, Hydraulic Modeling and Optimization of the Oil Gathering Network in the Peripheral Field Rama–Raa North, Hassi Messaoud (Algeria).....	275
Peter WONNEBERGER, Lydia KEIL, Paul SPICKENREUTHER, Peter LÖNNECKE, Evamarie HEY-HAWKINS, 1-Phospha-2-Azanorbornene as Precursor for 1-Phospha-Bicyclo[3.2.1]Octa-2,5-Diene	293

Studia Universitatis Babes-Bolyai Chemia has been selected for coverage in Thomson Reuters products and custom information services. Beginning with V. 53 (1) 2008, this publication is indexed and abstracted in the following:

- Science Citation Index Expanded (also known as SciSearch®)
- Chemistry Citation Index®
- Journal Citation Reports/Science Edition

CORROSIVE EFFECT OF ROLLING FAULTS INDUCED BY MICROSTRUCTURAL SEGREGATIONS IN A SILVER COIN ISSUED BY GABRIEL BETHLEN IN 1626

Ioan PETEAN^{a,*}, Emanoil PRIPON^b, Marzena GROCHOWSKA-JASNOS^c, Simona Elena AVRAM^d, Lucian Barbu TUDORAN^{e,f}, Gheorghe BORODI^f, Nicoleta IGNAT^{a,*}

ABSTRACT. Gabriel Bethlen's monetary reform in 1625 supposed to replace bad coins with good-quality silver issues. Some of these coins exhibit small, parallel surface lines caused by rolling faults in silver plates. This study investigates a 1626 silver groat minted at Baia-Mare, displaying prominent scratches extending from obverse to reverse. XRD and metallographic analyses reveal copper grain's oxidation to Cu₂O, localized compositional inhomogeneities, and lamination-induced micro-cracks resulting from silver-copper segregation. The coin's high relief is worn due to the circulation while the lower areas preserve the initial state. Metallographic observation reveal that the lower relief contain silver (83.7 wt.% α phase and eutectic) while the worn areas contains debased silver (65.5 wt.% eutectic and β grains) generating large copper micro – segregations, confirmed by SEM – EDX. These structural defects facilitated corrosion across the rolling direction, becoming more visible after coin cleaning. Such micro faults would have been undetectable after coin issue. The findings indicate that such pseudo-scratches represent not mechanical damage or intentional markings, but

^a Faculty of Chemistry and Chemical Engineering, Babes-Bolyai University, 11 Arany Janos Street, 400028 Cluj-Napoca, Romania.

^b Zalau County Museum of History and Art, 9 Unirii Street, 450042, Zalau, Romania.

^c Museum of Archaeology and History in Głogów Brama Brzostowska 1, 67-200 Głogów, Poland.

^d Faculty of Materials and Environmental Engineering, Technical University of Cluj-Napoca, 103-105 Muncii Bd., RO-400641, Cluj-Napoca, Romania.

^e Faculty of Biology and Geology, Babes-Bolyai University, 44 Gheorghe Bilascu Street, 400015 Cluj-Napoca, Romania.

^f National Institute for Research and Development of Isotopic and Molecular Technologies, 65-103 Donath Street, 400293 Cluj-Napoca, Romania.

* Corresponding authors: ioan.petean@ubbcluj.ro; nicoleta.cotolan@ubbcluj.ro



metallurgical anomalies associated with subtle debasement practices. This may suggest a controlled attempt to conceal minor reductions in silver fineness during Bethlen's monetary reform, intended to stabilize coin production while preserving the coin's visual and fiduciary integrity.

Keywords: *Gabriel Bethlen, silver groat, microstructural segregation, corrosion*

INTRODUCTION

There are some actual silver alloys titles: 83.5 wt.% (used for the most of the modern coins like the emissions of Latin Monetary Union (Belgium, France, Italy and Switzerland) during 1865 to 1926. Many countries issued coins at this standard like Spain, Greece, Romania, Austro-Hungarian Empire (since 1892) which were in use until the end of first world war; 92.5 wt.% also called sterling silver is often found in British coins and Unites States of America silver dollars. The silver title decreases at 75.0 wt.% in some coins issued after the first world war depending on the monetary politics of each country. Unfortunately the silver title was less standardized in the pre-modern times and was more affected by the socio-political factors.

The start of 30 years war in 1618 implies issuing of large amount of counterfeited coins which were produced most likely in annex workshops of the official mints. Literature reveal that most effective silvering technique was the immersion of the copper strips into melted silver ensuring an thin layer attached to the core by an intermediary layer of eutectic [1, 2]. The official coins were also debased by reducing silver title to about 50 % [3]. All belligerent countries use this strategy and subsequently their vaults were filled up with forged or debased coins. In fact, it was a manifestation of enormous inflation that raised the conversion rate of small change coins to the greater commercial coins like silver thaler or gold ducats. Literature mention that a standard thaler worth 72 kreuzers in 1600; 124 kreuzers in 1619 and over 600 kreuzers in 1622 [4, 5]. A financial crisis called Kipper und Wipperzeit occur where the coins were clipped for verifying their core content and weighted for ensuring that the sides were not cut off. There are no records about the forged coins spread, but for sure the debased coins of Gabriel Bethlen were released on the Transylvanian circulation mainly as 1 groat and wide groat (equivalent to 5 conventional silver denars). The Northern find record of such groat belongs to Gdansk (e.g. from Łagiewniki in 2006) consisting in a groat issued in 1626. As professor Paszkiewicz writes, it likely reached Gdańsk via the Polish market [6]. A close look to the published photograph of the coin reveals some corrosive scratches on its obverse which might be related to the coin's core title.

Another inflation coins are the 24-kreuzer issued by Gabriel Bethlen in Opole circulating mainly in Silesia but not in the Greater Poland where only Transylvanian groat emissions were recognized as official Bethlen's emissions [7]. Most of these debased 24 kreuzers coins minted in Opole feature minor scratches oriented under the silver stripe lamination – rolling direction [8]. Such marks look to be a technological characteristic for the small value coins with low silver title.

Monetary reform implemented by Gabriel Bethlen prince of Transylvania (1613-1629), in 1625 was designed to replace debased and forged coins with good silver issues produced under strict control. This reform followed a period of monetary instability caused by excessive minting of underweight coins what have been started during the preceding reigns. Bethlen's aim was to restore public trust in Transylvanian coinage and to demonstrate the principality's independence from the Habsburg monetary system [9, 10].

These new issues were preferred for hoarding as observed in the hoards discovered in Salaj County [11] as well in the hoards discovered in other places from Transylvania [12]. Surprising, some of them also feature minor scratches oriented in the rolling - lamination direction like those observed for debased coins. It is clearly that these marks are not generated by the circulation worn but were formed during the coins production. Circulation worn only could enhance their aspect because of local friction forces of the coins high relief. On the other hand, such scratches are rarely found on the high denominations like thaler which are made of good silver over 80 % fineness. Some of these valuable coins were deliberately marked with specific symbols related to the personal ownership marks, commemorative marks or bullion fineness marks (even alchemical symbols) described in literature as graffiti [13]. It is also reported that smaller denomination were not subjected to such deliberate inscriptions.

Another characteristic of the high denomination is their significantly increased width of about 1.5 – 2 mm while small denomination is very thin < 1 mm. Such an advanced thickness reduction within silver stripe of the small denomination implies supplementary rolling. The excessive rolling without annealing process induces progressive cold hardening of the grains and their subsequently failure through the development of dislocations forests within the tensioned grains [14]. The dislocations progress into fine micro-cracks predominantly oriented perpendicularly on the rolling direction which further induces macroscopic fissures if the annealing treatment is not applied [15]. On the other hand, silver has good deformability ensuring a proper rolling supporting large strain [16], perhaps this is the reason for less observation of these specific scratches on the high denomination. Smaller denominations are very often debased having uneven composition and microstructure produced in a metallurgical process without precise control of the temperature. In

consequence grain segregation most likely occurs at the ends of the silver alloy ingot due to the uneven cooling rate between ingot's surface and core [17]. Thus, the scratches formed along the rolling direction indicate a potential microstructural failure of some atypical segregated grains. Such hypothesis requires advanced physicochemical investigation to figure out the scratches nature and their possibility to be specific marks of the debased coins.

RESULTS AND DISCUSSION

A random discovery of a 1626 silver groat from Baia Mare (Nagybánya) provides valuable insight into the technical implementation of the reform of Gabriel Bethlen (Figure 1). Although visually well-preserved, the coin displayed a dark (black-brown) tarnish, induced by the advanced degradation of the copper grains within the silver alloy. The presence of such patinas and corrosion traces aligns with the high-temperature and rolling conditions typical of early-seventeenth-century minting technology. Silver sheets were laminated multiple times to ensure uniformity, but uneven cooling and imperfect alloying often induced micro-segregations of copper, which later served as preferential corrosion sites. At first sight, the coin seemed well preserved but covered with a dark brown-black oxide layer (Figure 1). Cleaning removed this patina and revealed parallel linear features on both obverse and reverse. These were initially interpreted as scratches caused by circulation but further examination proved them to be structural faults.



Figure 1. Photograph of the investigated coin before and after cleaning: silver groat issued by Gabriel Bethlen in 1626 minted at Baia Mare (N.B.). Medals alignment ↑↓.

Reflected light microscopy, taken at a low magnification, confirms that the upper relief of the coin – especially Madonna and Child and inscription characters – is worn by the circulation (Figure 2a). However, the lower areas are well preserved, without circulation worn. Such parallel defects (Figure 2a–b) are consistent with lamination defects (“rolling faults”) that appear when cold-worked Ag–Cu alloys experience localized strain hardening and copper segregation during the final rolling stage before striking coins.

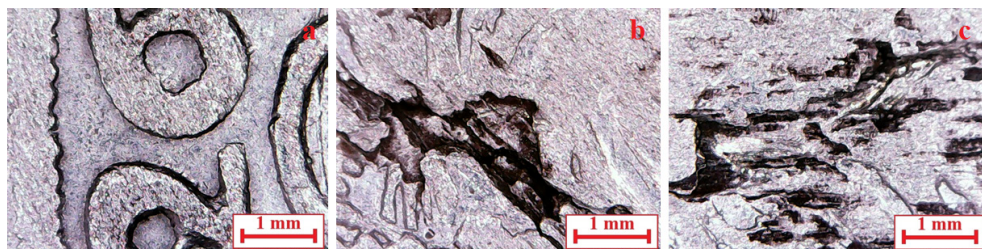


Figure 2. Reflected light microscopy of the coin surface: a) normal areas with worn relief and intact lower details, b) scratches on the obverse and c) scratches on the reverse.

The coin obverse has a deep scratch with a length of about 7 mm and a mean width of 600 μm , its detail can be observed in Figure 2b. The worn area belonging to Madonna’s knees and hand surrounds the scratch having firm rims. The scratch borders are irregular having the shape of some missing microstructural grains that were removed through the corrosion process. The scratches on the reverse start appearing approximate on the point where the obverse scratch disappears beneath the worn silver. These are distributed in shorter parallel branches of about 1 – 1.5 mm length and width of about 200 – 250 μm , Figure 2c. Their orientation keeps the rolling direction similarly to the obverse scratches. Their shape and spatial positioning indicate that the microstructural defect pass through the coins core.

X Ray Diffraction (XRD) analysis (Figure 3), confirmed that the initial patina of the coin contained copper oxide Cu_2O (crystallized as cuprite) while silver grains remained well preserved revealing their metallic state. After cleaning, the oxide layer fell below the diffractometer’s detection limit (e.g. 1 wt. %), demonstrating efficient removal of surface corrosion products. Unfortunately, the resting environment of the coin is unknown and no connection with the corrosion type can be followed. However, the coexistence of metallic silver with cuprite indicates an advanced oxidation of the copper grains within the coin surface microstructure particularly affecting the more reactive copper component. Ag does not possess a protective native oxide film and relies on natural immunity for corrosion protection in mild environments [18].

The complete cleaning of the coin removes oxides from its surface at a level below detection limit of the diffractometer (e.g. 1 wt.%). Removing the oxidized crystals from the copper grains make them available to the diffracting X-ray beam and become completely detectable. The XRD pattern reveals specific peaks for Ag having strong intensities and narrow aspect followed by Cu peaks having lower intensities but keeping their narrow aspect. It indicates that both silver and copper appear on the well developed grains. It is interesting finding since one of the phases should have been finely divided as thin lamellas within the eutectic composition according to the binary phase diagram [17]. Such refinement of the dispersed phase induces a significant broadening of the XRD patterns [19], a fact which was not observed in our case.

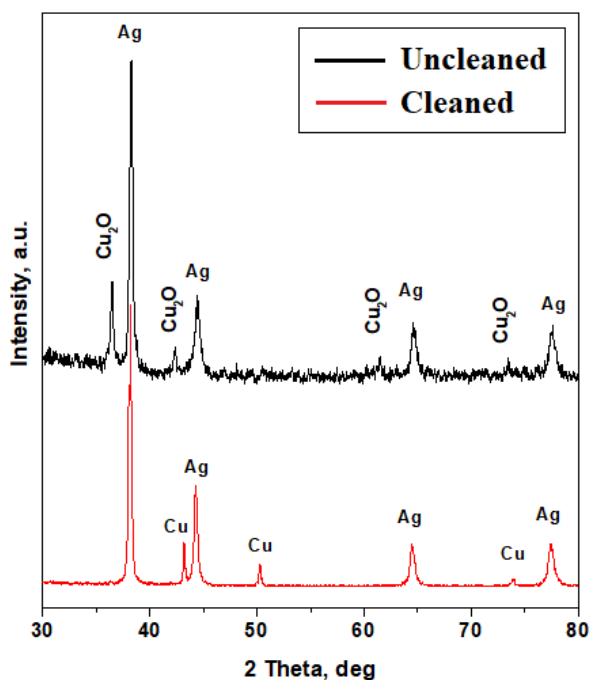


Figure 3. XRD patterns for the coin surface before and after cleaning process.

The overall silver and copper amount can be established on the XRD pattern in Figure 3 by applying the Relative Intensity Ratio Method (RIR) which correlates the relative intensities of Ag and Cu peaks with their corundum factor [1]. Finally results an overall weight composition of 76.12 % Ag and 23.88 % Cu. This result would indicate a good silver alloy situated in the hypoeutectic zone of the Ag-Cu phase diagram, just like the mint master

would have been wanted. The nice and good-looking aspect of the completely cleaned coin sustain this impression making this coin very desirable in 1626 to be kept from the circulation and nowadays to be exposed in a collection. But the obvious discordance between the shine of the worn surfaces regarding the preserved ones tells another story that the overall silver content might be uneven distributed into the coin surface.

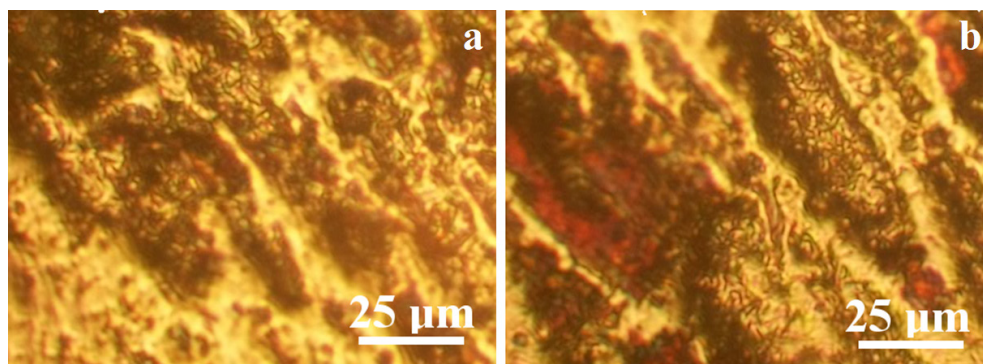


Figure 4. Metallographic observations: a) intact lower relief and b) worn high relief.

For metallographic observation, local spots of a few millimeters in size were manually selected, taking care to preserve the artifact's good condition. The lower relief areas reveal a good silver composition typical for hypoeutectic region of Ag – Cu phase diagram (approximately 83.7 wt.% Ag) revealing pure silver (α phase) grain having bright nuance mixed up with eutectic grains having a lamellar structure of silver and copper interlocked sheets (Figure 4a). The grains are elongated under the lamination direction indicating that the final stage of silver plate was kept without re-crystallization.

In contrast, the worn regions have a completely changed microstructure (Figure 4b). It contains predominantly eutectic grains with tiny elongated (α phase) surrounding their border. The abnormal microstructure is represented by copper segregation derived from the eutectic grains having dark red color (Figure 4b). In fact the coin's core is closer to the eutectic composition of Ag – Cu system (approx. 65.5 wt.% Ag) but the significant copper segregation move the alloy slightly into the hypereutectic region.

Such segregation appears in bigger ingots at their ends (e.g. head and the foot of the ingot when it is cast in vertical position). This inhomogeneity while visually imperceptible—may reflect intentional economic optimization: slightly reducing silver content in deeper, non-visible layers of the coin while maintaining a higher fineness on the surface to preserve trust in the currency. SEM investigation coupled with EDS spectroscopy fulfill this requirement.

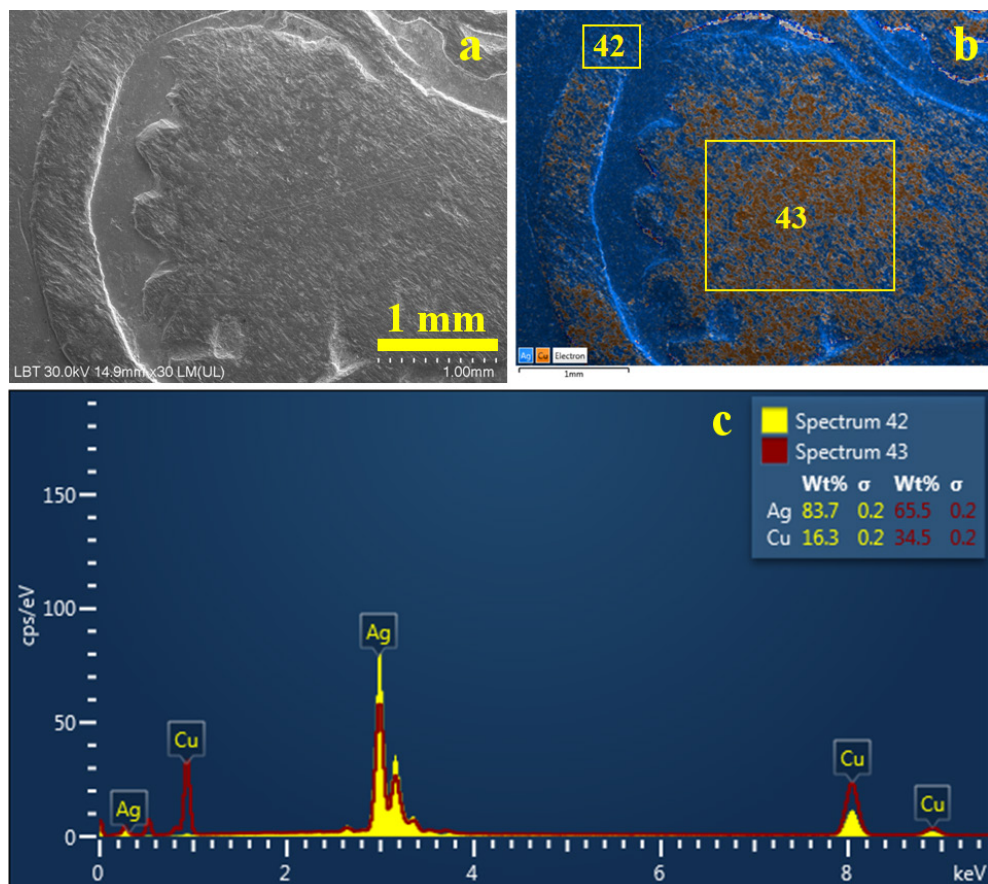


Figure 5. SEM investigation of the large area of the coin surface: a) SEI image, b) BSE image displaying elemental map and c) EDS spectra taken on specific positions.

Low magnification Secondary Electron Image (SEI) imaging (x30) reveals the overall aspect of the coin obverse (Figure 5a) in a complementary mode that reflected light microscopy does in Figure 2a. The worn areas (Madonna's head and halloo) reveal a grainy structure indicating that the eutectic grains were affected by the friction between circulating coins, in good observation with our pervious observation on worn coins [1]. The microstructural aspect of the lower relief confirms its well-preserved state without worn marks.

The backscattered electron image (BSE) display the elements distribution over the surface superimposed on the morphological details consisting in an elemental map (Figure 5b) Each element was assigned to a specific color such as blue for Ag and orange for Cu. The worn areas

clearly evidence a hypereutectic structure based on a dense mixture of eutectic grains (blue with fine orange spots) and β phase (e.g. pure Cu) phase. The microstructural observations are confirmed by the elemental composition of this area revealed by spectrum 43 (Figure 5c) having 65.5 % wt.% Ag and 34.5 wt. % Cu. The preserved areas reveal a different microstructure based on α phase (e.g. pure Ag) grains mixed with eutectic grains belonging to the hypoeutectic region of the phase diagram. The fact generates a compact blue appearance spotted with small orange points. Spectrum 42 reveal the elemental composition of 73.7 wt.% Ag and 16.3 wt.% Ag. It indicates that the coin was covered by a thin layer of standard silver while the core is made of debased silver.

The obvious scratch on the obverse is too deep for obtaining a reliable image and therefore we took a microstructural detail at the lower end of the scratch revealing a significant copper segregation (Figure 6).

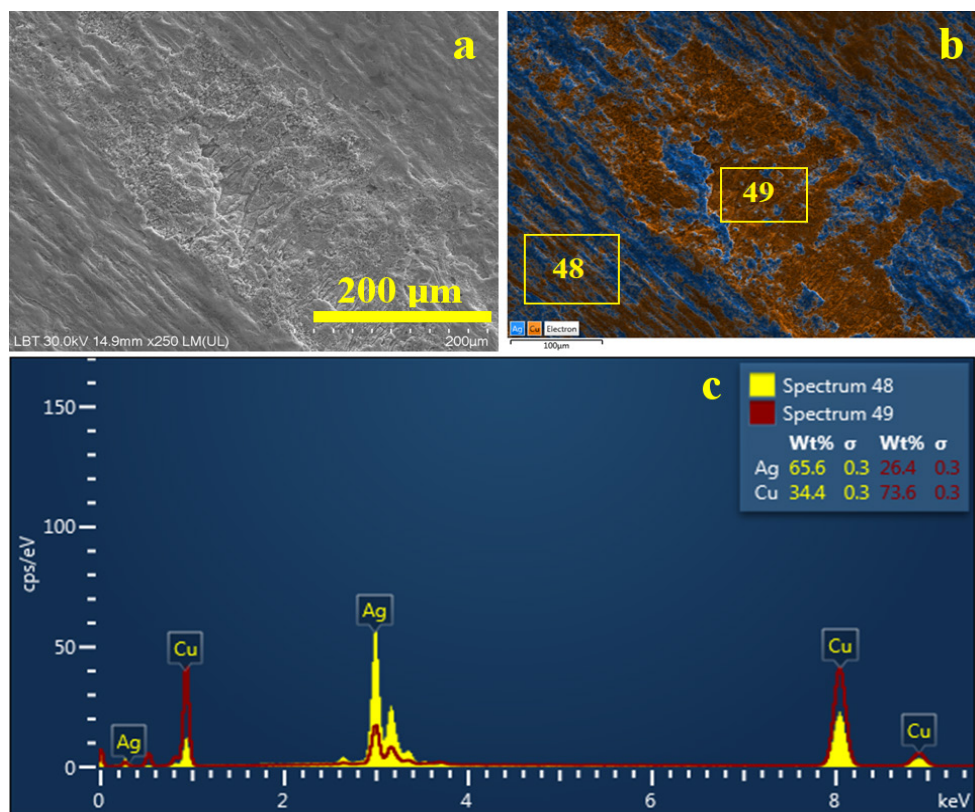


Figure 6. SEM investigation of the segregation overview: a) SEI image, b) BSE image displaying elemental map and c) EDS spectra taken on specific positions.

SEI image in Figure 6a reveal the typical hypereutectic microstructure elongated under the rolling direction interlocked with a compact area having a more refined microstructure. BSE image (Figure 6b) featuring the elemental map clearly reveals that the interlocked microstructural constituent is a large copper segregation which confirms the metallographic observation. The microstructure beside the copper segregation has a composition of 65.6 wt.% Ag and 34.4 wt.% Cu as observed in Spectrum 48 (Figure 6c) in good agreement with the worn area observed on the Madonna's head.

It is about a hypereutectic alloy situated in a close proximity of the eutectic composition. Of course, the liquid alloy cooling generates the precipitation of β grains enriching the melt in silver until the eutectic composition is achieved when it solidifies as eutectic grains. Unfortunately large ingots like ones used for coins minting causes an uneven distribution of the temperature under cooling allowing the coalescence of β grains which tends to extract excessively the copper from the remnant melt alloy generating large segregations.

The fact is proved by spectrum 49 indicating an appreciation of the copper content at 73.6 wt. % for the marked area. The shape of segregation is elongated under the rolling direction having a width of about 200 μm and the length exceeds the image frame on the lower right corner. So far, it looks similar to the scratches microstructural aspect.

A closer look to the copper segregation microstructure is necessary. A specific area without silver intercalation was chosen at higher magnification (x5000) in Figure 7. While the general aspect of the copper segregation is elongated under the rolling direction the microstructural details reveal small grains of about 5 μm having a cold hardened aspect with broken sub-grains of about 1 – 2 μm split by parallel cracks oriented perpendicularly on the rolling direction dealing with literature observations [16].

Since silver is more ductile than copper, thus Cu segregation induces rolling defect as observed. The micro-fissures have identical length with the segregation width and a width of about 1 μm ensuring enough space for water and corrosive agents' penetration beside the broken sub grains promoting corrosion. The elemental analysis reveal a composition of 93.7 wt.% copper with minor silver intercalation appearing as blue spots in the elemental map. Although copper does corrode (oxidized by oxygen and by hydrogen sulphide) at the surface, it can form a stable corrosion film or a passivation layer, which prevents it against further corrosion in most environments [20]. The non segregated alloy areas within Figure 6b looks well preserved most likely due to the passivation layer formed in contact with the coin resting ground.

CORROSIVE EFFECT OF ROLLING FAULTS INDUCED BY MICROSTRUCTURAL SEGREGATIONS
IN A SILVER COIN ISSUED BY GABRIEL BETHLEN IN 1626

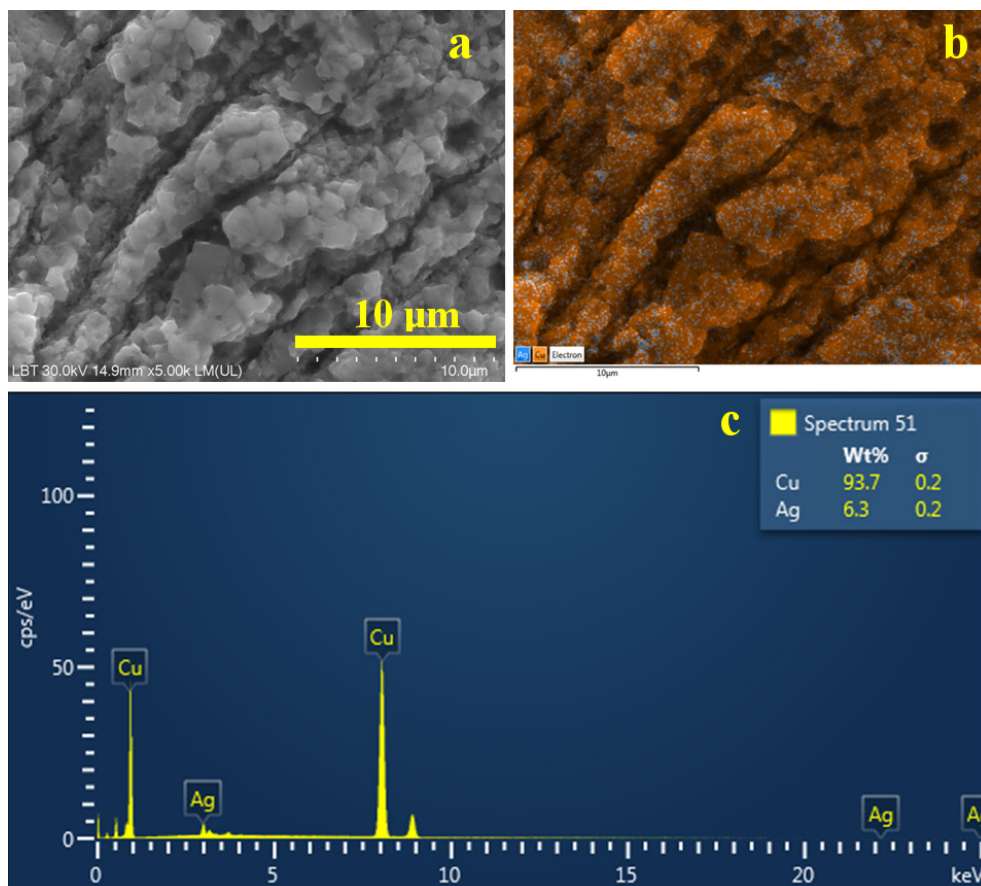
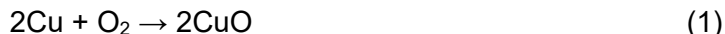


Figure 7. SEM microstructural details on the copper segregation: a) SEI image, b) BSE image displaying elemental map and c) EDS spectrum taken overall image.

The micro-fissures within the copper segregation along with the advanced internal fracture of the grains structure facilitate the penetration in depth of the oxidizing agents generating an advanced microstructural corrosion that prevent formation of passivation layer. It is difficult to discuss about the resting soil influence on the copper segregation corrosion while the coin discovery conditions are not known.

However, it is about the conjugated effect of water infiltration into the soil layers which mostly contains granular matter as quartz and calcite mixed with fine clay mixture based on kaolinite and muscovite [21, 22].

These minerals are able to release ions that might facilitate corrosion processes. The basic oxidation reactions use the oxygen present in the resting ground according to the following equations:



Taking into consideration the potential presence of sulfur within the resting ground there is a more complex of oxidation to cuprite according to the equation (3):



The soil's organic matter or the decomposing of organic remains beside the coin (e.g. vegetal fiber or leather bag containing a coin pile, or underground human body decay in case of graves discoveries) might release significant amounts of hydrogen sulphide [23, 24]. The well preserved state of the silver grains indicate low influence of sulfides that also attack silver (giving a black tarnish) and most likely oxidative corrosion facilitated by the mineral species within soil. The fact highlights the importance of archeological findings to be made by specialists with care for the information regarding the resting ground and its stratigraphy.

The current study limitation resides in the investigation of a single coin having the pseudo-scratches pattern oriented on the rolling direction. The random finding without knowing the characteristics of the resting environment for over 300 years also limits the physicochemical investigations. Literature data clearly indicate the importance of the finding place on the archeological discussions [25, 26].

The further analysis should be focused on larger coins number discovered in the precise archeological context which allows additional investigations of the resting ground. The detailed mineralogical investigations (X ray diffraction coupled with Mineralogical optical microscopy) of the resting ground might evidence some specific aspects regarding the coins corrosion and preservation state.

NUMISMATIC SIGNIFICANCE

Current physicochemical investigation reveal that copper segregation would have been difficult to be detected below of the good silver layer deposited during minting process ensuring a very nice appearance of the

coin. Hence, the core is made of a silver of about 65 wt.% the contemporary weighing would have been all right maintaining good silvery aspect if clipped. The intensive circulation causes intense friction over the coin surface erasing the good silver from the high relief details revealing the debased alloy. The repeated contact of debased silver with the hands induces oxidation of the copper β grains and segregations forming a passivated dark patina layer based on Cu_2O and CuO which appear natural beside the shiny good silver on the lower areas of the coin's topography. The problem occur after about 400 years after the minting because of different corrosion of β grains and copper segregations which further appear as pseudo-scratches on the coin surface.

Unfortunately, the present study is focused on a single random find coin which is a limitation. Further research should be conducted on similar coins belonging to well known archeological finds to reveal if the copper segregation and its corrosion is confirmed and could be appreciated as a typical sign for debased small denominations. Local Transylvanian hoards are abundant in such monetary type but it worth to see its spread on the other countries circulation through the commerce [12, 27].

As the findings show, Gabriel Bethlen groats reached central Europe, for example Poland. But we have only four finds of such so far: Gdańsk – Łagiewniki, Jarosław, Dabrowa Chełmińska, Mieścisko. From which only the one from Gdansk-Łagiewniki is available. However, these are much rarer finds than the most common gold coins of this ruler in deposits from Poland and Silesia. Gabriel Bethlen's wide groat occurred during archaeological research in the Łagiewniki district of Gdańsk. It can be found in a publication by Professor Borys Paszkiewicz [6].

Parallel scratches are also visible on this specimen, which probably became apparent after the coin was cleaned. Similar damage to that seen on the Gabriel Bethlen groat in question can also be seen on other copies of the same type. For example on one found on the website, where the damages are smaller but clearly [28]. In addition, such damages are common on 24-kreuzer coins minted by Gabriel Bethlen in the Duchy of Opole and Racibórz [8]. Interestingly, the inflationary 24-kreuzer coins were registered only in the territory of historical Silesia (where they were minted), while the groat coins were kept in deposits from Greater Poland, probably recognized as full-value Transylvanian coins, despite Bethlen's mints producing using worse money than the reform envisaged.

Visible, after conservation, damages on Bethlen coins reveal both the limits of seventeenth-century coin production technology and the economic urgency of minting. The incomplete homogenization of the Ag–Cu alloy caused copper micro-segregations that served as future corrosion nuclei.

CONCLUSIONS

The poor elaboration of debased silver alloy combined with less control of temperatures during the specific technological steps generates large copper segregations within its microstructure.

The rolling regime prove to be adequate for the debased alloy respectively to the hypereutectoid composition of eutectic and β grains but induces over cold hardening of the copper segregation becoming elongated in the rolling direction having small intra-crystalline micro-cracks perpendicular on the rolling direction.

The hypereutectic microstructure seems to be well passivated to the corrosion while the copper segregation is affected in depth by the corrosive agents. Thus, the cleaning procedure removes the formed oxides revealing pseudo-scratches.

Over centuries, these zones oxidized preferentially, producing linear reddish “scratches” observable on cleaned specimens—misleadingly interpreted as post-mint damage. In reality, they constitute tangible metallographic evidence of hidden inflationary stress in the early-modern Transylvanian economy.

EXPERIMENTAL SECTION

The object of current research is a wide groat issued by Gabriel Bethlen in 1626 at Baia Mare mint (N.B. Nagy Banya) presented in Figure 1. It is a random finding without archeological background and less information about the resting ground. The coin was cleaned using the standard procedure [29] as follows:

- The coins were subjected to ultrasound treatment for 10 minutes in aqueous environment;
- Immersed in EDTA solution 5 % for 15 minutes;
- Final ultrasound cleaning in water for 4 minutes.

Reflected light microscopy was effectuated using a Ulefone uSmart C01 microscope equipped with an integrated computer aided image acquiring system working on the Windows platform using png high resolution output format 720 x 1080 pixels.

Metallographic microscopy was effectuated with an IOR MC8 metallographic microscope (IOR, Bucharest, Romania) equipped with a digital image capture camera Sony 14 MPx (Sony Co., Minato, Japan). The chemical etching was effectuated by swabbing method using a reagent containing ferric chloride and sodium thiosulfate applied with a small cotton cloth for 5 seconds followed by rinsing with deionized water.

X ray diffraction (XRD) was performed with a Bruker D8 Advance diffractometer with Cu α monochromatic radiation having a wavelength of 1.540562 Å. The patterns were registered at a speed of 1°/min. in the range of 10 – 80°. Crystal phase identification was made upon the XRD peaks using Match 1.0 software (Crystal Impact Company, Bonn, Germany).

Scanning Electron Microscopy (SEM) was done with Hitachi SU8230 operated in high vacuum mode at an acceleration voltage of 30 kV. The samples were coated with a thin layer of Pt to ensure a proper electrical conductivity. The elemental analysis was effectuated with the Energy Dispersive Spectroscopy (EDS) detector X-Max 1160 EDX (Oxford Instruments, Oxford, UK). The Pt component was subtracted from the EDS results.

REFERENCES

1. I. Petean, G.A. Paltinean, A.C. Taut, S.E. Avram, E. Pripon, L. Barbu Tudoran, G. Borodi, *Materials*, **2023**, 16, 5809. <https://doi.org/10.3390/ma16175809>
2. I. Petean, L. Barbu Tudoran, G. Borodi, E. Pripon, *Acta Mvsei Porolissensis*, **2025**, 47, 387-395.
3. I. Petean, G.A. Paltinean, E. Pripon, G. Borodi, L. Barbu Tudoran, *Materials*, **2022**, 15, 7514. <https://doi.org/10.3390/ma15217514>
4. K.K. Karaman, S. Pamuk, S. Yıldırım-Karaman, *J. Monet. Econ.*, **2020**, 115, 279–300. <https://doi.org/10.1016/j.jmoneco.2019.07.007>
5. H. Boubaker, J. Cunado, L.A. Gil-Alana, R. Gupta, R. *Phys. A Stat. Mech. Its Appl.*, **2020**, 540, 123093. <https://doi.org/10.1016/j.physa.2019.123093>
6. B. Paszkiewicz, *Coin in old Gdańsk Archaeological research in 1997-2009 (in Polish: Moneta w dawnym Gdańsku badania archeologiczne w latach 1997-2009)*, Gdańsk, **2013**.
7. M. Grochowska-Jasnos, *Acta Musei Porolisensis*, **2025**, *Acta Mvsei Porolissensis*, **2025**, 47, 397-438.
8. Ł. Sroka, P. Milejski, *The Hoard of Prague Groschen and Seventeenth-century Coins from Osieczów, Bolesławiec District*, Bibliotheca Nummaria Leopoldina 2, Wrocław, **2020**.
9. F. Ciulavu, *Studii și Cercetări Numismatice – Serie nouă*, 2013, 4(16), 127-143.
10. F. Ciulavu, *Activitatea monetăriei de la Alba Iulia. Studiu numismatic, istoric și arheologic*, Editura Mega, Cluj-Napoca, **2020**.
11. E. Pripon, *Tezaure monetare medievale și premoderne descoperite pe teritoriul orașului Zalău (I)*, Editura Mega, Cluj-Napoca, **2018**.
12. Corina Toma, *Tezaure monetare și tezaurizare în Transilvania secolelor XV/ XVI-XVII*, Editura Muzeului Țării Crișurilor Oradea, Oradea, **2016**, 148, 132-148.
13. M. Grochowska-Jasnos, *Graffiti on post-medieval coins: practical, symbolic, and alchemical messages*, Book of abstracts, Numismatica Centroeuropea Conference, Legnica, Poland, **2025**, 61-63.

14. I.R. Souza Filho, M.J.R. Sandim, D. Ponge, H.R.Z. Sandim, D. Raabe, *Materials Science and Engineering: A*, **2019**, 754, 636-649.
<https://doi.org/10.1016/j.msea.2019.03.116>
15. S. Semboshi, S. Sato, G. Miyamoto, K. Ito, S. Kasatani, H. Hyodo, *Materials Science and Engineering: A*, **2025**, 941, 148638.
<https://doi.org/10.1016/j.msea.2025.148638>
16. X. Zhu, Z. Xiao, J. An, H. Jiang, Y. Jiang, Z. Li, *Journal of Alloys and Compounds*, **2021**, 883, 160769. <https://doi.org/10.1016/j.jallcom.2021.160769>
17. A.E. Gheribi, J. Rogez, F. Marinelli, J.C. Mathieu, M.C. Record, *Calphad*, **2007**, 31, 380-389. <https://doi.org/10.1016/j.calphad.2006.10.005>
18. B. Bozzini, G. Giovannelli, C. Mele, F. Brunella, S. Goidanich, P. Pedferri, *Corrosion Science*, **2006**, 48, 193-208,
<https://doi.org/10.1016/j.corsci.2004.11.024>
19. M. Di Fazio, F. Di Turo, L. Medeghini, L. Fabrizi, F. Catalli, C. De Vito, *Microchemical Journal*, **2019**, 144, 309-318. <https://doi.org/10.1016/j.microc.2018.09.016>
20. H. Huisman, R. Ackermann, L. Claes, L. van Eijck, T. de Groot, I. Joosten, F. Kemmers, N. Kerkhoven, J-W. de Kort, S. Lo Russo, D. Ngan-Tillard, B. van Os, M. Peter, C. Pümpin, J. Vaars, Z. Zhou, *Journal of Archaeological Science*, **2023**, 47, 103799. <https://doi.org/10.1016/j.jasrep.2022.103799>
21. S.E. Avram, L.B. Tudoran, G. Borodi, I. Petean, *Appl. Sci.*, **2025**, 15, 6445.
<https://doi.org/10.3390/app15126445>
22. S.E. Avram, L.B. Tudoran, G. Borodi, M.R. Filip, I. Ciotlaus, I. Petean, *Sustainability*, **2025**, 17, 2906. <https://doi.org/10.3390/su17072906>
23. B.S. van der Meulen-van der Veen, *Journal of Archaeological Science: Reports*, **2023**, 48, 103839. <https://doi.org/10.1016/j.jasrep.2023.103839>
24. M. Habibzadeh, O. Oudbashi, R. Naseri, S. Bahadori, *Journal of Archaeological Science: Reports*, **2025**, 65, 105186. <https://doi.org/10.1016/j.jasrep.2025.105186>
25. M. Grochowska-Jasnos, *Numismatyczny Sbornik*, **2022**, 36, 41.
26. C.C. Gavrila, M.Y. Lates, G. Grebenisan, *Sustainability*, **2024**, 16, 2322.
27. C. Toma, *Un tezaur monetar descoperit în localitatea Chișcău, jud. Bihor (sec. XVII)*, in I. Glodariu, G. Gheorghiu (ed.), *Studii de Istorie și Arheologie. Omagiu cercetătorului Dr. Eugen Iaroslavschi*, Cluj-Napoca, 2010, 292.
28. Siedmiogród, Gabriel *Bethlen (1613–1629)*. *Grosz szeroki 1626 CC, Koszyce*, <https://archiwum.niemczyk.pl/product/366185/siedmiogrod-gabriel-bethlen-1613-1629-grosz-szeroki-1626-cc-koszyce>, accessed on 9 october **2025**.
29. W. Mourray, *Metallic antiquities conservation from the archeological excavation to the museum*, Editura Tehnica, Bucuresti, **1998**.

ELECTROCHEMICAL pH-STAT AS ACIDITY MONITORING SYSTEM IN HIGH IONIC STRENGTH SOLUTIONS.

I. DESIGN CHALLENGES AND PRELIMINARY RESULTS

Gabriele-Mario BOGDAN^a , Sorin-Aurel DORNEANU^{b,*} 

ABSTRACT. Quantifying acidity has evolved from early attempts in the 1300s to the modern glass electrode pH sensor, which is difficult to implement for monitoring acid concentration in highly saline solutions. In this study a membrane-based filter-press electrochemical reactor functioning as a pH-stat that correlates current with acid concentration was tested. The behavior of HBr in KBr solutions was characterized, after which spectroscopic measurements of Alizarin Red S provided calibration curves used to validate glass electrode data. Reactor design principles and challenges were discussed, after which its behavior under non-polarized and polarized conditions was studied, concluding with two pH-stat tests, where different HBr concentrations were simulated by changing the acid molar flow rate, with pH values corroborated by spectroscopic measurements. A linear relationship was demonstrated between steady state current and acid molar flow rate. Imperfect membranes resulted in systematic errors between the amount of acid introduced and that neutralized. Preliminary results confirmed the feasibility of the electrochemical cell as an acid monitoring system, with future upgrades including PID control and design optimization.

Keywords: *glass electrode, pH-stat, electrochemical cell, acid concentration, high ionic strength*

INTRODUCTION

Quantifying the acidity of solutions has been attempted since at least the 1300s, when the first documented use of litmus was attributed to Arnaud de Villeneuve [1,2]. However, progress in understanding acidity was slow

^a Department of Chemical Engineering, Faculty of Chemistry and Chemical Engineering, Babeş-Bolyai University, 11 Arany Janos Street, RO-400028, Cluj-Napoca, Romania

^b Interdisciplinary Research Institute on Bio Nano Sciences, Babeş-Bolyai University, 42 Treboniu Laurian Street, RO-400271, Cluj-Napoca, Romania

* Corresponding author: sorin.dorneanu@ubbcluj.ro



until Arrhenius proposed the first modern acid-base theory, which was later refined by Brønsted and Lowry [3]. Defining acidity as a function of H^+ concentration led to the rapid development of detection and quantification methods and, eventually, to the invention of the glass electrode pH sensor, which is still widely used today [4]. A well-known limitation of glass electrodes is the so-called “sodium error”, where the sensor response becomes non-linear as it transitions from H^+ selectivity to Na^+ selectivity, phenomenon which also occurs, to a lesser extent, with K^+ [5,6]. In addition to the sodium error, Debye, Hückel (and later improvements to their theory) demonstrated that, in real solutions, ion-ion and ion-solvent interactions result in modified activity of solution components [6–9]. As a result, complex corrections based on activity coefficient models such as extended Debye-Hückel [7] and the Pitzer equations [10] must be implemented, both of which require precise information about solution composition and physical properties to provide accurate predictions. All these factors make the implementation of the classic glass electrode as H^+ concentration monitoring system very difficult or even impractical, especially in high ionic strength solutions.

Alternatively, another common method for monitoring H^+ concentration is acid-base titration using either chemical or electrochemical methods [11–14], with the main advantage of enabling precise composition monitoring through stoichiometry. One such apparatus is the classic pH-stat, which combines data from a pH sensor with an automated acid/base injection system to maintain pH at a constant value [15]. Various assembly variants and control schemes have been proposed in the almost one hundred years since its invention [11,12,16–19], but the topic receives increased attention especially in the biology modern literature. The aim of this paper is to design and test an ion exchange membrane (IEM) based filter-press electrochemical reactor (FPER) as pH-stat able to function as an acid concentration analyzer for a HBr/KOH electrosynthesis process. Our previous studies have demonstrated the possibility of using a four-compartment FPER for the electrosynthesis of KOH and HBr, with applications in a base metals recycling process from waste printed circuit boards (WPCBs) [20]. Preliminary process monitoring results have shown H^+ activities up to 20 times higher than expected for HBr in 2 M KBr solutions at most concentrations. In this work the discrepancy between H^+ concentration and measured pH was addressed and a more accurate and reliable real-time acidity monitoring system using a membrane-based electrochemical pH-stat was developed. To achieve this, first, the pH evolution was studied in HBr solutions of concentrations between $5 \cdot 10^{-5}$ M and $5 \cdot 10^{-1}$ M in KBr of $2 \cdot 10^{-3}$, $2 \cdot 10^{-2}$, $2 \cdot 10^{-1}$ and 2 M. Next, spectroscopic data for Alizarin Red S (ARS) was acquired, enabling the correlation between its absorption spectra at 522 and 422 nm with pH, which will serve to validate the glass

electrode data during pH-stat experiments. Finally, the FPER was tested, and its passive and active behavior determined. Increasing HBr concentrations were simulated by varying the molar flow rate of HBr, and its performance as an acidity monitoring system was evaluated.

RESULTS AND DISCUSSION

pH measurements in KBr solutions

Senanayake [21] proved the complex behavior of proton activity in HCl + CaCl₂ and highlighted the numerous factors (ion hydration number, liquid junction potential between the test solution and the reference solution inside the sensor, etc.) necessary to establish a reliable correlation between pH and real acid concentration.

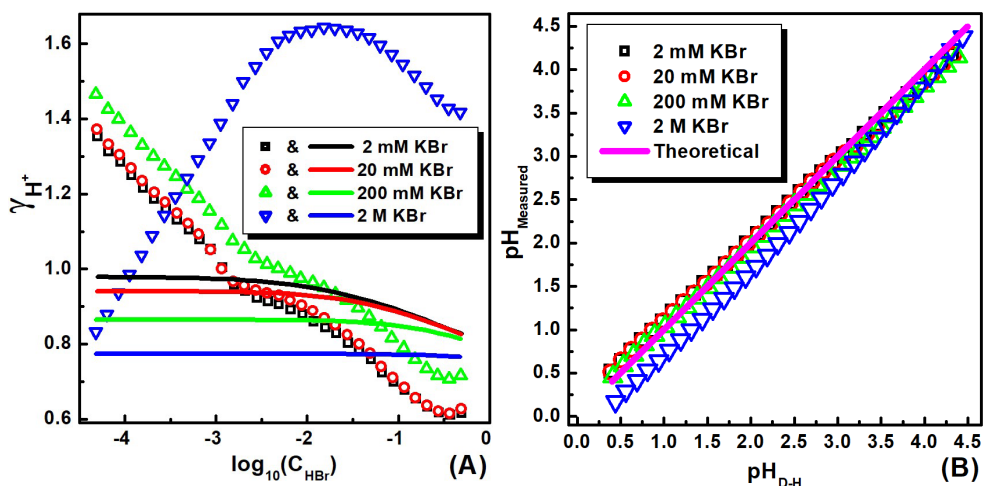


Figure 1. Correlation between the proton activity factor (γ_{H^+}) calculated by D-H (line) and from measured pH values (symbols) and $\log(C_{HBr})$ (A) and measured pH and computed pH using the D-H theory (B) for different concentrations of KBr indicated in inserts.

To determine the effect of these interactions in the HBr/KBr system, solutions of varying HBr and KBr concentrations were prepared to be used in controlled addition tests. Base solutions of $2 \cdot 10^{-3}$, $2 \cdot 10^{-2}$, $2 \cdot 10^{-1}$ and 2 M KBr with 10^{-5} M HBr were prepared, while the addition solutions had the same

concentrations of KBr with 1 M HBr. For the effective addition tests, 25 mL of base solution were introduced in a mixing cell using a calibrated pipette, over which 25 mL of addition solution was introduced in pre-calculated volumes using a calibrated peristaltic pump, resulting in constant KBr concentration and HBr concentrations ranging from $5 \cdot 10^{-5}$ M to $5 \cdot 10^{-1}$ M. Real activity coefficients were calculated by dividing the proton activity obtained from measured pH and real H^+ concentration and compared in Figure 1.A with the theoretical ones obtained with Debye-Hückel (D-H) theory. Furthermore, theoretical activity coefficients were used to compute theoretical pH values, which were plotted against the measured pH values, presented in Figure 1.B.

The results presented in Figure 1.A indicate that KBr concentration significantly impacts proton activity, especially at high concentrations. Interestingly, the calculated activity coefficients for HBr concentrations between $5 \cdot 10^{-5}$ and $5 \cdot 10^{-3}$ exceed unity in the lowest ionic strength solutions, in direct contradiction with D-H. This strange behavior at low H^+ concentrations can be attributed to CO_2 absorbed from the atmosphere, though its effect is negligible at higher HBr concentrations.

Additionally, it is evident that the D-H theory is insufficient to properly account for variations in the proton's activity factor. While D-H provides reasonable correction at 2, 20, and 200 mM KBr, even small pH errors translate into large concentration errors, especially in 2 M KBr. This confirms that, without proper and more complex corrections, glass electrodes are unsuitable for H^+ concentration monitoring under the required conditions.

Finally, the extremely large discrepancy between proton activity and concentration observed in our previous study could not be replicated, suggesting that the initial discrepancy observed may have been caused by a compromised pH electrode.

Spectroscopic measurements of Alizarin Red S

To validate the pH measurements obtained from our pH sensor, ARS was used as a reference pH indicator due to its three distinct colors: yellow, red, and purple in acidic ($pH < 6.3$), neutral and highly basic ($pH > 9.4$) solutions, respectively. Preliminary spectroscopic measurements were taken by controlled neutralization of HBr + 2 M KBr solutions with varying acid concentrations using KOH to obtain calibration curves. Example spectra for ARS under different pH conditions are presented in Figure 2.

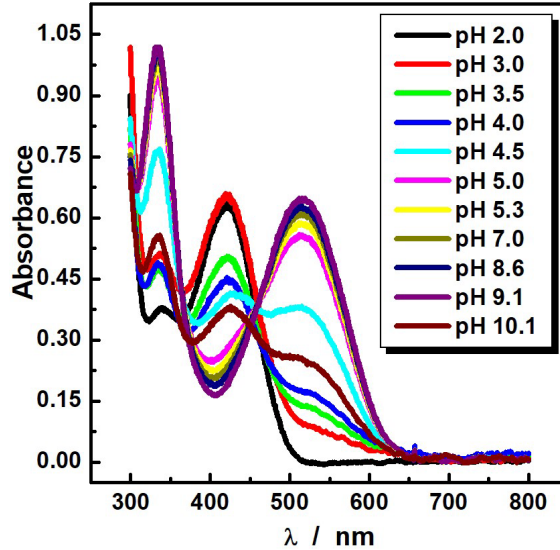


Figure 2. Examples of spectra obtained for ARS at different pH values during the neutralization tests.

The biggest absorption peaks can be observed around 422 nm under acidic conditions and 522 nm under basic conditions, with an inverse proportional relationship between the two. Inagawa et al. [22] proposed a relationship between pH and absorbance for indicators:

$$\log \frac{A(\lambda) - A_{In,\infty}}{A_{HIn,\infty} - A(\lambda)} = -pH + pK_a \quad (1)$$

where $A_{In,\infty}$ and $A_{HIn,\infty}$ represents the absorption of the indicator at the specific wavelengths in the protonated and deprotonated species, whereas $A(\lambda)$ represents the absorbance at a given wavelength. In the case of ARS, the specific wavelengths for the protonated and deprotonated forms are approximately 422 and 522 nm, respectively, which are also the wavelengths we study. To eliminate errors resulting from the experimental setup, the ratio between the absorption at 522 and 422 nm, called $R_{522/422}$, was used instead of $A(\lambda)$. In turn, the terms $A_{In,\infty}$ and $A_{HIn,\infty}$ become $R_{In,\infty}$ and $R_{HIn,\infty}$ and represent the ratio between the absorption in the deprotonated and protonated forms respectively, resulting in the following relationship:

$$\text{pH} = \log \frac{R_{\text{HIn},\infty} - R_{522/422}}{R_{522/422} - R_{\text{In},\infty}} + \text{pK}_a \quad (2)$$

The resulting ratios for the preliminary addition tests are presented in Figure 3. Optimal values for $R_{\text{HIn},\infty}$ and $R_{\text{In},\infty}$ and pK_a were obtained by non-linear fitting using JMP 18 Student Edition software.

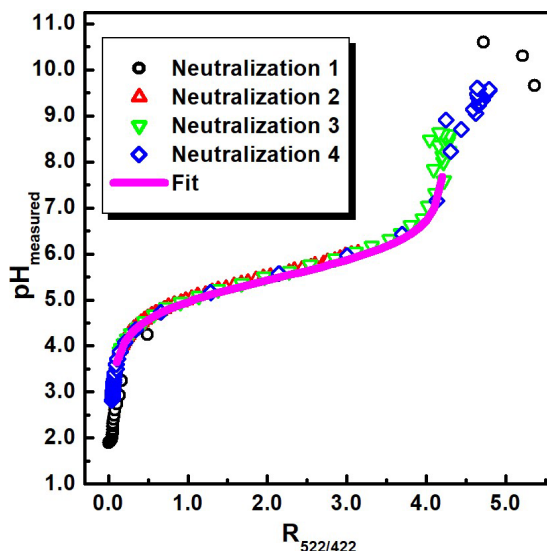


Figure 3. Preliminary calibration curves obtained through controlled neutralization and the resulting fit for ARS using equation (2).

The resulting pK_a value from the fit was 5.48, which is in excellent agreement with literature data for similar spectroscopic measurements of ARS [23]. This confirms that, around pH 5, the response of the glass electrode is accurate, even in high ionic strength solutions.

As can be observed from Figure 3, $R_{\text{HIn},\infty}$ and $R_{\text{In},\infty}$ represent the left and right vertical asymptotes of the graph, where $R_{\text{HIn},\infty}$ approaches 0 due to the complete absence of a peak at 522 nm in the protonated form, whereas $R_{\text{In},\infty}$ is 4.2 due to the large baselines of the surrounding peaks which increase the absorption value at 422 nm. These neutralization tests demonstrate the possibility of correlating spectroscopic measurements with real pH values; thus, Alizarin Red S can be used as a pH reference to validate glass sensor measurements.

FPER passive behavior tests

In order to evaluate the passive FPER behavior (without polarization), four diffusion tests (see experimental section) were performed using 0.1 M and 1 M KOH as anolyte and catholyte, with results presented in Figure 4. The time lag between the first three diffusion tests using 1 M KOH can be attributed to slightly different starting pH values. Due to the fast neutralization process using 1 M KOH, the behavior of 0.1 M KOH was also evaluated, resulting in a much slower neutralization speed.

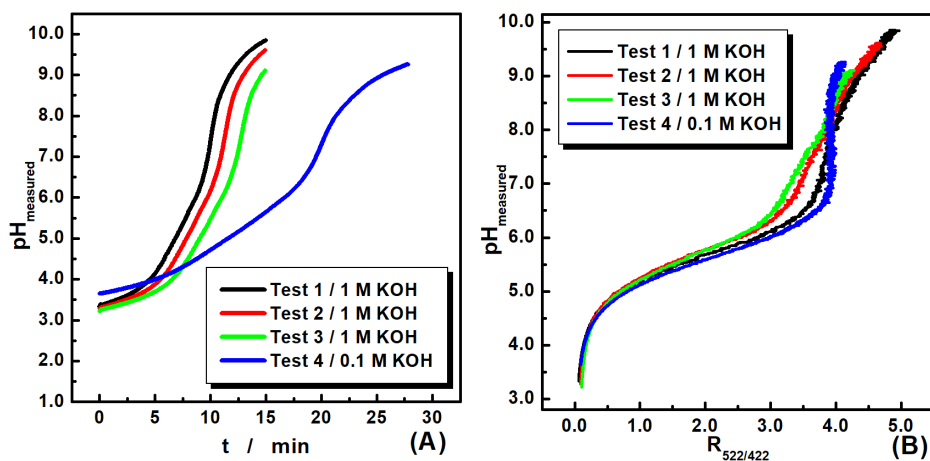


Figure 4. Results concerning the diffusion tests performed using 1 M and 0.1 M KOH as anolyte and catholyte: (A) evolution in time of measured pH; (B) the variation of measured pH in respect with the $R_{522/422}$ ratio.

For the first three diffusion tests the $\text{pH}_{\text{measured}} = f(R_{522/422})$ dependency does not follow the law described by Equation 2; however, the test using 0.1 M KOH fits very well. These unusual results obtained for the 1 M KOH diffusion tests can be attributed to insufficient mixing by the magnetic stirrer, which could not operate at high enough rotations per minute (RPM) due to risk of hitting the sensors. To solve this problem, a shielded electric motor designed for rotating disk electrodes was used, to which a stirring rod was attached using a brass collet. For precise control over mixing conditions, the electric motor was connected to a tachy-processor able to impose rotation speeds between 10 and 10000 RPM and was operated at 1000 RPM. Under the new mixing conditions, two diffusion tests were performed using 0.1 M KOH, and the results are presented in Figure 5. The resulting $\text{pH} = f(R_{522/422})$

correlation curves presented in Figure 5.B overlap perfectly, demonstrating the efficacy of the new mixing system and the reliability of ARS as a reference indicator.

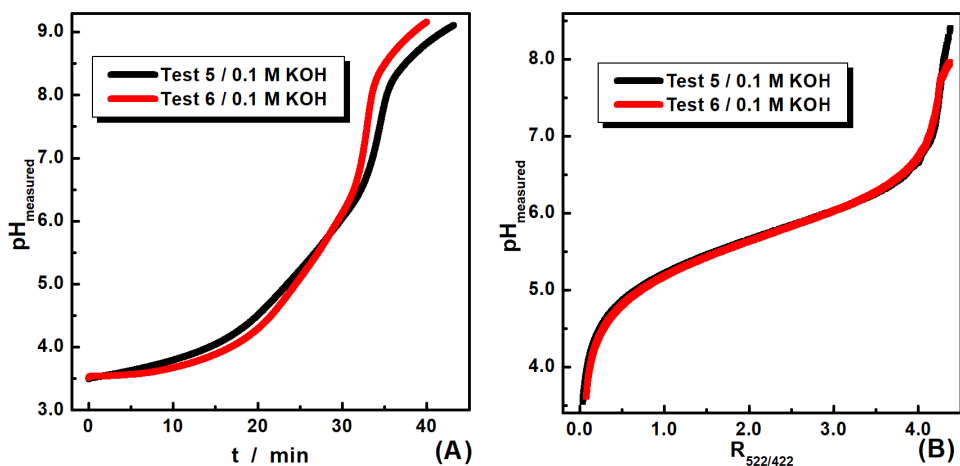


Figure 5. Results concerning the diffusion tests performed using 0.1 M KOH as analyte and catholyte using the improved mixing system: (A) evolution in time of measured pH; (B) the variation of measured pH in respect with the $R_{522/422}$ ratio.

Effectively, the process that took place in the reactor during the diffusion tests is called Donnan dialysis, where, under the driving force of concentration gradients (and cross-membrane potentials arising from these gradients), ions migrate selectively through the IEMs [24,25]. Consequently, the neutralization speed observed is the result of two main parallel processes: (i) the diffusion of OH^- through the anion exchange membrane (AEM) and the subsequent neutralization of H^+ , and (ii) the diffusion of H^+ through the cation exchange membrane (CEM) into the electrode compartment and its subsequent neutralization. To a lesser extent, since the membranes are not perfectly selective, a small quantity of H^+ diffused through the AEM into the cathodic compartment and, on the other side, a small quantity of OH^- diffused from the anodic compartment into the middle one. Additionally, K^+ and Br^- also migrated into the electrode compartments, thus contaminating the KOH fluxes with KBr. This is not an issue in our process due to specifics, however; different implementations must consider these ion diffusion effects when the reactor is idle.

The resulting correlation curves were fitted using Equation 2 in JMP 18 Student Edition for all diffusion tests performed using 0.1 M KOH and the resulting fitted coefficients are presented in Table 1.

Table 1. Fitted coefficients of equation (2) for preliminary controlled additions and all diffusion tests using KOH 0.1 M

Param.	Controlled Additions (Figure 3)	Test 4 0.1 M KOH	Test 5 0.1 M KOH	Test 6 0.1 M KOH	Average
pK_a	5.483	5.635	5.707	5.725	5.638
$R_{HIn,\infty}$	0.039	0.050	0.008	0.045	0.036
$R_{In,\infty}$	4.227	4.158	4.382	4.38	4.287

For validation of pH measurements, the averages of all fitted coefficients will be used. The average pK_a value is also within the reported pK_a range for ARS in literature [23].

Manual pH-stat experiments

After the passive behavior of the FPER was determined, the next step was to observe its behavior under operational conditions. To do this, 50 mL of 0.5 M HBr + 2 M KBr solution dyed with 1 mL of 0.0125 M ARS was prepared, which results in the same ARS concentration as that in the FPER. Fresh solutions of 1 M KOH were prepared and introduced in the buffer tanks of the electrode compartments after which the middle compartment and its liquid circuits were washed with distilled water then filled with the same solutions as described previously.

The first manual pH-stat experiment was conducted prior to identifying the mixing problem and it played a key role in debugging the experimental setup error. To start the experiment, the anodic compartment (AC) and the cathodic compartment (CC) were filled with the 1 M KOH solution from the buffer tanks. The electrodes were polarized, after which varying molar acid flow rates (N_{HBr}), meant to simulate increasing HBr concentration, were injected in the reactor. The current was manually adjusted until pH values remained relatively stable. The evolution of pH, current through the working electrode (I_{WE}) and N_{HBr} over the course of the experiment are presented in Figure 6. Additionally, glass electrode pH data was compared to pH values calculated from the measured $R_{522/422}$ ratio.

The HBr molar flow rate was adjusted 5 times in equal increments between 37.5 and 187.5 $\mu\text{mol/min}$ of HBr. The pH and spectroscopic measurements during this pH-stat test are very noisy due to improper mixing of the solution, which is evident at higher molar flow rates; however, they are in good agreement with each other.

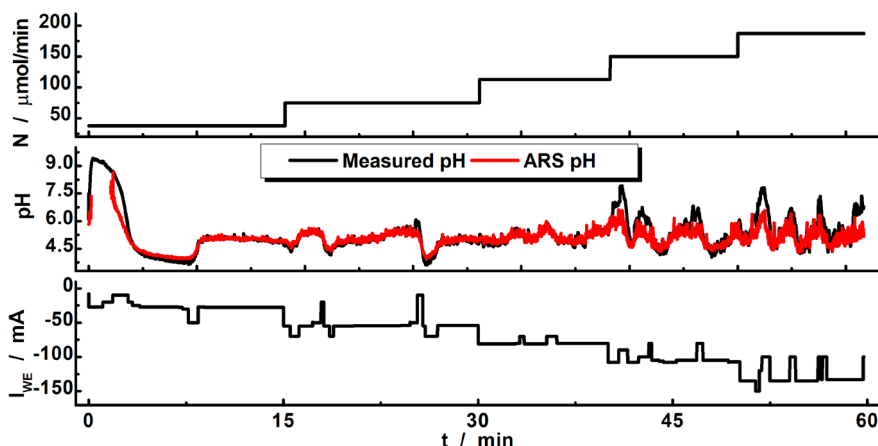


Figure 6. The evolution of N_{HBr} , measured and calculated pH from $R_{522/422}$ ratio, and current during the first manual pH-stat experiment.

After deploying the new and improved mixer, another manual pH-stat experiment was conducted. The FPER was set up in the same way as before, but the CC and AC were filled with 0.1 M KOH. Target pH was around 5, chosen due to the high sensitivity of the calibration curve in that area and faster response from the glass electrode compared to near-neutral solutions. Additionally, N_{HBr} was adjusted for times, in equal increments, between 7.5 and 30 $\mu\text{mol/min}$ of HBr. The evolutions of N_{HBr} , pH and I_{WE} over the course of the experiment are presented in Figure 7.

Using the improved mixing system, resulting pH values from the glass electrode and spectroscopic data show excellent agreement, with a significant reduction in measurement noise. For all acid injection flow rates, pH consistently stabilized around 5.2, indicating that the imposed current was sufficient for the complete neutralization of the introduced acid. To measure the effectiveness of the electrochemical cell as an acid concentration monitoring system, steady state current (I_{ss}) values were extracted for all tested N_{HBr} values and are presented in Figure 8.A. Additionally, the real amount of HBr neutralized, $N_{\text{HBr,neutralized}}$, was calculated using Faraday's law and compared against the theoretical value in Figure 8.B.

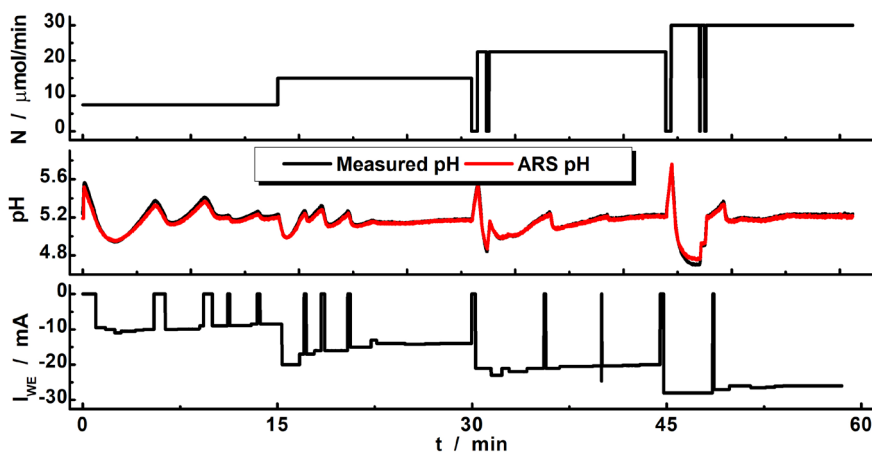


Figure 7. The evolution of N_{HBr} , measured and calculated pH from $R_{522/422}$ ratio, and current during the second manual pH-stat experiment.

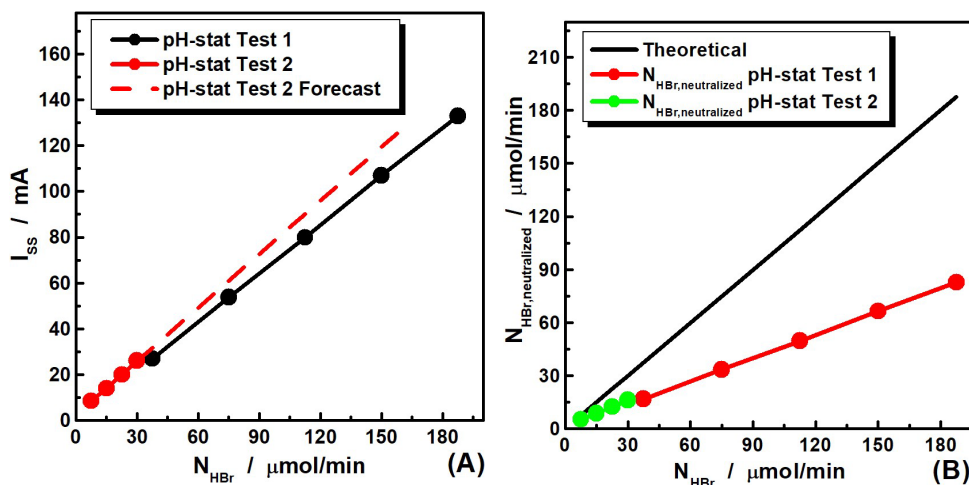


Figure 8. Influence of N_{HBr} on steady-state current during both manual pH-stat tests (A) and calculated neutralized molar fluxes using Faraday's law against theoretical values (B)

Figure 8.A shows that the relationship between N_{HBr} and I_{ss} is very linear ($R^2 > 0.999$) for both pH-stat tests, with a slight difference in slope. The difference in slope can be attributed to the faster diffusion of KOH through the IEMs at 1 M since, by extrapolating the data from the second pH-stat test, we can see that I_{ss} values are consistently lower than when

using 0.1 M KOH. Figure 8.B indicates that less acid than actually was neutralized, resulting in current efficiency over 100% for all N_{HBr} tested. This cannot be true, however, since for pH to remain constant, N_{HBr} and $N_{\text{HBr,neutralized}}$ must be equal. These conflicting results can be explained by the imperfect nature of the IEMs. In theory, under the influence of an electric field, the migration of ions towards the electrodes should account for the vast majority of mass transport through the membranes. However, Ozkul et al. [26] have shown that convection can represent up to 35% of the total ion flux through the membrane. Membrane charge density also plays a very important role in the ion selectivity of the membrane. Consequently, low charge density membranes induce significant membrane co-ion fluxes, negatively impacting ion selectivity [27,28]. The cumulative effect of these phenomena is constant, systematic and specific for a given system, meaning that it can be accounted for with periodic calibration of the FPER.

CONCLUSIONS

This study successfully elucidated the observed extremely large proton activity factor in the HBr + KBr system, simultaneously demonstrating the infeasibility of implementing glass electrode pH sensors as standalone H^+ concentration monitoring systems. Pertinent Alizarin Red S spectroscopic data was acquired, which enabled the obtaining of $\text{pH}=\text{f}(\text{R})$ correlation curves that served to validate glass electrode pH data. A filter-press electrochemical reactor using an anion exchange membrane and a cation exchange membrane was built and tested under passive and polarized conditions, which allowed for the identification and correction of design flaws. Two manual pH-stat tests were conducted by varying applied current for different acid injection flow rates, simulating real increase of HBr concentration during electrosynthesis, better results being obtained using the improved mixing system. FPER based pH-stat performance as an acidity monitoring system was evaluated, resulting in a very linear relationship between acid molar flow rate and steady state current. The discrepancy between the introduced acid molar flow rate and that neutralized calculated using Faraday's law was explained by imperfect membrane behavior. Further studies should focus on implementing PID (Proportional, Integral and Derivative) control of the system, acquiring more $I_{\text{SS}}=\text{f}(N_{\text{HBr}})$ data and optimizing the reactor design.

EXPERIMENTAL SETUP

Chemicals

All chemicals used were of analytical grade ($p > 99\%$). Solid KOH and KBr used in the preparation of all solutions containing these substances were purchased from Merck, Germany. HBr 48% from Merck, Germany was used for the preparation of stock HBr 2 M solution which was used for the preparation of all other solutions containing HBr. Standard buffer solutions HI 5007 of pH 7.01 and HI 5002 of pH 2.00 were purchased from Hanna Instruments, Romania and used for periodic calibration of the pH sensor. Alizarin Red S used for the preparation of stock 0.0125 M solution was also purchased from Merck, Germany. Double distilled water from a lab-grade distillation system was used for the preparation of all solutions in this study.

Filter press electrochemical reactor design

To neutralize the introduced acid, a three-compartment filter press electrochemical reactor equipped with an AEM, a CEM and two nickel electrodes was deployed. The electrochemical reaction taking place in the electrode compartments is water electrolysis in basic conditions. A detailed schematic of the reactor design is presented in Figure 9.

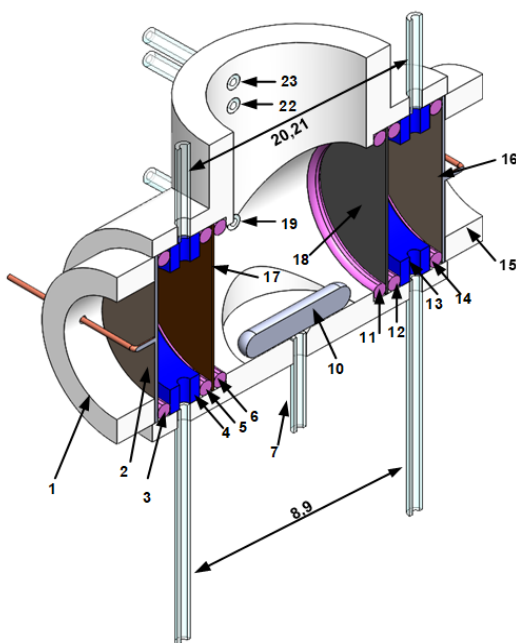


Figure 9. Detailed schematic of the initial FPER based pH-stat design. 1,15 – Pressing caps; 2,16 – Ni electrodes; 3,5,6,11,12,14 – Rubber O-rings; 4,13 – AC and CC spacers; 7 – Acid injection tube; 8,9 – AC and CC inlets; 10 – Magnetic stirrer; 17 – CEM; 18 – AEM; 19 – Z-cell inlet; 20-21 – AC and CC outlets; 22 – Overflow; 23 – Z-cell outlet

The reactor was assembled and pressed between two metal plates using screws. To ensure all the compartments are watertight, the screws were slowly tightened over the course of a few days to allow the O-rings to deform and maintain a good seal. Although not shown on the schematic, a glass electrode pH sensor and an LM35 temperature sensor connected to data acquisition hardware were placed in the middle compartment. The reactor was primed by filling the middle compartment with water and the electrode compartments with 1 M KOH to allow the membranes to swell and to exchange counter-ions.

Equipment

The following commercial equipment was used: one SP10T pH/T combined sensor (Consort, Belgium), one LM35 semiconductor-based temperature sensor, two Reglo Digital MS-2/8 peristaltic pumps called PP1 and PP2 (ISMATECH, Switzerland), one Reglo Analog MS-2/8 peristaltic pump called PP3 (ISMATECH, Switzerland), one NI PCI-6259M data acquisition board (National Instruments, USA) inside of a pre-built computer, one analogical tachy-processor (Radiometer Analytical, France), one DXC236 potentiostat/galvanostat (P/G-stat) (Datronix Computers, Romania). For spectrometric measurements, one USB-4000 modular UV-VIS diode array spectrophotometer, two QP600-025-SR UV optical fibers, a FIA-Z-SMA-PEEK flow spectrophotometric cell with 10 mm optical path, a UV-VIS-NIR DT-MINI-2-GS light source, all from Ocean Optics (USA) were used. The AEM and CEM used in the reactor are a FUMASEP FAB-PK-130 (FUMATECH BWT GmbH, Germany) and a Nafion 423 (DuPont, France) respectively. Several pieces of proprietary equipment and software developed by Author S.-A. Dorneanu were also used.

Experimental setup

A simplified scheme of the experimental setup used during the diffusion and manual pH-stat tests is presented in Figure 10. The main elements are the FPER, the optical setup, the data acquisition and signal generation equipment and the pumps vehiculating liquids inside their circuits.

The catholyte and anolyte tanks (TC and TA) contained the 1 M or 0.1 M KOH solutions pumped in the electrode compartments. The THA tank contains the HBr + KBr + ARS solution which was injected into the

middle compartment and all collected liquid which reached the overflow was directed in the waste tank (TW). The pH and temperature sensors were connected via a proprietary equipment to the data acquisition system.

The FPER electrodes were connected to the working electrode (WE) and the counter electrode (CE) terminals of the P/G-stat, respectively. Silver wires, serving as reference electrodes, were introduced in the inlets of the electrode compartment and were connected to the REF1 and REF2 terminals of the P/G-stat. Initial experimental setup did not have the Mixer element, instead a teflon magnetic rod was used for stirring using the magnetic stirrer below. Later, the magnetic rod was removed and replaced by the Mixer pictured below, which was connected to the tachy-processor, for which the speed was set manually.

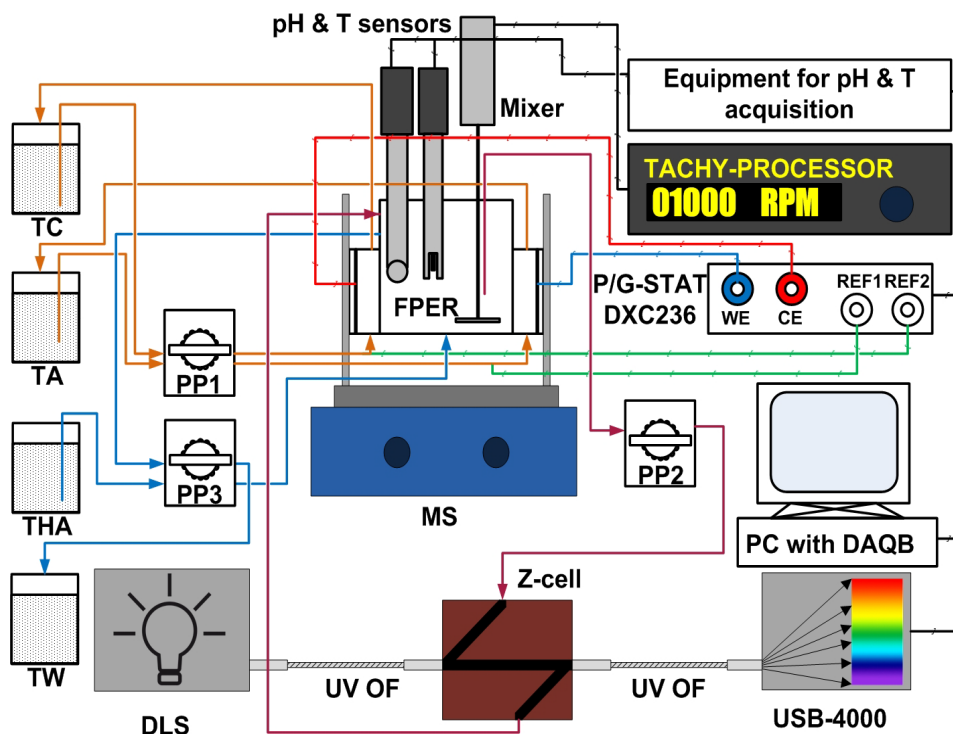


Figure 10. Experimental setup used for the diffusion and manual pH-stat tests: TC – Catholyte Tank; TA – Anolyte Tank; THA – HBr + ARS tank; TW – Waste Tank; PP – Peristaltic pump; MS – Magnetic Stirrer; DLS – Deuterium-Tungsten light source; UV OF – Ultra-violet optical fiber; FPER – filter press electrochemical reactor; P/G-STAT – potentiostat/galvanostat; PC with DAQB – PC with data acquisition board.

Though not shown on the schematic, the pumps, magnetic stirrer (and later tachogenerator) and light source were controlled by the computer through user input. Pump PP1 vehiculated the KOH solutions through the electrode compartments and pump PP2 completed the liquid circuit of the optical setup. Pump PP3 had a calibrated 1.5 mL/min tube which was used for acid addition and another tube of higher flow rate (20 mL/min) evacuating liquid from the overflow. For the initial standard addition tests of acid into ARS, PP1 was disconnected and the FPER was replaced with a simple mixing cell.

At the start of all FPER experiments, 36 mL of KBr 2 M and 0.7 mL of ARS 0.0125 M are added to the middle compartment of the reactor. TC and TA are filled with KOH solution and PP1 is run continuously over the course of the experiments. The HBr + KBr solutions used for addition were prepared in a 50 mL volumetric flask by adding appropriate volumes of stock KBr and HBr solutions and 1 mL of ARS 0.0125 M, resulting in approximately equal ARS concentrations for both addition and FPER solutions, thus avoiding the influence of indicator dilution. For diffusion tests, acid is added using PP2 until the desired pH is reached, after which it's stopped, and pH is monitored under no polarization. For pH-stat tests, pump PP2 is run continuously, and different currents are imposed by the P/G-stat through computer command. Current is manually adjusted until pH values stabilize.

Because of the complex behavior of proton activity and glass electrodes in high ionic strength solutions, we need to corroborate observed pH values using another method which functions on separate principles. Consequently, ARS was used as a witness pH indicator to validate pH values obtained by the glass electrode.

ACKNOWLEDGEMENTS

Author Gabriele-Mario Bogdan is grateful to Babeş-Bolyai University for the Special Scholarship for Scientific Activity (2024-2025), contract number 35809/28.11.2024.

REFERENCES

1. H. Marc; *La vie et les oeuvres de maitre Arnaud de Villeneuve*, Chamuel, Paris, **1896**.
2. G. Gauglitz; *Anal. Bioanal. Chem.*, **2018**, 410, 1–3.
3. M. S. Kamble; M. S. S. Chougule; *IJARST*, **2022**, 2.
4. D. J. Graham; B. Jaselskis; C. E. Moore; *J. Chem. Educ.*, **2013**, 90, 345–351.

5. F. G. K. Baucke; *Fresenius' J. Anal. Chem.*, **1994**, 349, 582–596.
6. L. Martell-Bonet; R. H. Byrne; *Mar. Chem.*, **2020**, 220, 103764.
7. G. M. Silva; X. Liang; G. M. Kontogeorgis; *Mol. Phys.*, **2022**, 120, e2064353.
8. M. N. Khan; P. Warrier; C. J. Peters; C. A. Koh; *J. Nat. Gas Sci. Eng.*, **2016**, 35, 1355–1361.
9. L. Sun; Q. Lei; B. Peng; G. M. Kontogeorgis; X. Liang; *Fluid Phase Equilib.*, **2022**, 556, 113398.
10. B. Anes; R. J. N. Bettencourt Da Silva; H. F. P. Martins; C. S. Oliveira; M. F. Camões; *Accred. Qual. Assur.*, **2016**, 21, 1–7.
11. C. Fenster; M. Rohwerder; A. W. Hassel; *Mater. Corros.*, **2009**, 60, 855–858.
12. R. E. Adams; S. R. Betso; P. W. Carr; *Anal. Chem.*, **1976**, 48, 1989–1996.
13. F. A. Posey; T. Morozumi; E. J. Kelly; *J. Electrochem. Soc.*, **1963**, 110, 1183.
14. A. D. Kalafatis; L. Wang; W. R. Cluett; *IFAC Proc. Vol.*, **2004**, 37, 823–828.
15. S. Lee; S. W. Sung; J. Lee; *Int. J. Control Autom. Syst.*, **2013**, 11, 442–449.
16. C. A. Pérez-Rojas; C. A. Martínez-Martínez; E. Palacios-Mechetnov; M. C. Lora-Vilchis; *Aquac. Eng.*, **2022**, 99, 102300.
17. M. C. Palancar; J. M. Aragón; J. S. Torrecilla; *Ind. Eng. Chem. Res.*, **1998**, 37, 2729–2740.
18. M. R. Pishvaei; M. Shahrokhi; *Ind. Eng. Chem. Res.*, **2000**, 39, 1311–1319.
19. S. W. Sung; I.-B. Lee; D. R. Yang; *Ind. Eng. Chem. Res.*, **1995**, 34, 2418–2426.
20. G.-M. Bogdan; M. I. Frîncu; S.-A. Dorneanu; *Studia UBB Chemia*, **2024**, 69, 177–191.
21. G. Senanayake; *Miner. Eng.*, **2007**, 20, 634–645.
22. A. Inagawa; A. Sasaki; N. Uehara; *Talanta*, **2020**, 216, 120952.
23. A. A. Shalaby; A. A. Mohamed; *RSC Adv.*, **2020**, 10, 11311–11316.
24. D. Asante-Sackey; S. Rathilal; E. Kweinor Tetteh; E. O. Ezugbe; L. V. Pillay; *Membranes*, **2021**, 11, 358.
25. H. Fan; N. Y. Yip; *ACS EST Eng.*, **2022**, 2, 2076–2085.
26. S. Ozkul; J. J. Van Daal; N. J. M. Kuipers; R. J. M. Bisselink; H. Bruning; J. E. Dykstra; H. H. M. Rijnaarts; *J. Membr. Sci.*, **2023**, 665, 121114.
27. M. Tedesco; H. V. M. Hamelers; P. M. Biesheuvel; *J. Membr. Sci.*, **2016**, 510, 370–381.
28. M. Tedesco; H. V. M. Hamelers; P. M. Biesheuvel; *J. Membr. Sci.*, **2017**, 531, 172–182.

STUDY OF ELECTROCHEMICAL BEHAVIOR OF VI-B GROUP METAL OXIDES IN TUNGSTATE MELT

Victor MALYSHEV^a, Angelina GAB^a, Ana-Maria POPESCU^{b*},
Virgil CONSTANTIN^{b*}

ABSTRACT. Thermodynamic assessment of the probability of interaction of metal oxides of group VI-B with tungstate melts, the results of the study of the acid-base properties of tungstate melt by potentiometric method. Analysis of the presented experimental data on the study of the electrochemical behavior of chromium, molybdenum and tungsten under equilibrium and non-equilibrium conditions allows us to conclude that it is possible to implement multi-electron reversible equilibria and electroreduction processes involving oxide forms of chromium, molybdenum and tungsten (VI) in tungstate melts. The mechanism and final product of electroreduction of oxide forms of metal (VI) depend on the acid-base properties of the medium. By setting the latter, it is possible to control the electrode process.

Keywords: VI-B group metals, thermodynamic assessment, electrochemical behavior, multielectron processes.

INTRODUCTION

Melts based on tungstates of alkali and alkaline-earth metals are practically important for the production of VI-B group metals in the form of dispersed powders [1-5] and coatings [1, 4, 6-9], of alloys and intermetallics [9-11], of oxides and bronzes of various stoichiometric compositions [1, 12, 13], as well as for the synthesis of compounds with nonmetals (carbides, borides, silicides, phosphides, sulfides) [13-16]. The composition of cathode precipitates

^a International European University, 42 V Academician Glushkov Avenue, 03187, Kyiv, Ukraine

^b Romanian Academy, "Ilie Murgulescu" Institute of Physical Chemistry, Laboratory of Electrochemistry and Corrosion, 202 Splaiul Independentei, 060021, Bucharest, Romania

* Corresponding authors: virgilconstantin@yahoo.com, popescuamj@yahoo.com



in these melts is largely determined by the acid-base properties of the melts [17-20]. As compounds influencing the acidity/basicity of tungstate melts, particularly VI-B group metal oxides can be used, which can act not only as acceptors of oxygen ions, but also as components in the electrochemical production of metals and in the synthesis of their compounds.

Statement of the problem. The aim of the work is to study the electrochemical behavior of VI-B group metal oxides in tungstate melts and to identify the possibility of the existence of equilibria involving VI-B group metal electrodes. Achieving this goal will make it possible to control the acid-base properties of melts and to use the results of studies of the electrochemical behavior of VI-B metal oxides in tungstate melts for the practical implementation of electrodeposition of VI-B metals and their compounds.

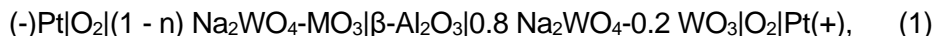
RESULTS AND DISCUSSION

1. Thermodynamic assessment of the probability of interaction of group VI-B metal oxides with tungstate melts. The literature contains virtually no information on the chemical interactions of tungstate melts with group VI-B metal oxides. We performed thermodynamic calculations of possible reactions of interaction of these oxides with sodium tungstate (Table 1). It can be seen that chromium (VI), molybdenum (VI), and tungsten (VI) oxides are likely to interact with these melts to form dimeric compounds. Although the performed thermodynamic calculations suggest only the possibility of reactions for tungstate melts, they can be quite useful in explaining the model of the ionic composition of the melt. According to the calculations, the most energetically beneficial reactions are those involving the formation of ditungstate compounds.

Table 1. Temperature dependence of the standard free energy ΔG°_T of the interactions of sodium tungstate with oxygen-containing group VI-B elements compounds.

Nr.	Reactions	ΔG°_T , kJ				
		298 K	900 K	1000 K	1100 K	1200 K
1.	$2\text{Na}_2\text{WO}_4 + 2\text{CrO}_3 = \text{Na}_2\text{Cr}_2\text{O}_7 + \text{Na}_2\text{W}_2\text{O}_7$	-131.37	-409.81	-365.01	-320.62	-284.88
2.	$2\text{Na}_2\text{WO}_4 + \text{CrO}_3 = \text{Na}_2\text{CrO}_4 + \text{Na}_2\text{W}_2\text{O}_7$	-79.73	-234.25	-211.19	-109.51	-165.81
3.	$\text{Na}_2\text{WO}_4 + \text{MoO}_3 = \text{Na}_2\text{MoO}_4 + \text{Na}_2\text{W}_2\text{O}_7$	-44.35	-53.51	-47.49	-43.60	-37.74
4.	$2\text{Na}_2\text{WO}_4 + 2\text{MoO}_3 = \text{Na}_2\text{Mo}_2\text{O}_7 + \text{Na}_2\text{W}_2\text{O}_7$	-79.91	-94.77	-83.68	-70.12	-57.32
5.	$\text{Na}_2\text{WO}_4 + \text{WO}_3 = \text{Na}_2\text{W}_2\text{O}_7$	-23.26	-32.30	-27.03	-23.93	-22.68

2. Study of tungstate melt acid-base properties by methods of potentiometry of cooled samples. To explain the experimental dependences of the tungstate melts behavior under equilibrium and nonequilibrium conditions, the following model of the ionic composition of such melts can be proposed, considering oxygen-containing compounds as conjugated acids-bases. It is assumed that in the Na_2WO_4 melt, the ions Na^+ , $(\text{WO}_4)^{2-}$, $(\text{W}_2\text{O}_7)^{2-}$, and $(\text{O})^{2-}$ are predominantly present, which are in equilibrium with each other. So, this can be considered as molten polytungstate electrolyte of the composition $2\text{Na}^+ + (\text{W}_n\text{O}_{2n+1})^{2-}$, where $n > 1$. The shift in interionic equilibria in such melt can be explained by a "quasi-chemical" approach. When chromium, molybdenum, and tungsten oxides are added to the tungstate melt, the following reactions are possible (Table 1): for CrO_3 - (1) and (2), MoO_3 - (3) and (4), WO_3 - (5). To study changes in the oxygen ions activity in such melts, electrochemical cells with oxygen electrodes can be used:



where $M = \text{Cr}, \text{Mo}, \text{or } \text{W}$. In this case, one of the electrodes is semi-immersed into a stable-composition melt with known oxygen ions activity. The study was carried out in air at a constant oxygen partial pressure above the melt ($P(\text{O}_2) = 21.3 \text{ kPa}$). The diffusion potential value between the studied melt and the reference electrode melt was negligible and, according to calculations, did not exceed $3 \cdot 10^{-3} \text{ V}$ (since alkali metal cations play a major role in the current transfer process [21, 22]). Therefore, the oxygen electrode potential is practically determined by the ratio of the oxygen ions activities in the studied melt and in the reference electrode melt. At low concentrations of oxygen ion acceptors, the tungstate melt consists mainly of Na^+ , $(\text{WO}_4)^{2-}$, $(\text{W}_2\text{O}_7)^{2-}$, and $(\text{O})^{2-}$ ions. At a high acceptors concentration, it is also necessary to take into account the presence of $(\text{W}_3\text{O}_{10})^{2-}$, $(\text{W}_4\text{O}_{13})^{2-}$, and other more complex particles.

From the dependence of the equilibrium potential of the oxygen electrode on the concentrations of group VI-B metal oxides (Fig. 1), it follows that its value shifts to the positive region when the oxides are introduced into the tungstate melt. Thus, these oxides are oxygen ions acceptors. Such a course of dependencies can be explained by considering oxygen-containing compounds as conjugated acids-bases. There is an equilibrium in the tungstate melt:



with an equilibrium constant (K):

$$K = \frac{a_{\text{WO}_4^{2-}}^2}{a_{\text{W}_2\text{O}_7^{2-}} a_{\text{O}^{2-}}} \quad (3)$$

When CrO_3 , MoO_3 , or WO_3 oxides are added to the sodium tungstate melt, dichromate, dimolybdate, and ditungstate ions can also be formed according to reactions (1), (4), and (5), respectively.

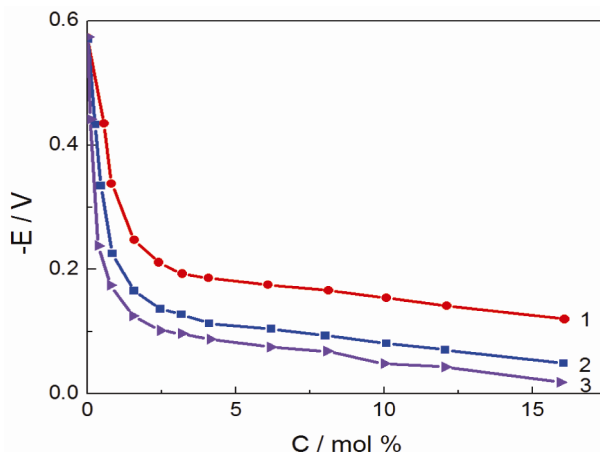


Figure 1. Equilibrium potentials of the oxygen electrode when metal oxides of group VI-B are introduced into the sodium tungstate melt: 1 - Cr_2O_3 ; 2 - MoO_3 ; 3 - WO_3 ; $T = 1173 \text{ K}$.

3. Electroreduction of chromium (VI), molybdenum (VI) and tungsten (VI) oxides on the background of tungstate melt. In the stationary and non-stationary voltammetric dependences (Figs. 2a and 2b) of the tungstate melt containing group VI-B metal oxides with an oxidation degree of metal equal to +6, a reduction wave was observed at potentials from -0.7 V to -1.0 V for CrO_3 , from -0.9 V to -1.2 V for MoO_3 , and from -1.1 V to -1.3 V for WO_3 . At concentrations of MoO_3 and WO_3 of around $(3\div 6) \times 10^{-4} \text{ mol/cm}^3$, the main wave is preceded by an alloying wave. The possibility of the existence of intermetallics is confirmed by data [23]. At higher oxides concentrations, the alloying wave disappears, because the potential of the main process becomes more positive. In the case of addition of CrO_3 to the tungstate melt, the alloying wave is not observed, since in this case the electroreduction product is chromium (III) oxide rather than chromium metal. An increase in the concentration of all three oxides leads to an increase in the wave height and its shift to the positive potentials region. In this case, the transformation of the extended wave into a sickle-like one is observed. The reduction process occurs in one stage. Increasing the scan rate up to 10 V/s does not allow one to detect the process stages sequence.

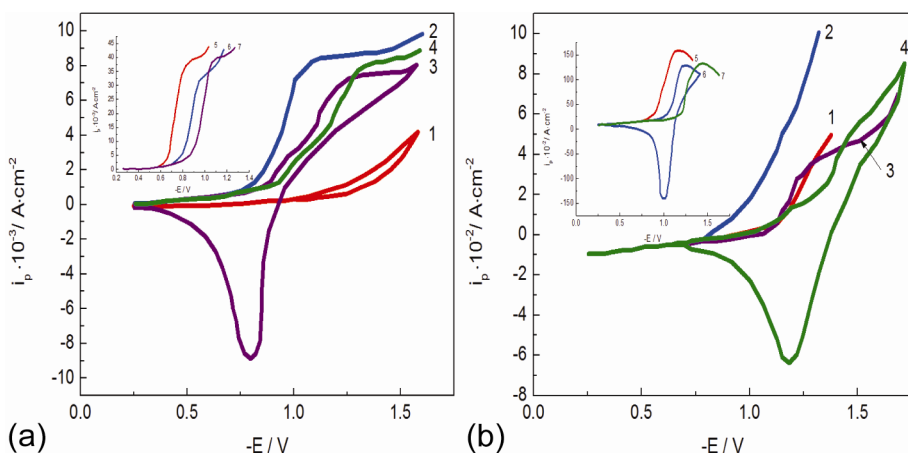


Figure 2. Stationary voltammetric dependences of the melt containing
a) MO_3 (M: Cr, Mo, W); 1 - Na_2WO_4 background; 2, 5 - CrO_3 addition [CrO_3]: $4 \cdot 10^{-4}$ mol/ cm^3 , $9 \cdot 10^{-4}$ mol/ cm^3 ; 3, 6 - MoO_3 addition [MoO_3]: $4 \cdot 10^{-4}$ mol/ cm^3 , $9 \cdot 10^{-4}$ mol/ cm^3 ; (4, 7) - WO_3 addition, [WO_3]: $4 \cdot 10^{-4}$ mol/ cm^3 , $9 \cdot 10^{-4}$ mol/ cm^3 ; T = 1173 K, working electrode - platinum, scan rate - 0.02 V/s;
b) Na_2WO_4 melt; 1 - Na_2WO_4 background; 2, 5 - CrO_3 addition; [CrO_3]: $6 \cdot 10^{-4}$ mol/ cm^3 , $1 \cdot 10^{-3}$ mol/ cm^3 ; 3, 6 - MoO_3 addition [MoO_3]: $6 \cdot 10^{-4}$ mol/ cm^3 , $1 \cdot 10^{-3}$ mol/ cm^3 ; 4, 7 - WO_3 addition, [WO_3]: $6 \cdot 10^{-4}$ mol/ cm^3 , $1 \cdot 10^{-3}$ mol/ cm^3 ; T = 1173 K, cathode - platinum, scan rate - 1.0 V/s.

Potentiostatic electrolysis at the observed wave potentials reveals the following products: in the case of CrO_3 - Cr_2O_3 oxide powder within the entire studied concentration range. This is confirmed by further calculations of the number of electrons for electrochemical processes that occur at platinum and chromium electrodes. In the case of WO_3 - metallic tungsten up to WO_3 concentrations 20 mol %, and in the case of MoO_3 - metallic molybdenum up to MoO_3 concentrations 4 mol %. If the concentration limits are exceeded, the electrolysis products are tungsten and molybdenum dioxides, respectively.

The peak current dependences on the oxide concentration at different scan rates are characterized by a directly proportional current increase with the oxide concentration change (Fig. 3). The ratio $i_p/v^{1/2}$ values from dependences of $i_p/v^{1/2}$ on $v^{1/2}$ remain practically constant within a wide range of scan rates from 0.04 up to 2.00 V/s (Fig. 4). The mass transfer constants i_p/nF_c for stationary waves (calculated within the range of MO_3 (M = Mo, W) concentrations $(5 \div 15) \cdot 10^{-4}$ mol/ cm^3) are $(0.73 \div 2.23) \cdot 10^{-4}$ cm/s and are commensurate with those for diffusion delivery. The direct proportional dependence of the limiting current on the metal (VI) oxide concentration, the constancy of the $i_p/v^{1/2}$ ratio values within a wide scan rates range, as well as

the i_p/nF_c ratio value, indicate that the electrode process is limited by the diffusion of electroactive particles to the electrode surface. So, under these polarization regimes, the electroactive particles formation rate does not impose restrictions on the electrode process.

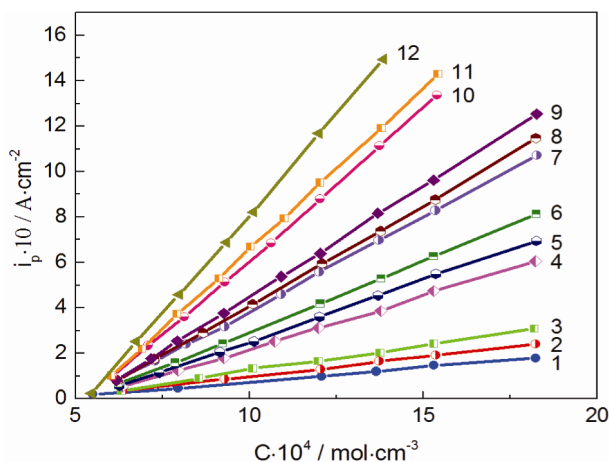


Figure 3. Peak current density dependence on the concentration of MO_3 ($M = \text{Mo}, \text{W}$) at different scan rates. 1 - MoO_3 , 0.02 V/s; 2 - WO_3 , 0.02 V/s; 3 - Cr_2O_3 , 0.02 V/s; 4 - MoO_3 , 0.50 V/s; 5 - WO_3 , 0.50 V/s; 6 - Cr_2O_3 , 0.50 V/s; 7 - MoO_3 , 1.00 V/s; 8 - WO_3 , 1.00 V/s; 9 - Cr_2O_3 , 1.00 V/s; 10 - MoO_3 , 5.00 V/s; 11 - WO_3 , 5.00 V/s; 12 - Cr_2O_3 , 5.00 V/s; $T = 1173 \text{ K}$.

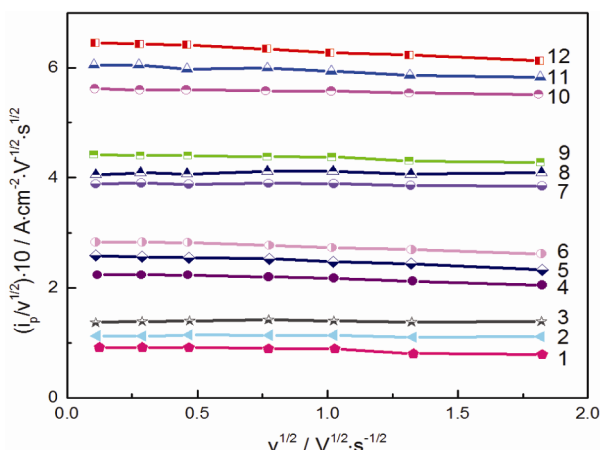
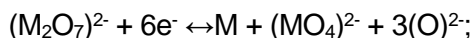


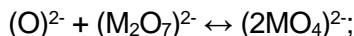
Figure 4. Dependence of $i_p/v^{1/2}$ on $v^{1/2}$ for the electroreduction process of chromium, molybdenum, and tungsten containing ions at $[\text{MO}_3] \times 10^4, \text{ mol/cm}^3$: (1-3) - 7.0; (4-6) - 8.0; (7-9) - 10.0; (10-12) - 12.0; (1, 4, 7, 10) - MoO_3 ; (2, 5, 8, 11) - WO_3 ; (3, 6, 9, 12) - CrO_3 . $T = 1173 \text{ K}$, cathode - platinum, scan rate - 1.0 V/s

The mechanism of electroactive particles formation becomes clear if we proceed from the concept of the existence of acid-base equilibria in tungstate melts. The decrease in the activity of oxygen ions when MO_3 is added to the tungstate melt is evident in the dependences of the equilibrium potentials of the oxygen electrode (Fig. 1). The addition of MO_3 shifts this electrode potential toward positive values, i.e., reduces the oxygen ions activity in the melt. The sodium tungstate melt is quite stable and can be used as a background solvent for the electroreduction of chromium (molybdenum, tungsten) (VI) oxide forms. The first additions of MO_3 lead to the formation of predominantly monomeric $(\text{MO}_4)^{2-}$ ions; the concentration of dimeric $(\text{M}_2\text{O}_7)^{2-}$ ions is negligible. Monomeric forms exhibit electrochemical activity at potentials comparable to the background electrolyte decomposition potential. The further MO_3 addition leads to an increase in the concentration of dimeric $(\text{M}_2\text{O}_7)^{2-}$ ions which exhibit electrochemical activity at much more positive potentials.

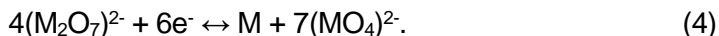
These ideas are also confirmed by our thermodynamic calculations of possible reactions of MO_3 oxides with sodium tungstate (sodium molybdate). In the case of metal deposition, the electrode process can be summarized as follows:



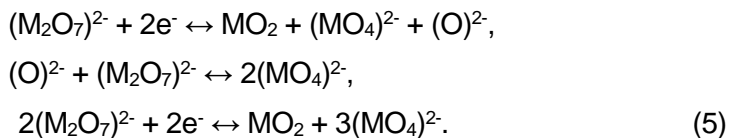
or, taking into account the subsequent rapid chemical ionic reaction,



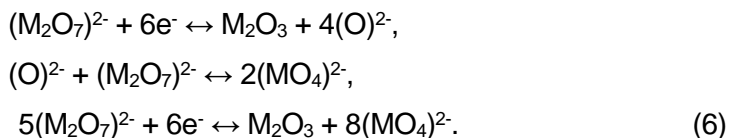
the gross equation of the electrode process will be as follows:



In the case of metal (IV) oxide deposition, these equations can be written as follows:



In the case of metal (III) oxide deposition, these equations take the following form:



To clarify the nature of the charge transfer stage (4)-(6), and to determine the number of electrons transferred in the electrode process, the stationary voltammetric dependences obtained at platinum electrodes were analyzed in the semilogarithmic coordinate system $E\text{-lg}(i_d-i)$. The sickle-like shape of the stationary waves necessitates the use of the Kolthoff-Lingane equation. The composition of electrolysis products was studied by measuring the concentration in mol%. The slope of the $E\text{-lg}(i_d-i)$ dependences for different CrO_3 concentrations is 39-42 mV, and the value of $n = 5.8\text{-}6.1$ (Fig. 5a). The theoretical value of the slope for the six-electron reversible reaction is 39 mV.

The slopes of $E\text{-lg}(i_d-i)$ dependences for MoO_3 concentrations up to 4 mol % are 37-44 mV, and the values of $n = 5.3\text{-}6.2$. At the concentration of MoO_3 above 4 mol %, the slope of this dependence is 105-128 mV, and the value of $n = 1.8\text{-}2.1$ (Fig. 5b).

A polarization rate of $2 \text{ mV}\cdot\text{s}^{-1}$ corresponds to steady-state conditions. At such values, it is advisable to use the Kolthoff-Lingane equation (Table 2).

Table 2. The number of electrons transported in the electrode process of MoO_3 electroreduction in the Na_2WO_4 melt.

$C(\text{MoO}_3) \cdot 10^4, \text{ mol}\cdot\text{cm}^{-3}$	$\Delta E/\lg(i_d-i)$	n
1.0	0.038	6.1
2.0	0.039	5.9
4.0	0.042	5.5
6.0	0.105	2.2
8.0	0.117	2.0
9.0	0.112	2.1
11.0	0.120	1.9
13.0	0.125	1.9

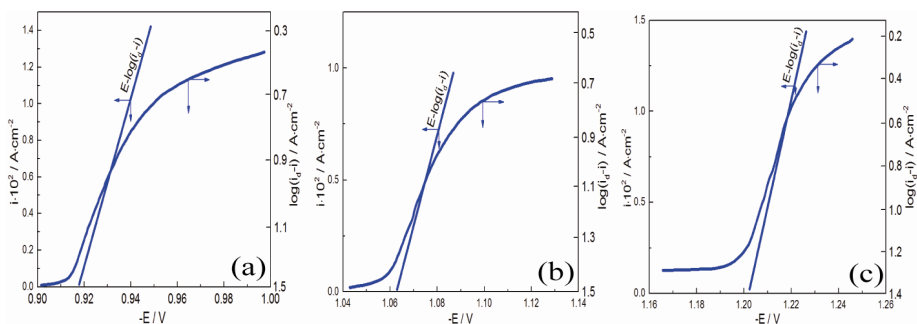


Figure 5. Analysis of steady-state voltammetric dependences in the semilogarithmic coordinate system. Scan rate - 2 mV/s ; $T = 1173 \text{ K}$; cathode - platinum;
a) $[\text{CrO}_3] = 2.5 \text{ mol } \%$; b) $[\text{MoO}_3] = 3 \text{ mol } \%$; c) $[\text{WO}_3] = 2.5 \text{ mol } \%$.

The theoretical slope value for the two-electron reversible reaction is 112 mV. The slope of the $E\text{-}\lg(i_d-i)$ dependences for different concentrations of WO_3 is 38-45 mV, and the value of $n = 5.5\text{-}6.2$ (Fig. 5c). The coincidence of the slopes determined from the experimental data with the theoretical ones indicates the reversible nature of the charge transfer stages (4)-(6).

The reversible nature of the charge transfer stages also follows from the experimental results obtained.

The deposition potential and the half-wave potential do not depend on the scan rate up to 0.2-0.5 V/s (Fig. 6a). Deposition potential is the electrode potential at which the deposition of the electrolysis product on the electrode surface begins.

The number of electrons involved in the electrode process was also determined from the half-width of the non-stationary voltammetric dependences. For different CrO_3 concentrations, and for scan rates within 0.05-0.2 V/s range, $n = 5.7\text{-}6.2$. For MoO_3 concentrations up to 4 mol %, $n = 5.7\text{-}6.0$, and for concentrations above 4 mol % - 1.7-2.0. In the case of WO_3 , for different concentrations, $n = 5.7\text{-}6.1$.

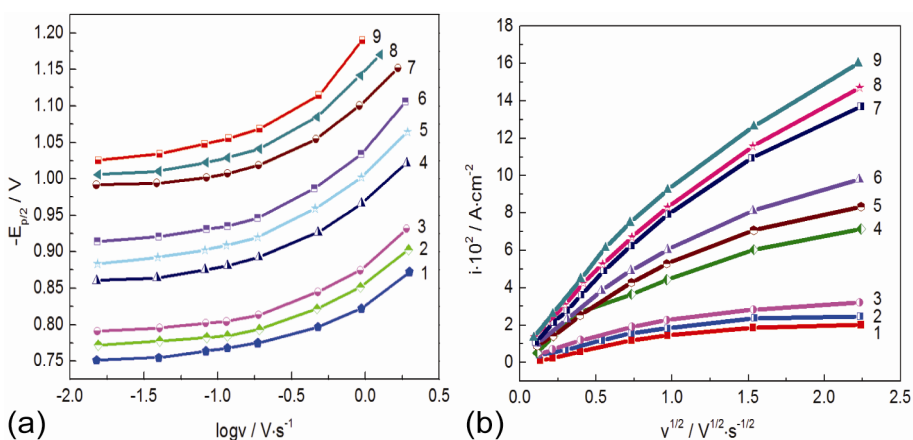
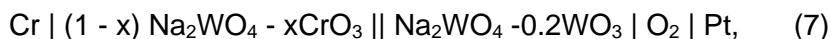


Figure 6. a) Dependence of the half-wave potential on the scan rate at $[\text{MO}_3] \times 10^4$, mol/cm³: (1,4,7) - 14.0; (2,5,8) - 12.0; (3,6,9) - 10.0; (1-3) - CrO_3 additive; (4-6) - MoO_3 ; (7-9) - WO_3 ;
b) Dependence of the peak current on the scan rate at $[\text{MO}_3] \times 10^4$, mol/cm³: (1-3) - 6.0; (4-6) - 8.0; (7-9) - 12.0; (1, 4, 7) - MoO_3 addition; (2, 5, 8) - WO_3 addition; (3, 6, 9) - CrO_3 addition.

4. Electrochemical behavior of group VI-B metals in tungstate melts. The group VI-B metals were chosen as electrode materials for the study of multi-electron equilibria and processes. During the study of electroreduction of oxide forms of chromium (molybdenum, tungsten) (VI) on the background of

a tungstate melt, the possibility of the following electrode reactions occurrence was revealed: (4) metal deposition; (5) metal (IV) oxide deposition; (6) metal (III) oxide deposition. To confirm the occurrence of reactions (4) - (6), the electrochemical behavior of chromium (molybdenum, tungsten) electrodes under equilibrium and stationary conditions at a low (2-10 mV/s) scan rate at the same material electrode was studied.

The main method of investigation under equilibrium conditions was potentiometry. For this purpose, we chose the following electrochemical circuits:



The EMFs of circuits (7)-(9) were measured in the range of MO_3 concentrations 0.5÷15 mol % (Fig. 7). The indicator electrodes were chromium (molybdenum, tungsten) polycrystalline rods of the "reagent" grade suspended on a platinum wire. The measurement procedure was similar to that for platinum-oxygen electrodes

Corrosion studies of chromium (molybdenum, tungsten) have revealed corrosion of metals in melts containing small additives of MO_3 . This may be why it is not possible to obtain reproducible EMF measuring results at $x < 0.5$ mol % MO_3 . The expressions for the potentials of metal and oxide electrodes in accordance with (4)-(6) can be written as follows:

$$E = E^0 + \frac{2.3RT}{6F} \lg \frac{[\text{M}_2\text{O}_7^{2-}]^4}{[\text{M}][\text{MO}_4^{2-}]^7} \quad (10)$$

in the case of melt-metal equilibrium;

$$E = E^0 + \frac{2.3RT}{2F} \lg \frac{[\text{M}_2\text{O}_7^{2-}]^2}{[\text{MO}_2][\text{MO}_4^{2-}]^3} \quad (11)$$

in the case of melt equilibrium with MO_2 oxide;

$$E = E^0 + \frac{2.3RT}{6F} \lg \frac{[\text{M}_2\text{O}_7^{2-}]^5}{[\text{M}_2\text{O}_3][\text{MO}_4^{2-}]^8} \quad (12)$$

in the case of equilibrium of the melt with oxide M_2O_3 . The calculation of the number of electrons per one electrochemically active particle, calculated from the pre-logarithmic dependence coefficient $dE/d\lg[\text{MO}_3]$ (Fig. 7), showed compliance with the six-electron equilibrium for the MoO_3 concentration

range 1÷4 mol %, and for CrO_3 and WO_3 – 1÷15 mol %. The values of E for the corresponding current density values are taken from the experimental dependences in Fig. 8. The two-electron equilibrium corresponds to the MoO_3 concentration range 4÷15 mol %. Electrode reactions (4), (5), and (6) correspond to these values of “ n ”. Melts Na_2WO_4 - (1÷15) mol % CrO_3 are in equilibrium with chromium (III) oxide. Melts Na_2WO_4 - (1÷4 mol %) MoO_3 are in equilibrium with metallic molybdenum, and Na_2WO_4 – (4÷15 mol %) MoO_3 – with MoO_2 oxide. Metallic tungsten is in equilibrium with melts Na_2WO_4 - (1÷15) mol % WO_3 .

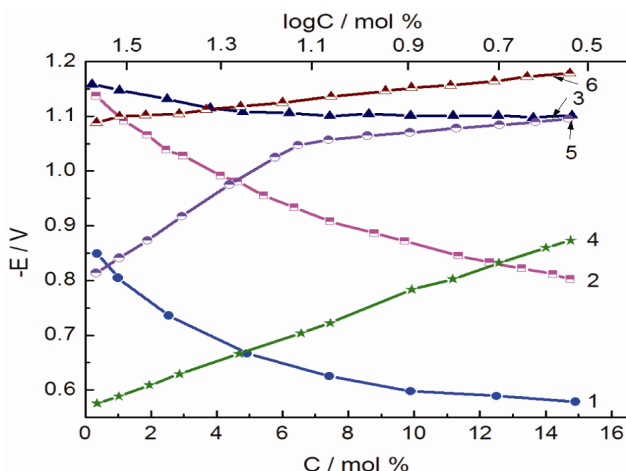


Figure 7. Dependences of the equilibrium potentials of chromium (1, 4), molybdenum (2, 5), and tungsten (3, 6) electrodes on the concentration of the respective oxides in ordinary (1-3) and logarithmic (4-6) coordinates.

The concentration dependences of the equilibrium potentials (4)-(6) are well described by the Nernst equations.

To clarify the nature of the charge transfer stages (4)-(6) for these conditions and to determine the number of electrons transferred in the electrode process, the stationary voltammetric dependences were analyzed in the semilogarithmic coordinate system $E-\lg(i_d-i)$. The pre-logarithmic coefficients of the $E-\lg(i_d-i)$ dependence for the CrO_3 concentrations 1÷15 mol %, MoO_3 – 1÷4 mol %, and WO_3 – 1÷15 mol. % correspond to reactions involving six electrons (Fig. 8). For the MoO_3 concentrations 4÷15 mol %, the pre-logarithmic coefficient corresponds to the reaction involving two electrons. The good agreement of the coefficients determined from the experimental data with the theoretical ones indicates the reversible nature of the charge transfer stages (4)-(6).

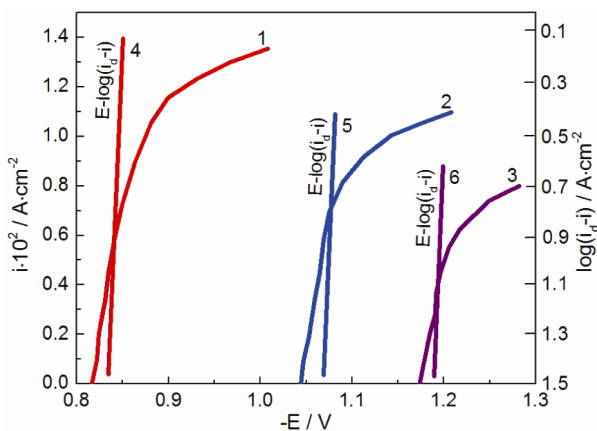


Figure 8. Steady-state voltammetric dependences (1-3) and their analysis in the semilogarithmic coordinate system (4-6). Scan rate = 2 mV/s, $T = 1173 \text{ K}$; 1,4 – Cr cathode, $[\text{CrO}_3] = 3.5 \text{ mol \%}$; 2,5 – Mo cathode, $[\text{MoO}_3] = 2.5 \text{ mol \%}$; 3,6 – W cathode, $[\text{WO}_3] = 2.0 \text{ mol \%}$.

Galvano- and potentiostatic electrolysis at CrO_3 concentrations 1÷15 mol % reveals Cr_2O_3 , at concentrations of 1÷4 mol % MoO_3 – molybdenum, and at higher concentrations of MoO_3 – molybdenum dioxide. Tungsten is the only product of the electrolysis of systems Na_2WO_4 - (1÷15) mol % WO_3 .

CONCLUSIONS

1.The analysis of the present experimental data allows to conclude that multi-electron reversible equilibria involving oxide forms of chromium, molybdenum, and tungsten (VI) can be realized in a sodium tungstate melt.

2.The mechanism and the final product of the electroreduction of metal (VI) oxide forms depend on the acid-base properties of the medium. By setting the latter, the electrode process can be controlled.

3.Of particular note is the uniqueness of the electrode equilibrium involving six electrons at a certain melt basicity.

EXPERIMENTAL SECTION

The study of electrochemical behavior of VI-B group metal oxides in the tungstate melt includes thermodynamic substantiation of the interaction of VI-B group metal oxides with this melt and study of acid-base properties of the tungstate melt by potentiometric method.

The probability of possible interactions between VI-B group metal oxides and sodium tungstate was estimated over a wide temperature range based on the calculations of the change in the standard Gibbs energy (ΔG_T). To calculate ΔG_T , the literature values of the thermodynamic values of the compounds under consideration were used [24, 25].

For potentiometric studies, the melt Na_2WO_4 -0.2 mol % WO_3 was chosen as the electrolyte for platinum-oxygen (Pt/O_2) reference electrode in the tungstate melts. The excess of oxygen ion acceptor in it contributes to the oxygen electrode potential stability, which is necessary for the reference electrode functioning. The design of Pt/O_2 reference electrodes of similar composition with a $\beta\text{-Al}_2\text{O}_3$ membrane, the rationale for their use, as well as the method for measuring the equilibrium potentials of Pt/O_2 electrodes, were described in [26, 27].

Na_2WO_4 was selected as the background melt for studying the electrochemical behavior of oxide forms of Group VI B metals. To prepare it, sodium tungstate of the "Reagent" brand was dried at a temperature of 423-473 K for 10-12 hours. It was then calcined at a temperature of 773-873 K for 3-4 hours. The quality of the background melt was determined by measuring the residual voltammetric currents. Their low value at a potential significantly more negative than that of the platinum-oxygen electrode (6 mA/cm² at -1.6 V) indicated sufficient purity and suitability for electrochemical measurements. The purity of the background melt was also checked using emission IR spectra. The absence of characteristic bands in the spectrum of the solidified melt meant the absence of impurities.

Metal oxides (VI) of group VI B of the "Reagent" brands were pre-dried at a temperature of 423-473 K for 5-6 hours, and then calcined at 673-773 K for 2-3 hours.

Equilibrium electrode potentials were measured using a SHCH-68003 digital voltmeter. The established value was taken as the one that did not change by ± 0.05 unit within 1 hour. Steady-state and transient volt-ampere dependencies were obtained using a PI-50.1 pulse potentiostat. Stationary dependencies were recorded with a two-coordinate recorder PDP-4, and non-stationary ones with an oscilloscope OWON SDS-1022.

A high-temperature cell made of quartz was used to perform electrochemical measurements. A platinum-oxygen electrode was used as a reference electrode, which was a platinum wire with a diameter of 1 mm, half-immersed in a melt of Na_2WO_4 – 20 mol. WO_3 . The electrolyte of the reference electrode was separated from the electrolyte under study by an alundum tube with a diameter of 6-8 mm, which acted as a diaphragm. The wall thickness of the tube was 0.5-1 mm. The open end of the tube was connected to the atmosphere. Measurements were carried out in an air atmosphere ($p(\text{O}_2)$ 21.3 kPa).

The electrodes used in electrochemical measurements were platinum, chromium, molybdenum, and tungsten wires with a diameter of 0.5-1 mm immersed in the melt. Platinum crucibles served as containers for the melt.

Automatic temperature control with a KVP-1 electronic potentiometer made it possible to maintain the melt temperature with an accuracy of ± 2.5 K.

The electrochemical behavior of group VI-B metal oxides in tungstate melt was studied in the range of scan rates 0.02-5.00 V/s using platinum electrodes at a temperature 1173 K, and using electrodes made of group VI-B metals at a scan rate 2 mV/s and a temperature 1173 K.

Diagnostics and estimation of the kinetic parameters of the electrode process were performed based on the theory of stationary and nonstationary electrode processes.

REFERENCES

1. O. Medvezhynska; A. Omelchuk; *Ukr. Chem. J.*, **2023**, 89(11), 3-34. <https://doi.org/10.33609/2708-129X.89.11.2023.3-34>
2. M. Erdogan; I. Karakaya; *Metall. Mater. Trans. B*, **2010**, 41, 798-804. <https://doi.org/10.1007/s11663-010-9374-4>
3. D. Tang; W. Xiao; H. Yin; L. Tian; D. Wang; *J. Electrochem. Soc.*, **2012**, 159, E139. <https://doi.org/10.1149/2.113206jes>
4. V. Malyshev; A. Gab; A.M. Popescu; V. Constantin; *Chem. Res. Chin. Univ.*, **2013**, 29, 771-775. <https://doi.org/10.1007/s40242-013-3003-0>
5. V. Malyshev; **2011**, *Mater. Sci.*, 47(3), 345-354. <https://doi.org/10.1007/s11003-011-9402-9>
6. N.B. Sun; Y.C. Zhang; F. Jiang; S.T. Lang; M. Xia; *Fusion Eng. Des.*, **2014**, 89(11) 2529-2533. <https://doi.org/10.1016/j.fusengdes.2014.05.027>
7. V. Malyshev; A. Gab; D. Shakhnin; C. Donath; E.I. Neacsu; A.M. Popescu; V. Constantin; *Rev. Chim.*, **2018**, 69(9), 2411-2415. <https://doi.org/10.37358/RC.18.9.6544>
8. A. Gab; V. Malyshev; D. Shakhnin; A.M. Popescu; V. Constantin; *Studia UBB Chemia*, **2024**, 69(1), 35-50. <https://doi.org/10.24193/subbchem.2024.1.03>
9. Y.H. Liu; Y.C. Zhang; Q.Z. Liu, X.L. Li; F. Jiang; *Fusion Eng. Des.*, **2012**, 87(11), 1861-1865. <https://doi.org/10.1016/j.fusengdes.2012.09.003>
10. V. Malyshev; A. Gab; A.M. Popescu; V. Constantin; *Rev. Chim.*, **2011**, 62(11), 1128-1130. <https://doi.org/10.37358/Rev.Chim.1949>
11. V. Malyshev; A. Gab; A. Survila; C. Donath; E.I. Neacsu; A.M. Popescu; V. Constantin; *Rev. Chim.*, **2019**, 70(3), 871-874. <https://doi.org/10.37358/RC.19.3.7023>
12. M. Mann; S.E. Shter; G.M. Reisner; G.S. Gideon; *J. Mater. Sci.*, **2007**, 42, 1010-1018. <https://doi.org/10.1007/s10853-006-1384-x>
13. V. Malyshev; H. Kushkhov; V. Shapoval; *J. Appl. Electrochem.*, **2002**, 32, 573-579. <https://doi.org/10.1023/A:1016544524468>

14. V. Malyshev; A. Gab; D. Shakhnin; A.M. Popescu; V. Constantin; *Rev. Roum. Chim.*, **2010**, 55(4), 233-238.
15. V. Malyshev; D. Shakhnin; A. Gab; I. Astrelin; L. Molotovska; V. Soare; C. Donath; E.I. Neacsu; V. Constantin; A.M. Popescu; *Rev. Chim.*, **2016**, 67(12), 2490-2500. <https://doi.org/10.37358/Rev.Chim.1949>
16. V. Malyshev; A. Gab; D. Shakhnin; C. Donath; E.I. Neacsu; A.M. Popescu; V. Constantin; *Rev. Chim.*, **2018**, 69(9), 2411-2415.
<https://doi.org/10.37358/RC.18.9.6544>
17. V.L. Cherginets; *Electrochim. Acta*, **1997**, 42(10), 1507-1514.
[https://doi.org/10.1016/S0013-4686\(96\)00308-8](https://doi.org/10.1016/S0013-4686(96)00308-8)
18. V.L. Cherginets; *Oxoacidity: Reactions of Oxo-compounds in Ionic Solvents*. Elsevier Science, **2005**. ISBN: 978-0-444-51782-1
19. V.A. Onischenko; V.V. Soloviev; L.A. Chernenko; V.V. Malyshev; S.N. Bondus; *Materialwiss. Werkst.*, **2014**, 45(11), 1030-1038.
<https://doi.org/10.1002/mawe.201400222>
20. V.V. Malyshev; V.V. Soloviev; L.A. Chernenko; V.N. Rozhko; *Materialwiss. Werkst.*, **2015**, 46(1), 5-9. <https://doi.org/10.1002/mawe.201400331>
21. NIST-JANAF, in: J.M.W. Chase; Ed., *Thermochemical Tables*
22. fourth ed., Proceedings of the American Chemical Society and the
23. American Institute of Physics, New York, NY, **1999**.
24. C.E. Lucke; *Handbook of Thermodynamic Tables and Diagrams*. Forgotten Books. **2020**. ISBN: 978-0484660105
25. G. Inzelt; A. Lewenstam; F. Scholz; Eds., *Handbook of Reference Electrodes*. Heidelberg: Springer Berlin. **2013**. ISBN: 978-3-642-44873-7
26. NIST-JANAF *Thermochemical Tables*. Malcolm W. Chase Jr., Ed. *Anal. Chem.*, **1999**, 71(5), 218A. 1952 p. <https://doi.org/10.1021/ac991732g>
27. C.E. Lucke; *Handbook of Thermodynamic Tables and Diagrams*. Forgotten Books, **2018**. 256 p. ISBN: 978-0484660105
28. S. Somia; *Handbook of Advanced Ceramics. Materials, Applications, Processing, and Properties*. Academic Press, **2013**. ISBN: 978-0-12-385469-8
29. S.Y. Kwon; R.J. Hill; I.H. Jung; *A model for multicomponent diffusion in oxide melts. CALPHAD* **72**, 102246, **2021**.
<https://doi.org/10.1016/j.calphad.2020.102246>

EFFICIENCY ANALYSIS OF SOME ZEOLITE MEDIA IN THE TREATMENT OF TECHNOLOGICAL WASTEWATER IN AGRO-ZOOTECHNICAL UNITS

Sebastian Ionuț OGNEAN^a, Emilia Valentina PANTEA^{b,*},
Valer MICLE^a, Daria-Maria-Ecaterina FENEȘAN^c

ABSTRACT. The present study aimed to evaluate the efficacy of two filtration media—Rupea natural zeolite (ZNR) and Turbidex—in reducing the pollutant load of wastewater from agro-zootechnical units. Both media were tested under identical operational conditions to explore their potential for sustainable wastewater valorization with minimal environmental impact. Results showed that ZNR exhibited higher adsorption rates for nitrites, nitrates, and ammonium, whereas Turbidex achieved greater retention for COD, total suspended solids (TSS), and turbidity. Filtration through both zeolitic media effectively reduced microbial loads, as indicated by the elimination of coliform bacteria and enterococci, along with a significant decrease in heterotrophic plate counts at 22°C and 37°C. These findings demonstrate the potential of small-scale zeolite filtration systems as eco-friendly solutions for agro - zootechnical wastewater treatment.

Keywords: *adsorption, clinoptilolite, ZNR (natural zeolite from Rupea), Turbidex, wastewater*

^a Technical University, Faculty of Materials and Environmental Engineering, Department of Environment Engineering and Entrepreneurship of Sustainable Development, 30 Fantanele St., RO-400294 Cluj-Napoca, Romania

^b University of Oradea, Faculty of Environmental Protection, Department of Environmental Engineering, 26 Gen. Magheru St., 410087, Oradea, Romania

^c University of Agricultural Sciences and Veterinary Medicine, Faculty of Veterinary Medicine, Mănăștur St., nr. 3-5, 400037, Cluj-Napoca, Romania

* Corresponding author: emipantea@gmail.com



INTRODUCTION

Economic and urban development have increasingly intensified pressures on freshwater resources, resulting in a progressive decline in water availability and posing significant risks to human, economic, and environmental security [1–3]. The protection and sustainable management of natural freshwater reserves remain critical challenges, particularly in rural areas lacking access to potable water, where agricultural activities depend on reliable water supplies [2–4]. The Water Framework Directive (WFD) underscores the importance of maintaining water quality at both national and European scales, not only for environmental protection but also to support water-intensive sectors such as agriculture. Data from the WFD further demonstrate the substantial impact of agricultural practices on the deterioration of water quality, with uncontrolled wastewater discharge from small-scale agricultural units emerging as a major threat to surface water resources [4]. The increasing scarcity of freshwater resources underscores the need to explore alternative water sources, including the reuse of wastewater for irrigation [5]. Recent studies highlight that the integration of sustainable technologies and smart monitoring tools in agricultural practices constitutes a forward-looking approach to wastewater management and water resource protection. [6,7].

International research emphasizes the adoption of environmentally friendly materials capable of supporting innovative wastewater treatment technologies. In this context, ecological filter media have emerged as a viable alternative for managing wastewater from small agro-zootechnical units [8]. Zeolites have attracted significant attention due to their ability to remove both organic and inorganic pollutants from wastewater.

Their effectiveness is attributed to their crystalline and microporous structure, large surface area, uniform pore distribution, high stability, rapid adsorption - desorption kinetics and low energy consumption for regeneration [9-16].

Zeolites such as clinoptilolite, mordenite, chabazite, and erionite have demonstrated high efficiency in wastewater treatment [18]. Clinoptilolite is the most widely used zeolite for the removal of contaminants such as heavy metals, ammonia, dyes, phenols, and phenolic derivatives from aqueous solutions [18-21]. Recent research has also highlighted their role in reducing the ecological impact generated by the presence of nitrites and nitrates in wastewater [13,20]. In Romania, zeolites from Mârsid and Pâglișa have been successfully applied to decrease NH_4^+ , COD, and BOD_5 levels in wastewater [22].

Multiple studies have demonstrated the effective use of zeolites in targeted pollutant removal processes. For example, copper ions can be adsorbed using a clinoptilolite–chitosan composite, while NH_4^+ ions are

efficiently removed at concentrations of 10.4–12.3 mg/g from synthetic solutions at 20°C and pH 6.09 using natural zeolite from the Rupea region [23,24]. In addition, zeolites can also function as biofilters for the removal of pathogenic microorganisms.

The use of natural zeolites in water treatment is further supported by their low cost, environmental compatibility, high ion exchange capacity, cation selectivity, chemical and physical stability, as well as their renewability and reusability [24]. These properties make zeolites highly suitable for integration into sustainable wastewater management strategies, particularly in small-scale agro-zootechnical systems [25-28].

RESULTS AND DISCUSSION

Analysis of the physicochemical indicator parameters

The evolution of pH can be characterized by wide oscillations (6.31-8.10) in the set of raw and filtered wastewater samples. The distribution of recorded values reveals a clear tendency of alkalinization of the water upon filtration through the zeolitic material bed (Figure 1), a phenomenon attributable to the inherently elevated pH of the zeolite itself. The pH values recorded post-filtration of the wastewater are within the range outlined for agricultural irrigation water, which must not oscillate outside the permissible limits (6.5-8.5) allowed by current legislation [30].

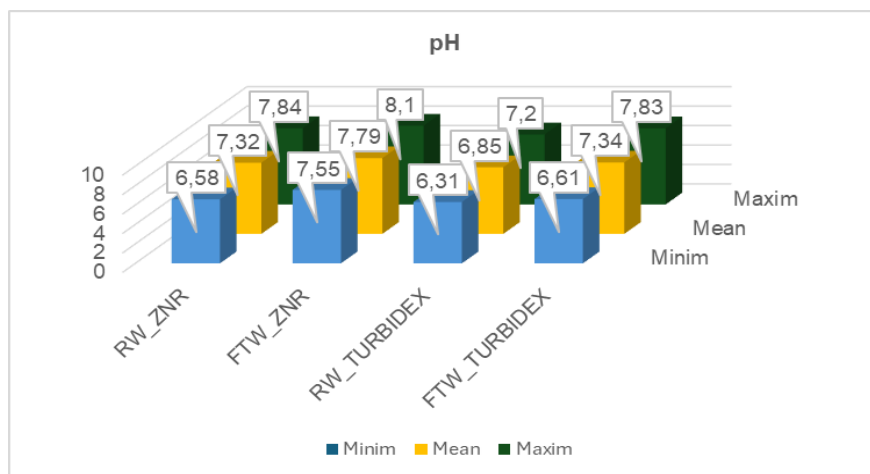


Figure 1. The evolution of the pH levels of wastewater [RW] and treated/ filtered water [FTW] on ZNR and Turbindex filtering media

The evolution of electrical conductivity (EC) was characterized by important oscillations, at the same operating temperature (25°C), for the wastewater that was filtered through Rupea zeolite (808-1320 $\mu\text{S}/\text{cm}$) and Turbidex (824-1117 $\mu\text{S}/\text{cm}$), respectively. A decreasing trend was observed after filtration, with mean values decreasing from 1277 $\mu\text{S}/\text{cm}$ to 1110 $\mu\text{S}/\text{cm}$ for Rupea zeolite and from 1025 $\mu\text{S}/\text{cm}$ to 933 $\mu\text{S}/\text{cm}$, for Turbidex.

This decreasing trend in conductivity can be correlated with the increase in alkalinity of the filtered water [21].

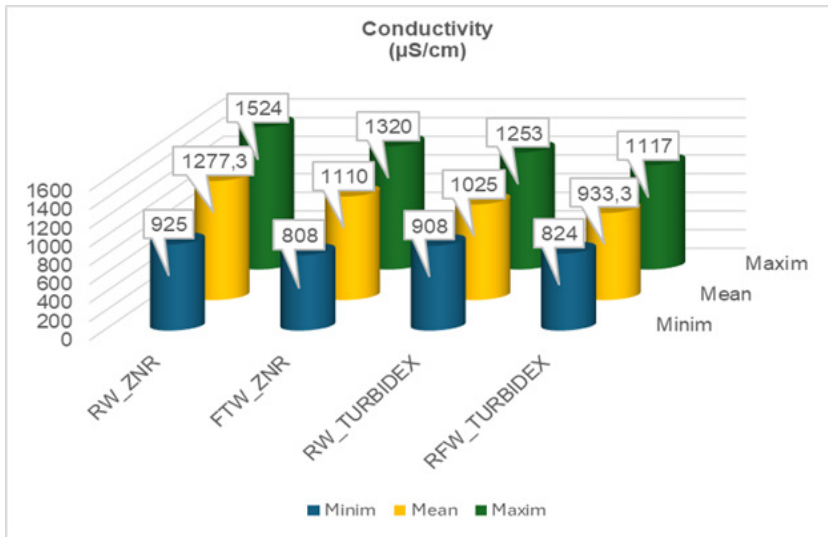


Figure. 2. The evolution of the electrical conductivity of wastewater [RW] and treated/filtered water [FTW] on ZNR and Turbidex filtering media

The use of the filter media (ZNR and Turbidex) allowed a significant reduction in the *turbidity* of agro-zootechnical wastewater. Thus, a decrease in the average turbidity values is observed from 18.44 to 5.45 NTU for ZNR and from 20.11 to 5.12 NTU for Turbidex, respectively. The quantification of these data indicated a good filtration efficiency of the two zeolite substrates, with a lower filtration rate for the Rupea zeolite (70.44%) compared to Turbidex (74.54%), but with very close average values (5.45 NTU and 5.12 NTU, respectively) (Figure 3).

EFFICIENCY ANALYSIS OF SOME ZEOLITE MEDIA IN THE TREATMENT OF TECHNOLOGICAL WASTEWATER IN AGRO-ZOOTECHNICAL UNITS

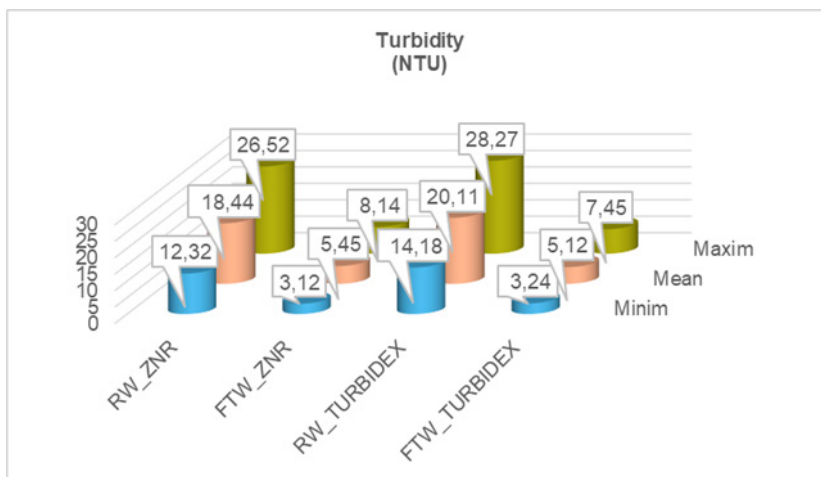


Figure. 3. The evolution of turbidity of wastewater [RW] and filtered/treated water [FTW] on ZNR and Turbidex filtering media

Turbidex demonstrated a higher average COD retention (35.35%) than Rupea zeolite (32.36%) (Figure 4). Retention efficiency declined with increasing influent concentrations, dropping to 25.8% for Rupea zeolite and 17.53% for Turbidex at concentrations above 150 mg/L, highlighting the need to optimize operational conditions according to both filter media properties and wastewater characteristics.

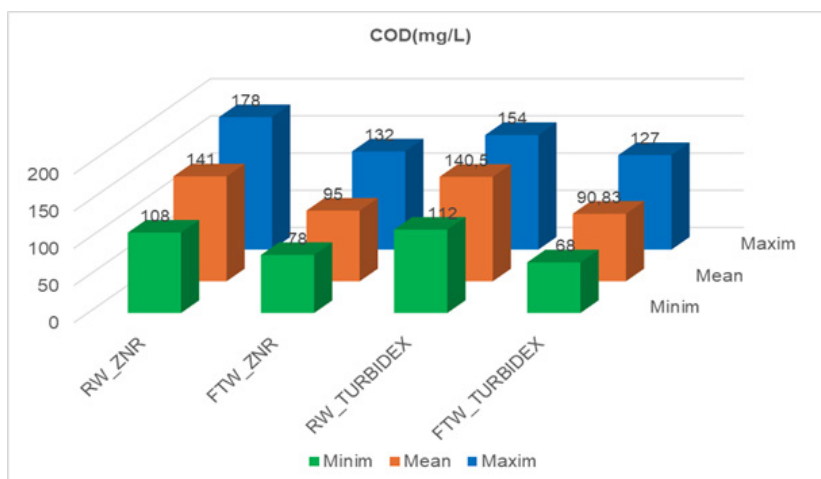


Figure 4. The evolution of COD of wastewater [RW] and filtered/treated water [FTW] on ZNR and Turbidex filtering media

As shown in the attached graph (Figure 5), the highest average percentage reduction in total suspended solids was achieved using Turbidex (74.54%) compared to Rupea zeolite (70.44%). The selected operational conditions, in relation to the type of filter media (Turbidex and Rupea zeolite), resulted in an effluent with TSS concentrations that comply with the standards established by NTPA 001/2002 [42].

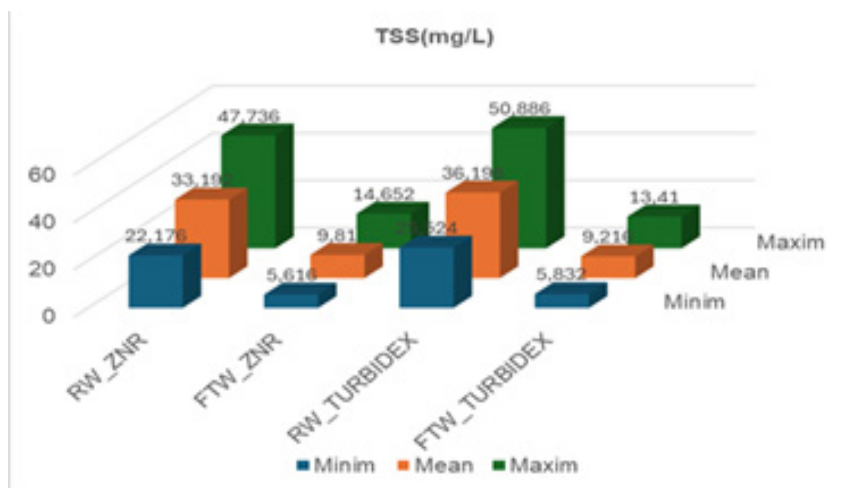


Figure 5. The evolution of total suspended solids of wastewater [RW] and filtered/treated water [FTW] on ZNR and Turbidex filtering media

The filtration of wastewater using Rupea zeolite and Turbidex resulted in high retention rates, with Rupea zeolite performing slightly better (88.54% vs. 86.85%). Despite this, under the operational conditions applied in this study, the average ammoniacal nitrogen concentration remained 3.74 mg/L for Rupea zeolite and 4.78 mg/L for Turbidex. This indicates that the adsorption of ammoniacal nitrogen was not sufficient to reduce its concentration to levels compliant with the effluent standards set by NTPA 001/2002, highlighting a limitation of the filtration process under the tested conditions [42].

When utilizing wastewater from agro-zootechnical units, particular attention is paid to the content of nitrites and nitrates. The discharge of insufficiently treated wastewater into outfalls generates the phenomenon of eutrophication, and in the case of distribution on land, it can lead to groundwater contamination.

EFFICIENCY ANALYSIS OF SOME ZEOLITE MEDIA IN THE TREATMENT OF TECHNOLOGICAL WASTEWATER IN AGRO-ZOOTECHNICAL UNITS

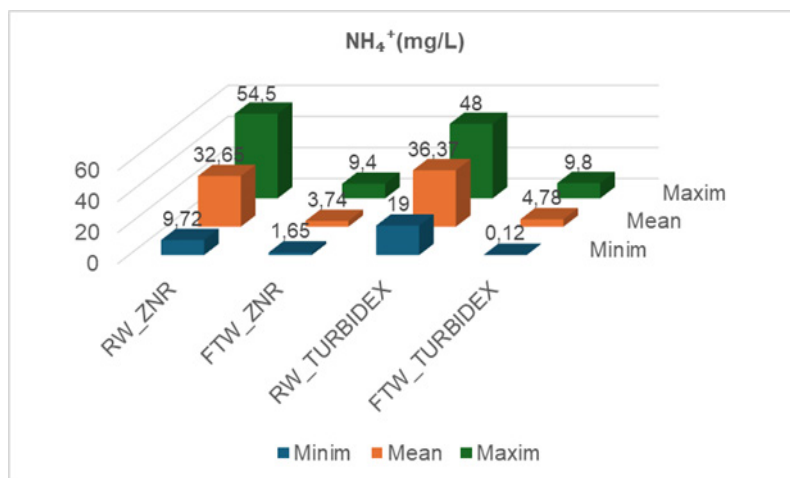


Figure. 6. The evolution of ammonium of raw water [RW] and filtered/treated water [FTW] on ZNR and Turbidex filtering media

The nitrites present in the raw wastewater exhibited levels slightly exceeding the permissible limits in the case of several samples. Following filtration through ZNR, the mean values decreased from 1.99 ± 0.33 mg/L to 1.33 ± 0.35 mg/L, and after filtration through Turbidex, they decreased from 2.31 ± 0.60 mg/L to 1.61 ± 0.42 mg/L (Figure 7). Monitoring of NO_2^-

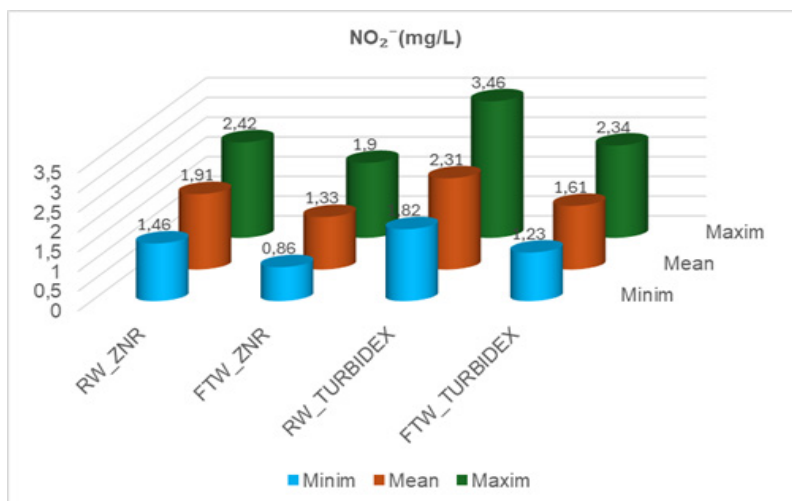


Figure. 7. The evolution of nitrites of wastewater [RW] and filtered/treated water [FTW] on ZNR and Turbidex filtering media

concentrations revealed a constant decrease in values post-filtration through both zeolite media, with these values falling within the permissible range for wastewater discharged into natural outfalls [46], except one sample whose values remained slightly elevated. The adsorption rate derived from these values outlined nitrite retention proportions from the wastewater of 30.36% for ZNR and 30.30% for Turbidex, respectively. Efficient treatment for nitrite removal can be based on denitrification, reverse osmosis filters or ion-exchange media, such as zeolitic materials [12, 18].

The nitrates detected in the raw wastewater exhibited concentrations slightly exceeding the permissible limits in most samples, with mean values reaching 59.42 ± 14.37 mg/L and 67.70 ± 17.93 mg/L, respectively. After filtration, the values decreased to 52.83 ± 10.16 mg/L and 62.05 ± 15.72 mg/L, respectively: the NO_3^- adsorption rate being 11.09% for ZNR and 8.34% for Turbidex, respectively (Figure 8). Overall, the evolution of this parameter showed slight decreases in values post-filtration for each analysed sample, with only 50% of them falling within the allowed range.

The obtained data is closely related to other research conducted in this field, especially the ones that investigated the use of clinoptilolite in the treatment of certain categories of wastewater [16-18].

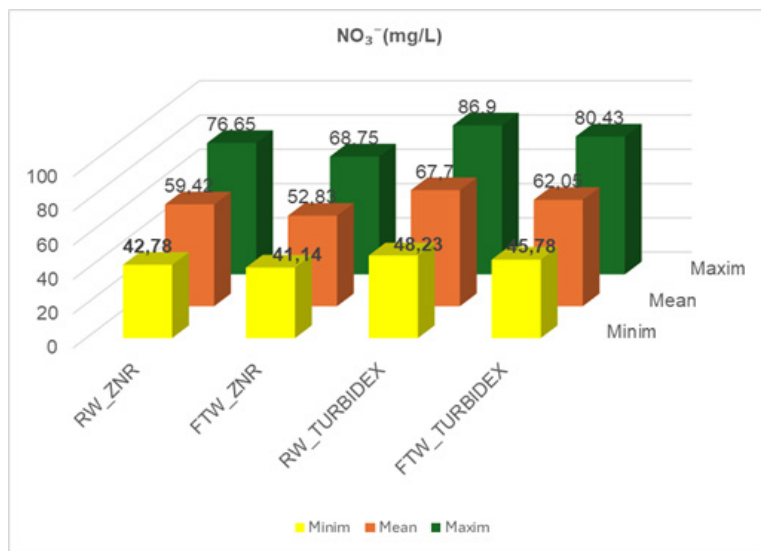


Figure. 8. The evolution of nitrates of wastewater [RW] and filtered/treated water [FTW] on ZNR and Turbidex filtering media

Analysis of microbiological parameters

This analysis included monitoring of indicative microbiological contaminants: *E. coli*, coliform bacteria, enterococci, the total colony count (CFU) at 22°C and the total colony count (CFU) at 37°C. Microbiological parameter testing revealed notable fluctuations in the obtained values, which are presented in (Table 1). The microbial load recorded in the case of influent for the ZNR substrate of the experimental station was characterised by 7 positive tests for coliform bacteria and enterococci, a level of 701.1 CFU/100 mL for the total colony count at 22°C parameter and 1132.7 CFU/100 mL for colonies at 37°C.

Table 1. Results from microbiological parameters testing of wastewater

Parameter	<i>Escherichia coli</i> (No/100mL)		B. Coliform (No/100mL)		Enterococci (No/100mL)		The total colony count at 22°C (CFU/mL)		The total colony count at 37°C (CFU/mL)	
MAC*	0		0		0		No abnormal changes		No abnormal changes	
Unit	RW	FTW	RW	FTW	RW	FTW	RW	FTW	RW	FTW
(A) Wastewater – ZNR substrate										
I	0	0	+	0	0	0	1025.0	323.0	1848.7	15.5
II	0	0	+	0	+	+	362.0	210.2	1264.6	12.0
III	0	0	+	+	+	0	865.3	163.0	1298.6	252.0
IV	0	0	+	0	+	0	820.0	23.4	711.7	20.0
V	0	0	-	-	0	0	736.2	25.0	1077.4	565.5
VI	0	0	0	0	-	-	398.0	12.0	595.4	171.6
Mean	0	0	+	0	+	0	701.1	126.1	1132.7	127.8
Maximum	0	0	+	+	+	+	1025.0	323.0	1848.7	565.5
Minimum	0	0	0	0	0	0	362.0	12.0	595.4	12
Standard deviation	-	-	-	-	-	-	266.1	127.3	453.1	216.5
RR [%]							82.01		88.71	
(B) Wastewater – Turbidex substrate										
VII	0	0	+	0	+	0	351.0	0	759.9	115.5
VIII	0	0	+	+	+	+	320.5	210.2	720.2	145.0
IX	0	0	+	0	+	0	315.2	163.0	731.5	123.0
X	0	0	+	+	+	+	220.0	23.4	578.4	115.3
XI	0	0	+	0	+	0	400.5	25.0	646.4	135.0
XII	0	0	0	0	0	0	180.7	12.0	358.9	110.3
Mean	0	0	+	0	+	0	297.9	72.3	632.6	124.7
Maximum	0	0	+	+	+	+	400.5	210.2	759.9	145.0
Minimum	0	0	0	0	0	0	180.7	0	358.9	110.3
Standard deviation	-	-	-	-	-	-	82.4	90.3	149.5	51.8
RR [%]							75.73		80.39	

RR- reduction rate, MAC*-Maximum admitted concentration [36]

The comparative analysis of the microbiological parameters of the effluent filtered by ZNR revealed that in 5 out of 7 tests, no coliform bacteria and enterococci were identified, and the total colony count at 22°C was reduced to 126.1 CFU/100 ml, respectively, to 127.8 CFU/100 ml at 37 °C.

Comparatively, raw wastewater from the Turbidex model system yielded positive results for both coliform bacteria and enterococci, which were recorded in 10 tests. The total colony count, following incubation at 22°C, was determined to be 297.9 the total colony count per 100 mL (CFU/100 mL) and respectively of 632.6 CFU/ 100 ml at 37°C.

Following filtration, neither coliform bacteria nor enterococci were detectable within 6 of the treated water samples. Moreover, total colony counts performed at 22°C and at 37°C, respectively, were significantly reduced (72.3 and 40.7 CFU/100 mL).

CONCLUSIONS

This study demonstrates that natural Rupea zeolite (ZNR) and the zeolitic substrate Turbidex are effective filter media for the treatment of wastewater from small agro-zootechnical holdings. Comparative results showed minor differences between the two materials, with ZNR exhibiting slightly higher adsorption for conductivity, ammonium, nitrites and nitrate, while Turbidex achieved superior retention of COD, turbidity, and total suspended solids. Both media significantly reduced microbial load, including complete removal of coliform bacteria and enterococci, and a marked decrease in colony counts at 22°C and 37°C.

These findings highlight the overall efficiency of zeolite-based filtration under pilot-scale conditions and emphasize the importance of optimizing operational parameters.

The integration of Rupea zeolite- and Turbidex-based filtration systems offers a sustainable approach for agro-technical wastewater management, supporting internal recycling and safe reuse of treated effluents for irrigation. Such systems contribute to environmental protection, nutrient recovery, and compliance with European and Romanian water quality standards, while aligning with international efforts to promote resource efficiency and sustainable water management.

EXPERIMENTAL SECTION

Wastewater samples

The study investigated the efficiency of eco-friendly filter materials, natural Rupea zeolite and Turbidex, for the sustainable management of wastewater originating from small agro-zootechnical units located in rural areas of the Someșul Mare river basin (Cluj and Bistrița-Năsăud counties). Research was conducted on three commercial micro-farms and nine traditional agricultural households, all discharging wastewater either into surface waters or onto adjacent land. Table 2 summarizes the coding and technological characteristics of the source units.

Table 2. The identification of wastewater [Ww] samples based on origin

Code water sample	Unit (Type)	Technological traits
I/ Ww	Micro farms	Young cattle fattening facility with septic tank
II/ Ww		Swine fattening facility without septic tank
III/ Ww		Dairy sheep farm, without septic tank
VI/ Ww	Farmstead	Mixed- swine and poultry with manure platform
V/ Ww		Mixed-lactating cows and swine with manure platform
VI/ Ww		Mixed-lactating cows and swine with manure platform
VII/ Ww	Farmstead	Mixed- swine and poultry without manure platform
VIII/ Ww		Mixed-lactating cows, with dairy facility and manure platform
IX/ Ww		Mixed- swine without manure platform
X/ Ww		Mixed- lactating cows with dairy facility and manure platform
XI/ Ww		Mixed- lactating cows, with dairy facility and manure platform
XII/ Ww		Mixed- swine and poultry without manure platform

The performance of the filter media was evaluated through key physicochemical parameters, including pH, electrical conductivity, turbidity, total suspended solids (TSS), chemical oxygen demand (COD), ammonium, nitrites, and nitrates. Additionally, the reduction of microbiological contaminants was closely monitored to assess the overall treatment effectiveness.

These indicators were specifically selected due to their critical role in determining the feasibility of reusing treated effluents in agricultural applications.

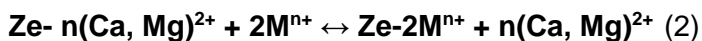
The filter media (ZNR and Turbidex)

The selection of zeolitic filter media for the treatment of agro-zootechnical wastewater was based on their inherent adsorption capacity, ease of regeneration, and potential for subsequent reuse as soil amendments. These considerations, supported by extensive literature, provided the basis

for investigating Rupea natural zeolite (ZNR) and the Turbidex substrate as adsorbent media in a pilot-scale wastewater treatment facility.

Rupea natural zeolite (ZNR) originates from a significant geological deposit in Romania and has well-established applications in water treatment, wastewater purification, environmental protection, and agriculture. ZNR primarily contains clinoptilolite, which exhibits a high ion-exchange capacity, making it suitable for the removal of a wide range of pollutants.

The adsorption mechanism involves the exchange of mobile cations (Na^+ , K^+ , Ca^{2+} , Mg^{2+}) within the zeolitic framework with cations (M^{n+}) present in the external solution, according to the following general relationship [29]:



The following two tables summarize the main compositional, mineralogical and physicochemical characteristics which are the basis of the ZNR characterisation [25, 31].

Table 3. Physicochemical characteristics of ZNR

Physical characteristics		Chemical composition [%]	
Softening point [°C]	1250	SiO_2	68.75-71.3
Melting point [°C]	1320	Fe_2O_3	1.90-2.1
Melting temperature [°C]	1400	Al_2O_3	11.35-13.1
Color	Grey-green	MgO	1.18-1.20
Smell	Odorless	CaO	2.86-5.2
Porosity (%)	32-44	Na_2O	0.82-1.30
Porous diameter (nm)	0.4-0.6	K_2O	3.17-3.40
Water hardness [Mohs scale]	3.5-4	Loss on ignition	8.75-8.86
pH [-]	8.75		
Density [Tons/m ³]	2.377		

Table 4. Mineralogical composition of ZNR

Evaluation type	Parameter / The principle of the test		UM	Values
Mineralogical composition	Clinoptilolite		%	87-90
	Plagioclase		%	2-5
	Anhydrite		%	2-3
	Cristobalite		%	4-5
Absorbent capacity	Pb	Absorption rate at different time intervals	%, 1a 2h	98,28
	Cd			99,51
	Cr			99,91
	Cu			99,46

EFFICIENCY ANALYSIS OF SOME ZEOLITE MEDIA IN THE TREATMENT OF TECHNOLOGICAL
WASTEWATER IN AGRO-ZOOTECHNICAL UNITS

Evaluation type	Parameter / The principle of the test		UM	Values
Cation exchange capacity	Ca ²⁺	Determination of cationic adsorption or substitution and electrical charge differences	meq/100g	237.5
	Mg ²⁺			160.4
	K ⁺			38.4
	Na			39

Initially, the manufacturing company provided the study with three commercial series of ZNR, distinguished by size of granulation (0.5-1.5mm, 1.5-3 mm, and 3-5 mm). Following the preliminary literature reviews, the variant exhibiting the finest granulation (0.5-3 mm) was selected for inclusion in this study [9, 25, 32]. For the initial stage of the preparation of zeolite samples intended for laboratory investigations, a facile procedure, as delineated by Zeolites Group and corroborated by other pertinent research within this domain, was implemented [9,32]. This protocol involved the laving of the granulated zeolite with distilled water until the water remained clear, followed by desiccation at a temperature of 105°C, subsequent cooling, and finally, storage within a desiccator [17].

Turbidex is a naturally occurring zeolite extensively utilized in the United States of America due to its exceptionally high clinoptilolite content. It is identified by a characteristic chemical formula:



The expression of the adsorbent potential of this clinoptilolite medium, which is dictated by its distinct physical characteristics (ion exchange), is also influenced by the appropriate sizing and adaptation of the filter bed to the dimensions of the tank in which it is employed [46].

Table 5. The identification and composition of Turbidex zeolite substrate

	Characteristics
Chemical name	Clinoptilolite Zeolite/Potasium, Calcium, Sodium Aluminosilicate, Hydrated
Chemical formula	$K_2, Ca_2, Na_2)O \cdot Al_2O_3 \cdot 10SiO_2 \cdot 8H_2O$.
CAS Registry	12173-10-3
Natural zeolites granules	100%
Density	2.2.-2.4 Tons/m ³

Experimental plant and filtration of wastewater samples

The purification potential of zeolitic filter media was evaluated using an experimental water treatment station (Figure 6). The pilot plant featured a height of 750 mm and a zeolite filter volume of 40 L, operating at a filtration pressure of 3 bar and an influent flow rate of $1 \text{ m}^3 \cdot \text{h}^{-1}$. Filtration through both zeolite materials was performed under identical operational conditions, with at least two composite samples collected for analysis before and after each cycle. Each filtration cycle lasted approximately 2 hours and was followed by regeneration of the zeolitic medium.

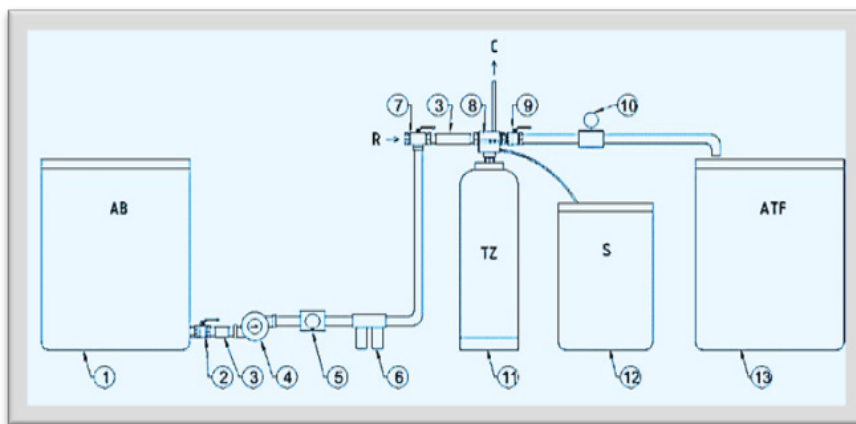


Figure. 9. The general blueprint for the experimental wastewater treatment plant: 1-raw wastewater recipient tank (AB); 2-faucet; 3-flexible connection; 4-pump; 5-electro pressure switch; 6-filter; 7-three-way valve Dn; 8-electro valve; 9-faucet; 10-water meter; 11-zeolite tank (TZ); 12-brine tank (S); 13-filtered water tank (WTF); R-water network; C-sewer discharge.

Methodology used for wastewater sample testing

The samples were organized into two experimental models, based on wastewater type and filter medium: Wastewater – ZNR (A) and Wastewater – Turbidex (B). Collected wastewater samples were transported to the laboratory and stored under refrigeration at 4°C until analysis.

Qualitative assessment was carried out by comparing the obtained data with the limit values established by the relevant national legislation in the field. The reliability of the chemical analyses was ensured through the use of high-purity reagents (Merck, România) and, certified experimental methods, alongside laboratory equipment validated for high-precision chemical measurements.

EFFICIENCY ANALYSIS OF SOME ZEOLITE MEDIA IN THE TREATMENT OF TECHNOLOGICAL
WASTEWATER IN AGRO-ZOOTECHNICAL UNITS

Both influent and effluent were characterized to evaluate the treatment performance of Rupea Zeolite and Turbidex as filtration media.

The following table summarizes the analytical methods utilized for the monitored indicators.

Table 6. Tested parameters and the used methods

No.	Parameter [UM]	Method and equipment	NTPA- 001/2002
1.	pH [U. pH]	SR ISO 10523:2012; Water quality. Determination of pH, Romanian	6.5 – 8.5
2.	EC [mS/cm]	SR EN 27888:1997; Water quality. Determination of electrical conductivity	-
3.	Turbidity [NTU]	SR EN ISO 7027-1:2016. Water quality. Determination of turbidity. Partea 1:	-
4.	COD ⁻ [mg/L]	SR ISO 6060-96 Water quality Determination of the chemical oxygen demand	125.0
5.	TSS ⁻ [mg/L]	STAS 6953-81: Water Quality. Determination of total suspended solids	35.0 (60.0)
6.	NH ⁴⁺ [mg/L]	SR ISO 7150-1: 2001: Water Quality. Determination of ammonium content	2.0 (3.0)
7.	NO ²⁻ [mg/L]	SR EN 26777:2002/C91:2006; Water Quality. Determination of nitrite content. The Method by Molecular Absorption Spectrometry.	1.0 (2.0)
8.	NO ³⁻ [mg/L]	SR ISO 7890-3/2000; Water Quality: Determination of nitrate content: PART 3. Sulfosalicylic acid spectrometric method).	25 (37)
9.	<i>Escherichia coli</i> [CFU /100mL]	ISO 9308-1; Water quality. Enumeration of <i>Escherichia coli</i> and Coliform bacteria. Part 1: Membrane filtration method	0
10.	Total coliforms [CFU/100mL]	SR EN ISO 9308:1:2015/A:2017 Water quality. Enumeration of <i>Escherichia coli</i> and Coliform bacteria. Part 1: Membrane filtration method	<10
11.	Enterococci [CFU/100mL]	SR EN ISO 7899-2/2002. Water quality. Detection and enumeration of intestinal enterococci. Part 2: Membrane filtration method. (The determination was made after incubating the membrane, 48 h at 36°C, on Slanetz Bartley medium)	-
12.	The total colony count at 22°C [CFU/m]	SR EN ISO 6222:2004 Water quality. Enumeration of culture microorganisms. (Colony counting by seeding in agar-agar culture medium at a temperature of 22°C, incubated for 72 hours	-
13.	The total colony count at 37°C [CFU/m]	SR EN ISO 6222:2004: Water quality. Enumeration of culture microorganisms. (Colony counting by seeding in agar-agar culture medium at a temperature at 37°C incubated for 24 hours).	-

The adsorption capacity of the zeolitic substrates was evaluated by determining the retention rate of the analysed indicators, according to the following equation

$$R[\%] = \frac{C_i - C_f}{C_i} \times 100$$

where:

C_i represents the initial concentration (mg/L) of the analysed pollutant.

C_f represents the final concentration (mg/L) of the analysed pollutant.

ACKNOWLEDGMENTS

The authors would like to extend their thanks to the SC Zeolites Group Cluj-Napoca and of the Department of Environmental Engineering and Sustainable Development Entrepreneurship of the Technical University of Cluj-Napoca, University of Agricultural Sciences and Veterinary Medicine of Cluj-Napoca, Institute of Life Sciences and the microbiological determinations in the Faculty of Veterinary Medicine for infrastructure facilities and support for conducting the aforementioned research.

REFERENCES

1. P. Chen; *J. Environ. Manag.*, **2024**, 365.
2. C. Tortajada; *NPJ Clean Water*, **2020**, 3(1), 22.
3. S. Tong; R. Xia; J. Chen; W. Li; Y. Chen; *J. Hydrol.: Reg. Stud.*, **2024**, 56, 102040.
4. Directive 2000/60/EC of the European Parliament and of the Council of 23 October 2000 establishing a framework for Community action in the field of water policy (OJ L 327, 22.12.2000, pp. 1–73).
5. D. Mooney; T. H. Kelley; *Journal of Agricultural and Resource Economics*, **2023**, 48 (1), 202-18 (Doi: 10.22004/ag.econ.320671)
6. F. Jamil; M. Abdulgadir; M. Tesfaye; *Green Chem. Lett. Rev.*, **2024**, 17(1), 1–15.
7. S. Kumari; J. Chowdhry; M. Kumar; M. Garg; *Environ. Res.*, **2024**, 119782.
8. V. Giurgiu; D.I. Berean; A. Ionescu; M.S. Ciupe; C.R. Cimpean; C.I. Radu; D.G. Bitica; S. Bogdan; M.L. Bogdan; *Vet. Anim. Sci.*, **2024**, 23, 100333.
9. M. Senila; O. Cadar; *Helyon*, **2024**, 10(3), e25303.
10. I.F. Voicea; I.C. Moga; E. Marin; D. Dumitru; C. Persu; D. Cujbescu; *E3S Web Conf.*, **2020**, 180, 03010.
11. F. Bud; S. Perța-Crișan; Cl. Ursachi; Șt.S. Gavrilaș; F.D. Munteanu; *St. Cerc., St. CICBIA*, **2024**, 25(3), 255–264.
12. Y. Wang; Y. Chen; Q. Wang; Z. Liang; *Agronomy*, **2023**, 13(2), 327.

13. D. Mooney; T.H. Kelley; *J. Agric. Resour. Econ.*, **2023**, 48(1), 202–218.
14. G. Amin; S. Konstantinovic; I. Jordanov; D. Djordjevic; *Studia UBB Chemia*, LXVIII, **2023**, 1, 179–192.
15. K. Ignatowicz; J. Łozowicki; B. Łozowicka; J. Piekarski; *Energies*, **2023**, 16(2), 660.
16. M. Senila; O. Cadar; L. Senila; B.S. Angyus; *Agriculture*, **2022**, 12, 321.
17. N. Bolan; M. Kumar; E. Singh; A. Kumar; L. Singh; S. Kumar; K.H. Siddique; *Environ. Int.*, **2022**, 158, 106908.
18. S. Ayalew; A. Dagne; E. Alemayehu; T. Alemu; S. Leta; *PLOS ONE*, **2022**, 17(5), e0268146.
19. S. Bouarroudj; H. Aksas; H. Lounici; N. Mameri; *Sustainability*, **2022**, 15(3), 1892.
20. M. Bálintová; M. Holub; *Acta Chim. Slovaca*, **2019**, 12(1), 68–75.
21. S. Babel; T.A. Kurniawan; *J. Hazard. Mater.*, **2003**, 97(1-3), 219–243.
22. D. Rios Reyes; D. Appasamy; C. Roberts; *Dyna*, **2011**, 78(170), 125–134.
23. S. Wang; Y. Peng; *Chem. Eng. J.*, **2010**, 156(1), 11–24.
24. L. Wang; J. Wei; H. Zhang; *Environ. Sci. Pollut. Res.*, **2020**, 27(11), 12325–12340.
25. S.I. Ognean; V. Micle; O. Tamas-Krumpe; D. Feneşan; D. Agape; L. Ognean; *Merit Res. J. Agric. Sci. Soil Sci.*, **2023**, 11(2), 16–21.
26. M. Wekesa; G. Mutua; G. Ogendi; *Int. J. Eng. Res. Technol.*, **2018**, 7(6), 37–43.
27. P. Chen; *J. Environ. Manag.*, **2024**, 365.
28. D. Proca; C. Micu; F. Manea; C. Danieleescu; In *Exposure and Risk Assessment of Chemical Pollution – Contemporary Methodology*; Springer: Netherlands, **2009**, pp. 509–516.
29. A.I. Tetişan; Doctoral Thesis, Universitatea „Babeş-Bolyai”, Cluj-Napoca, 2010.
30. D. Marşavina; Doctoral Thesis, Universitatea Politehnica Timişoara, 2010.
31. S.I. Ognean; V. Micle; Octavia Tamas-Krumpe; Daria Feneşan; L. Ognean; *Rev Rom Med Vet*, **2023**, 33/3, 89-96
32. T.H. Abed; D.S. Stefan; D.C. Berger; N.C. Marinescu; *Water. Sustainability*, **2024**, 10, 16(18), 7888 (<https://doi.org/10.3390/su16187888>)
33. European Parliament and Council. Directive 2000/60/EC, OJ L 327, 22.12.2000, pp. 1–73.
34. SR ISO 10523:2012; Romanian Standardization Association: Bucharest, 2012.
35. SR EN 27888:1997; Romanian Standardization Association: Bucharest, 1997.
36. SR EN ISO 7027-1:2016; Romanian Standardization Association: Bucharest, 2016.
37. SR ISO 6060-96; Romanian Standardization Association: Bucharest, 1996.
38. STAS 6953-81; Romanian Standardization Association: Bucharest, 1981.
39. SR EN 26777:2002/C91:2006; Romanian Standardization Association: Bucharest, 2006.
40. SR ISO 7890-3:2000; ISO, Geneva, 2000.
41. SR EN ISO 6222:2004; Romanian Standardization Association: Bucharest, 2004.
42. ISO 9308-1; Romanian Standardization Association: Bucharest, 2000.
43. SR EN ISO 7899-2:2002; Romanian Standardization Association: Bucharest, 2002.

SEBASTIAN IONUȚ OGNEAN, EMILIA VALENTINA PANTEA,
VALER MICLE, DARIA-MARIA-ECATERINA FENEȘAN

44. NTPA-001/2002; NORMATIV privind stabilirea limitelor de încărcare cu poluanți a apelor uzate industriale și urbane la evacuarea în receptorii naturali, 28.02.2002.
45. *** <https://zeolitesproduction.com/>
46. *** <http://www.turbidex.com/parameters.htm>

STUDIES ON THE ADSORPTION OF CONGO RED ANIONIC DYE FROM SYNTHETIC AQUEOUS SOLUTIONS USING WASTE EGGSHELL BIOMASS

Silvia BURCĂ^a  and Cerasella INDOLEAN^{a,*} 

ABSTRACT. In this study, waste eggshells (WES) were investigated as an efficient biosorbent for the removal of Congo Red (CR) dye from aqueous solutions. The adsorption performance was quantified using UV–Vis spectroscopy at 498 nm. Fourier Transform Infrared (FTIR) spectroscopy confirmed the presence of hydroxyl, carbonyl, and methylene functional groups in WES, as well as structural modifications following CR adsorption.

Batch adsorption experiments were conducted to evaluate the effects of contact time, initial dye concentration, temperature, and pH on the adsorption capacity and efficiency. The highest CR removal efficiency (98.80 %) was achieved at pH 5.94, using a solid-to-liquid ratio of 5 g/100 mL and an initial CR concentration of 97.75 mg/L. The maximum adsorption capacity of WES was determined to be 9.12 mg CR/g WES. Optimized adsorption conditions were established using 4 g WES/100 mL at 295 K, pH 5.94, and an initial concentration of 97.97 mg CR/L under static conditions.

Thermodynamic analysis revealed the spontaneous and exothermic nature of the adsorption process, as indicated by a negative enthalpy change ($\Delta H = -40.708 \text{ kJ mol}^{-1}$). These findings demonstrate the feasibility of employing waste eggshells as an effective and sustainable biosorbent for the removal of azo dyes from contaminated water.

Keywords: eggshell, Congo Red, adsorption, wastewater, thermodynamics

^a Babeş-Bolyai University, Faculty of Chemistry and Chemical Engineering, 11 Arany Janos str., RO-400028, Cluj-Napoca, Romania.

* Corresponding author: liliana.indolean@ubbcluj.ro



INTRODUCTION

Safe drinking water and sanitation are human rights. Without access to these services, a life of stability and good health is virtually impossible [1].

According to the United Nations estimate, over 95 trillion gallons of wastewater are produced yearly. Only 20% of wastewater is currently treated, according to the reports released by the Global Commission on the Economics of Water (GCEW). It was predicted that by 2030, the fresh water demand will rise above availability by 40% [2].

The textile industry extensively uses dyes to colour its products, consuming substantial volumes of water in the process. Consequently, it generates large quantities of coloured wastewater. It is estimated that over 100,000 commercially available dyes are generated annually, with a total output exceeding 700,000 tonnes of dyestuff [3]. Approximately 5–10% of these dyes are lost in industrial effluents [4]. The direct discharge of such effluents into natural water bodies leads to significant environmental concerns, primarily due to their high organic load, toxicity, and persistent coloration. This contamination reduces light penetration and impairs photosynthesis, thereby negatively impacting aquatic ecosystems. Moreover, many dyes are known to be toxic, mutagenic, or even carcinogenic.

Particularly, an anionic diazo dye known as Congo red (CR) has been employed extensively for dyeing cotton, hemp, and silk fabrics and paper [5]. Congo red dye ($C_{32}H_{22}N_6Na_2O_6S_2$), having azo groups with aromatic ring and sulphonate groups, is a very harmful dye that is used in many industries. Due to its structural stability, CR is difficult to biodegrade. This dye is known to metabolize to benzidine, a known human carcinogen [6].

The eggshell is mainly the outer shield of the hard-shelled egg, and the weight of this shell is 11% of the overall weight of a single egg. The constituent materials of eggshells are $CaCO_3$, $MgCO_3$, $Ca_3(PO_4)_2$, and various organic matters, while the percent distributions are 94%, 1%, 1%, and 4%, respectively [7, 8].

Various methods such as adsorption, coagulation, advanced oxidation, and membrane separation are used in the removal of dyes from wastewater [9]. Adsorption is one of the most effective processes of advanced wastewater treatment which industries employ to reduce hazardous inorganic/organic pollutants present in the effluent [10].

RESULTS AND DISCUSSION

1. Optical Microscopy

Optical microscopy images of the WES (waste eggshells) surfaces before and after Congo Red (CR) adsorption were obtained using a Motic BA310Pol microscope. As shown in Fig. 1, a noticeable difference in surface roughness is observed between the unmodified WES sample (Fig. 1a) and the CR-loaded WES (Fig. 1b). The WES sample presents an irregular, rough and porous surface, with high granularity, and several tubular holes distributed in the mass of the adsorbent. The initial WES surface exhibited a porous morphology (Fig. 1a)., while the WES-CR sample displayed a distinct change in both colour and surface morphology, indicating the successful fixation of CR dye within the WES pores (Fig. 1b).

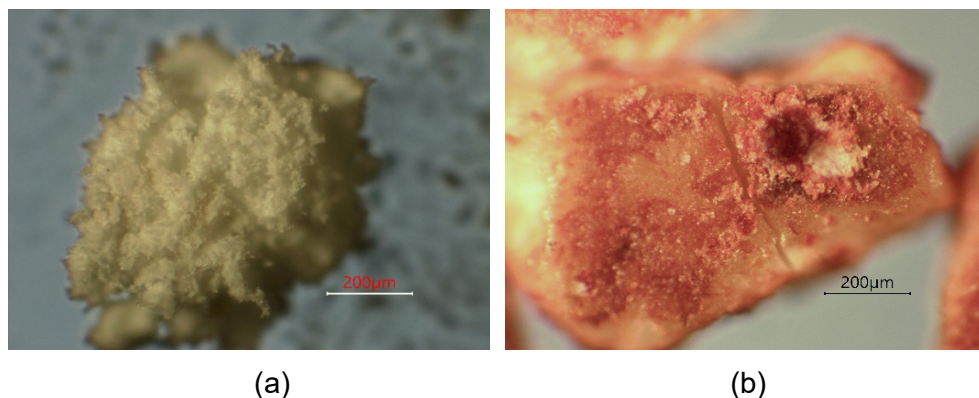


Figure 1. Optical microscope images of the WES samples before (a) and after (b) CR adsorption.

2. The FTIR Analysis

The FT-IR absorption spectra were recorded in reflection configuration with a Jasco 6000 spectrometer, at room temperature, in the range 400–4000 cm^{-1} ; spectral resolution of 4 cm^{-1} ; using the well-known KBr pellet technique.

From the spectral analysis, peaks at 407 cm^{-1} and 405 cm^{-1} are observed before and after the adsorption process, respectively. These fall within the fingerprint region. The band at 700 cm^{-1} can be assigned to vibrational modes associated to organic compounds with C-H, N-H, or C-O bonds [11]. After adsorption, these bands shift to 714 cm^{-1} , and remain only one peak, indicating a structural change in the N-H, C-H or C-O groups due to interaction with the adsorbate. A band at 751 cm^{-1} is present before adsorption and can be attributed to the out-of-plane deformation of the (=C-H) group. After adsorption, this band shifts slightly to 714 cm^{-1} , indicating a structural change in the (=C-H) group due to interaction with the adsorbate. Also, a rather important change is observed after CR adsorption on WES, in the sense that, the peaks at 595 and 640 cm^{-1} disappear, and also, the peak at 751 cm^{-1} is no longer founding the FTIR spectrum after CR uptake (Figure 1a, b). These important changes in the $500\text{--}800\text{ cm}^{-1}$ area support the adsorption process of the CR dye onto biomass surface. Moreover, by consulting the data from the literature [12,13] it results that these transformations are specific of calcite zone. The bands at 714 cm^{-1} and 877 cm^{-1} (after adsorption) are also associated with in-plane and out-of-plane deformations of calcium carbonate [12]. Additionally, band at 1014 cm^{-1} suggests stretching vibrations of the (C-O) functional group. A band at 1233 cm^{-1} is detected before adsorption, which shifts to 1206 cm^{-1} after the process, indicating deformation of the (C=S) group. The band at 1178 cm^{-1} disappears after the adsorption of CR, suggesting changes in the C-O stretching vibrations of compounds such as alcohols, ethers, esters, etc. A distinct band at 1347 cm^{-1} is attributed to the bending vibration of the C-H bond in alkane or aliphatic compounds from biocomposite (consisting of eggshell and its organic membrane), exhibits aromatic and aliphatic C-H stretching vibrations disappear also after CR uptake onto WES [7]. The band at 1653 cm^{-1} in the absorption spectrum from Figure 1 (up), specific for the stretching vibrations of C=C in aromatic compounds, is shifted and modified in amplitude from 1658 cm^{-1} (Figure 1 down). Additionally, the absorption band at 3498 cm^{-1} corresponds to the O-H stretching vibration associated with hydroxyl groups from alcohols, phenols, etc., from the organic part of eggshells was shifted at 3504 cm^{-1} after adsorption. In addition, the bands at 2371 , 2541 , and 2930 cm^{-1} that appear after the adsorption of CR are due to the characteristic functional groups of the CR dye structure [14].

STUDIES ON THE ADSORPTION OF CONGO RED ANIONIC DYE FROM SYNTHETIC
AQUEOUS SOLUTIONS USING WASTE EGGSHELL BIOMASS

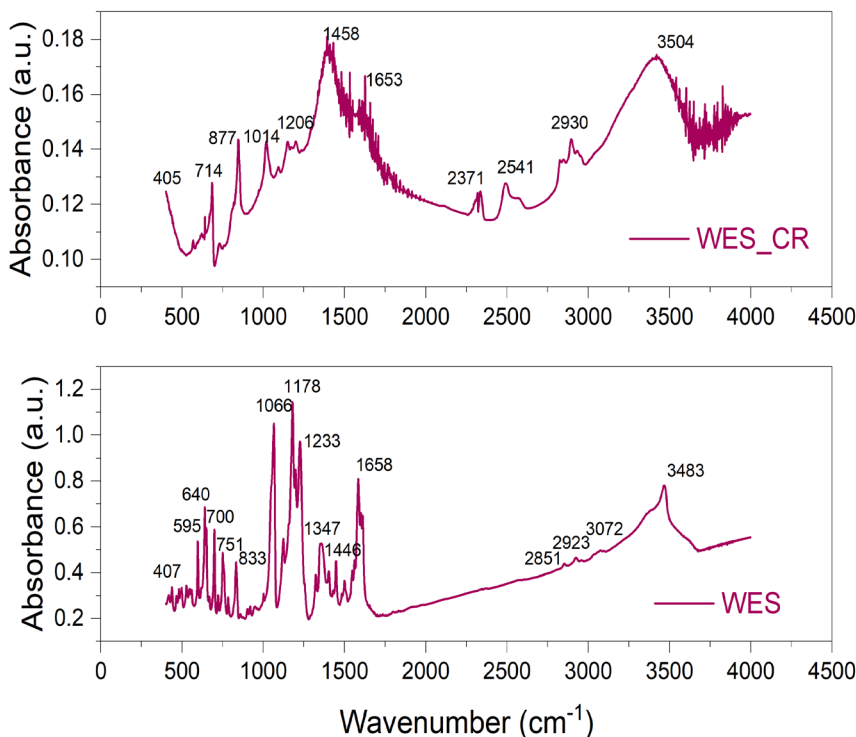


Figure 2. The FTIR spectra of the WES surfaces before (down) and after (up) CR adsorption.

3. Factors affecting efficiency of CR dye adsorption onto WES biomass

3.1. Effect of biomass quantity

The effect of biomass quantity on the adsorption of CR was studied using different masses of WES, ranging from 1 to 5 g/100mL CR solution.

Adsorption capacity determines the efficiency (E, %) and effectiveness of adsorption techniques for wastewater treatment.

Adsorption capacity refers to the quantity of adsorbate that a given mass of adsorbent can capture in specific conditions (Q, mg/g) [7].

Adsorption efficiency, expressed as percentage, was calculated with equation (1) [15.16]:

$$E = \frac{C_0 - C_e}{C_0} \times 100 \quad (1)$$

where C_0 and C_e are the initial and equilibrium concentrations of CR, respectively (mg/L).

The amount of pollutant (CR) adsorbed per gram of biomass (mg/g) was calculated using equation (2) [15,16]:

$$q_e = \frac{(C_0 - C_e) \cdot V}{m} \quad (2)$$

where V is solution volume (L) and m is WES quantity (g).

All presented values are the arithmetic mean of three series of data recorded from repetitions of the same experiment.

The effect of contact time on CR adsorption is presented in Fig. 3a. This evaluation is crucial, as it provides essential information regarding the time required to reach equilibrium. In all five cases (corresponding to 1–5 g of WES per 100 mL CR solution), equilibrium was achieved after 10 days under immobile phase conditions.

As shown in Fig. 3b, the maximum removal efficiency ranged from 98.61% (1 g WES) to 98.80% (5 g WES).

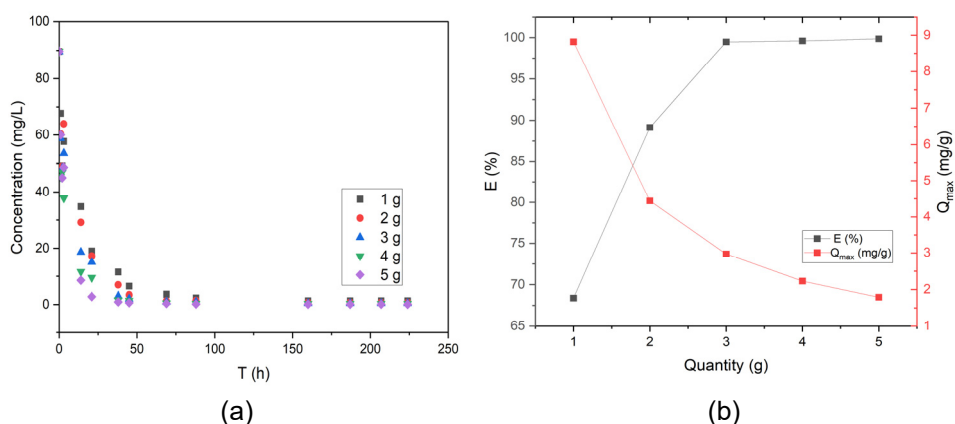


Figure 3. (a) Influence of the WES biomass dosage over the time evolution of RC concentration, in batch conditions; (b) The effect of biomass quantity (1-5 g WES) on the adsorption of CR dye efficiency (E , %) and maximum adsorption capacity (Q_{\max} , mg/g); 100 mL CR solution; $C_i = 97.75$ mg CR/L; particle size, $d < 0.2$ mm, immobile phases regime, 10 days.

The highest efficiencies were obtained with 4 g (98.78%) and 5 g (98.80%) of WES. The use of 5 g/100 mL solution CR produced a dense suspension that was difficult to handle; therefore, a dose of 4 g WES was employed in subsequent experiments.

3.2. Effect of initial CR concentration

In batch adsorption processes, the initial ion concentration of dyes in the solution plays an important role. Therefore, the amount of dye adsorbed is expected to be higher with a higher initial concentration of dye ions [14].

Also, the effect of initial CR concentration is closely related to the sites present on the adsorbent surface. In general, the percentage of dye removal decreases with increasing initial dye concentration, which leads to a saturation of adsorption sites on the adsorbent surface [15].

During the experiment, the adsorption of the anionic dye CR onto WES biomass was investigated at different initial dye concentrations ranging from 40.38 to 203.62 mg CR/L. The effect of contact time onto initial CR concentration is presented in Figure 4a. The results demonstrate that, regardless of the initial concentration of the dye solution, the residual concentration of CR in the solution approaches zero once equilibrium is reached (after 10 days). This observation supports the authors' claim that the biomass studied could constitute a very effective and valuable adsorbent material in future applications for water pollution remediation.

Figure 4b illustrates both the removal efficiency and the equilibrium adsorption capacity of CR as a function of the initial CR concentration.

In each test, 4 g of WES (particle size < 0.2 mm) was added to 100 mL of CR solution and left under immobile phases conditions at room temperature ($295 \pm 2\text{K}$), without pH adjustment (initial pH of CR solution = 5.94). As shown in Figure 4b, the adsorption capacity of WES increased with increasing initial CR concentration, between 96.5 mg CR/g to 98.6 mg CG/g WES, while the efficiency increases in all 5 experiments from 67.70% for initial concentration of 40.38 mg CR/L to 99.91 % for 203.62 mg CR/L utilized.

3.3. Effect of particle size

To evaluate the effect of particle size on the adsorption process, the WES material was ground and sieved into five different size fractions (< 0.2, 0.2-0.4, 0.4-1.0, 1.0-1.6 and >1.6 mm, Fig. 5a).

To establish the optimum adsorbent grain size, experiments were realized in the following conditions: 100 mL CR aqueous solution of $C_i=97.75$ mg/L was contacted with 1 g of WES, with grain sizes of $d >1.6$ mm; 1.6-1.0 mm; 1.0-0.4 mm; 0.4-0.2 mm or <0.2 mm. CR adsorption experiments were conducted in batch conditions, with immobile phases regime, at $pH=5.94$ and room temperature ($T = 295K$).

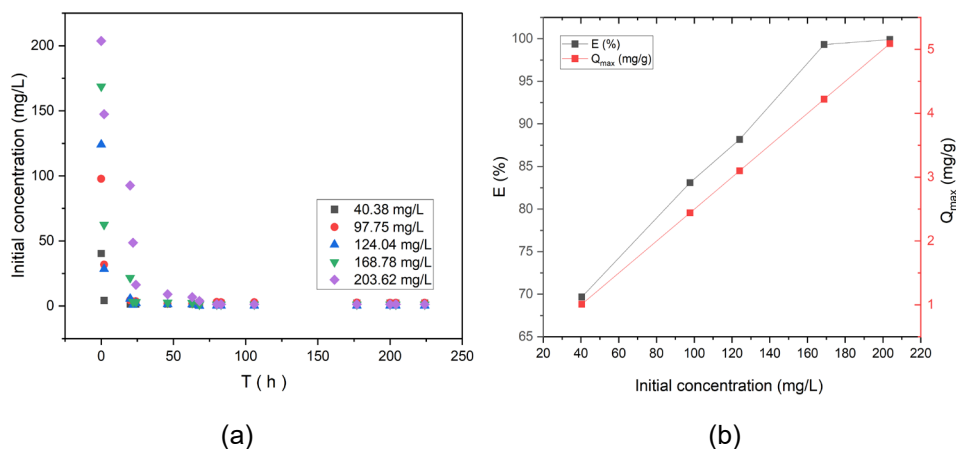


Figure 4. (a) Effect of contact time on the initial concentration of CR dye using WES biomass; $C_i = 40.38$ – 203.62 mg CR/L, 4 g WES, $d < 0.2$ mm, 295 K, $pH = 5.94$, 10 days, immobile phases regime; (b) Influence of the initial CR dye concentration over the adsorption capacity and removal efficiency on WES biomass; $C_i = 40.38$ – 203.62 mg CR/L, 4 g WES, $d < 0.2$ mm, 295K, $pH = 5.94$, 10 days, immobile phases regime.

As can be seen (Figure 5a, b), the small particle sizes result in a larger specific surface area of WES, and consequently, increase the adsorption yield from 75.62 %, for $d >1.6$ mm to 96.62 % for $d < 0.2$ mm WES grain sizes. When larger particles were ground into particles with smaller diameters, some tiny channels could be opened which might then become available for biosorption. This behaviour is in good agreement with other data from the literature [16].

STUDIES ON THE ADSORPTION OF CONGO RED ANIONIC DYE FROM SYNTHETIC AQUEOUS SOLUTIONS USING WASTE EGGSHELL BIOMASS

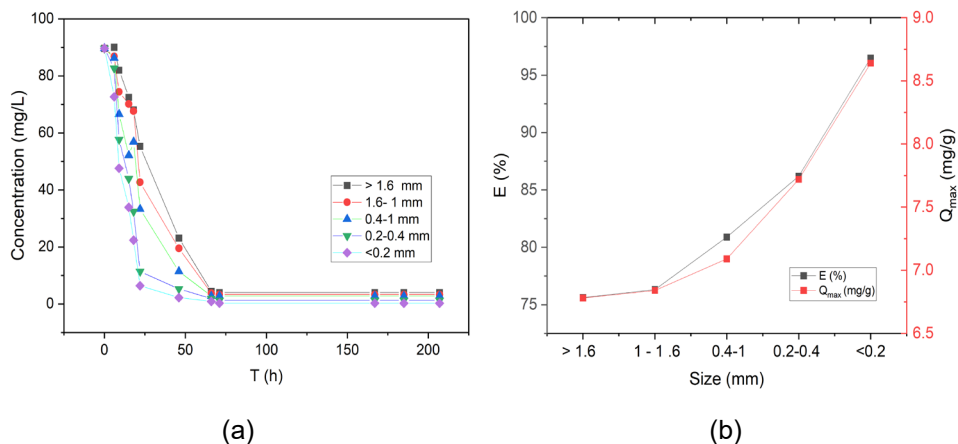


Figure 5. (a) CR concentrations time evolution for different particle sizes of WES adsorbent ($d > 1.6$ mm; 1.6-1.0 mm; 1.0-0.4 mm; 0.4-0.2 mm and < 0.2 mm); (b) Representation of particle size effect of WES on CR adsorption efficiency ($C_i = 97.75$ mg CR/L, 1 g WES, 295 K, pH=5.94, 10 days, immobile phases regime).

The results obtained revealed that intraparticle diffusion within the pores of the WES adsorbent plays a significant role in governing the overall adsorption process. A substantial increase in adsorption capacity was observed with decreasing WES particle diameter, a behaviour consistent with trends previously reported in the literature [15, 17].

3.4. Effect of initial CR dye solution pH

The pH is one of the most important controlling parameters in the biosorption process of dyes from wastewater [18].

The pH of aqueous solution can highly affect the WES surface charge. In acidic media, the surface of the adsorbent is protonated, while in a basic medium its surface deprotonates.

From the literature data result that adsorption was favourable in acidic media [19, 20]. This may happen because of an electrostatic attraction between functional groups present in WES adsorbent and sulfonate (SO_3^-) group of CR [7].

The adsorption process was investigated by varying the pH of the aqueous solution within the range of 5.94–10.93. As presented in Figure 6, the highest adsorption efficiency for CR dye was obtained at pH 5.94 (99.7%), while in all cases the efficiency (E, %) remained above 98%. Upon

reaching adsorption equilibrium, the equilibrium concentration (C_e) corresponded to a final pH value of approximately 7 for all tested solutions (initial pH = 5.94, 6.68, 8.66, 9.46, and 10.93).

This result indicates that WES possesses an intrinsic buffering or neutralizing capacity, effectively stabilizing the pH of the dye solutions near neutrality regardless of the initial conditions.

In the future, this experimental finding could be extensively exploited, as WES appears to be a highly efficient adsorbent and a potential pH corrector.

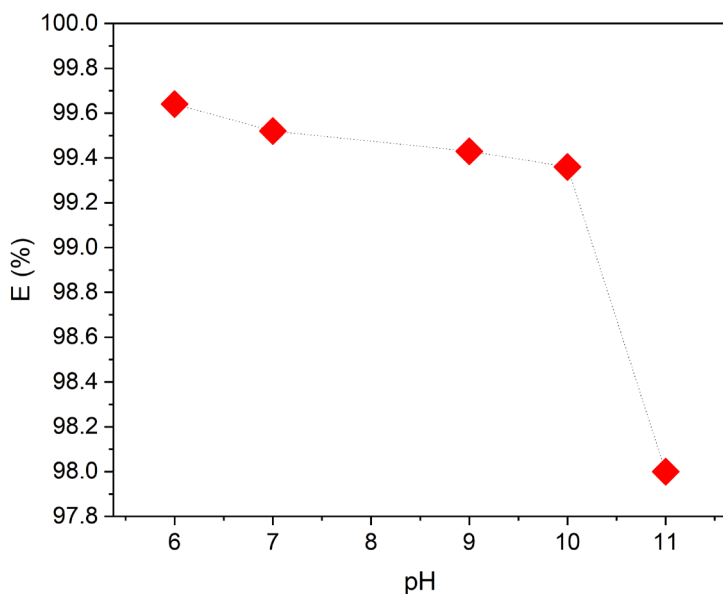


Figure 6. The effect of initial pH on percentage removal values for CR adsorption onto WES ($C_i = 97.75$ mg CR/L, 4 g WES/100 mL, $d < 0.2$ mm, 295 K, 10 days, immobile phases regime).

3.5. Thermodynamic aspects of CR adsorption onto WES biomass

3.5.1. Effect of temperature onto adsorption process

To describe the thermodynamic behaviour of the biosorption of CR onto WES biomass, standard thermodynamic parameters, including the changes in standard free energy (ΔG°), enthalpy (ΔH°) and entropy (ΔS°) were calculated using the following equations:

$$\Delta G^{\circ} = -RT \ln K_d \quad (3)$$

$$\Delta G^{\circ} = \Delta H^{\circ} - T\Delta S^{\circ} \quad (4)$$

where, R is the universal gas constant (8.314×10^{-3} kJ/K·mol), T is absolute temperature (K), and K_d is the distribution coefficient (L/g) calculated as q_e/C_e , where q_e is biosorption capacity (mg/g) and C_e is CR concentration in solution at equilibrium.

The enthalpy (ΔH°) and entropy (ΔS°) parameters were estimated from the equation Van't Hoff [15,19]:

$$\ln K_d = -\frac{\Delta H^{\circ}}{RT} + \frac{\Delta S^{\circ}}{R} \quad (5)$$

The effect of temperature on adsorption of 97.75 mg CR/L initial concentration of CR dye on 4 g/100 mL WES adsorbent dose was investigated. The experiments were completed at 295 K, 305 K, and 325 K (Fig. 7a). ΔH° and ΔS° values were obtained from the slope and the intercept of this plot, respectively. The standard free energy change (ΔG°), standard enthalpy change (ΔH°) and standard entropy change (ΔS°) were obtained using Equations (3) and (4) and their values associated with the adsorption of CR onto WES biomass are listed in Table 2.

From Fig. 7a, it can be noted that the effect of temperature has no very negative impact on adsorption capacity. Its values decrease, but not very much (between 2.430 mg/g, at 295 to 2.397 mg/g at 315K) as temperature increases from 295 to 325 K.

Further, the data obtained by plotting $\ln (Q_e/C_e)$ vs. $1/T$ were subject for thermodynamic study in order to establish the nature of adsorption process, Table 1 and Fig. 7b, shows the thermodynamic parameters of CR dye adsorption on WES.

Table 1. Thermodynamic parameters for CR adsorption onto WES at various temperatures ($C_i = 97.75$ mg CR/L, 40 g WES /L, $d < 0.2$ mm, pH=5.94).

ΔS° kJ/K·mol	ΔH° kJ/mol	ΔG° kJ/mol		
		295 K	305 K	315 K
-0.128	-40.708	-2.948	-1.667	-0.388

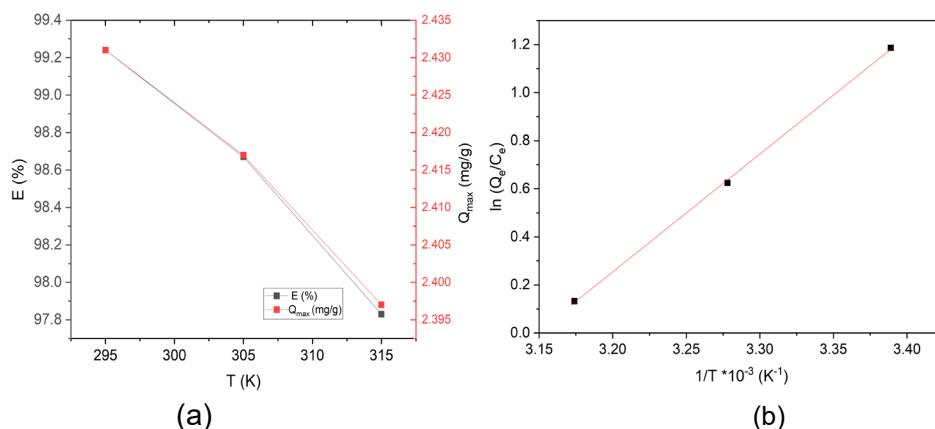


Figure 7. (a) The effect of temperature on removal efficiency for CR adsorption onto WES (b) Van't Hoff plot for the determination of thermodynamic parameters for the adsorption of CR onto WES as adsorbent ($C_i = 97.75$ mg CR/L, 4 g WES/100 mL, $d < 0.2$ mm, $\text{pH}=5.94$).

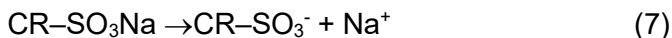
The values of ΔH , ΔS and ΔG are shown in Table 2. The negative values of ΔG that increased from -2.948 kJ/mol to -0.388 kJ/mol with an increase in temperature from 295 K to 315 K suggesting that adsorption can be dominated by weak physical interactions and that the physical adsorption predominate.

Also, the thermodynamic parameters indicate the feasibility of the process and the spontaneous nature of the adsorption.

The negative enthalpy change ($\Delta H = -40.708$ kJ/mol) confirms the exothermic nature of the biosorption process, indicating that heat is released during the adsorption of the solute onto the WES adsorbent surface [21].

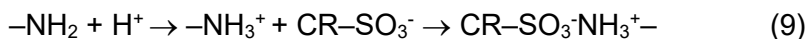
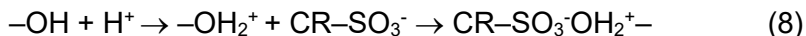
3.5.2. Mechanism of CR Dye Adsorption onto WES surface

Primarily, in aqueous solution, the Congo Red (CR) dye ($\text{CR}-\text{SO}_3\text{Na}$) undergoes dissolution and subsequent dissociation, yielding dye anions ($\text{CR}-\text{SO}_3^-$), as illustrated in Equation (7).



The surface of WES is enriched with polar functional groups, primarily $-\text{NH}_2$ and $-\text{OH}$ moieties (Figure 2). At low pH conditions ($\text{pH} = 5.94$), these groups undergo protonation, resulting in the formation of $-\text{NH}_3^+$ and $-\text{OH}_2^+$

species, respectively. Consequently, electrostatic interactions are likely established between these positively charged surface functionalities and the negatively charged dye anions, as illustrated in Equations (8) and (9).



Therefore, the plausible adsorption mechanism can be attributed to a synergistic interplay of electrostatic attractions between the positively charged protonated functional groups of the adsorbent and the anionic species of the Congo Red (CR) dye, complemented by hydrogen bonding interactions and additional non-covalent forces such as π - π stacking and van der Waals interactions. [22, 23]

3.5.3. Effect of diffusion onto adsorption process

The intraparticle diffusion model proposed by Weber and Morris [24] was applied to elucidate the diffusion mechanisms governing the adsorption process.

The influence of intraparticle diffusion resistance on adsorption can be evaluated using the following relationship (Eq. 10), in which the intraparticle diffusion rate constant (k_{ip} , $\text{mg g}^{-1} \text{min}^{-0.5}$) proposed by Weber and Morris was fitted to the experimental data:

$$Q_t = k_{ip} t^{1/2} + C \quad (10)$$

Weber–Morris intraparticle diffusion model, where $Q_t(\text{mg g}^{-1})$ is the amount of adsorbate at time t , $k_{ip}(\text{mg g}^{-1} \text{min}^{-0.5})$ is the intraparticle diffusion rate constant, and $C(\text{mg g}^{-1})$ represents the boundary layer thickness or intercept (Table 2).

A larger C value indicates a greater boundary layer effect, while a higher k_{ip} value reflects a faster diffusion rate within the adsorbent particles.

The diffusion mechanism was evaluated using the intraparticle diffusion model, which generally comprises three linear regions corresponding to film diffusion, pore diffusion, and adsorption equilibrium [25, 26]. The intraparticle diffusion plots for CR adsorption onto WES biomass (Figure 8a) display a multilinear trend, indicating that multiple diffusion processes govern the overall adsorption mechanism.

Table 2. Intra-particle diffusion rate coefficients and liquid film diffusion rate coefficients for CR uptake on WES biomass; $C_i=40.38$ -124.04 mg CR/L, 4 g CR, $d < 0.2$ mm, 295 K, pH=5.94, immobile phases regime, 10 days.

Internal diffusion			
Initial concentration (mg/L)	k_{ip} (mg/g·h ^{0.5})	Intercept	R^2
124.04	0.332	1.472	0.904
97.75	0.229	1.315	0.998
40.38	0.033	0.828	0.985
External diffusion			
Initial concentration (mg/L)	K_{fd} (1/h)	Intercept	R^2
124.04	0.109	0.867	0.940
97.75	0.118	0.885	0.996
40.38	0.061	1.915	0.942

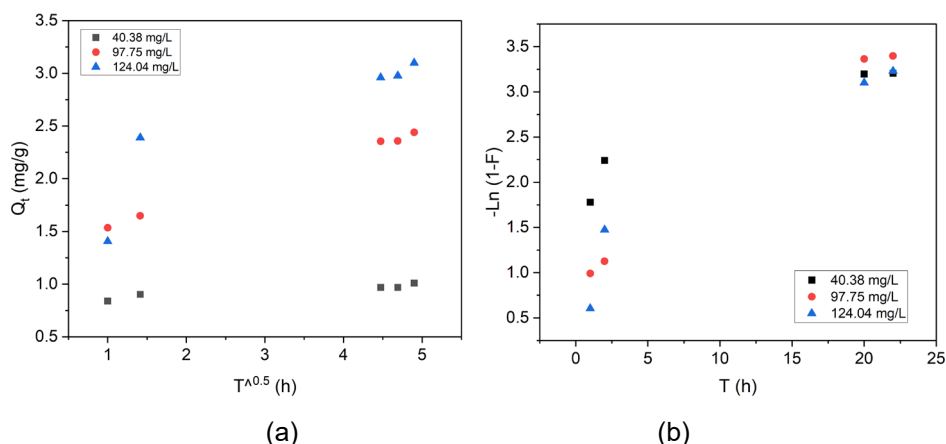


Figure 8. Plots of the (a) intraparticle diffusion (Weber–Morris) and (b) liquid film diffusion (Boyd) model for CR adsorption using WES biomass; $C_i = 40.38$, 97.75 and 124.04 mg CR/L, $d < 0.2$ mm, 295 K, pH 5.94, 10 days contact time, immobile phases regime.

Plots of Q_t versus $t^{1/2}$ were linear (with corresponding R^2 values shown in Table 2), but the intercepts, C values, (0.828–1.472) did not pass through the origin for the initial CR concentrations of 124.04 and 97.75 mg/L, suggesting that intraparticle diffusion was not the sole rate-controlling step. At the lowest concentration (40.38 mg/L), a smaller intercept value indicates that intraparticle diffusion contributed more significantly to the adsorption

process. This behaviour implies that at low dye concentrations, reduced boundary layer resistance facilitates dye diffusion into the internal pores of the WES biomass, whereas at higher concentrations, both film and intraparticle diffusion jointly influence the adsorption rate.

If it is considered that external diffusion (through the liquid film on the surface of the adsorbent granule) can be the rate-determining step, the pore diffusion constant can be calculated using the equation derived by Boyd [27], the liquid film diffusion model (Table 2):

$$\ln(1 - F) = -k_{fd} \cdot t \quad (11)$$

where, $F = q_t/q_e$ and k_{fd} is the rate constant of diffusion through the liquid film, in L/min.

At higher initial concentrations (124.04 and 97.75 mg/L), the subunit intercept values (0.867 and 0.885, respectively; Table 2) further confirm that the adsorption process was primarily governed by external (film) diffusion. The higher concentration gradient likely enhanced mass transfer from the bulk solution to the biomass surface, favouring film diffusion over pore diffusion. These results are consistent with previous studies [7, 28, 29], indicating that external diffusion predominates at elevated solute concentrations.

Although the use of WES biomass represents a promising approach for the removal of Congo Red (CR) dye from wastewater, several inherent limitations remain, posing significant scientific and technological challenges for future research. These challenges include:

- *low adsorption capacity* – the primary constituent of WES, calcium carbonate (CaCO_3), possesses a relatively low specific surface area and a limited number of active functional sites, resulting in inferior adsorption performance compared to activated carbon, biochar, or surface-modified adsorbents.
- *limited structural stability and regeneration efficiency* — the desorption and subsequent reuse of WES-based adsorbents are often inefficient, which hinders their long-term applicability in cyclic adsorption–desorption operations.
- *management of spent adsorbent* — following dye adsorption, the disposal of dye-laden eggshell material must be carefully addressed, as improper handling, such as direct landfilling or incineration, may induce secondary environmental contamination.

In view of these limitations, future research should focus on enhancing the adsorption capacity of WES biomass, developing efficient strategies for the management and regeneration of spent adsorbent, and extending investigations to complex wastewater matrices containing multiple pollutants beyond Congo red dye.

CONCLUSIONS

The whole eggshell matrix (WES), consisting of the eggshell and the eggshell membrane, represents a promising low-cost and eco-friendly adsorbent for dye removal from aqueous solutions. This study investigates the potential of WES as an adsorbent for Congo Red (CR) dye.

Results show that 1.0 g of eggshell material was sufficient to remove more than 90% of the pollutants analyzed. The WES effectively adsorbed CR at low concentrations, although the percentage removal decreased with increasing dye concentration. Adsorption equilibrium was reached after 10 days, under static conditions (in immobile phases regime). The maximum biosorption efficiency (99.93%) was obtained at pH 5.94 and 295 K, using a 97.75 mg L⁻¹ CR solution and 4 g of WES with a 10-day contact time.

The adsorption process was found to be pH-dependent, with optimum performance at pH 5.94. The effect of pH on sorption capacity was mainly attributed to ionic interactions between the surface of the WES and the CR molecules. Due to the porous structure of the eggshell—composed predominantly of calcium carbonate and offering a high surface area for dye interaction—WES exhibited remarkable adsorption behavior across a range of initial pH values. Interestingly, regardless of the initial pH of the synthetic wastewater, the final pH after adsorption consistently reached neutrality (pH=7).

Temperature (295, 305, and 315 K) had a noticeable but limited influence on dye adsorption. The observed temperature dependence was attributed to the increased mobility of CR ions, which may desorb from the solid phase back into the solution at higher temperatures.

Overall, the findings demonstrate that WES is an efficient, sustainable, and low-cost biosorbent for the decolorization of synthetic wastewater containing Congo Red dye.

EXPERIMENTAL SECTION

Biosorbent

The biomass used as adsorbent material for the removal of CR dye from wastewater was chicken eggshells, a residue that can be easily procured and found in large quantities. The adsorbent material (WES) was employed without any preliminary chemical treatment. It was thoroughly washed with distilled water, oven-dried at 105 °C.

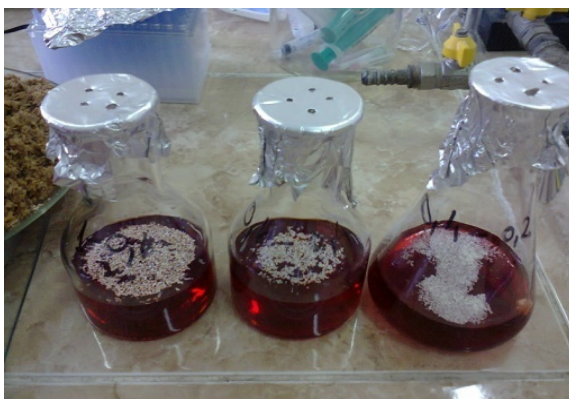
Sieving and Particle Size Fractionation

The dried sample was subjected to mechanical sieving to separate it into defined particle size fractions. A stainless steel sieve set (Retsch AS 200) was used, comprising sieves with mesh openings ranging from > 1.6 mm to <0.2 mm (corresponding to sieve sizes: >1.6 mm, 1.0-1.6 mm, 0.4-1.0 mm, 0.2-0.4 mm, 125 µm, and <0.2 mm).

Approximately 100 g of the dried material was placed on the uppermost sieve, and the stack was secured and mounted on the mechanical shaker. Sieving was performed for 10 minutes at an amplitude of 1.5 mm (vibration intensity setting 70%) to ensure efficient separation without particle degradation. After sieving, each fraction retained on the sieves was carefully collected, weighed, and stored in airtight containers for further analysis.



(a)



(b)

Figure 9. (a) The general macroscopic aspect of eggshells, before their physical processing; (b) Adsorption experiments of CR removal by WES, in a regime with immobile phases.

The sieved biosorbent was then stored in an airtight box before its utilization. No further chemical treatments were considered at this stage. Optical microscope images of biosorbent were obtained with an apparatus on samples.

Chemicals

Congo Red (CR, Direct Red 28, C.I. 22120, azo dye, $C_{32}H_{22}N_6Na_2O_6S_2$, molecular weight 696.7, selected as anionic dye) was purchased from Penta (Czech Republic) and used without further purification. The stock solution, 1000 mg/L of Congo Red was prepared by dissolving the solid in distilled water. The required concentrations were obtained by diluting the stock solution to the desired concentrations, in 40–200 mg/L range. CR concentration was determined using a double beam UV-visible spectrophotometer (GBC Cintra 202) at $\lambda = 498$ nm. HCl (0.1 M) and NaOH (0.1 M) volumetric solutions were used to adjust the solution pH. All chemicals used were of analytical grade.

Biosorption Experiments

The biosorption experiments were carried out under batch conditions in a static regime, by contacting a defined mass of adsorbent (1–5 g) with 100 mL of Congo Red (CR) dye aqueous solution at concentrations ranging from 40 to 204 mg L⁻¹. Adsorption was allowed to proceed until equilibrium was reached, as determined from preliminary experiments. The residual dye concentration in the solution was determined at predefined time intervals following preliminary centrifugation (5 min at 6000 rpm) and appropriate dilution.

The solid fraction of WES was separated by centrifugation using a Hettich EBA 200 centrifuge equipped with an angled rotor, operated at a relative centrifugal force (RCF) of approximately 3461×g. Solid–liquid separation of the eggshell-derived adsorbent from the supernatant was routinely conducted using this procedure. The absorbance of the supernatant was measured at the maximum wavelength (λ_{max}) of CR, and dye concentrations were calculated from the corresponding calibration curve.

To evaluate the effect of temperature on the adsorption process, experiments were conducted at 295, 305, and 315 K using 100 mL of CR solution (97.75 mg L⁻¹) and 4 g of WES.

Fourier transform infrared (FTIR) spectra of the adsorbent before and after adsorption were recorded in triplicate using a Varian FT-IR 670 spectrometer over the range 4000–400 cm⁻¹. Each sample was finely ground, mixed with KBr at a mass ratio of 1:50 (sample:KBr), and pressed into pellets for analysis.

Stability of CR dye solutions

To determine the wavelength corresponding to the maximum absorbance (λ_{\max}) and its variation with pH, a 5 mg L⁻¹ solution of CR was prepared. The pH of the solution was adjusted over the range of 5.94 to 10.93 using 0.1 M HCl or 0.1 M NaOH. Visible absorption spectra were then recorded at room temperature using a double-beam UV–Vis spectrophotometer (GBC Cintra 202). The maximum absorbance was observed at a wavelength of 498 nm.

Decolorization was quantified by correlating the absorbance at this wavelength. The CR dye adsorbed by the WES biomass was calculated from the difference between initial concentration and the final concentration in the supernatant and was calculated using the equations (1) and (2).

ACKNOWLEDGMENTS

The authors express their gratitude to their colleague, lecturer Cosmin Coteț, PhD, for performing the optical microscopy analyses.

Also, the authors thank Mrs. Miuța Filip for recording the FTIR spectra.

REFERENCES

1. UN World Water Development Report 2024 | UN-Water
2. J. Ambigadevi and P. Senthil Kumar, *Int. J. Chem. Eng.*, **2025**, *1*, 1-19
<https://doi.org/10.1155/ijce/5541488>.
3. Kusumlata, B. Ambade, A. Kumar, S. Gautam, *Limnol. Rev.*, **2024**, *24*(2), 126-149; <https://doi.org/10.3390/limnolrev24020007>.
4. K. Litefti, M.S. Freire, M. Stitou, J. G. Álvares, *Nature Sci. Rep.*, **2019**, *9*, 16530; <https://doi.org/10.1038/s41598-019-53046-z>.
5. H. Bai, Y. Feng, C. Zhu, P. Guo, J. Wang, Y. Zhou, L. Zhang, S. Li, J. Chen, *J. Taiwan Inst. Chem. Eng.*, **2024**, *164*, 105689 - 105695.
<https://doi.org/10.1016/j.jtice.2024.105689>.
6. V. S. Mane and P.V.V. Babu, *J. Taiwan Inst. Chem. Eng.*, **2013**, *44*(1), 81-88.
<https://doi.org/10.1016/j.jtice.2012.09.013>

7. P. E. Emumejaye, S. C. Ikpeseni, M. Ekpu, S. O.-O. Sada, P. O. Ohwofadjeke, *J. Sci. Technol. Res.*, **2023**, 5(4), 128-137.
8. S. Parvin, Al-M., F. Rubbi, Md. A. Ruman, Md. M. Rahman, B. K. Biswas, *Aceh. Int. J. Sci. Technol.*, **2020**, 9(2) 63-74, <https://doi.org/10.13170/aijst.9.2.16767>
9. M.T. Yagub, T. K. Sen, S. Afroze, H.M. Ang, *Adv. Col Interface Sci*, **2014**, 209, 172-184, <https://doi.org/10.1016/j.cis.2014.04.002>.
10. S. Satyam, S. Patra, *Helyion*, 2024, 10(9), e29573 - 29597. <https://doi.org/10.1016/j.helyion.2024.e29573>.
11. P.E. Emumejaye, S.C. Ikpeseni, M. Ekpu, S.O.O. Sada, P. Ohwofadjeke, *J. Sci. Technol. Res.*, **2023**, 5(4), 128-137.
12. R. de Oliveira Zonato, B. R. Estevam, I. D. Perez, V. A. dos Santos Ribeiro, R.F. Boina, *Clean Chem. Eng.*, **2022**, 2, 100023-100032. <https://doi.org/10.1016/j.clce.2022.100023>.
13. A.Soltani, M. Faramarzi, S.A. Mousavi Parsa *Water Quality Res. J.*, **2021**, 56 (4),181-193. <https://doi.org/10.2166/ wqrj.2021.023>.
14. R.A Nassif., *J. Multidiscipl. Eng. Sci. Technol.*, **2019**, 6(9), 10611-10613.
15. M.K. Dahri, M.R.R. Kooh, L.B.L. Lim, *J. Environ. Chem. Eng.*, 2014, 2(3), 1434-1444 <https://doi.org/10.1016/j.jece.2014.07.008>.
16. M. Harja, G. Buema, D. Bucur, *Nature. Sci. Reports*, **2022**, 12, 6087-6105. <https://doi.org/10.1038/s41598-022-10093-3>
17. K. M. Ravi, G. M., Wondalem, P.S. Satya, J.J. Lakshmi, A.S. Ashager, P. King, M. Vijay, G. Baburao, *Chem. Methodol.*, **2023**, 7, 605-612. <https://doi.org/10.22034/CHEMM.2023.395359.1676>.
18. S. Burcă, A.Măicăneanu, C. Indolean, *Rev. Roum. Chim.*, **2014**, 59(10), 817-824.
19. M.A. Abdel-Khalek, M.K. Abdel Rahman, A.A. Francis, *J. Environ. Chem. Eng.*, **2017**, 5(1), 319-327. <https://doi.org/10.1016/j.jece.2016.11.043>
20. N. K. Kinaytürk, B. Tunali, D.T. Altug, *R. Soc. Open Sci.*, **2021**, 8, 210100-210114. <https://doi.org/10.1098/rsos.210100>
21. J. R. Njimou, A. Măicăneanu, C. Indolean, C.P. Nanseu-Njiki, E. Ngameni, *Environ. Technol.*, **2016**, 37(11), 1369–1381. <http://dx.doi.org/10.1080/09593330.2015.1116609>
22. N. F. Al-Harby, E. F. Albahly, N. A. Mohamed, *Polymers*, **2021**, 13(24), 4446-4478. <https://doi.org/10.3390/polym13244446>
23. R. Kumar, S.A. Ansari, M.A. Barakat, A. Aljaafari, M.H. Cho, *New J. Chem.*, **2018**, 42, 18802–18809.
24. W.J. Weber, J.C. Morris, J.C., (1963) *J. Sanitary Eng. Div., Am. Soc. Civil Eng.*, **1963**, 89, 31-60.
25. Meghana, C., Juhi, B., Rampal, N., Vairavela, P., *Desalination Water Treat.*, **2020**, 207, 373–397, <http://doi.org/10.5004/dwt.2020.26389>
26. K.Wu, X.Pan, J. Zhang, Xi. Zhang, A. Salahzene, Y. Tian, **2020**, *ACS Omega*, 5(38), 24601-24612. <https://doi.org/10.1021/acsomega.0c03114>.
27. J. Wang , X. Guo, *J. Hazard. Mater.*, **2020**, 390, 122156-12274. <https://doi.org/10.1016/j.jhazmat.2020.122156>

STUDIES ON THE ADSORPTION OF CONGO RED ANIONIC DYE FROM SYNTHETIC
AQUEOUS SOLUTIONS USING WASTE EGGSHELL BIOMASS

28. P. S Kumar, S.J. Varjani, S. Suganya, *Bioresour. Technol.*, **2017**, 250, 716–722.
<https://doi.org/10.1016/j.biortech.2017.11.097>
29. G.O. Ogunlusi, O.D. Amos, O.F. Olatunji, *J Iran. Chem. Soc.*, **2023**, 20, 817–830. <https://doi.org/10.1007/s13738-022-02721-6>.

A NEW REAGENT FOR SYNTHESIS OF NITRILES FROM ALDOXIMES USING ALUMINIUM (III) TRIFLATE

Nesimi ULUDAG^{a*} , Alper SANLI^a 

ABSTRACT. We report a new, highly efficient, and straightforward method for the dehydration of aldoximes to nitriles using aluminium (III) triflate [Al(OTf)₃] as a catalyst in acetonitrile. This one-step transformation proceeds with moderate to excellent yields (44–94%) and tolerates a wide range of substrates, including those with aromatic, functionalized aryl, heteroaryl, alkyl, and cycloalkyl moieties. This approach serves as a practical method for the synthesis of nitriles from aldoximes, yielding valuable synthetic intermediates for the pharmaceutical and agrochemical industries. In addition, the method's operational simplicity and the convenient isolation of the final product are its key advantages.

Keywords: Aluminum triflate; Nitriles; Reaction mechanism; Catalysis; Dehydration

INTRODUCTION

Compounds containing the nitrile derivatives are widely used industrially important in the fields of organic chemistry for production of agrochemicals, pharmaceuticals as well as material sciences [1-6]. Deoximation for the regeneration of nitriles from the corresponding oximes is still a worthwhile topic of study in organic chemistry [7-16]. Therefore, the versatility of the recent literature revealed that numerous reagents have been used for this purpose with different degrees of success. A number of efficient examples from literature include methyl N-(triethylammonium-sulfonyl)carbamate (Burgess reagent) [17], Cu(OAc)₂/ultrasound [18], Pd/Mn [19], diethyl phosphorocyanidate

^a Namık Kemal University, Faculty of Science and Arts, Department of Chemistry, 59030, Tekirdag-Turkey

* Corresponding author: nuludag@nku.edu.tr



[20], Rosenmund-von Braun reaction [21], $[\text{RuCl}_2(p\text{-cymene})]_2/\text{molecular sieves}$ [22], $\text{Ga}(\text{OTf})_3$ [23], Ceric ammonium nitrate (CAN) [24], $\text{Ph}_3\text{PO} / (\text{COCl})_2$ [25], NCS/PPh_3 [26], $\text{Ac}_2\text{O}/\text{K}_2\text{CO}_3/\text{DMSO}$ [27], and $\text{PEG-SO}_3\text{H}$ [28] has also been used to carry out deoximation. Additionally, Recognizing the limitations of current aldoxime-to-nitrile conversion methods, including harsh conditions, low yields, lack of generality, and the use of costly or less accessible reagents, as well as high microwave power. To advance synthetic transformations and introduce a new perspective in organic chemistry, and the key compound, aldoximes, was prepared by following the literature for the deoximation reaction [29-32]. Firstly, according to our research, different aldehydes were used to make aldoximes with different structures and electron-withdrawing or electron-donating properties. For this purpose, aluminium (III) triflate was selected for preliminary studies, and the optimal conditions were determined to afford the corresponding nitrile.

Herein, Our aim was to develop a new method for the synthesis of nitriles from aldoximes using an aluminium (III) triflate-catalyzed dehydration reaction. and also work on understanding the mechanism of aluminium (III) triflate-mediated deoximation (Scheme 1).

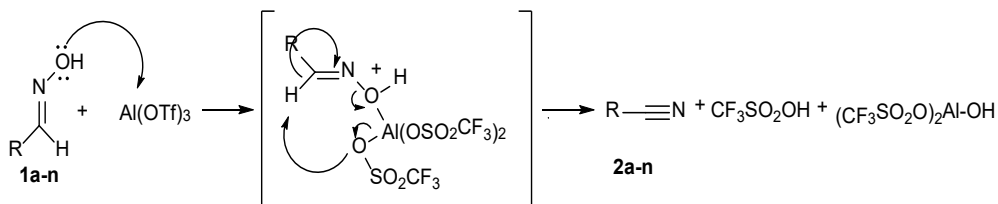
Considering several advantages from this reaction, the development of a new method, good to excellent yields, and a wide scope of applicability, we report an investigation into the effect of substituents on the rate of deoximation using various derivatives bearing electron-withdrawing and electron-donating groups. In contrast to previous methods, which require in situ preparation or involve commercially less accessible reagents, the use of aluminum triflate afforded the desired products in moderate to good isolated yields for the first time in our study. Another advantage is that aluminum (III) triflate has been found to be a highly effective Lewis acid catalyst for the deoximation reaction.

RESULTS AND DISCUSSION

We discovered from our literature study that aluminum triflate has not been used in very much work for deoximation reaction. Previously, we reported that trifluoromethanesulfonic anhydride [15] and methoxymethyl bromide [16] are efficient and mild reagents for dehydration of aldoximes to nitriles under mild conditions. In continuation of our interests in developing a new method for conversion of aldoximes to nitriles, we herein wish to report the first application of aluminum triflate to the efficient synthesis of nitriles from aldoximes under efficient method as such a reagent. This study, therefore, examined the effectiveness of aluminium (III) triflate as a Lewis

acid for the dehydration of aldoximes. At this point, our initial work commenced with screening of solvent so as to obtain optimal reaction condition. In order to obtain the scope and efficiency of the optimum reaction conditions, benzaldehyde oxime **1** was reacted with various solvents. The results are shown in Table 1. From the results in Table 1 it is evident that use of acetonitrile with aluminium (III) triflate led to the efficient conversion of aldoxime an in good yield 79% upon refluxing for 3 hours as model substrates for this reaction (Entry 9). Several other solvents were evaluated, including DMSO, CH₂Cl₂, THF, EtOH, DMF, MeOH, dioxane, and toluene, but were all found to be much less efficient than MeCN, and the results are summarized in Table 1. Thus, we observed that in the presence of aluminium (III) triflate, dehydration of aldoximes gave nitriles upon refluxing after 2-4 h. A wide range of organic aldoxime compounds, mainly aromatic, functionalized aryl, heteroaryl, alkyl, and cycloalkyl moieties, was used as starting materials and the starting oximes were synthesised according to the literature [30]. All reactions were checked by TLC, FT-IR, and MS analysis, and final products were determined by ¹H NMR and ¹³C NMR. The spectral analyses of nitriles verified the cyano group with the appearance of specific peaks at around 2200 cm⁻¹ (-C≡N). The procedure for obtaining benzonitrile **2a** was then successfully extended to aldoximes **1b-n** (Scheme 1). To further expand the scope of the process, we examined the reaction mechanism between benzaldoxime **1a** and aluminium (III) triflate. As expected, in the first stage, the OH group attacks aluminium, which is a Lewis acid, due to its high Lewis acidity. This efficiency arises from the triflate anion (-OTf), which is a very weak base and does not strongly interact with the Lewis acid Al⁺³ ion. The triflate anion (-OTf) formed as an anion removes the hydrogen bonded to the C=N bond, resulting in the formation of -CN. We also investigated how the temperature affected this reaction's result. The results revealed that increasing the temperature to refluxing led to an increase in the yield **2a** to 79% (Table 1, entry 9). Acetonitrile was identified as the optimal solvent for the conversion of aldoximes to the corresponding nitriles (Table 1). We conducted a series of test experiments in which **1a** was reacted with aluminium (III) triflate under different reaction conditions. On the other hand, the desired benzonitrile product **2a** was obtained in a 61% yield when the reaction was carried out with 1 equiv of **1a** and 1 equiv of aluminium (III) triflate at reflux in acetonitrile. In another experiment, using 1 equivalent of **1a** and 2 equivalents of aluminum (III) triflate resulted in the formation of compound **2a** with a yield of 79%. When using 1 equiv of **1a** and 3 equiv of aluminium (III) triflate under the same conditions, the reaction yield remained unchanged. Thus, the optimization studies showed that the best reaction conditions for the formation of **2a** were reflux in acetonitrile with 2 equiv of

aluminium (III) triflate. All other aldoxime substrates were efficiently converted into the corresponding substituted nitriles in high yields using aluminium (III) triflate (Table 2). This transformation is tolerated for various substituents on the phenyl ring of the aldoxime substrates, including both electron-donating and electron-withdrawing groups (**1b-1h**). However, substitution with a 4-trifluoromethyl group resulted in a slightly lower yield because of its strong electron-withdrawing effect (Table 2, entry 5). In addition, aldoximes containing electron-donating groups such as 4-Me (**2f**) and 4-MeO (**2g**) provided their corresponding nitrile derivatives (**2f**, 92% and **2g**, 91%) in excellent yields. Furthermore, heteroatom-containing substrates (S, N, and O) afforded yields in the range of 53–64%. 1-Naphthonitrile was also synthesized in high yield (90%). Subsequently, alkyl and cycloalkyl aldoximes were smoothly converted into nitriles in good yields (Table 2, entries 9, 10).



Scheme 1. Synthesis and mechanistic proposal for the conversion of aldoximes to nitriles

Table 1 Optimization of reaction conditions

Entry	Oxime	Solvent	T (° C)	Yield 2a
1	1a	DMSO	Reflux	63
2	1a	CH ₂ Cl ₂	Reflux	41
3	1a	THF	Reflux	30
4	1a	EtOH	Reflux	65
5	1a	DMF	Reflux	61
6	1a	MeOH	Reflux	67
7	1a	MeCN	rt	10
8	1a	MeCN	50	55
9	1a	MeCN	Reflux	79
10	1a	Dioxane	Reflux	66
11	1a	Toluene	Reflux	54

Aluminum (III) triflate (2 mmol) and benzaldehyde oxime (**1a**, 1 mmol) were used in the reaction, which was conducted in a variety of solvents.

Table 2. Efficient conversion of aldoximes to nitriles using Al(OTf)₃

$ \begin{array}{ccc} \begin{array}{c} \text{NOH} \\ \parallel \\ \text{R}-\text{C}-\text{H} \\ \textbf{1a-n} \end{array} & \xrightarrow[\text{Reflux}]{\text{Al(OTf)}_3} & \text{R}-\text{C}\equiv\text{N} \\ & & \textbf{2a-n} \\ & & \text{R = aryl, heteroaryl, alkyl, cycloalkyl} \end{array} $				
Entry	R	Time(h)	Isolated yield (%)	m.p. (°C)
1	C ₆ H ₅ -	3	79	Oil
2	4-FC ₆ H ₄ -	3	66	Oil
3	4-ClC ₆ H ₄ -	4	72	92-94 [19]
4	4-BrC ₆ H ₄ -	5	84	112-114 [19]
5	4-CF ₃ C ₆ H ₄ -	4	41	Oil
6	4-CH ₃ C ₆ H ₄ -	2	92	Oil
7	4-CH ₃ OC ₆ H ₄	2	91	56-57 [19]
8	4-NO ₂ C ₆ H ₄ -	3	76	147-149 [38]
9	Cyclohexyl-	2	72	Oil
10	<i>n</i> -C ₆ H ₁₃ -	4	79	Oil
11	2-Pyridyl-	3	74	Oil
12	2-Furan-	2	52	Oil
13	2-Thiophene-	2	63	Oil
14	1-Naphtyl-	2	90	Oil

CONCLUSIONS

In conclusion, we have developed a highly efficient and straightforward method for the preparation of nitriles from various aldoximes. This aluminium (III) triflate-assisted dehydration protocol, performed in acetonitrile, effectively converts a broad range of substrates, including aromatic, functionalized aryl, heteroaryl, alkyl, and cycloalkyl aldoximes. The method's key advantages its operational simplicity, mild conditions, high yields, and short reaction time—make it a practical alternative for deoximation reactions, which are an important transformation in organic synthesis and synthetic industry. Thus, our new dehydration protocol could afford a practical method for synthesizing nitriles from various aldoximes.

EXPERIMENTAL SECTION

^1H and ^{13}C NMR spectra were recorded on a Bruker DPX-400 MHz High-Performance Digital FT-NMR spectrometer, with operating frequencies of 400 MHz for ^1H and 101 MHz for ^{13}C . The compounds were dissolved in CDCl_3 using tetramethylsilane (TMS) as the internal standard. Infrared (IR) spectra were obtained on a 1000 FT-IR spectrometer using the KBr pellet technique. Mass spectra were recorded on a GEC-21 100B Finnigan Mat 1210 mass spectrometer. Thin-layer chromatography (TLC) was performed on silica gel 60 F254 plates. For purification, silica gel 60 (230-400 mesh, Merck) was used. All solvents were purified according to international standards.

Typical general procedure for the synthesis of 2a-n. To a solution of benzaldoxime **1a** (121.1 mg, 1.0 mmol) was dissolved in 30 mL of MeCN under an atmosphere of nitrogen, and then $\text{Al}(\text{OTf})_3$ (948.4 mg, 2.0 mmol) was added in one portion. The resulting mixture was heated reflux for 2-4 hour. Reaction progress was monitored by thin-layer chromatography (TLC, ethyl acetate) to monitor the progress of the reaction. Then it was cooled, the solvent was removed and treated with a 10% aqueous solution of NaHSO_4 (20 mL) and extracted with methylene chloride (2×30 mL). The combined organic extracts were washed with a saturated aqueous solution of NaCl, dried over anhydrous Na_2SO_4 and filtered. After the solvent was removed under reduced pressure, the crude oil product was purified by column chromatography on silica gel using ethyl acetate. The solvent was then evaporated to yield the corresponding nitrile **2a-n**.

Benzonitrile (2a) [19]. Oil, 81.3 mg, 79%. IR spectrum ν , cm^{-1} : 3071, 2265, 1488, 1451, 751; ^1H NMR (CDCl_3), δ : 7.42-7.48 (m, 2H, ArH), 7.56-7.61 (m, 1H, ArH), 7.66-7.68 (m, 2H, ArH). ^{13}C NMR spectrum, δ , ppm (J , Hz): 111.5, 117.9, 128.1, 131.2, 131.8; MS (EI, 70 eV): m/z (%) 103 [M^+] (100), 76 (30).

4-Fluorobenzonitrile (2b) [19]. Oil, 79.7 mg, 66%; IR spectrum ν , cm^{-1} : 3071, 2988, 2234, 1610, 1503, 1241, 848, 681, 542. ^1H NMR spectrum, δ , ppm (J , Hz): 7.09 (t, $J = 8.3$ Hz, 2H, ArH), 7.57-7.62 (m, 2H, ArH). ^{13}C NMR spectrum, δ , ppm (J , Hz): 106.5 (d, $J_{\text{C-F}} = 3.4$ Hz), 114.8 (d, $J_{\text{C-F}} = 21.5$ Hz), 116.0, 134.7 (d, $J_{\text{C-F}} = 9.3$ Hz), 165.0 (d, $J_{\text{C-F}} = 251.9$ Hz). MS (EI, 70 eV): m/z (%) 122 (11), 121 [M^+] (70), 105 (14).

4-Chlorobenzonitrile (2c) [33]. Crystallized from diethyl ether, mp 92-94°C (lit. 93-94 °C), 99.7 mg, 72%. IR spectrum ν , cm^{-1} : 3448, 3081, 2221, 1587, 1476, 1079, 831, 540. ^1H NMR spectrum, δ , ppm (J , Hz): 7.43 (d, $J = 8.1$

Hz, 2H, ArH), 7.63(d, $J = 8.4$ Hz, 2H, ArH). ^{13}C NMR spectrum, δ , ppm (J , Hz): 111.8, 117.0, 128.7, 134.4, 138.6; MS (EI, 70 eV): m/z (%) 139 (28), 137 [M^+] (100), 101 (44).

4-Bromobenzonitrile (2d) [34]. Crystallized from diethyl ether, mp 112–114 °C (lit. 113–114 °C), 153.0 mg, 84%. IR spectrum ν , cm^{-1} : 3272, 2222, 1474, 1065, 1010, 826, 542. ^1H NMR spectrum, δ , ppm (J , Hz): 7.51 (d, $J = 8.5$ Hz, 2H, ArH), 7.66 (d, $J = 8.4$ Hz, 2H, ArH). ^{13}C NMR spectrum, δ , ppm (J , Hz): 112.3, 117.1, 127.0, 131.7, 134.4; MS (EI, 70 eV): m/z (%) 183 (61), 181 [M^+] (55), 102 (100).

4-(Trifluoromethyl)benzonitrile (2e) [19]. Oil, 69.3 mg, 41%; %. IR spectrum ν , cm^{-1} : 3062, 2234, 1731, 1687, 1264, 1091, 1022, 814, 678. ^1H NMR spectrum, δ , ppm (J , Hz): 7.58 (d, $J = 8.3$ Hz, 2H, ArH), 7.71 (d, $J = 8.3$ Hz, 2H, ArH). ^{13}C NMR spectrum, δ , ppm (J , Hz): 114.0, 118.5, 122.1 (d, $J_{\text{C-F}} = 274.4$ Hz), 127.2 (q, $J_{\text{C-F}} = 3.5$ Hz), 133.7, 135.5 (d, $J_{\text{C-F}} = 32.3$ Hz); MS (EI, 70 eV): m/z (%) 172 [$\text{M}^+ + 1$] (11), 147 (18).

4-Methylbenzonitrile (2f) [34]. Oil, 108.3 mg, 92%. IR spectrum ν , cm^{-1} : 3052, 2981, 2221, 1611, 1173, 814, 535. ^1H NMR spectrum, δ , ppm (J , Hz): 2.68 (s, 3H, CH_3), 7.29 (d, $J = 8.3$ Hz, 2H, ArH), 7.55 (d, $J = 8.3$ Hz, 2H, ArH). ^{13}C NMR spectrum, δ , ppm (J , Hz): 22.8, 108.3, 118.2, 127.9, 131.0, 144.7; MS (EI, 70 eV): m/z (%) 118 (11), 117 [M^+] (100), 116 (54).

4-Methoxybenzonitrile (2g) [33]. Crystallized from petroleum ether, mp 56–57 °C (lit. 55–57 °C), 121.2 mg, 91%. IR spectrum ν , cm^{-1} : 3014, 2988, 2211, 1611, 1505, 1261, 1168, 1017, 841, 678, 543. ^1H NMR spectrum, δ , ppm (J , Hz): 7.63 (d, $J = 8.1$ Hz, 2H, ArH), 6.93 (d, $J = 9.1$ Hz, 2H, ArH), 3.81 (s, 3H, CH_3O). ^{13}C NMR spectrum, δ , ppm (J , Hz): 54.6, 103.0, 113.8, 118.3, 133.0, 163.9; MS (EI, 70 eV): m/z (%) 134 (23), 133 [M^+] (100), 103 (36).

4-Nitrobenzonitrile (2h) [35]. Crystallized from ether, mp 147–149 °C (Lit. 149 °C), 112.2 mg, 76%; IR spectrum ν , cm^{-1} : 3052, 2967, 2922, 2851, 2227, 1731, 1681, 1578, 1508, 1377, 1348, 1238, 1151, 1066, 1011, 963, 804, 771, 694, 583, 451. ^1H NMR spectrum, δ , ppm (J , Hz): 7.96 (d, $J = 8.7$ Hz, 2H, ArH), 8.32 (d, $J = 8.6$ Hz, 2H, ArH). ^{13}C NMR spectrum, δ , ppm (J , Hz): 115.8, 117.3, 123.2, 134.4, 151.0; MS (EI) m/z (%): 148 [M^+].

Cyclohexanecarbonitrile (2i) [36]. As a clear oil, 78.8 mg, 72%. IR spectrum ν , cm^{-1} : 2938, 2221, 1645, 1283, 1043. ^1H NMR spectrum, δ , ppm (J , Hz): 1.31-1.43 (m, 4H), 1.60-1.71 (m, 4H), 1.74-1.83 (m, 2H), 2.54-2.65 (m, 1H). ^{13}C NMR spectrum, δ , ppm (J , Hz): 23.0, 24.3, 27.9, 28.5, 123.6; MS (EI, 70 eV): m/z (%) 110 (32), 109 [M^+] (100), 68 (36).

Heptanenitrile (2j) [19]. Oil, 88.2 mg, 79%. IR spectrum ν , cm^{-1} : 2952, 2931, 2858, 2243, 1640, 1461, 1422, 1378, 1271. ^1H NMR spectrum, δ , ppm (J , Hz): 2.32 (t, $J = 7.1$ Hz, 2H), 1.62 (t, $J = 7.4$ Hz, 2H), 1.47 (t, $J = 7.3$ Hz, 2H), 1.31-1.36 (m, 4H), 0.93 (t, $J = 6.7$ Hz, 3H). ^{13}C NMR spectrum, δ , ppm (J , Hz): 14.9, 18.1, 23.3, 26.3, 29.3, 31.9, 118.8.

2-Pyridinecarbonitrile (2k) [37]. Oil, 77.2 mg, 74%. IR spectrum ν , cm^{-1} : 3051, 2923, 2234, 1681, 1644, 1579, 1461, 1431, 1358, 1288, 991, 780, 733, 554; ^1H NMR (CDCl_3), δ : 7.63 (s, 1H, ArH), 7.78 (s, 1H, ArH), 7.94 (s, 1H, ArH), 8.73 (s, 1H, ArH). ^{13}C NMR spectrum, δ , ppm (J , Hz): 116.2, 126.1, 127.6, 134.9, 136.2, 152.1; MS (EI, 70 eV): m/z (%) 104 (100) [M^+], 78 (5).

Furan-2-carbonitrile (2l) [19]. Oil, 48.5 mg, 52%. IR spectrum ν , cm^{-1} : 3191, 2244, 1258, 1093, 1021, 807, 753, 691. ^1H NMR spectrum, δ , ppm (J , Hz): 6.43-7.46 (m, 1H, ArH), 7.02 (d, $J = 3.5$ Hz, 1H, ArH), 7.54 (s, 1H, ArH). ^{13}C NMR spectrum, δ , ppm (J , Hz): 111.4, 122.9, 124.4, 145.3. MS (EI, 70 eV): m/z (%) 93 [M^+] (5), 76 (7).

Thiophene-2-carbonitrile (2m) [19]. Oil, 68.6 mg, 63%. IR spectrum ν , cm^{-1} : 3028, 2221, 1441, 1380, 1265, 1070, 807, 778, 450. ^1H NMR spectrum, δ , ppm (J , Hz): 7.10-7.16 (m, 1H, ArH), 7.63-7.67 (m, 2H, ArH). ^{13}C NMR spectrum, δ , ppm (J , Hz): 107.6, 113.2, 128.7, 134.7, 136.4. MS (EI, 70 eV): m/z (%) 109 [M^+] (100).

1-Naphthonitrile (2n) [24]. Oil, 138.1 mg, 90%. IR spectrum ν , cm^{-1} : 3066, 2229, 1511, 1374, 1217, 810, 770. ^1H NMR spectrum, δ , ppm (J , Hz): 7.22-7.61 (m, 3H, ArH), 7.86-8.09 (m, 3H, ArH), 8.18 (t, $J = 8.3$ Hz, 1H, ArH). ^{13}C NMR spectrum, δ , ppm (J , Hz): 111.1, 116.8, 123.9, 126.0, 128.0, 129.6, 129.7, 133.3, 133.6, 133.9, 134.3. MS (EI, 70 eV): m/z (%) 154 (15), 153 [M^+] (100).

ACKNOWLEDGMENTS


The authors are grateful to Namık Kemal University for the structural analysis of the study. They also wish to thank Prof. Dr. Tuncer Hökelek for his assistance and guidance with the English language, as well as for editing and reviewing the revised manuscript.

REFERENCES

1. M. Sundermeier; A. Zapf; M. Beller M; J. Sans; *Tetrahedron Lett.*, **2001**, 42, 6707-6710.
2. F. Santos; S. Esther; F. S. C. Juan; P. Julio P; A. Amparo; *Chem. Comm.*, **2003**, 844-845.
3. P. Hu; J. Chai; Y. Duan; Z. Liu; G. Gui; L. Chen; *J. Mater. Chem., A* **2016**, 4, 10070-10083.
4. E. Pascual E; F. Sivera F; U. Yasothan; P. Kirkpatrick; *Nat. Rev. Drug. Discov.*, **2009**, 8, 191-192.
5. F. F. Fleming; L. Yao; P. C. Ravikumar; B. L. Funk; C. Shook; *J. Med. Chem.*, **2010**, 53, 7902-7917.
6. J. Gurjar; J. Bater; V. V. Fokin; *Chem. Eur. J.*, **2019**, 25, 1906-1909.
7. Y. Zhang; W. Li; Z. Hu; X. Jing; L. Yu; *Chin. Chem. Lett.*, **2024**, 35, 108938.
8. F. Wang; C. Yang; Y. Shi; L. Yu; *Mol. Catal.*, **2021**, 514, 11849.
9. J. A. Campbell; G. McDougald; H. McNab; L. V. C. Rees; R. G. Tyas; *Synthesis*, **2007**, 3179-3184.
10. M. K. Sing; M. K. Lakshman; *J. Org. Chem.*, **2009**, 74, 3079-3084.
11. L. D. S. Yadav; V. P. Srivastava; R. Patel; *Tetrahedron Lett.*, **2009**, 50, 5532-5535.
12. A. Rai A; L. D. S. Yadav; *Eur. J. Org. Chem.*, **2013**, 10, 1889-1893.
13. N. Uludag; *Org. Prep. Proced. Int.*, **2024**, 56, 516-522.
14. O. Asutay; N. Hamarat; N. Uludag; N. Coskun; *Tetrahedron Lett.*, **2015**, 56, 3902-3904.
15. N. Uludag; *Russ J. Org. Chem.*, **2020**, 56, 1640-1645.
16. N. Uludag; O. N. Giden; *Rev. Roum. Chim.*, **2019**, 64, 993-998.
17. C. P. Miller; D. H. Kaufman; *Synlett*, **2000**, 8, 1169-1171.
18. N. Jiang; A. J. Ragauskas; *Tetrahedron lett.*, **2010**, 51, 4479-4481.
19. D. Zhang; Y. Huang; E. Zhang; R. Yi; C. Chen; L. Yu; Q. Xu; *Adv. Synth. Catal.*, **2018**, 360, 784-790.
20. K. S. Lee; H. S. An; C. Y. Hwang; *Bull. Korean. Chem. Soc.*, **2012**, 33, 3173-3174.
21. K. W. Rosenmund; E. Struck; *Ber. Dtsch. Chem. Ges.*, 1919, 2, 1749-1756.
22. S. H. Yang; S. Chang; *Org. Lett.*, **2001**, 3, 4209-4211.
23. P. Yan P; P. Batamack; G. S. Prakas; G. A. Olah; *Catal. Lett.*, **2005**, 101, 141-143.

24. J. Bird; D. G. M. Diaper; *Can. J. Chem.*, **1969**, 47, 145-150.
25. R. M. Denton; J. An; P. Lindovska; W. Lewis; *Tetrahedron*, **2012**, 68, 2899-2905.
26. N. Iranpoor; H. Firouzabadi; G. Aghapour; *Synt. Commun.*, **2002**, 32, 2535-2541.
27. Y. Song; D. Shen; Q. Zhang; B. Chen; G. Xu; *Tetrahedron Lett.*, **2014**, 55, 639-641.
28. X. C. Wang; L. Li; Z. J. Quan; H. P. Gong; H. L. Ye; X. F. Cao; *Chin. Chem. Lett.*, **2009**, 20, 651-655.
29. M. Terhorst; C. Plass; A. Guntermann; T. Jolme; J. Rösler; D. Panke; H. Gröger; D. Vogt; A. J. Vorholt; T. Seidensticker; *Green Chem.*, **2020**, 22, 7974-7982.
30. I. Damljanić; M. Vukićević; R. D. Vukićević; *Monatsh. Chem.*, **2006**, 137, 301-305.
31. X. Jiang; X. Hu; Y. Lin; Y. Yan; P. Li; R. Bai; Y. Xie; *Tetrahedron*, **2018**, 74, 5879-5885.
32. R. Ding; Y. Liu; M. Han; W. Jiao; J. Li; H. Tian; B. Sun; *J. Org. Chem.*, **2018**, 83, 12939-12944.
33. S. M. Masjed; B. Akhlaghinia; M. Zarghani; N. Razavi; *Aust. J. Chem.* **2016**, 70, 33-43.
34. A. Ghorbani-Choghamarani; M. A. Zofigol; M. Hajjami; S. Sardari; *Synth. Commun.*, **2013**, 43, 52-58.
35. A. R. Sardarian; Z. Shahsavari-Fard; H. R. Shahsavari; Z. Ebrahimi; *Tetrahedron Lett.* **2007**, 48, 2639-2643.
36. X. Liu; C. Wu; P. Zhou; M. Jia; L. Zhu; Z. Zhang; *Angew. Chem. Int. Ed.*, **2025**, 64, e202413799.
37. C-H. Yang; J. M. Williams; *Org. Lett.*, **2004**, 6, 2837-2840.
38. R. Li; J. Shi; X. Zhou; Z. Li; Y. Zhao; Z. Liu; J. Wang; *ACS Sustain. Chem. Eng.*, **2024**, 12, 11338-11346.

WASTE GRAPE POMACE FOR FOOD PACKAGING

Daniel BOMBOȘ^a, Gabriel VASILIEVICI^{b,*} , Ana Maria MANTA^c ,
Loredana Irena NEGOIȚĂ^c, Ioan SAROSI^d, Andrei MOLDOVAN^d,
Filip MIUTA^e , Andra-Ioana STĂNICĂ^f, Stanca CUC^e 

ABSTRACT. The use of waste wine byproducts in packaging manufacture can offer an alternative to plastic pollution. Thus, grape pomace possesses properties that could improve the performance of plastic materials. In this work, the conditioning of grape pomace was studied for the purpose of adding PLA films. Resveratrol was extracted from grape pomace, which was then incorporated into PLA films to enhance their performance. The obtained biopolymers were characterized by determining the mechanical, thermal, and structural properties. The tensile strength of the composites has similar values for the composite with pomace and those with resveratrol, and a similar flexibility of the analyzed samples. The thermal stability of the pomace waste and the composites to which pomace and resveratrol were added was high. DSC tests of PLA-based composites revealed two endothermic peaks at temperatures above 120 °C, probably caused by the melting of amorphous structures. Surface examination indicated a relatively uniform distribution of pomace or resveratrol particles in the polymer matrix, and surface roughness parameters calculated by atomic force microscopy indicated a low to moderate level of roughness, with higher values for pomace-containing films than for resveratrol-based ones, highlighting the more hydrophilic nature of pomace-containing films compared to resveratrol-based ones.

Keywords: grape pomace, resveratrol, biopolymer, PLA composite

^a S.C. Medacril S.R.L, 8 Carpați Street, Mediaș, Sibiu County, Romania

^b National Institute for Research Development for Chemistry and Petrochemistry-ICECHIM-Bucharest, 202 Spl. Independenței, 060021 Bucharest, Romania

^c Petroleum-Gas University of Ploiești, 39 București Blvd., 100680, Ploiești, Romania

^d Department Environmental Engineering and Sustainable Development Entrepreneurship, Technical University of Cluj-Napoca, 400641 Cluj-Napoca, Romania

^e Institute of Chemistry “Raluca Ripan”, Babes-Bolyai University, 30 Fântanele Street, 400294 Cluj-Napoca, Romania

^f Technological High School “Toma Socolescu”, Gheorghe Grigore Cantacuzino St., 328, 100466, Ploiești, Romania

* Corresponding author: gvasilievici@icechim.ro



INTRODUCTION

Grape pomace, one of the main by-products of winemaking, describes approximately 20% of the total mass of processed grapes; it is a complex product composed of polysaccharides, pectins, phenolic compounds, lignin, structural proteins and phenols [1]. Thus, it has been highlighted that grape pomace contains bioactive compounds that can be obtained along with other value-added products, to bring socio-economic and environmental benefits [2-3].

The field of nanotechnology reveals innovative solutions for waste valorisation through the synthesis of nanomaterials with special chemical and physical properties, making them suitable for numerous applications, including safety protocols and environmental monitoring [4-8].

Directing bio-wastes on new pathways to usable products or raw materials has gained a lot of popularity [9-12]. In recent years, there has been great development underway to improve bio-waste transformation processes to generate different raw materials, especially for bioplastic production [13]. Thriving use of renewable resources will not only help changeover to the circular economy but will also lead to significant ecological advantages such as decreasing greenhouse gas emissions, reducing the volume of harmful pollutants, and protecting ecosystems and biodiversity [14-17].

According to previous studies, the winemaking by-products contain a significant number of fatty acids and phenolic compounds with viable applications in the food industry [18]. Pomace has been partially valorised by now, mainly for oil extraction from the grape seeds in view of utilising it in the pharmaceutical industry for its antioxidant and antibacterial properties [19].

In addition, sustainable food packaging materials have been developed from polyphenols and associated fibre extracted from pomace. The use of these active extracts in the development of biodegradable active packaging materials serves as a striking substitute for food preservation, adding value to bioplastics by enhancing their functionality [20-22]. The food packaging materials have to protect food against UV light and should also be supplemented with probiotics, a class of microorganisms with great importance for the digestive system, which can improve digestion when they reach the stomach along with the packed food [23-24].

The increased consumer demand for fresh and natural foods comes along with innovative concepts of smart food packaging with an extended shelf life, competitive price and greater accessibility during storage and transportation [25]. Antimicrobial agents impregnated on packaging materials can slowly diffuse onto the food surface to combat food-borne microorganisms [26]. The grape skin cell wall contains cellulose, hemicellulose, pectin, and lignin, which

form a complex structure, while the main components of grape seeds are cellulose and pectin. Cellulose Nano Crystals (CNCs) are the best options for the development of nano-composite materials, due to their high crystallinity and large surface area, which are important properties for high-performing composites [27]. These active compounds can be extracted by various methods, such as ultrasound, high interest in using environmentally friendly solvents, like subcritical water, instead of conventional organic solvents. The efficiency and selectivity of the process depend on the state parameters, water-increasing temperature being the most important factor, which reduces the dielectric constant and the polarity of water molecules, thus enhancing the dissolution of less polar compounds in water [28].

Polysaccharide films investigated for food packaging have a good oxygen barrier, but their humidity resistance is weaker. A solution to this problem is bilayer films made by crosslinking and PLA addition. Cellulosic multilayer films proved to offer a good barrier for oil and gas, although they require chemical modification through esterification or etherification processes. The results demonstrate that multi-layer structures of PLA, fully biodegradable by natural microorganisms such as bacteria and fungi, can be designed with the aim of enhancing performance in food packaging [29].

Among the available biobased polymers, there is polybutylene succinate (PBS), which has convenient mechanical properties in comparison to petrochemical polymers such as polyethylene or polypropylene. The main inconvenience to PBS is its tendency to degrade by thermo-oxidative mechanisms. To prevent unwanted degradation processes, there comes the need to stabilize the polymers by adding functional stabilizers. Resveratrol, another important component of the grape seeds, has also proven to be able to slow the oxidative chain reaction of polymers through a peroxy radical scavenging mechanism, while it has little effect on the direct photolytic cleavage of the ester bonds [30-31].

The food packaging industry is expected to grow, as the use of waste such as wine by-products minimizes food waste and offers an alternative to plastic pollution, with a negative impact on the environment. Grape pomace possesses favorable properties for the addition of plastics and, through physical processes such as extraction or chemical processes such as maceration, active principles can be obtained that can contribute to improving the performance of biopolymers to obtain valuable packaging materials with favorable mechanical properties, flexibility, as well as improved antibacterial activity. This work addresses the valorization of grape pomace in order to obtain active food packaging based on polylactic acid (PLA). The pomace waste was conditioned in powder form or was recovered by extracting a concentrated fraction of resveratrol. The two additives, namely pomace and

resveratrol, were characterized and used in the preparation of PLA-based composites, which were characterized by determining the mechanical, thermal, and microstructural characteristics.

RESULTS AND DISCUSSION

Characterization of grape pomace

Scanning Electron Microscopy (SEM)

From the SEM images, bundles with a fibrous structure, under 100 μm , with numerous holes formed as a result of the entanglement of the fibers are observed (figure 1).

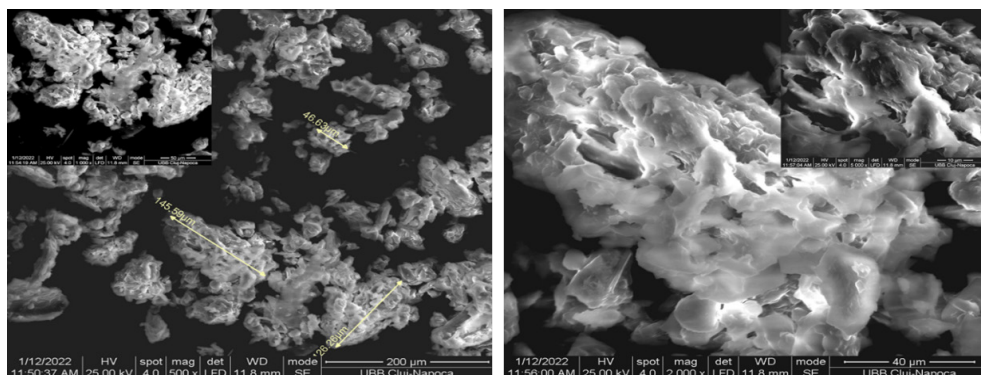


Figure 1. SEM images of grape pomace powder

Thermogravimetric Analysis (TGA)

The thermal decomposition of PLA Cu samples is depicted in Figure 2. Three important areas are observed. (1) The first one is an area with a mass loss of up to 6.45% by weight, the area located at temperatures of up to approximately 225°C. (2) The second one is an area with a mass loss of up to 16.90% by weight, the area located at temperatures of 225-325°C. (3) The last one is an area with a mass loss of up to 63.60% by weight, the area located at temperatures of 325-500°C. Mass losses for the first two zones are due to the evaporation of water and compounds with different volatilities, such as polyphenols, carboxylic acids, etc., and for the third zone, they are due to the thermal decomposition processes of hardly volatile compounds such as carbohydrates, lignin, resveratrol etc.

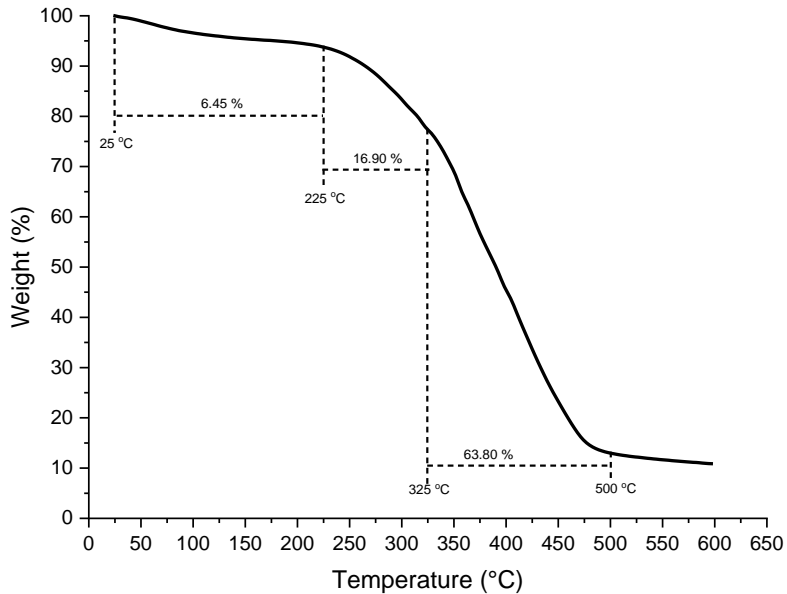


Figure 2. Thermogravimetric analysis (TGA) for grape pomace

Characterization of resveratrol

SEM analysis

Resveratrol powder particles have geometric or irregular shapes, with flat, shiny surfaces and sharp edges, on which deposits of much smaller powder particles can be noticed (Figure 3). Most cylindrical particles have lengths below 100 μm .

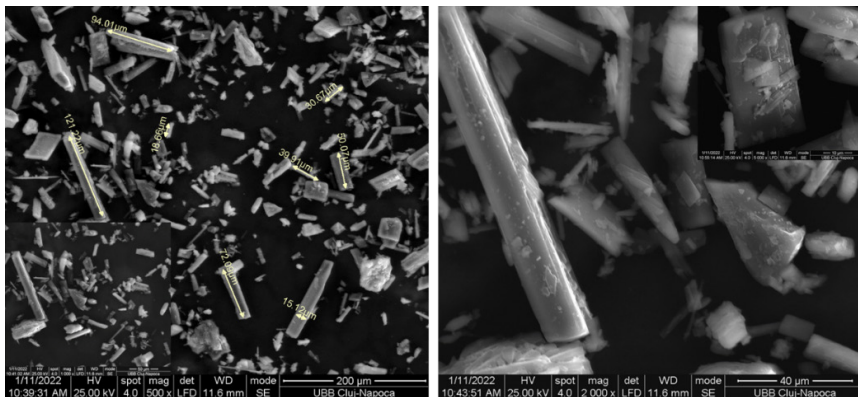


Figure 3. SEM images of resveratrol

HPLC analysis

The HPLC chromatogram of the resveratrol extract after concentration and the resveratrol standard are shown in Figures 4 and 5. The HPLC chromatograms show the presence of a relatively small number of components in the concentrated resveratrol extract. Based on this analysis, the efficiency of the purification process of the concentrated resveratrol extract can be highlighted, considering the large number of components present in such products.

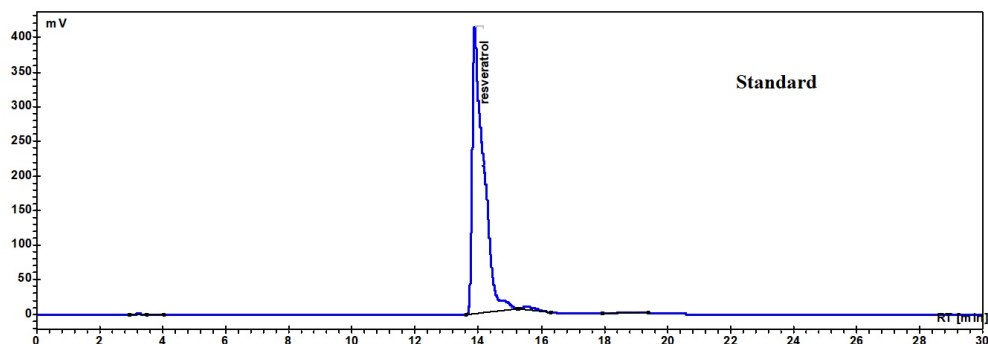


Figure 4. HPLC chromatogram of the resveratrol standard.

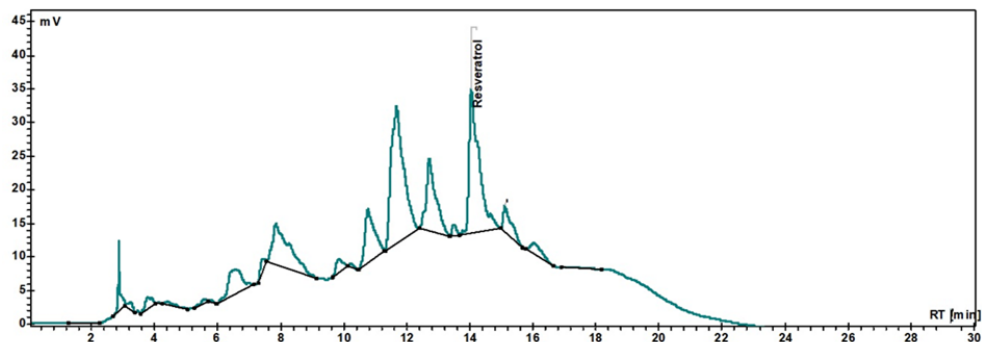


Figure 5. HPLC chromatogram of concentrated resveratrol extract

FTIR analysis of grape pomace

In Figure 6, the asymmetric and symmetric stretching vibrations of the CH_2 groups are observed at 2919 and 2852 cm^{-1} , respectively. These are mainly associated with the hydrocarbon chains of lipids or lignins as noted

by Lucarini et al. [33]. The spectral band at 1741 cm^{-1} is attributed to the absorption of the C=O bonds of ester groups and is related to the presence of fatty acids and their glycerides, as well as pectins and lignins as noted by Gao et al. [34]. The fingerprint region from 1500 to 800 cm^{-1} is very rich in peaks originating from different stretching, bending, rocking, shearing and torsion modes. This region is, on the one hand, very rich in information, but, on the other hand, difficult to analyze due to its complexity. This region provides important information about the organic compounds, such as sugars, alcohols and organic acids, present in the sample. The aliphatic C-O stretch at 1261 cm^{-1} is related to alcohols. The aromatic C-H stretch at 1143 cm^{-1} can be attributed to phenolic compounds. The O-C-C stretch at 1457 cm^{-1} indicate the presence of the phenolic compounds as noted by Heredia-Guerrero et al. [35]. The out-of-plane CH_3 bending at 1064 cm^{-1} is related to polysaccharide structures as noted by Gao et al. [34]. The band at 788 cm^{-1} is due to the CH_2 swing of phenolic compounds as noted by Lucarini et al. [32].

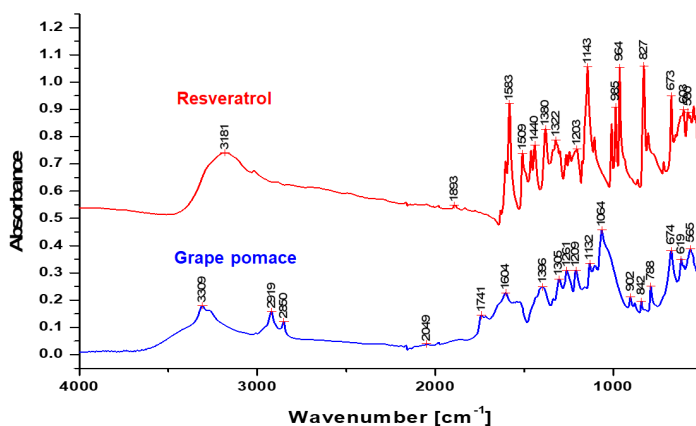


Figure 6. FT-IR spectra of grape pomace and resveratrol

Characterization of synthesized recipes

The prepared PLA films were homogeneous, opaque, faintly colored, and did not contain embedded air bubbles.

Tensile test results

As can be seen in Table 1, the tensile strength of the composites has similar values for the composites with pomace and those with resveratrol. Young's modulus has higher values for the composites with pomace and the breaking elongation has higher values for the composites with resveratrol.

Table 1. Tensile test results

Sample Code	Tensile strength (MPa)	Maximum load (N)	Breaking Strength (N)	Breaking Elongation (mm)	Young's modulus (MPa)	Breaking Stress (MPa)
PT1	16.31±2.84	157.97±51.77	159.69	34.290	556.11	15.01
PT 2	15.45±5.97	159.69±38.26	159.69	23.600	532.22	13.38
PT3	18.726±4.68	189.29±50.21	181.60	54.356	593.68	15.98
PR1	19.40±6.84	194.88±49.15	194.88	103.78	126.71	19.40
PR2	25.99±6.87	237.89±47.56	237.89	127.14	15.23	25.96
PR3	19.38±4.33	201.54±45.85	201.54	118.28	11.42	19.28
p-value	*	**	**	***	***	**

* first relevant statistic group ($p < 0.05$) ** second relevant statistical group ($p < 0.05$)

*** the third statistical relevant group ($p < 0.05$)

Flexural Strength Testing

The results obtained for the three-point bending tests are depicted in Table 2. From the investigation of the bending tests it is observed that the flexibility of the samples presents close values for all the analyzed samples. The Young's modulus of the samples is directly proportional to the maximum force supported and is inversely proportional to the elongation and decreases with increasing additive concentration.

Table 2. The obtained results for three points Flexural Tests

Sample Code	Maximum Load (N)	Young Modulus (MPa)	Bending Stiffness (Nm ²)	Maximum Bending Stress at Maximum Load (MPa)	Elongation (mm)
PT1	44.24±4.14	214.7690±40.16	0.0044	22.45±2.85	9.22±1.01
PT 2	40.48±0.57	196.24±16.72	0.0047	19.07±1.33	9.12±0.6
PT3	12.49±4.08	105.02±58.44	0.0030	5.50±1.95	8.86±0.5
PR1	5.02±2.70	383.31±1.79	0.0016	2.12±0.58	5.56±1.57
PR2	12.33±1.44	155.96±50.86	0.0029	6.72±0.53	8.74±0.34
PR3	42.48±1.23	59.17±40.92	0.0066	22.16±1.32	9.79±0.46
p-value	**	***	*	**	*

* first relevant statistic group ($p < 0.05$) ** second relevant statistical group ($p < 0.05$)

*** the third statistical relevant group ($p < 0.05$)

The elongation value did not change significantly with the content of pomace or resveratrol, probably due to the mobility induced by the nature of the plasticizer used in the experiments.

Thermogravimetric analysis

The behavior of PLA films added with grape pomace is illustrated in Figure 7 through TG curves and in Figure 8 through DTG curves. For the three composites it is observed that the mass losses are insignificant at temperature values lower than 300 °C and are due to the vaporization of the more volatile components present in the pomace or plasticizer. These mass losses become significant at temperatures above 300 °C and are due to the homolytic dissociations of the C-O and C-C bonds in the plasticizer and polyester molecules. The mass losses decrease at temperatures of almost 380 °C. The cracking residue at temperatures above 400 °C has relatively low values (tends to zero).

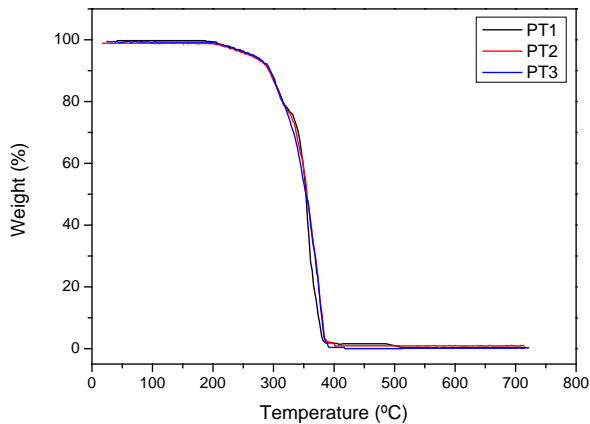


Figure 7. TGA curve for grape pomace-based composites

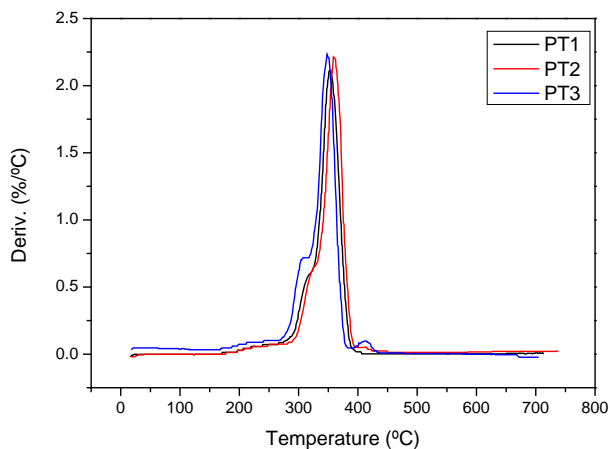


Figure 8. DTG curve for grape pomace-based composites

The thermal stability of PLA composite containing 0.5 to 1.5 wt.% resveratrol is illustrated in Figures 9 and 10. Both the TG and DTG curves show that the three resveratrol-based composites exhibit similar thermal stability to the pomace-based composites.

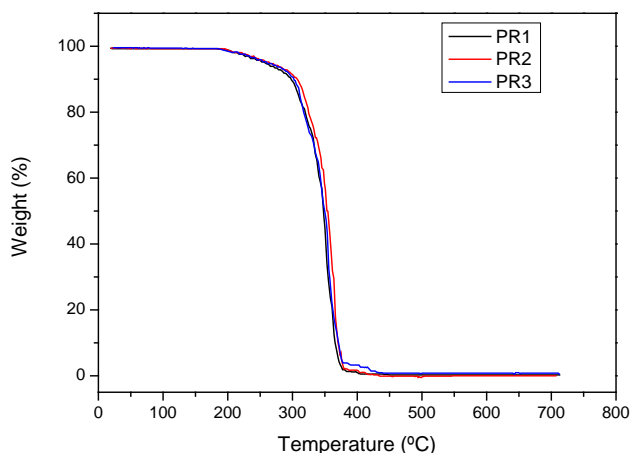


Figure 9. TGA curve for resveratrol-based composites

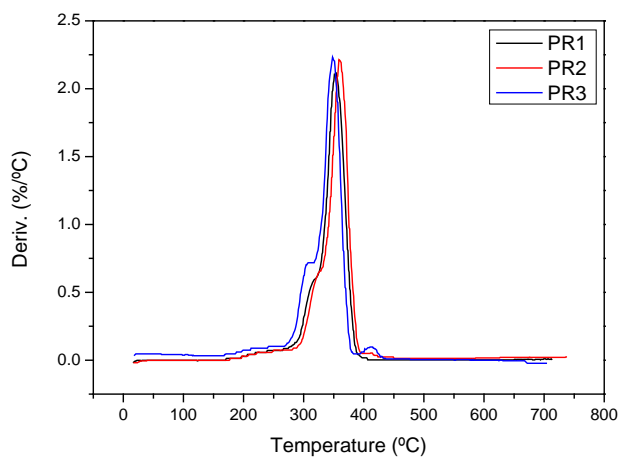


Figure 10. DTG curve for resveratrol-based composites

DSC analysis

The influence of grape pomace and resveratrol on the thermal transitions of PLA composites is shown in DSC thermograms Figure 11 and in Table 3. As can be seen, the addition of pomace to PLA induced the appearance of two endothermic transformations located at temperature values higher than 120 °C. Also, over the temperature range studied, the transition from the glassy state to the thermoplastic state was not identified, T_g therefore having values lower than 25 °C. This behavior is attributed to the improvement of PLA mobility due to the characteristics of the plasticizer that enhance the decrease of the glass transition temperature, regardless of the pomace concentration value. In the case of samples to which resveratrol was added, a similar behavior was observed, with two endothermic peaks being evident at temperatures above 120 °C, probably caused by the melting of amorphous structures, the size of the peaks being proportional to their concentration.

Table 3. Characteristic temperatures for PLA films added with pomace and resveratrol

Sample	Quantity (mg)	DSC		The process type
		Temperature interval (°C)	Temperature transformation (°C)	
PT1	13.9020	25-135	Onset 119 132	endothermic process
		135-200	145	endothermic process
PT2	13.9380	25-135	Onset 121 133	endothermic process
		135-200	146	endothermic process
PT3	10.3000	25-135	Onset 122 131	endothermic process
		135-200	146	endothermic process
PR1	16.0600	25-135	Onset 124 132	endothermic process
		135-200	146	endothermic process
PR2	11.4540	25-135	Onset 118 131	endothermic process
		135-200	146	endothermic process
PR3	13.8850	25-135	Onset 121 131	endothermic process
		135-200	146	endothermic process

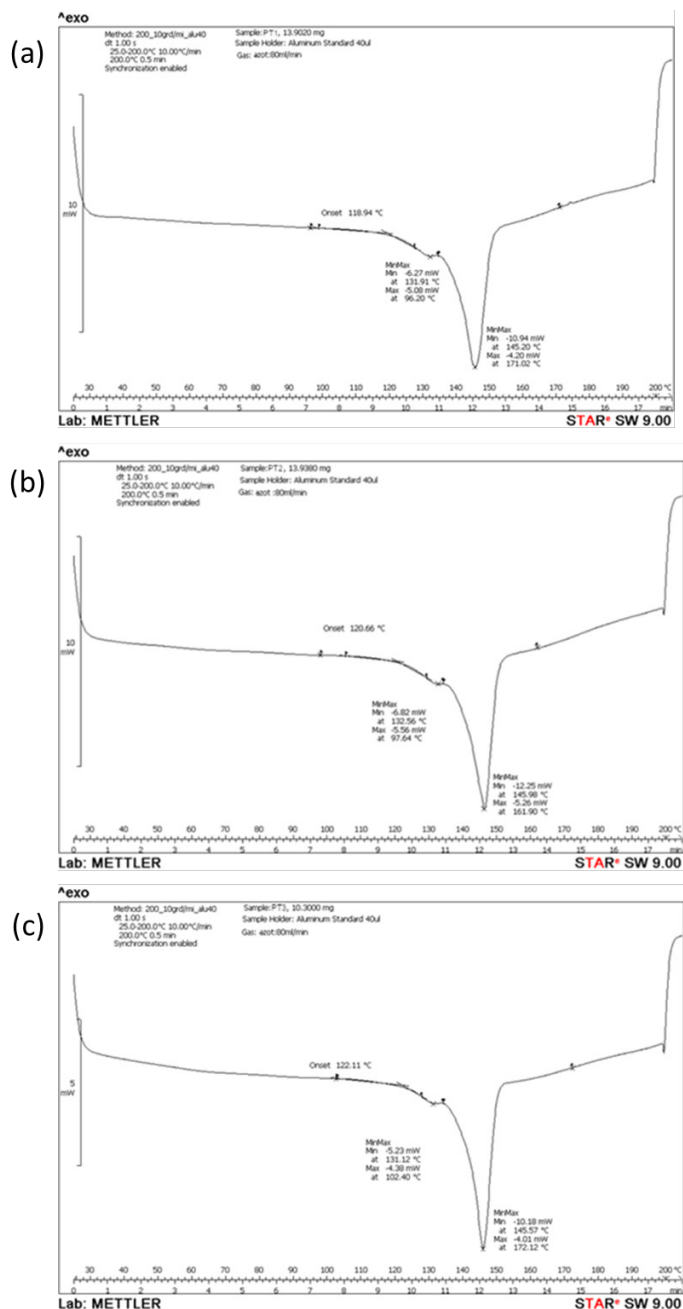


Figure 11. DSC curve for: (a) PT1 composite, (b) PT2 composite, (c) PT3 composite.

WASTE GRAPE POMACE FOR FOOD PACKAGING

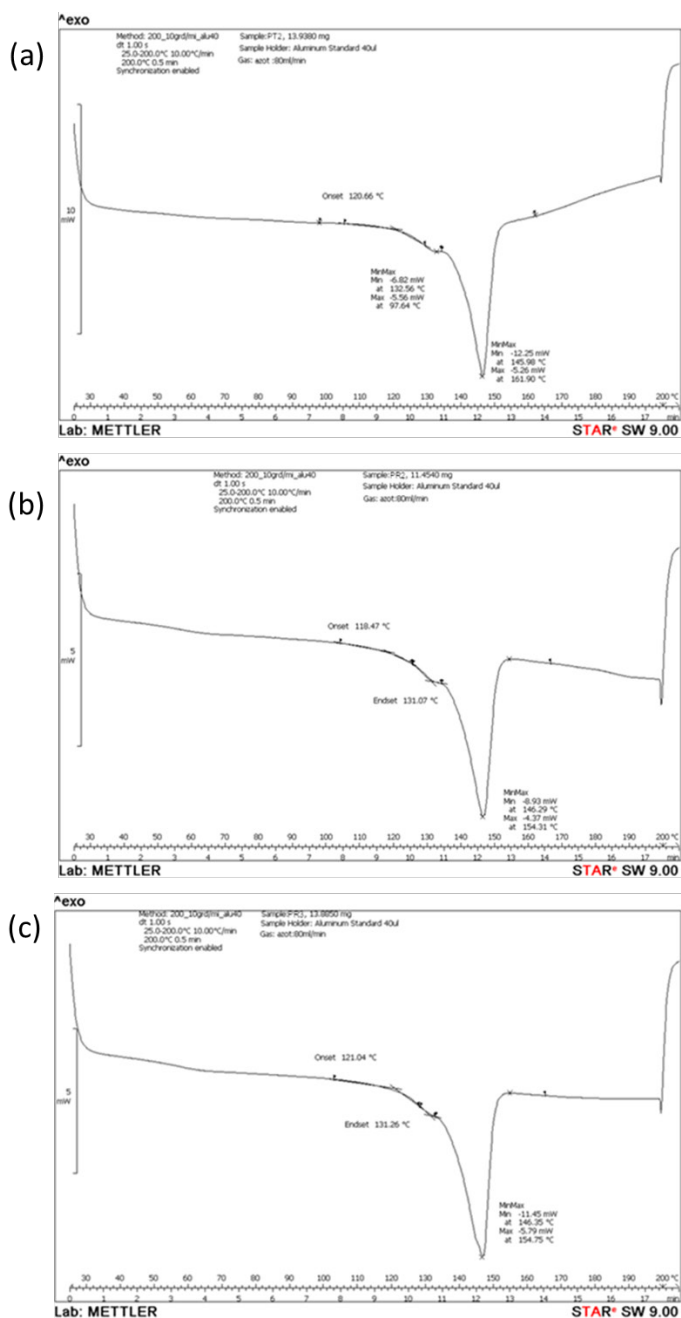


Figure 12. DSC curve for: (a) PR1 composite; (b)PR2 composite; (c) PR3 composite.

Scanning electron microscopy (SEM) analysis

Scanning electron microscopy analysis of PLA films doped with pomace or resveratrol (PT1-3 and PR1-3), performed at 2000 magnifications (40 μm) (Figures 13), reveals a relatively uniform distribution of pomace or resveratrol particles in the polymer matrix, probably facilitated by the close polarity of the plasticizer with the two additives. The presence of additive microclusters is observed in all samples, especially at higher resolutions. Increasing the additive concentration determined the increase in the size of the microclusters, a more obvious increase in the case of the PLA film doped with pomace. In conclusion, the SEM micrographs demonstrate that the incorporation of the two additives into the PLA matrix was successful, with minimal surface defects, which makes the material potentially suitable for packaging applications.

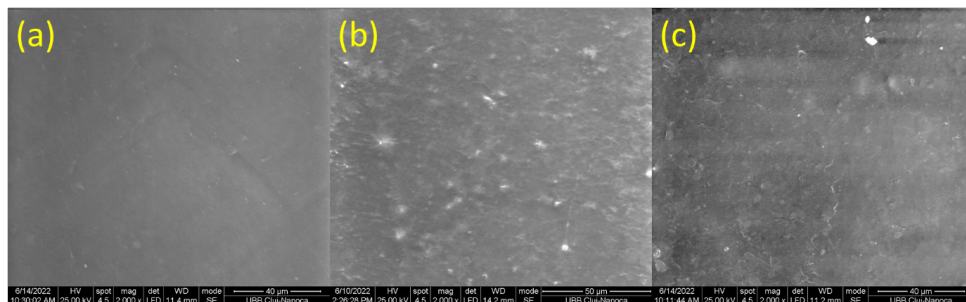


Figure 13. SEM micrographs of: (a) PT1; (b) PT2; (c) PT3 sample at 2000 magnifications.

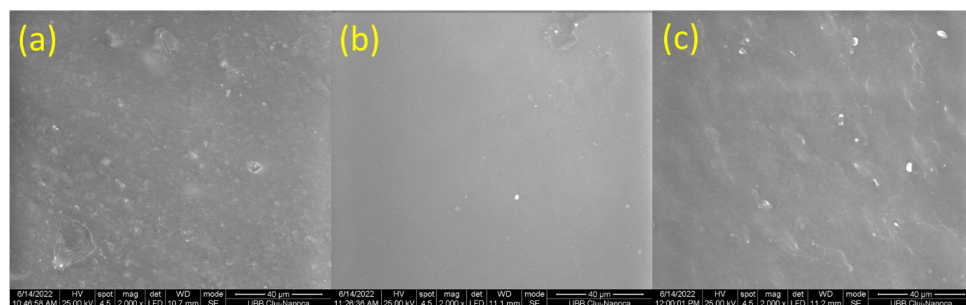


Figure 14. SEM micrographs of: (a) PR1; (b) PR2; (c) PR3 sample at 2000 magnifications.

Atomic force microscopy (AFM) analysis

Analysis of the surface of PLA-based films, previously stored in saline solution, by atomic force microscopy (AFM) provided a more detailed picture of the microstructural units and their topographical characteristics.

The analysis of the PLA film surface by atomic force microscopy provided more detailed images of the microstructural units, as well as the topographical features. Both the advanced dispersion of the pomace (Figure 15) and resveratrol nanoparticles (Figure 16), but also variations in the film thickness are highlighted. The topographical image reveals clusters of pomace or resveratrol, with a more or less uniform distribution, suggesting a relatively good compatibility between the PLA matrix and the two additives. The three-dimensional profile of the film surface highlights a texture whose homogeneity decreases with increasing pomace or resveratrol content. The calculated surface roughness parameters, an average roughness (R_a) and a root mean square roughness (R_q) at a low to moderate roughness level, with higher values for the films containing pomace than for those based on resveratrol and increasing with the additive content. This behavior is due to a higher water absorption in the pomace-based PLA film, probably due to its more hydrophilic character compared to resveratrol.

Literature data reveal that the proper dispersing of the filler particles ensures an optimal cohesion within the composite material [36, 37]. The mineral filler (e.g., such a small micro fraction) dispersion is very susceptible to the fluidity of the dispersion environment [38]. Mugnaini et al. reveal that the grape pomace addition into the composite material causes a relative increase of the surface roughness from about 40 nm up to 60 nm due to the enhancing of the hydrophilic behavior that interacts with the cantilever's tip [39]. Similar behavior is observed by de Souza Cohelo et al. [40]. Thus, the initial fluidity of the composite material plays an important role in the even particle distribution, which is kept after polymerization.

Furthermore, a smooth and uniform surface has a small roughness as observed by Atomic Force Microscopy [41] and the composite materials' roughness strongly depends on the filler particles reaching the outermost layers [42,43]. The initial well-done lamination of the filler particles keeps the surface roughness as low as possible. Literature reveal that the lateral pressure [44] associated with any liquid penetration might cause delamination of the outermost filler particles increasing the surface roughness. Resveratrol has spreading into the composite nanostructure increases the surface roughness in a pronounced manner via local hydrophilicity associated with highly negative charged surface as observed by Tan et al. [45]. The roughness increase is caused by the increasing of contact angle from $88.2 \pm 4.58^\circ$ to

about $115.54 \pm 1.12^\circ$ induced by resveratrol (Brahamian et al.) making the composite ideal for proactive food packaging. [46] The proactive role of the relative increased roughness under bioactive behavior of resveratrol filled composites is also confirmed by Wu et al. [47]. The local heights of the gelatin–resveratrol increase from about 20 nm to about 40 nm as consequence of its uniform distribution within the matrix (Fu et al.) [48].

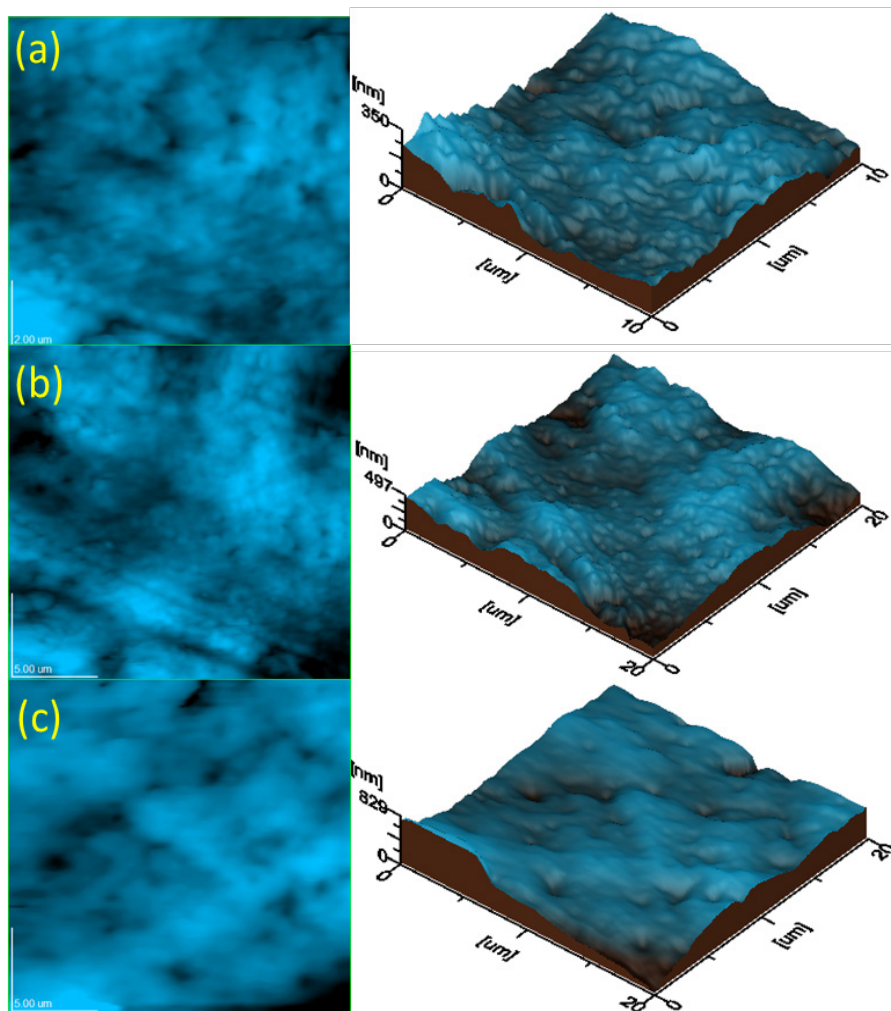


Figure 15. Topographic characteristics of: (a) PT1 - scanned area $10 \mu\text{m} \times 10 \mu\text{m}$, Ra area 31.6 nm; Rq area 40.5 nm; (b) PT2 - scanned area $20 \mu\text{m} \times 20 \mu\text{m}$, Ra area 63.6 nm; Rq area 78.5 nm; (c) PT3 - scanned area $20 \mu\text{m} \times 20 \mu\text{m}$, Ra area 61.5 nm; Rq area 85.0 nm.

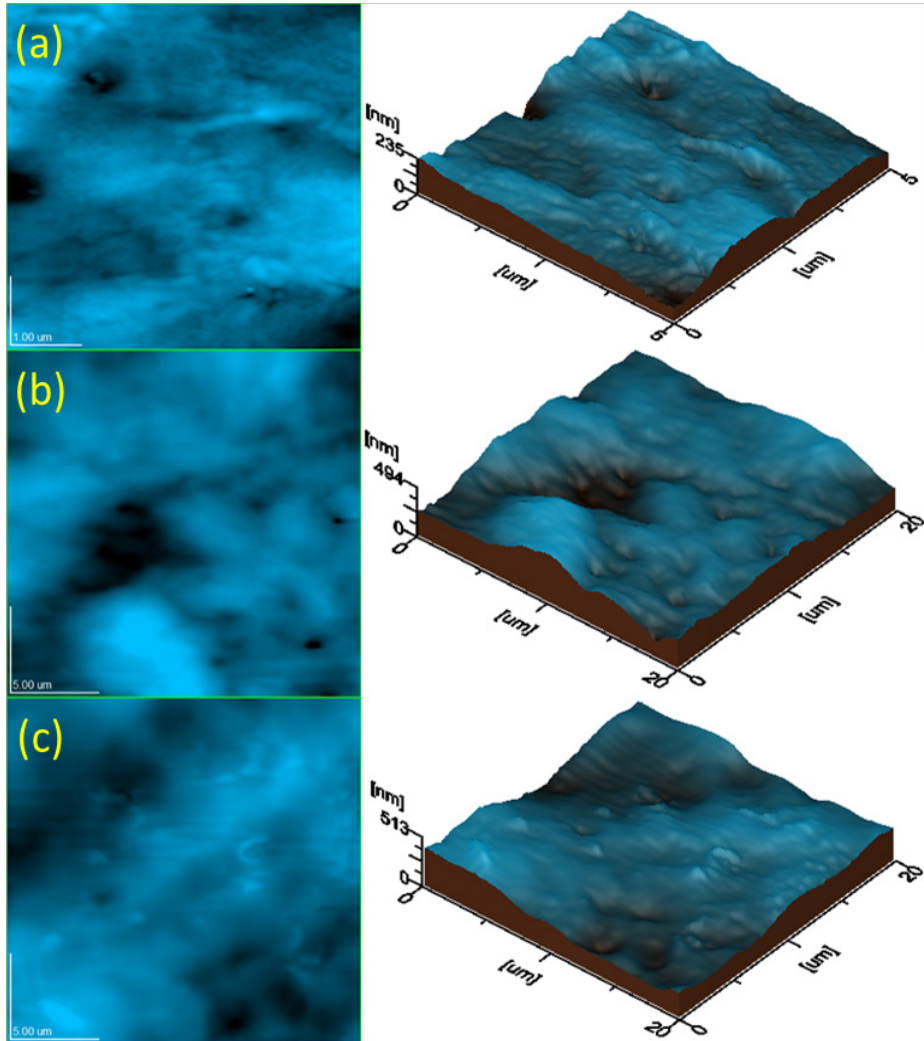


Figure 16. Topographic characteristics of: (a) PR1 - scanned area $5\ \mu\text{m} \times 5\ \mu\text{m}$, R_a area 21.4 nm; R_q area 27.1 nm; (b) PR2 sample - scanned area $20\ \mu\text{m} \times 20\ \mu\text{m}$, R_a area 47.5 nm; R_q area 61.3 nm; (c) PR3 - scanned area $20\ \mu\text{m} \times 20\ \mu\text{m}$, R_a area 56.6 nm; R_q area 68.1 nm.

The limitations of the current study are generated by the low concentrations of the powdered additive (below 1.5%), either due to the color change of the PLA film favored by the pomace, or due to the high price of resveratrol.

Future research directions consider optimizing the composition of the plasticizer mixture in order to improve the film elongation and performing bacteriological studies of the optimized formulations.

CONCLUSIONS

Grape pomace waste was conditioned in powder form or was recovered by extracting a concentrated fraction of resveratrol. The two additives, respectively pomace and resveratrol, were characterized and used in the preparation of PLA-based composites that were characterized by determining the mechanical, thermal and microstructural characteristics. The tensile strength of the composites has similar values for the composites with pomace and those with resveratrol, with Young's modulus having higher values for the composites with pomace. Bending tests revealed a similar flexibility of the analyzed samples and values of Young's modulus directly proportional to the maximum force supported. The thermal stability of the grape pomace waste and the composites added with pomace and resveratrol obtained was evaluated by thermogravimetric analysis, highlighting their good thermal stability. DSC tests of PLA-based composites revealed two endothermic peaks at temperatures above 120 °C. The melting of the amorphous structures, the size of the peaks being proportional to their concentration probably cause these. The mobility of PLA macromolecules induced by the plasticizer tributyl 2-acetylcitrate favored the decrease of T_g and the obtaining of an elongation of applicative interest for the two types of composites studied. Surface examination indicated a relatively uniform distribution of pomace or resveratrol particles in the polymer matrix with small micro-clusters of additive aggregates, especially in composites where the additive concentration is higher. Surface roughness parameters calculated by atomic force microscopy indicated a mean roughness (Ra) and root mean square roughness (Rq) at a low to moderate roughness level, with higher values for pomace-containing films than for resveratrol-based ones, highlighting the more hydrophilic nature of pomace-containing films compared to resveratrol-based ones.

EXPERIMENTAL SECTION

Materials and Methods

Poly(lactic acid (PLA, Ingeo® brand, NatureWorks LLC, Tokyo, Japan), Proviplast® 2624 by Proviron (tributyl 2-acetylcitrate), chloroform, methanol and

ethyl acetate from Aldrich-Sigma (Schnelldorf, Germany). In this study, grape pomace was from the grape variety “Vitis” interspecific crossing “Noah”, family Vitaceae.

Preparation of the Biomass

The pomace was washed in three stages with distilled water at a mass ratio of water/pomace 10/1, then dried in an oven at 60 °C for 24 hours and cut into smaller pieces. The resulting dried pomace was finely ground with a GRINDOMIX GM 200 knife mill, manufactured by Retsch GmbH, and sieved to a powder with a particle size $\leq 200 \mu\text{m}$.

Resveratrol was obtained from grape pomace according to the procedure described by Trifoi A. et al. [32]. Thus, we macerated 100 g of dried and ground grape pomace in 1000 ml of methanol at room temperature for 24 h, after which the mixture was subjected to a reflux extraction process for 60 min., under continuous stirring, at a rotation of 400 rpm. After reflux extraction, the mixture was filtered and the extract solution was concentrated under vacuum, then dispersed in water adjusted to pH 1 with hydrochloric acid, at an extract: water ratio of 1:10 and subjected to the hydrolysis process for 20 h, at 60°C. To recover resveratrol from the hydrolyzed aqueous solution. The aqueous solution of resveratrol was subjected to a three-stage liquid-liquid extraction process in a separatory funnel in the presence of ethyl acetate at a volumetric ratio of 1/1. Then the extract was decolorized with TONSIL bleaching earth, and the resveratrol was recovered by precipitation in water and filtered.

Preparation of PLA-based films

The solubilization of polylactic acid (PLA) was carried out at a controlled temperature of 50°C, using a stirring speed of 500 rpm. After complete dissolution of PLA, the plasticizer and then the additive (pomace or resveratrol powder) were successively added to the solution. The resulting homogeneous mixture was then poured into sterile Petri dishes for solvent evaporation to form the film. Three active formulations based on powdered pomace and three active formulations based on resveratrol were prepared, as shown in Table 4.

Table 4. Composition of PLA-based films

Sample no.	Polylactic Acid (% w/w)	Proviplast 2624 (% w/w)	Grape pomace (% w/w)	Resveratrol (% w/w)
PT1	79,5	20,0	0,5	-
PT2	79,0	20,0	1,0	-
PT3	78,5	20,0	1,5	-
PR1	79,5	20,0	-	0,5
PR2	79,0	20,0	-	1,0
PR1	78,5	20,0	-	1,5

Biomass and PLA composite characterization

The obtained pomace powder was analyzed by SEM microscopy, FTIR analysis and TGA. Resveratrol was analyzed by SEM microscopy and by HPLC chromatography. To evaluate the physicochemical characteristics of the developed PLA-based composite films, mechanical thermal, and surface analyses were performed using state-of-the-art techniques. These characterizations aimed to evaluate the impact of pomace and resveratrol additives on the performance of the films.

HPLC analyses were performed on a Jasco HPLC chromatograph (Japan) equipped with an HPLC pump (Model PU-980), a ternary gradient unit (Model LG-980-02), a column thermostat, a UV-Vis detector (Model UV-975), and an injection valve equipped with a 20 μ L sample loop (Rheodyne). Samples were manually injected with a Hamilton Rheodyne syringe (50 ml). The HPLC system was controlled and the experimental data were analyzed with ChromPass software.

The microstructural characteristics of the samples were determined using scanning electron microscopy (SEM) and atomic force microscopy (AFM). SEM images were acquired using an Inspect S- SEM microscope (FEI, Hillsboro, OR, USA) operated under high vacuum at an accelerating voltage of 30 kV. This method enabled detailed visualization of the dispersion of fillers, phase separation, and surface homogeneity. The surface topography of the samples was investigated by scanning Atomic Force Microscopy (AFM) performed with a JEOL JSPM 4210 device, produced by JEOL, Japan, Tokyo. Fourier Transform Infrared Spectroscopy (FTIR): was employed to investigate the molecular structure and the specific functional groups present in the pomace.

Fourier transform infrared (FT-IR) spectra were recorded on a Spectrum BX (Perkin Elmer, Waltham, MA, USA) FTIR spectrometer, equipped with an ATR accessory (PIKE MIRacle™), with a diamond crystal plate in attenuated total reflection (ATR) mode.

Thermogravimetric analysis assessed the thermal stability of biomass and biochar using the thermogravimetric/derivative apparatus TGA/DTG (TGA 2 Star System Mettler Toledo, Zurich, Switzerland). Differential Scanning Calorimetry (DSC) was carried out with the help of a 630e, 700C Mettler-Toledo calorimeter (Switzerland). Measurement conditions: aluminum crucible-40 μ L; heating speed: 10 $^{\circ}$ C/min; temperature range 25–200 $^{\circ}$ C; final landing 0.5 min; atmosphere: nitrogen; flow rate: 80 mL/min.

The rectangular specimens specific to this test were subjected to tensile tests using the Lloyd LR5k Plus universal mechanical testing machine (Lloyd Instrumente, AmetekIns, West Sussex, England), with a maximum allowed capacity of 5KN, at a loading force of 0.5 N and a speed of 1 mm/minute at ambient temperature (25 $^{\circ}$ C), according to the ASTM D638-14, using

Nexygen software (version 4.0). The flexural strength was achieved by the 3-point technique, according to ASTM D 790; the data were processed using the Nexygen software (version 4.0). All the data are the average of at least seven measurements. The statistical differences between the groups of investigated samples were statistically analyzed using the one-way ANOVA test.

ACKNOWLEDGMENTS

“Development of innovative food packaging without negative impact on the environment (AMBAL-INOV)”, My SMIS: 120994, contract: 375/ 390051/ 30.09.2021, Competition: 63/POC/163/1/3/LDR.

REFERENCES

1. E.T. Nerantzis, P. Tataridis, *E-J. Sci. Technol.*, **2006**, 1, 79–89. 32 Handbook of Grape Processing By-Products
2. N. Jimenez-Moreno, I. Esparza, F. Bimbela, L.M. Gandía, C. Ancín-Azpilicueta, **2020**, 50(20), 2061–2108. <https://doi.org/10.1080/10643389.2019.1694819>
3. N. P. Nirmal, A. C. Khanashyam, A. S. Mundanat, K. Shah, K. S. Babu, P. Thorakkattu, et al., *Foods*, **2023**, 12(3), 556, <https://doi.org/10.3390/foods12030556>
4. M. Primožic, Z. Knez, M. Leitgeb, M., *Nanomaterials*, **2021**, 11(2), 1–31. <https://doi.org/10.3390/nano11020292> MDPI AG
5. M. Sanda, I. Onuțu, C. M. Dușescu-Vasile, G. Vasilievici, D. Bomboș, M. Băjan, G. Brănoiu, *Molecules*, **2025**, 30 (9), 1962, <https://doi.org/10.3390/molecules30091962>
6. D. Popovici, C. Dușescu, M. Neagu, *Revista de Chimie*, **2016**, 67(4), 751-756
7. M. Neagu, D.R. Popovici, C. M. Dușescu, C. Calin, *Revista de Chimie*, **2017**, 68(1), 139-142
8. D.R. Popovici, M. Neagu, C.M. Dușescu-Vasile, D. Bombos, S. Mihai, E.E. Oprescu, *Reaction Kinetics, Mechanisms and Catalysis*, **2021**, 133 (1), 483-500
9. C. Dușescu, I. Bolocan, *Revista de Chimie*, **2012**, 63(3), 305-309
10. C. Dușescu, I. Bolocan, *Revista de Chimie*, **2012**, 63(7), 732-738
11. C. Dușescu, P. Roșca, D. Bombos, T. Jugănar, D. Popovici, R. Dragomir, *Revista de Chimie*, **2012**, 63(2), 229-231
12. V. Gheorghe, C.G. Gheorghe, A. Bondarev, V. Matei, M. Bombos, *Revista de Chimie*, **2019**, 70(8), 2996-2999
13. M. Carmona-Cabello, I.L. Garcia, D. Leiva-Candia, M.P. Dorado, *Curr. Opin. Green Sustain. Chem.* **2018**, 14, 67-79. <https://doi.org/10.1016/j.cogsc.2018.06.011> 2018
14. O. V. Săpunaru, A.E. Sterpu, C. A. Vodounon, J. Nasr, C. Dușescu-Vasile, S. Osman, C. I. Koncsag, *Lubricants*, **2024**, 12(6), 197, <https://doi.org/10.3390/lubricants12060197>

- 15.R. Shogren, D. Wood, W. Orts, G. Glenn, *Sustain. Prod. Consum.*, **2019**, 19, 194–215. <https://doi.org/10.1016/j.spc.2019.04.007>
- 16.S. Viswanathan, S. Periyasamy, S. Kandasamy, *Studia UBB Chemia*, **2025**, LXX(2), 163-178 DOI:10.24193/subbchem.2025.2.11
- 17.M. Sengottian, C.D. Venkatachalam, S.R.Ravichandran, S. Sekar, *Studia UBB Chemia*, **2024**, LXIX(1), 17-34, DOI:10.24193/subbchem.2024.1.02
- 18.X. E. Qin, G. F. Deng, Y.J. Guo, H.B. Li, *International. Journal Molecular Sciences*, **2010**, 11, 622-646
- 19.M. Meini, I. Cabezudo, C.E. Boschetti, D. Romanini, *Food Chem.*, **2019**, 283, 257-264
- 20.F. J. Vazquez-Armenta, B. A. Silva-Espinoza, M. R. Cruz-Valenzuela, G. A. Gonzalez-Aguilar, F. Nazzaro, F. Fratianni, J. F. Ayala-Zavala, *Journal of Adhesion Science and Technology*, **2017**, DOI: 10.1080/01694243.2017.1387093
- 21.A.Bondarev, S. Cuc, D. Bomboș, I. Perhaită, D. Bomboș, *Studia UBB Chemia*, **2023**, LXVIII(2), 73-84, DOI:10.24193/subbchem.2023.2.05
- 22.A.C. Joe, I. Onuțu, D. Bomboș, G. Vasilevici, A. Baioun, L. Silaghi-Dumitrescu, Ioan Petean, *Studia UBB Chemia*, **2025**, LXX(2), 129-147, DOI:10.24193/subbchem.2025.2.09
- 23.P. J. P. Espitia, N. de F. F. Soares, J. S. dos Reis Coimbra, N. J. de Andrade, R. S. Cruz, E. A. A. Medeiros, *Food and Bioprocess Technology*, **2012**, 5(5), 1447–1464
- 24.J. Miao, W. Peng, G. Liu, Y. Chen, F. Chen, Y. Cao, *Food Control*, **2015**, 56, 53–56
- 25.S. Jafarzadeh, M. Hadidi, M. Forough, A.M. Nafchi, A. Mousavi Khaneghah, *Crit. Rev. Food Sci. Nutr.* **2022**, <https://doi.org/10.1080/10408398.2022.2031099>
- 26.F. Garavand, M. Rouhi, S. Jafarzadeh, D. Khodaei, I. Cacciotti, M. Zargar, S.H. Razavi, *Front. Nutr.* **2022**, 9, 880520
- 27.J. Garcia-Lomillo, M.L. González-SanJosé, L.H. Skibsted, S. Jongberg, *Food Bioproc Technol.*, **2016** 9(3), 532–542
- 28.J. Gabaston, C. Leborgne, J. Valls, E. Renouf, T. Richard, P. Waffo-Teguo, J. M. Merillon, *Industrial Crops and Products*, **2018**, 126, 272–279
- 29.K. Huang, Y. Wang, *Curr. Opin. Food Sci.*, **2022**, 43, 7–17, <https://doi.org/10.1016/j.cofs.2021.09.003>
- 30.S. A. Salazar, N. Gamez-Meza, L. Medina-Juárez, H. Soto-Valdez, P. Cerruti, *ACS Sustain. Chem. Eng.*, **2014**, 2(6), 1534–1542
- 31.Moldovan, S. Cuc, D. Prodan, M. Rusu, D. Popa, I. Petean, D. Bomboș, O. Nemes; *Polymers*; **2023** 15, 2855
- 32.Trifoi, T. Gherman, O. Blajan, M. Velnazarov, R. Doukeh, *Rev.Chim. (Bucharest)*, **2019**, 70, (12), 4133
- 33.M. Lucarini, A. Durazzo, J. Kiefer, A. Santini, G. Lombardi-Boccia, E. B. Souto, A. Romani, A. Lampe, S. F. Nicoli, P. Gabrielli, N. Bevilacqua, M. Campo, M. Morassut, F. Cecchini, *Foods*, **2020**, 9(1), <https://doi.org/10.3390/foods9010010>

34. Y. Gao, J. U. Fangel, W. G. T. Willats, M. A. Vivier, J. P. Moore, *Carbohydrate Polymers*, **2015**, 133, 567–577. <https://doi.org/10.1016/j.carbpol.2015.07.026>.
35. J. A. Heredia-Guerrero, J. J. Benítez, E. Domínguez, I. S. Bayer, R. Cingolani, A. Athanassiou, A. Heredia, *Frontiers in Plant Science*, **2014**, 5, 1–14, <https://doi.org/10.3389/fpls.2014.00305>.
36. S.E. Avram, L.B. Tudoran, C. Cuc, B. Borodi, B.V. Birle, I. Petean, *J. Compos. Sci.*, **2024**, 8, 542. <https://doi.org/10.3390/jcs8120542>
37. S.E. Avram, L. Barbu Tudoran, C. Cuc, G. Borodi, B.V. Birle, I. Petean, *Sustainability*, **2024**, 16, 1123. <https://doi.org/10.3390/su16031123>
38. S.E. Avram, L.B.; Tudoran, G.; Borodi, I.; Petean, *Appl. Sci.* **2025**, 15, 6445. <https://doi.org/10.3390/app15126445>
39. G. Mugnaini, M. Bonini, L. Gentile, O. Panza, M.A. Del Nobile, A. Conte, R. Esposito, G. D'Errico, F. Moccia, L. Panzella, *Journal of Food Engineering*, **2024**, 361, 111716. <https://doi.org/10.1016/j.jfoodeng.2023.111716>
40. C. Corrêa de Souza Coelho, R.B.S. Silva, C.W.P. Carvalho, A.L. Rossi, J.A. Teixeira, O. Freitas-Silva, L.M.C. Cabral, *International Journal of Biological Macromolecules*, **2020**, 159, 1048–1061. <https://doi.org/10.1016/j.ijbiomac.2020.05.046>.
41. Petean, A. Peşan, H. Pop, S.E. Avram, L.B. Tudoran, G. Borodi, *Journal of Archaeological Science: Reports*, **2025**, 67, 105424. <https://doi.org/10.1016/j.jasrep.2025.105424>
42. S.E. Avram, L.B. Tudoran, G. Borodi, M.R. Filip, I. Ciotlaus, I. Petean, *Sustainability*, **2025**, 17, 2906. <https://doi.org/10.3390/su17072906>
43. S.E. Avram, L. Barbu Tudoran, C. Cuc, G. Borodi, B.V. Birle, I. Petean, *J. Compos. Sci.*, **2024**, 8, 219. <https://doi.org/10.3390/jcs8060219>
44. S.E. Avram, B.V. Birle, C. Cosma, L.B. Tudoran, M. Moldovan, S. Cuc, G. Borodi, I. Petean, *Materials*, **2025**, 18, 1715. <https://doi.org/10.3390/ma18081715>
45. Q. Tan, W. Zhang, C. Lai, X. Zhi, L. Xia, F. Meng, S. Zhao, *Journal of Membrane Science*, **2025**, 735, 124501. <https://doi.org/10.1016/j.memsci.2025.124501>
46. B. Bahramian, R. Abedi-Firoozjah, A. Ebrahimi, M. Tavassoli, A. Ehsani, M. Naebe, *Trends in Food Science & Technology*, **2024**, 154, 104761. <https://doi.org/10.1016/j.tifs.2024.104761>
47. H. Wu, T. Li, L. Peng, J. Wang, Y. Lei, S. Li, Q. Li, X. Yuan, M. Zhou, Z. Zhang, *Food Hydrocolloids*, **2023**, 139, 108509. <https://doi.org/10.1016/j.foodhyd.2023.108509>
48. T. Fu, Y. Feng, S. Zhang, Y. Sheng, C. Wang, *Food Chemistry: X*, **2025**, 25, 102182. <https://doi.org/10.1016/j.fochx.2025.102182>

QUALITY ASSESSMENT OF HANDMADE SOAPS, PLANT-BASED OILS, AND SKINCARE CREAMS: PHYSICOCHEMICAL AND MICROBIOLOGICAL ANALYSIS

Ana BALEA^a, Irina CIOTLĂUȘ^{a*}, Rahela CARPA^b,
Mihaela-Cecilia VLASSA^a, Sonia ANDREȘ^a

ABSTRACT. The aim of this study was to evaluate the quality and safety of handmade cosmetic and hygiene products through physicochemical and microbiological determinations, prior to their placement on the market. Three types of samples were analyzed, namely: solid soaps, creams, and cosmetic oils, using standardized methodologies compliant with current European and international regulations. The results demonstrated variations in pH, moisture levels, total alkali and Total Fatty Matter (TFM) content and viscosity, as well as quality indices in the case of oils, alongside the absence of pathogenic microorganisms, with detection occurring in only one sample. Additionally, Gas chromatograph coupled with mass spectrometer (GC-MS) and Fourier transform infrared spectroscopy (FTIR) analyses were performed on representative samples. These findings emphasize the necessity of continuous monitoring and quality assessment of cosmetic products to ensure consumer safety.

Keywords: *handmade cosmetic products, microbiological analysis, total alkali, peroxide index, acidity index*

INTRODUCTION

Cosmetics and personal care products have long been used to cleanse, protect, and hydrate the skin. Soaps, creams, ointments, and vegetable oils remain key categories in topical care. Recently, interest in

^a Babeș-Bolyai University, "Raluca- Ripan" Institute for Research in Chemistry, 30 Fântânele str., RO-400294, Cluj-Napoca, Romania

^b Babeș-Bolyai University, Faculty of Biology and Geology, Molecular Biology and Biotechnology Department, 1 M. Kogalniceanu str., 400084, Cluj-Napoca, Romania

* Corresponding author: irina.ciotlaus@ubbcluj.ro



handmade and natural products has increased, driven by a preference for bioactive ingredients and avoidance of synthetic compounds [1,2].

Microbial contamination is a persistent concern, arising from raw material impurities, production conditions, or poor hygiene [3,4]. Microbiological control is essential to ensure safety throughout a product's shelf life [5,6]. Contamination can reduce both efficacy and safety [7], especially for products applied to sensitive skin.

Topical product quality depends on physicochemical properties and microbiological safety. For soaps, important indicators include pH, alkali content, moisture, and Total Fatty Matter (TFM) [8,9]. A pH close to skin's natural value helps maintain the stratum corneum and prevents irritation or atopic conditions [10–12]. Despite this, pH is rarely indicated on packaging.

Creams and ointments are semisolid forms with cosmetic and therapeutic uses. Their pH should match that of healthy skin (5.4–5.9) to preserve the microbiota and barrier function [13–15]. Viscosity also plays a key role in formulation stability and user experience.

Cosmetic oils are evaluated by parameters such as density, acid and peroxide values, which affect their stability and therapeutic potential [16]. Since cosmetics often support microbial growth and are not sterile, contamination with bacteria like *Pseudomonas aeruginosa*, *Staphylococcus aureus*, or filamentous fungi remains a concern [7,18–20].

This study aimed to evaluate the physicochemical and microbiological quality of various cosmetic products, including soaps, creams, ointments, and oils, using standardized methods aligned with current regulations. The antimicrobial activity of selected samples was tested in vitro on Gram-positive bacteria.

The novelty of this research lies in its multidisciplinary evaluation of cosmetic products, combining physicochemical parameters, chromatographic techniques, and microbiological assessments to establish a comprehensive quality profile prior to their market release.

RESULTS AND DISCUSSION

1. Physicochemical analyses

Analysis of Handmade Solid Soaps

The physicochemical analysis of ten handmade solid soap samples is presented in Figures 1–4. The evaluated soap properties: pH, moisture and volatile matter, density, free alkalis, total alkalis, and TFM are presented in the normalized heat map in Figure 1.

QUALITY ASSESSMENT OF HANDMADE SOAPS, PLANT-BASED OILS, AND SKINCARE CREAMS: PHYSICOCHEMICAL AND MICROBIOLOGICAL ANALYSIS

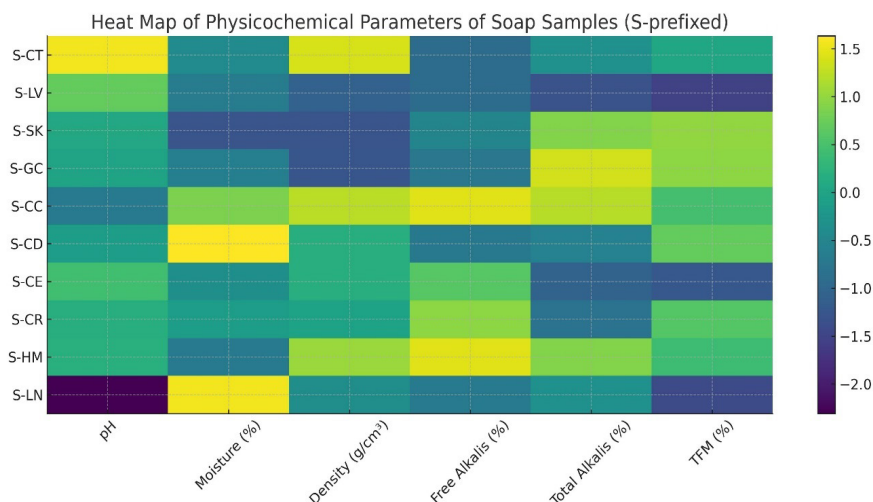


Figure 1. Normalised Heat Map for Soap Properties

S-SK, S-GC, S-CD, S-CR, and S-HM show high normalized TFM scores, indicating that they are the richest in fatty matter.

S-CC and S-HM present high normalized alkali values, which may suggest increased skin harshness if not properly buffered.

S-LN displays low normalized pH and alkali levels, reflecting a comparatively milder and more skin-friendly formulation.

S-LV, S-CE, and S-LN cluster with lower normalized TFM and alkali scores, suggesting lighter soaps that may be less emollient.

The **pH values** of the analyzed soaps ranged between **9.10 and 10.51**, which is slightly alkaline compared to the natural skin pH (~5.4–5.9). This alkalinity may potentially disrupt the skin's acid mantle if used frequently, increasing the risk of irritation [10,12]. We considered a classification of soaps as follows: pH < 6 acidic, pH= 7 neutral and pH> 8 alkaline. In our study, we have found that all of the samples had a pH value between 9.1 and 10.51, they are alkaline soaps, not very skin-friendly. In Romania [2] have reported pH values for commercial soaps between 9 and 11, consistent with alkaline formulations.

Moisture content varied from **4.5% to 13.78%**, reflecting differences in formulation and drying processes. Some values are lower than, while others are similar to, those reported in previous studies in Romania [2]. High moisture content can lead to hydrolysis of unsaponified fats, forming free fatty acids and glycerol, which affects soap hardness and quality.

Considering that moisture and volatile components contribute to the integrity, storage stability, and sensory profile of solid soaps, Figure 2 explores their variation relative to pH across the studied samples.

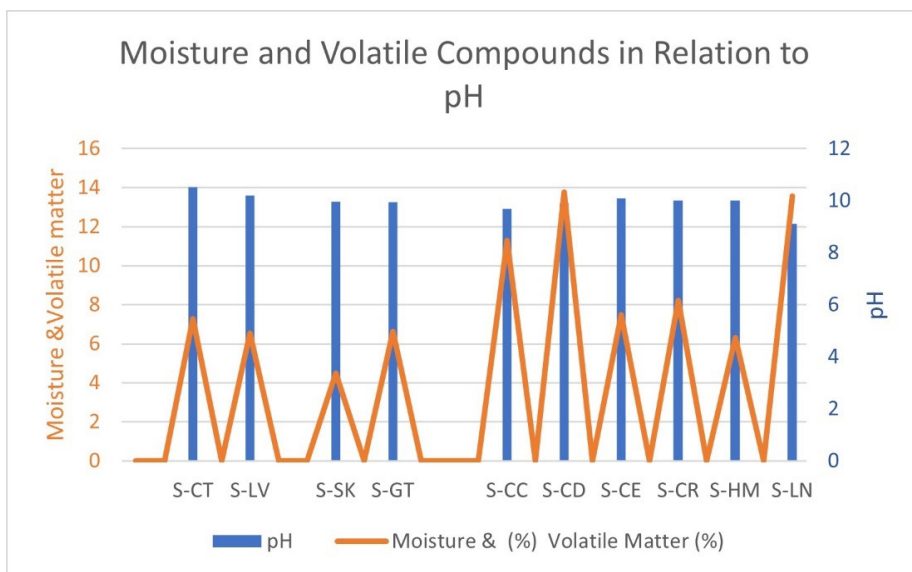


Figure 2. Relationship Between Moisture, Volatile Compounds, and pH

Based on the experimental data, the pH values showed a relatively narrow variation range (9.1–10.51), indicating good alkaline stability across all formulations. In contrast, moisture and volatile matter content exhibited substantial variability (4.5–13.78%), suggesting marked differences in composition and water retention capacity between samples.

A general inverse tendency was observed: formulations with higher pH values tended to present lower moisture and volatile content (e.g., S-SK, S-GT), whereas samples with slightly lower pH showed markedly higher moisture levels (e.g., S-LN, S-CD, S-CC). This suggests a potential negative correlation between pH and moisture/volatile content, indicating that higher alkalinity may be associated with reduced water affinity or volatile retention within the formulations.

Density values ranged from **1.019 to 1.17 g/cm³**, consistent with typical handmade soap characteristics.

The **free and total alkali content** remained low in most samples, indicating an adequate saponification process. According to ISO standards, total alkali levels in high-quality soaps should be below 2%, while the Bureau of Indian Standards (BIS) recommends less than 5% for premium soaps [21]. High total alkali may indicate excess NaOH, ensuring complete saponification, whereas low total alkali can suggest incomplete reaction or insufficient fatty acids.

Total Fatty Matter (TFM), a key indicator of soap quality, ranged from **59.4% to 76.4%**. Total fatty matter (TFM) reflects the richness and quality of soap. Soaps with higher TFM provide better hardness, lather, and moisturizing properties. Low TFM is associated with poor quality, lower hardness, and reduced consumer satisfaction [22]. In the case of the manufacturers sometimes prefer a small excess of NaOH to ensure complete saponification, obtaining a soap with a high TFM.

Notably, soaps with added natural oils or butters (e.g., green tea and charcoal, calendula, and citronella & rosemary) presented higher TFM values, which aligns with their intended moisturizing and therapeutic effects.

There is an inverse relationship between TFM (Total Fatty Matter) and total alkalinity in a soap. As the fatty matter content increases, total alkalinity decreases, indicating a product richer in fully saponified fats and containing fewer free alkaline salts. Theoretically, this correlation reflects soap quality: high TFM combined with low alkalinity corresponds to a milder, less irritating soap, whereas low TFM with high alkalinity indicates a harsher and more aggressive product, Figure 3.

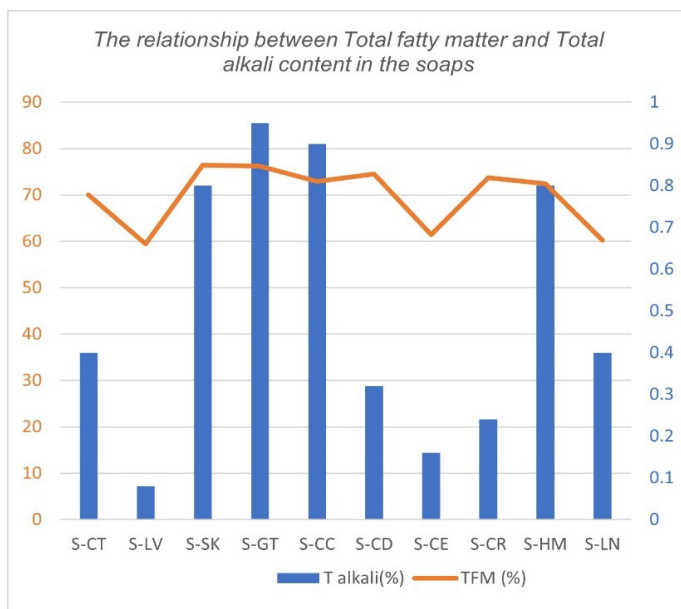


Figure 3. The relationship between Total fatty matter and Total alkali content in the soaps

Low alkalinity + low TFM, may indicate incomplete saponification due to lack of base or insufficient raw material in fatty acids.

High total alkalinity + high TFM, may be due to a complete reaction, a lot of bases used, but also a slight excess of free soda.

This general pattern, illustrated in Figure 3 through the combined visualization of TFM and total alkalinity, is further clarified in Figure 4. The scatter plot with linear regression provides a quantitative view of the relationship between these parameters, highlighting the degree of correlation across the soap samples.

The results indicate a moderate positive correlation ($R^2 = 0.446$), which was expected given the diversity of manufacturers and the significant variation in technological processes and product formulations analyzed.

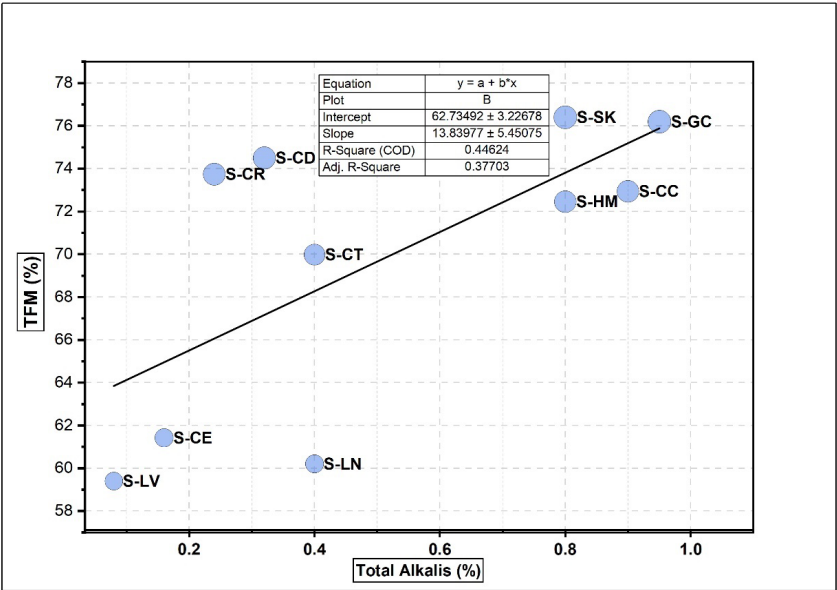


Figure 4. Linear Relationship Between Total Alkalies and TFM in the Soap Samples

Very low total alkalinity values (e.g., S-LV – 0.08%, S-CE – 0.16%) are associated with reduced TFM, which may indicate an incomplete saponification process or excess moisture. In contrast, soaps with high total alkalinity (e.g., S-SK, S-GC, and S-CC at 0.8–0.95%) show elevated TFM levels (~76%), suggesting a well-balanced formulation and an efficient conversion of fatty

acids into soap. This trend is consistent with the principles of saponification, where an adequate amount of base promotes the conversion of fatty acids. Intermediate samples (S-CD, S-CR, S-CT, S-LN, S-HM) reflect the typical variability of commercial products, where TFM levels depend on both the lipid composition and the amount of base used in the manufacturing process. Our results are in agreement with recent studies on commercial soaps, which show that physicochemical parameters such as total alkali and TFM are essential for evaluating product quality [23].

Overall, the physicochemical profiles of the analyzed handmade soaps suggest that while most meet quality criteria, the slightly high pH values may require careful consideration for frequent use on skin, especially for sensitive skin types.

Analysis of creams and ointments samples

The physicochemical analysis of ten cosmetic creams and ointments samples is presented in Figure 5-6. Properties such as **pH, viscosity, and moisture content** determine texture, absorption, and product stability [24].

The analyzed samples of creams and ointments showed **pH values ranging between 4.95 and 9.1**, indicating a wide variation depending on formulation and intended use. Most samples exhibited pH values within or near the physiological skin range (5.4–5.9), considered optimal for maintaining the balance of the skin microbiome and the integrity of the **stratum corneum** [16]. Most cosmetic creams had slightly acidic to neutral pH values (4.95–7.7), suitable for maintaining the physiological balance of the skin's acid mantle. By contrast, the diaper ointment showed a higher pH (9.1), consistent with its protective and barrier-forming purpose.

In terms of **density**, the formulations ranged from 0.78 to 1.16 g/cm³, reflecting differences in formulation type (oil-in-water vs. water-in-oil emulsions). **Viscosity values** were highly variable (from approximately 1000 to over 5900 mPa·s), confirming differences in texture and rheological behavior among the tested samples. Higher viscosity values were recorded for ointments containing herbal extracts such as *Calendula officinalis* with *Hypericum perforatum*, and *Arnica montana*, likely due to the presence of lipophilic bioactive compounds that increase the consistency of the base.

These plant-derived compounds include **triterpenoids** (faradiol, arnidiol, taraxasterol) from *Calendula officinalis* [25,26], **floroglucinols and phloroglucinol derivatives** such as **hyperforin** and **adhyperforin** from *Hypericum perforatum* [27,28] and **sesquiterpene lactones** like **helenalin** and **dihydrohelenalin** from *Arnica montana* [29,30]. These **lipophilic bioactives**

not only enhance viscosity and formulation stability but also contribute to the **anti-inflammatory**, **wound-healing**, and **antimicrobial** properties of the preparations.

The **moisture and volatile substance content** varied significantly, from 0.01% in ointments to over 80% in certain moisturizing or exfoliating creams, corresponding to the ratio between aqueous and lipidic phases.

The viscosity of a cream is inversely proportional to its water content (humidity). As humidity increases, the aqueous phase dilutes the network of viscous molecules (fats, polymers, or gelling agents), reducing intermolecular interactions and, consequently, the resistance to flow (Figure 5).

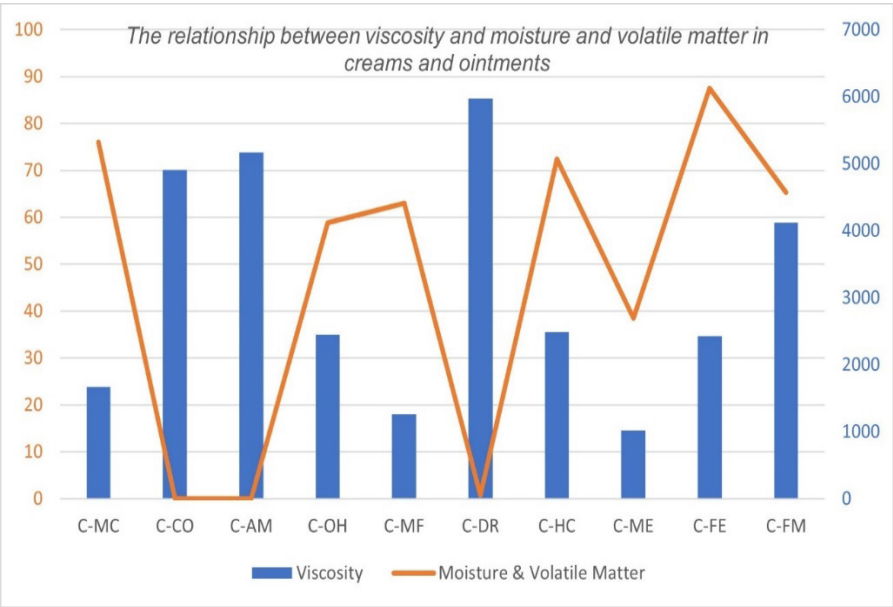


Figure 5. Relationship between Moisture Content and Viscosity in the Analyzed Samples

Compared to Figure 5, which illustrates the distribution based solely on moisture and viscosity, Figure 6 provides an extended representation that also includes density as a parameter (represented by bubble size) with clearly highlighting the three product categories: creams, ointments, and facial exfoliants.

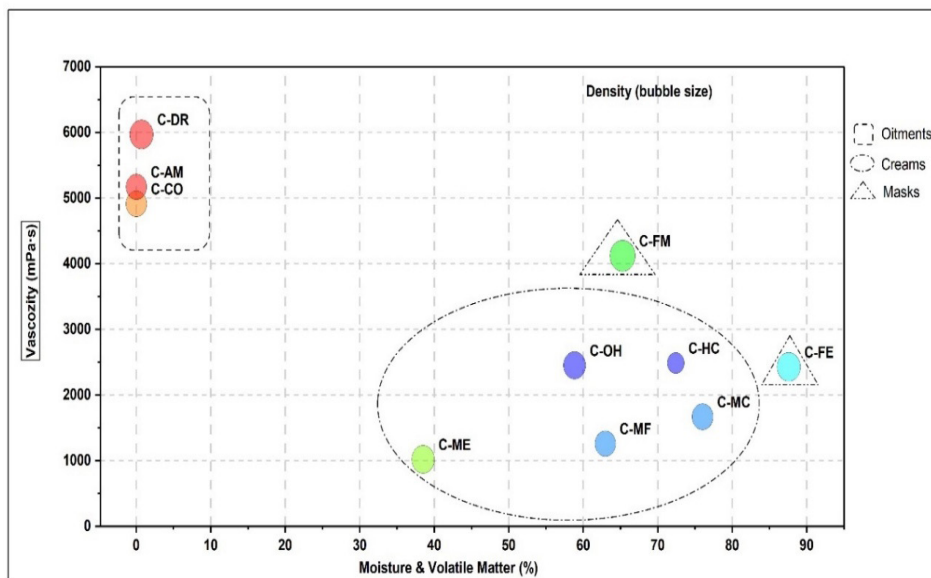


Figure 6. Dispersion of the Tested Formulations Based on Moisture, Viscosity, and Density

The C-AM, C-CO, and C-DR samples (moisture 0–1%, viscosity 4900–6000 mPa·s) appear clustered in the upper left area of the chart. These are typical for ointments, where the minimal water content leads to a dense structure and very high viscosity values. Their density is moderate and uniform. In contrast, the creams (C-MC, C-MF, C-HC, C-OH, C-ME) exhibit higher moisture levels (40–80%) and moderate viscosities (1000–2500 mPa·s), characteristic of fluid emulsions. The facial exfoliant (C-FE) and the mask (C-FM) show both high moisture content and increased viscosity and density, suggesting a formulation-specific structuring. Overall, the figure highlights the general trend of decreasing viscosity with increasing moisture and the clear separation between the rheological profiles of ointments and creams.

A classification of the quality of creams and ointments according to the main physicochemical is presented below:

Moisturizing creams

Results: 1260–1670 mPa·s. Interpretation: low–medium viscosity → Light texture, suitable for normal/oily skin, easily absorbed, ideal for pump-type dispensers; therefore, perfect for a slightly fluid daytime moisturizer. Typical reference range: 1000–5000 mPa·s.

Hand cream

Result: 2453 mPa·s; Interpretation: medium consistency — pleasant, easy to apply, not very greasy, absorbs quickly. Typical range: 2000–6000 mPa·s.

Ointments

Results: 4912–5171 mPa·s; Interpretation: high viscosity, dense, greasy texture forming a protective film (specific to ointments). These values indicate a W/O type emulsion or a base with a high content of fats/waxes, as expected for ointments. Typical range: 4000–10000 mPa·s.

A viscosity of approximately 1021 mPa·s for moisturizing and emollient face cream is at the lower end of the typical range for moisturizing creams (1000–5000 mPa·s). A cream with a viscosity of ~1020 mPa·s is mainly recommended for normal, combination, and oily skin. For dry skin it may be too light.

Analysis of oil samples

Oils, especially those used in therapeutic or cosmetic applications, are assessed for acidity, peroxide index, viscosity, moisture and density and results are described below and in Figures 7-9.

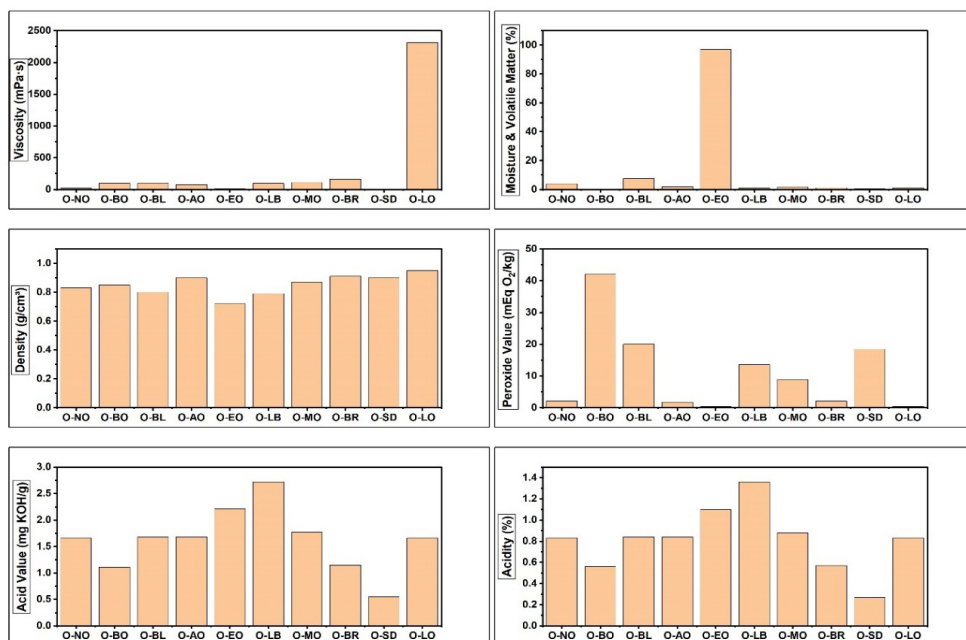


Figure 7. Physicochemical analyzes for handmade oils

The cosmetic oil samples showed a **wide variation in viscosity**, ranging from **10 mPa·s** in essential lavender oil to **over 2,300 mPa·s** in lip oil formulations, reflecting differences in oil type, purity, and formulation viscosity modifiers. Lower viscosity values were characteristic of **essential and volatile oils**, while higher viscosities were observed in complex formulations such as **lip oils** or **massage blends**, which include heavier triglycerides or waxy emollients.

The **moisture and volatile content** ranged between **0.16% and 3.89%** for most oils, except for the **lavender essential oil (97%)**, where the value reflects its highly volatile nature. **Density values** varied between **0.728 and 0.953 g/cm³**, consistent with typical cosmetic oil formulations composed of esters and natural triglycerides.

Regarding **oxidative stability**, the **peroxide values** ranged from **0.38 to 42.0 mEq O₂/kg**, indicating different degrees of lipid oxidation. The highest peroxide value was found in the **body oil containing a blend of grape seed, almond, and jojoba oils**, which could be attributed to the unsaturated fatty acid profile of these ingredients, making them more prone to peroxidation. Lower peroxide values (below 2 mEq O₂/kg) were characteristic of **pure essential or refined oils**, demonstrating good oxidative stability. Fresh oils typically have low acidity and peroxide values, while higher values indicate oxidation, hydrolysis, or degradation, often due to improper storage [24].

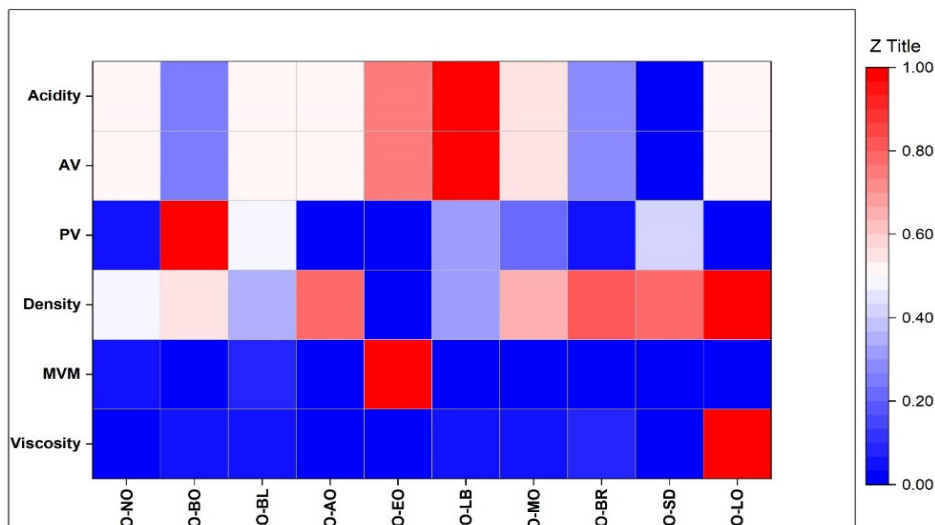


Figure 8. Heat Map of PhysicoChemical Profiles – 10 Types of Handmade Oils

The **acid value** ranged from **0.55 to 2.72 mg KOH/g**, corresponding to **acidities between 0.27% and 1.36%**, within the limits recommended by cosmetic quality standards (generally <2 mg KOH/g for cold-pressed cosmetic oils). Higher acid values, as observed in some lavender-based oils, may indicate partial hydrolysis of triglycerides or prolonged storage before testing.

A heat map representation was selected because it allows a simultaneous visualization of all measured parameters, highlighting patterns, correlations, and sample groupings that are not easily identifiable through individual plots.

The two indices, **Peroxide Value (PV)** and **Acid Value (AV)**, measure different degradation processes: oxidation in the case of PV and hydrolysis in the case of AV. Together, they provide complementary information: one index may indicate oil deterioration over time, while the other can demonstrate product compliance [31].

Cosmetic oils showed acceptable density, PV, and AV /acidity, indicating good oxidative stability and overall quality. The combination of PV and AV allowed the assessment of both oxidative and hydrolytic degradation, while acidity values confirmed that all oils fell within the **excellent to good range**. Microbiological analyses confirmed high safety, with no pathogenic microorganisms detected in any of the samples.

Overall, the results highlight the importance of continuous monitoring of handmade cosmetic products to ensure physicochemical quality, microbiological safety, and product stability. The study demonstrates that careful formulation, use of high-quality raw materials, and proper handling can produce handmade cosmetics that meet both safety and performance standards, making them suitable for consumer use.

The comparative analysis of the cosmetic oils shows that most products display high chemical stability and excellent microbiological safety, confirming an overall strong quality profile. Products such as Nutritive Oil, Anticellulite Massage Oil, Beard Oil, and Lip Oil stand out through a well-balanced combination of moisturizing properties and stability, making them suitable for regular use. Formulas with a heavier texture (e.g., *Beard Oil*, *Lip Oil*) prioritize emollience over lightness, which is appropriate for their intended function.

Lavender-based oils and body oil blends demonstrate good moisturizing performance but may benefit from improved oxidative stability, as certain botanical components are more sensitive to degradation. Overall, the product selection offers a diverse range of options tailored to different skin needs — from very light, fast-absorbing textures to richer, more protective formulations.

QUALITY ASSESSMENT OF HANDMADE SOAPS, PLANT-BASED OILS, AND SKINCARE CREAMS: PHYSICOCHEMICAL AND MICROBIOLOGICAL ANALYSIS

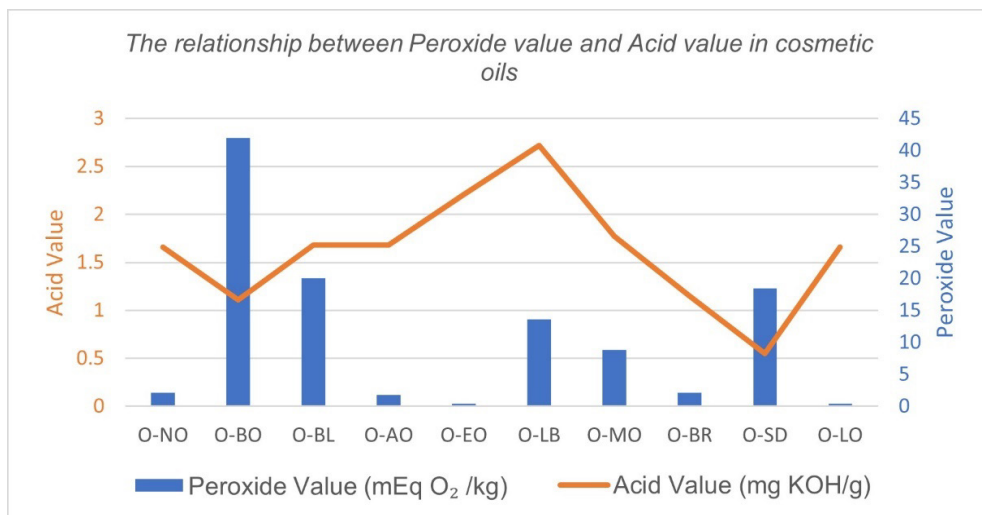


Figure 9. Relationship between Peroxide Value and Acid value in cosmetic oils

GC-MS analysis Lavender Essential Oil

To extend the physicochemical analyses with an accurate molecular compositional profile, the *Lavender oil* sample was selected for GC-MS investigation due to single-origin essential oil, unlike the other commercial, non-essential oil products, included in the study, which may contain additives or blends.

The Figure 10 shows the total ion chromatogram (TIC) of the sample, with major constituents identified based on mass spectral matching (NIST library) and retention indices. The main compounds detected were: beta-myrcene (RT = 13.95 min; 6.19%), trans-beta-ocimene (RT = 15.30 min;

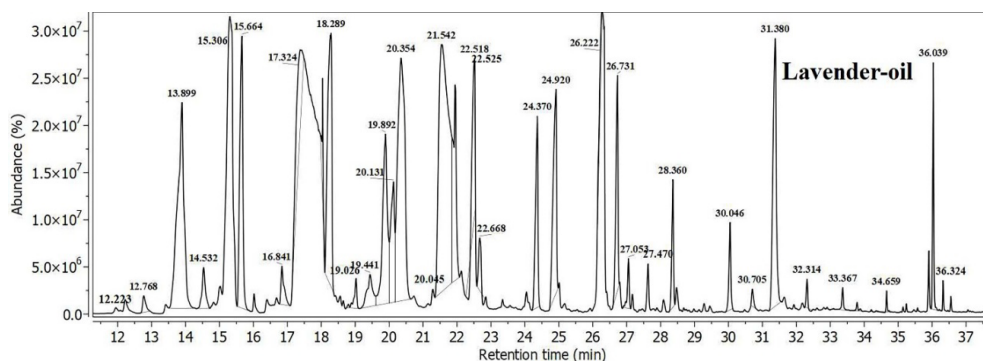


Figure 10. Chemical Profile of Lavender Essential Oil by GC-MS

8.11%), linalool (RT = 17.38 min; 21.91%), allo - ocimene (RT = 18.15 min; 5.00%), alpha-terpineol (RT = 20.35 min; 6.12%), linalyl acetate (RT = 21.513 min; 14.54%), lavandulyl acetate (RT = 22.52 min; 3.64%), and caryophyllene (RT = 26.24 min; 7.31%). Minor constituents (each <5%) included a series of monoterpenes and sesquiterpenes such as α -pinene, cis-beta-ocimene, terpinen-4-ol, geranyl acetate, beta-farnasene, and tau-cadinol. The presence of characteristic lavender markers such as linalool, linalyl acetate, terpinen-4-ol, ocimene isomers, lavandulyl acetate, and β -caryophyllene confirms the authenticity of the essential oil and is consistent with published profiles of *Lavandula angustifolia* [32,33].

FTIR-Based Physicochemical Structural Characterization

FTIR spectroscopy was selected for the analysis of creams and oil products due to its ability to rapidly characterize formulation matrices at a molecular level, based on the intrinsic physicochemical behavior of chemical bonds and infrared absorption of functional groups. This technique enables reliable identification of major compositional features such as esters, alcohols, carbonyls, and hydrocarbon chains, which are defining structural elements in semisolid and lipidic formulations. FTIR also provides valuable insight into molecular interactions within complex mixtures, without requiring prior separation or chemical modification of the sample. The obtained spectra showed well-defined characteristic bands consistent with the expected functional group profiles reported in the literature, supporting both sample integrity and the suitability of FTIR for comparative physicochemical screening and structural validation in this study. Figure 11 illustrates the FTIR spectra of the oat-based cream and the arnica ointment formulation and spectral profiles of lavender essential oil and the antifungal oil.

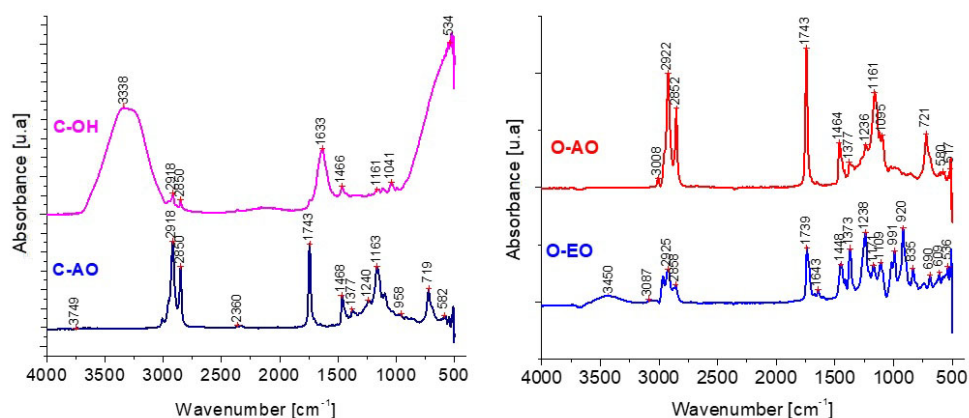


Figure 11. The FTIR-ATR spectra of colloidal Oat meal and Orange hand cream, ointment with Arnica, antifungal oil and Lavender oil

Lavender oil was chosen for its single-origin traceability and consistent spectral fingerprint, whereas the antifungal oil blend was selected to identify characteristic absorption bands of its bioactive compounds, ensuring IR-based evaluation of functional composition over botanical origin.

Because the antifungal oil (O-AO) is a mixture of six essential oils (eucalyptus oil, clove oil, frankincense oil, almond oil, lavender oil) and vitamin E, its FTIR spectrum is marked by the absorption bands of the major component. As can be seen in that spectrum, the strong absorption peak of C–H stretching appears at 2852 cm^{-1} and 2922 cm^{-1} , methyl asymmetric and symmetric bending peaks appear at 1464 cm^{-1} and 1377 cm^{-1} respectively; C–O stretching of the phenol appears at 1236 cm^{-1} ; ether group appears at 1161 cm^{-1} belonging to vitamin-E [34]. The band at $3450\text{--}3087\text{ cm}^{-1}$ represents the stretching vibration of the -OH groups of the linalool substances, and another band at 2925 cm^{-1} is correlated with the antisymmetric stretching vibration of the -CH₂ groups in lavender oil (O-EO) [35,36]. Also, the strong band at 1739 cm^{-1} corresponds to the C=O stretching vibration of the ester compositions in lavender oil [35]. The linalyl acetate ester in this oil shows the C=CH₂ in-plane deformation vibration that occurs near the value of 1443 cm^{-1} [37]. Frankincense essential oil contains majority diterpene alcohols, which show two strong bands, in the $1377\text{--}1464\text{ cm}^{-1}$ region, while the second band, assigned to the C-O stretching vibration, are shown at 1161 cm^{-1} , respectively. [37] The FTIR spectrum of clove oil shows several distinct peaks at 1095 cm^{-1} , attributed to the C-O stretching vibration of the eugenol compound. Other peaks should be present at 841.1 cm^{-1} , due to the C-H bending vibration, a peak at 2920.4 cm^{-1} due to the C-H stretching vibration of the methylene group, and a peak at 1279 cm^{-1} , due to the C-H rotational vibration of the isoeugenol compound present in clove oil. These peaks are either too small due to dilution or overlap with the peaks of the majority compounds.

Regarding hand creams, the colloidal oatmeal(C-OH) presents a large peak at 3338 cm^{-1} , which can be attributed to N–H stretching vibration due to the presence of protein content. The peaks at 2918 and 2860 cm^{-1} are attributed to C–H stretching vibrations. The peak at 1633 cm^{-1} is attributed to the N–H bending, and peak at 1406 cm^{-1} belong to the C–N bending [38].

For hand cream with arnica(C-AO): the FTIR band at 2918 cm^{-1} in oils corresponds to the asymmetric C-H stretching vibration of aliphatic methylene -CH groups. This peak is typically seen alongside a symmetric -CH stretching vibration at a lower wavenumber, at 2850 cm^{-1} . The arnica oil presents a strong band at 1743 cm^{-1} , which is characteristic of carbonyl C=O groups, and band at 1163 cm^{-1} , corresponds to C-O stretching vibrations such as sesquiterpene lactones from this plant [37].

2. Microbiological Analysis

Microbiological analyses for creams and ointments

In the case of creams and ointments, microbiological safety is essential; the presence of pathogenic bacteria or fungi can cause infections or adverse reactions (Table 1).

Regarding **microbiological safety**, all products except the facial mask sample were free of pathogenic bacteria, fungi, and aerobic microorganisms. The **facial mask** showed contamination with potentially pathogenic microorganisms, with microbial colonies visible on most culture media in counts of several hundred (Figure 12).

The **microbiological contamination** or biological load of a cosmetic product is a very important component in product safety. Microbial growth can change physicochemical and organoleptic properties that affect marketing and consumer satisfaction. In addition to skin problems, microbial growth can change the color of a cosmetic product, or affect the viscosity, which gives the product a lumpy appearance or makes it more liquid, and also alter the shape of the packaging [39,40].

Cosmetic companies are not required to create sterile products. But they are responsible for guaranteeing the product's safety to the prospective buyer [41]. The determination of the microorganisms present in cosmetic products consisted of isolating and identifying possible microorganisms that could contaminate cosmetic products either during their formulation or during storage.

Table 1. Microbiological analyses for creams and ointments

No.	Sample	Microbiological Analysis
1	C-MC	Pathogenic bacteria, pathogenic fungi, and aerobic bacteria – ABSENT
2	C-CO	Pathogenic bacteria, pathogenic fungi, and aerobic bacteria – ABSENT
3	C-AM	Pathogenic bacteria, pathogenic fungi, and aerobic bacteria – ABSENT
4	C-OH	Pathogenic bacteria, pathogenic fungi, and aerobic bacteria – ABSENT
5	C-MF	Pathogenic bacteria, pathogenic fungi, and aerobic bacteria – ABSENT
6	C-DR	Pathogenic bacteria, pathogenic fungi, and aerobic bacteria – ABSENT
7	C-HC	Pathogenic bacteria, pathogenic fungi, and aerobic bacteria – ABSENT
8	C-ME	Pathogenic bacteria, pathogenic fungi, and aerobic bacteria – ABSENT
9	C-FE	Pathogenic bacteria, pathogenic fungi, and aerobic bacteria – ABSENT
10	C-FM	PRESENCE of potentially pathogenic microorganisms observed on all tested media; microbial colonies in the range of hundreds were detected on most culture plates.

QUALITY ASSESSMENT OF HANDMADE SOAPS, PLANT-BASED OILS, AND SKINCARE CREAMS:
PHYSICOCHEMICAL AND MICROBIOLOGICAL ANALYSIS

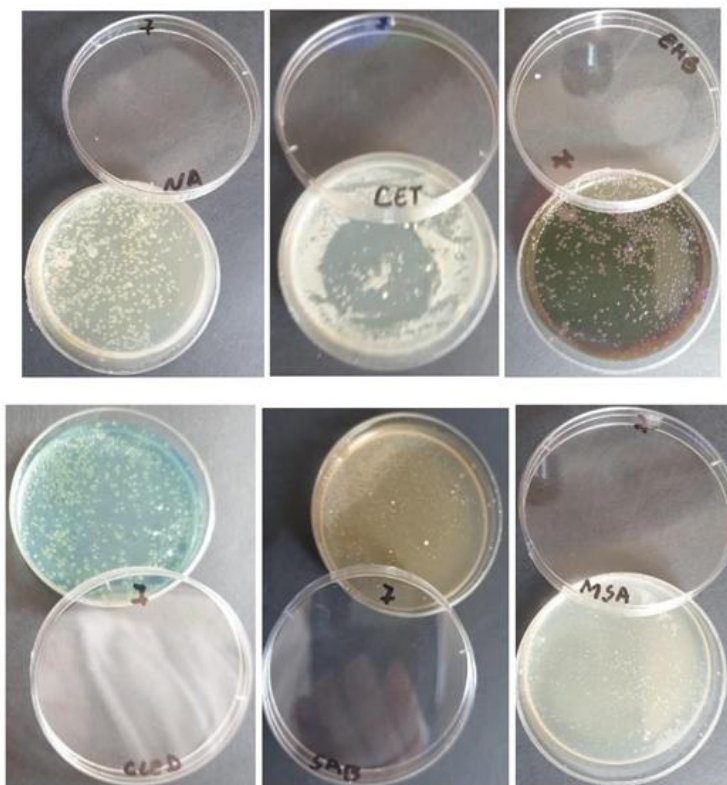


Figure 12. Microbial colonies developed on selective and non-selective test media developed for sample10; (NA = Nutrient Agar; Cet = Cetrimide Agar; EMB = Eosin Methylene Blue Agar; CLED = Cystine-Lactose-Electrolyte-Deficient medium; MSA = Mannitol Salt Agar; Sab = Sabouraud Chloramphenicol Agar)

This result indicates either inadequate preservation or contamination during the manufacturing process, emphasizing the need for strict hygienic practices and continuous microbiological monitoring of handmade cosmetic products.

Overall, the analyzed creams and ointments met the major physicochemical quality parameters, with the exception of one contaminated sample. These findings underline the importance of monitoring both formulation parameters (pH, viscosity, moisture) and microbiological safety to ensure consumer protection and product efficacy.

Microbiological Analyses of Handmade Oils

The results are detailed in Table 2.

Table 2. Microbiological Analyses of Handmade Oils

No.	Sample	Microbiological Analysis
1	O-NO	Negative for <i>E. coli</i> , <i>P. aeruginosa</i> , <i>Enterobacter</i> sp., <i>S. aureus</i> , <i>C. albicans</i> ; total aerobic bacteria absent
2	O-BO	Negative for pathogenic microorganisms; total aerobic bacteria absent
3	O-BL	Negative for pathogenic microorganisms; total aerobic bacteria absent
4	O-AO	Negative for pathogenic microorganisms; total aerobic bacteria absent
5	O-EO	Negative for pathogenic microorganisms; total aerobic bacteria absent
6	O-LB	Negative for pathogenic microorganisms; total aerobic bacteria absent
7	O-MO	Negative for pathogenic microorganisms; total aerobic bacteria absent
8	O-BR	Negative for pathogenic microorganisms; total aerobic bacteria absent
9	O-SD	Negative for pathogenic microorganisms; total aerobic bacteria absent
10	O-LO	Negative for pathogenic microorganisms; total aerobic bacteria absent

From a microbiological perspective, all analyzed oil samples were negative for pathogenic microorganisms, including *Escherichia coli*, *Pseudomonas aeruginosa*, *Enterobacter* spp., *Staphylococcus aureus*, and *Candida albicans*. Total aerobic bacterial counts were also negative, confirming that the oils met the microbiological purity requirements for cosmetic products.

Overall, the results indicate that the analyzed handmade cosmetic oils were microbiologically safe, exhibited physicochemical parameters within acceptable cosmetic standards, demonstrated how PV and AV can be used together to monitor product stability and quality.

Continuous monitoring of peroxide and acid values is recommended to ensure product stability and maintain quality throughout storage and distribution.

CONCLUSIONS

This study evaluated the physicochemical and microbiological quality of 30 handmade cosmetic products including creams, ointments, oils, and soaps, using standardized methods prior to market release. The novelty of the research lies in the pre-market assessment of these formulations, enabling early identification of potential risks related to skin compatibility and microbiological safety, while also supporting regulatory compliance and consumer protection.

The analyses demonstrated that:

The analyzed **solid soaps** exhibited a wide range of physicochemical properties, including pH, total and free alkalis, and total fatty matter, reflecting variability in formulation and composition. While most samples met quality standards, the slightly elevated pH values may require attention for frequent use on sensitive skin. Functional profiles varied from mild, moisturizing formulations suitable for daily cleansing to more abrasive or aromatic variants designed for intensive use.

The evaluated **creams and ointments** exhibited pH values within the physiological range, appropriate viscosity and density for topical application, and satisfactory microbiological safety. Viscosity measurements confirmed consistency with their intended uses — from light, fast-absorbing moisturizing creams suitable for normal to oily skin, to denser ointments with occlusive properties ideal for protective and reparative purposes. Plant extracts such as *Hypericum perforatum*, *Calendula officinalis*, and *Arnica montana* contributed to emulsion stability and potential therapeutic benefits through their lipophilic bioactive compounds.

The analyzed **cosmetic oils** demonstrated good chemical stability and excellent microbiological safety, with peroxide and acid values confirming minimal oxidative and hydrolytic degradation. Products such as Nutritive Oil, Anticellulite Massage Oil, and Beard Oil presented a balanced profile of moisturization and stability, supporting regular use. Higher-viscosity formulations (e.g., Beard Oil, Lip Oil) emphasized emollience and protection, while lavender-based blends showed good hydration but may benefit from enhanced oxidative stability.

EXPERIMENTAL SECTION

Materials and Methods

1. Materials

A total of 30 handmade cosmetic and hygiene products were analyzed, consisting of 10 samples from each category divided into three main categories:

Creams and Ointments (10 samples): 2 Hand creams, 1 Moisturizing face cream, 2 Ointments with medicinal plant extracts, 5 additional samples of various creams and ointments: Moisturizing cream (**C-MC**), *Calendula officinalis* and *Hypericum perforatum* Ointment (**C-CO**), *Arnica montana* Ointment (**C-AM**), Oat Hand Cream (**C-OH**), Moisturizing Face Cream (**C-MF**), Diaper Rash Ointment (**C-DR**), Hand Cream with *Calendula officinalis* and Glycerin (**C-HC**), Moisturizing and Emollient Face Cream (**C-ME**), Facial Exfoliant (**C-FE**), Facial Mask (**C-FM**). (*Semisolid formulations intended for topical application*).

Cosmetic Oils (10 samples): 3 Body oils, 1 Antimicrobial oil, 1 Essential oil, 5 additional oils for body or massage, including plant extract-enriched formulations: Nutritive Oil (**O-NO**), Body Oil (Grape Seed + Almond + Jojoba) (**O-BO**), Body Oil with Lavender (**O-BL**), Antifungal Oil (**O-AO**), Lavender Essential Oil (**O-EO**), Lavender Body Oil (**O-LB**), Anticellulite Massage Oil with Plants (**O-MO**), Beard Oil (**O-BR**), Body Oil “Silky Drops” (**O-SD**), Lip Oil (**O-LO**). (*Liquid formulations intended for skin application.*)

Solid Soaps (10 samples): 10 Handmade toilet soaps, including scented, exfoliating, and plant-enriched formulations: Citrus Scented Solid Soap (**S-CT**), Lavender and Violet Solid Soap (**S-LV**), Handmade “SKIN” Solid Soap (**S-SK**), Green Tea and Charcoal Solid Soap (**S-GC**), Coffee, Honey, and Cinnamon Soap (**S-CC**), Calendula Soap (**S-CD**), Coffee Exfoliating Soap (**S-CE**), Citronella and Rosemary Soap (**S-CR**), Honey and Oat Milk Soap (**S-HM**), Luxury Natural Soap (**S-LN**). (*Solid cleansing products produced by classical alkaline saponification or semi-synthetic methods.*)

2. Physicochemical Analyses

2.1 pH Determination:

For solid soaps, pH was measured in a 10% w/w aqueous solution using a Hanna Instruments pH meter, according to STAS SR EN 1262/2004 [42].

For aqueous solutions of creams, pH was determined according to STAS 8619/3-90 [43] and measured with a HALO 2 Wireless pH Meter.

2.2 Dynamic Viscosity:

Measured with a B-One Viscometer (LAMY RHEOLOGY) at 250 rpm for 60 s. For creams: RV4 spindle; for oils: RV1 spindle.

2.3 Moisture & Volatile Matter:

Determined according to SR:ISO 672:1996 [44] using a BIOBASE oven and RADWAG analytical balance.

2.4 Appearance and Stability:

Organoleptic evaluation and accelerated stability tests were performed, involving alternating exposure to low and high temperatures ($4\text{ }^{\circ}\text{C} \leftrightarrow 40\text{ }^{\circ}\text{C}$, 24 h per cycle, for 4–6 cycles).

2.5 Quality Factors for Oils:

2.5.1 Peroxide Value (PV): Determined by iodometric titration according to ISO 3960/2017 [45], representing the amount of iodine released from potassium iodide by peroxides in the sample. The peroxide value for all determinations is calculated by the equation:

$$PV = \frac{1000(V_0 - V_1) \times c}{m}$$

where: V_1 is the volume in mL of thiosulphate solution used for titration, V_0 is the volume in mL of thiosulphate solution used for titration of a control, c is the mol L⁻¹ thiosulphate concentration and m the amount of sample.

2.5.2 Acid Value (AV): Determined according to SR EN ISO 660:2020 [46] representing the amount of KOH (mg) required to neutralize the free fatty acids in 1 g of oil. It indicates the degree to which the triglycerides in the oil have decomposed to release free fatty acids.

The acid value was calculated by the equation:

$$AV = \frac{M \times C \times V}{m}$$

where: AV - the acid value expressed as a mass fraction, M is the molar mass, in grams per mole, for KOH, C is the L⁻¹ mole concentration of the standard volumetric solution of potassium hydroxide KOH used, V is the volume, in milliliters, of KOH and m is the mass, in grams, of the oil sample.

2.6 Determination of Alkalis and Fats in Soaps:

2.6.1 Free alkalis were determined according to SR:ISO 684:1996 [47]

The principle of the method consists of dissolving the soap in an ethanolic solution and neutralizing the free alkalis with a sulfuric acid solution whose known excess is back titrated with an ethanolic solution of potassium hydroxide. The total content of free alkali, expressed as sodium hydroxide (NaOH) in mass percent, is given by the formula:

$$\%NaOH = 0.040 \times \frac{V_0 T_0 - V_1 T_1}{m} \times 100 ,$$

where: m is the mass, in grams, of the test portion; V_0 is the volume, in milliliters, of the standard volumetric acid solution used; V_1 is the volume, in milliliters, of the standard volumetric potassium hydroxide solution used; T_0 is the exact normality of the standard volumetric acid solution; T_1 is the exact normality of the standard volumetric potassium hydroxide solution.

2.6.2 Total alkalis, and total fatty matter (TFM) were determined according to SR:ISO 685:2020 [48]. The principle of the method consists in decomposition of the soap by a known volume of standard volumetric mineral acid solution, extraction and separation of the liberated fatty matter with light petroleum and determination of the total alkali content by titration of the excess of acid contained in the aqueous phase with a volumetric

standard sodium hydroxide solution. After evaporation of the light petroleum from the extract, dissolution of the residue in ethanol and neutralization of the fatty acids with a standard volumetric potassium hydroxide solution. Evaporation of the ethanol and weighing of the soap formed to determine the total fatty matter content. Calculate *the total alkali content*, expressed as a percentage mass fraction of sodium hydroxide (NaOH) for sodium soaps, w NaOH, using formula:

$$w \text{ NaOH} = 0.040 \times (V_0 T_0 - V_1 T_1) \times \frac{100}{m},$$

where: m is the mass, in grams, of the test portion; V_0 is the volume, in milliliters, of the standard volumetric acid solution used; V_1 is the volume, in milliliters, of the standard volumetric sodium hydroxide solution used; T_0 is the exact normality of the standard volumetric acid solution T_1 is the exact normality of the standard volumetric sodium hydroxide solution.

Calculate *the total fatty matter content*, expressed as a percentage mass fraction, w , using formula:

$$w = [m1 - (V \times T \times 0,038)] \frac{100}{mn},$$

where: m is the mass, in grams, of the test portion; $m1$ is the mass, in grams, of the dried potassium soap; V is the volume, in milliliters, of the standard volumetric ethanolic potassium hydroxide solution used for the neutralization; T is the exact normality of the standard volumetric ethanolic potassium hydroxide solution.

2.7 GC-MS Analysis:

The lavender essential oil was analyzed using on gas chromatograph coupled with mass spectrometer instrument Model Agilent 7890 & 5975 Series MSD, equipped with a HP-5MS (5% phenyl)-methyl polysiloxane fused silica column Agilent (30 m x 0.25 mm x 0.25 μ M). The oil sample (0,1g) diluted in hexan (1 mL) and a volume of 1 μ l was injected into the GC device. GC-MS data was obtained under the following conditions: carrier gas helium (He 6.0), flow rate 1ml/min, injector temperature was 260°C, splitless mode. The temperature program was the following: Oven temperature was programmed as 40°C for 1 min and an increase by 5 °C /min to 200 °C. From 200 °C to 240 °C, increase with 20 °C /min. It is maintained at 240 °C for 5 minutes. Mass spectra: electron impact (EI+) mode, 70 eV and ion source temperature, 230°C. Mass spectra were recorded over 50-500 a.m.u. range, scan mode. All analyses were carried out in duplicate. Data

acquisition and processing were performed using MSD ChemStation software. NIST library was used for identification/confirmation of the structure components. In addition, a C8-C20 standards alkanes (Alkane Standard Solution C8-C20, Sigma Aldrich) was used for calculation of the linear retention index (LRI), and matching the experimental values with those reported in the literature for similar chromatographic columns, in the same condition. The qualitative analysis was based on the percent area of each peak of the sample compounds [49].

2.8 FTIR analysis:

An analysis was performed using a Fourier-transform infrared spectrophotometer (FTIR) (Jasco FTIR-610) (Jasco® International Co., Ltd., Tokyo, Japan) equipped with an attenuated total reflectance (ATR) accessory with a horizontal ZnSe crystal (Jasco PRO400S). The samples were placed in direct contact with the ZnSe crystal and then the spectra were recorded at a resolution of 4 cm⁻¹. The scans were repeated 100 times.

3. Microbiological Analyses

Detection of microbial contamination:

- Manitol Salt Agar (MSA) medium for detection of *Staphylococcus aureus*
- Cetrimide Agar for detection of *Pseudomonas aeruginosa*;
- Sabouraud Chloramphenicol Agar for detection of *Candida albicans*;
- Cystine-Lactose-Electrolyte-Deficient (CLED) medium, for detection of *Enterobacter* sp.;
- Eosin Methylene Blue (EMB) agar for detection of *Escherichia coli*;
- Nutrient Agar for detection of total aerobic bacteria [50,51].

Sample preparation involved 1:10 dilution: 1 g of sample added to 9 mL of Eugon LT 100 Broth.

Dilutions were inoculated on selective media for detection of potential pathogenic microorganisms. Plates were incubated at 37 °C for 24 h (for bacterial strains) and 48 h (for fungal strains), after which microbial growth was evaluated. All microbiological analyses were performed according to ISO 17516:2014 [52].

REFERENCES

1. K. Smith; L. Jones; R.Taylor; *JCS*, **2020**, 71(4),215-228
2. V. Popescu; A. Soceanu; S. Dobrinias; G. Stanciu; D. T. Epure; *Sci. Study Res.*, **2011**, 12(3), 257-261

3. I. H. Jung; J. H. Kim; Y. J. Yoo; B. Y. Park; E. S. Choi; H. Noh; *JOH*, **2019**, 61(4), 297-304
4. M. J. Rasheed; *JDU*, **2023**, 26(2), 501-508
5. J. D. da Silva; F. A. M. Silva; C. F. Rodrigues; *Cosmetics*, **2025**, 12(5), 198, 1-19
6. M. F. Irimescu; D. Ene; D. Margina; *Studia UBB Chemia*, LXIX, **2024**, 2, 67-80
7. A. Bashir, P. Lambert, *J. Appl. Microbiol.* **2020**, 128(2), 598–605
8. J. Abba; I. Y. Magaji; H. O. Opara; D. I. Onyemachi; *Niger. J. Chem. Res*, **2021**, 9, 334-339
9. E. M. Rédei; O. Péterfi; R. A. Vlad; P. Antonoaea; N. Todoran; A. Ciurba; I. Fülöp; E. Barabás; E. Sipos; *Studia UBB Chemia*, **2024**, LXIX, 4, 67-83
10. J. Blaak; P. Staib; *Curr. Probl. Dermatol*, **2018**, 54, 132 – 142
11. A. S. Evora; M. J. Adams; S. A. Johnson; Z. Zhang; *Skin Pharmacol Physiol*, **2021**, 34(3), 146-161
12. G. Yosipovitch; L. Misery; E. Proksch; M. Metz; S. Ständer; M. Schmelz; *Acta Derm Venereol*, **2019**, 99(13), 1201-1209
13. O. Braun-Falco; & H. C. Korting; *Hautarzt*, **1986**, 37(3), 126-129
14. S. Dikstein; A. Zlotogorski; *Acta Derm Venereol Suppl*, **1994**, 185, 18-20
15. J. Tarun; J. Susan; J. Suria; V. J. Susan; S. Criton; *Indian J Dermatol*, **2014**, 59(5), 442-444
16. M. Lukić; I. Pantelić; S. D. Savić; *Cosmetics*, **2021**, 8, 69, 1-18
17. C. Brozos; J. G. Rittig; S. Bhattacharya; E. Akanni; C. Kohlmann; A. Mitsos; *Colloids Surf.B.*, **2024**, 694, 1-10
18. F. M. Alshehrei; J. Saudi; *Biol Sci.*, **2023**, 30(12), 1-15
19. S. Sreeparna; R. Braj; A. Alok; *Indian J. Microbiol*, **2017**, 57(4), 448–460
20. S. F. Hayleeyesus; A. M. Manaye; *Asian Pac. J. Trop. Biomed.*, **2014**, 4(1), 312–317
21. A. V. Narayana; B. Sumalatha; D. J. Babu; T. C. Venkateswarulu; K. Chandrasekhar; I. Rashmik; V. Triveni; V. Sushma; V. Chandrika; *J. Biochem. Technol.*, **2024**, 15(1), 6-11
22. J. K. Betsy; M. Jilu; F. Reshma; J. T. Varkey; *Asian j. appl. sci. technol*, **2013**, 2(1), 8-12
23. J. F. Nova; S. Z. Smrty; M. Hasan; M. Tariquzzaman; M. A. A. Hassain; M.T. Islam; M.R. Islam; S. Akter; M.S. Rahi; M. T. R. Joy; Z. Cowser; *Heliyon*, **2025**, 11(4), 1-14
24. P. K. Ojha; D. K. Poudel; A. Rokaya; S. Maharjan; S. Timsina; A. Poudel; R. Satyal; P. Satyal; W. N. Setzer; *Compounds*, **2024**, 4, 37-70
25. K. C. Preethi; R. Kuttan; *J Basic Clin Physiol Pharmacol*, **2009**, 20(1), 73-79
26. D. Logia; A. Tubaro; S. Sosa; H. Becker; S. Saar; O. Issac; *Planta med.*, **1994**, 60, 516-520
27. Z. Saddiqe; I. Naeem; A. Maimoona; *J. Ethnopharmacol*, **2010**, 131(3), 511-521
28. I.P. Suntar; E.K. Akkol; D. Yilmazer; T. Baykal; H. Kirmizibekmez; M. Alper; E. Yesilada; *J. Ethnopharmacol*, **2010**, 127(2), 468-477
29. G. Lyss; T. Schmidt; I. Merfort; H. Pahl; *Biol. Chem.*, **1997**, 378(9), 951-961
30. T. Schmidt; *Plants*, **2023**, 12(20), 3532, 1-20

31. A. Balea; I. Ciotlăuș; M. P. Feneșan; R. Carpa; *Studia UBB Chemia*, **2023**, LXVIII, (1), 285-301
32. C. F. Oroian; A. Odagiu; C. P. Rácz; I. G. Oroian; I. C. Mureșan; M. M. Duda; M. Ilea; I. Brașovean; C. Iederan; Z. Marchiș; *Not. Bot. Horti Agrobot. Cluj-Na.*, **2019**, 47 (3), 643-650
33. D. Nedeltcheva-Antonova; K. Gechovska; S. Bozhanov; L. Antonov; *Plants*, **2022**, 11(22),3150,1-13
34. W. Pang; J. Wu; Q. Zhang; G. Lib; *RSC Adv.*, **2017**, 7, 55536-55546
35. C. Yuana; Y. Wang; Y. Liu; B. Cui; *Ind. Crop. Prod*, **2019**, 130, 104-110
36. M. I. Morar; F. Fetea; A. M. Rotar; M. Nagy; C. A. Semeniuc; *Bull. Univ. Agric. Sci. Vet. Med. Cluj-Napoca Food Sci. Technol*, **2017**, 74(1), 37-39
37. S. Agatonovic-Kustrin; P. Ristivojevic; V. Gegechkori; T. M. Litvinova; D. W. Morton; *Appl. Sci.*, **2020**, 10, 7294;1-12
38. S. Bhartia; S. Mishraa; L. V. Narendrab; T. Balarajua; K. Balrajuc; *Desalination and Water Treatment*, **2016**, 56, 12777-12792
39. S. D. Orth; I. J. Kabara; P. S. Denger; K. S. Tom; *Cosmetic and Drug Microbiology; Informa healthcare*, 1st, edition, Boca Raton, New York, London. **2006**, pp. 233-240
40. P. A. Geis; *Cosmetic Microbiology – A Practical Approach, Third edition*, **2021**
41. A. Budecka; A. Kunicka-Styczyńska; *Biotechnology and Food Science*, **2014**, 78(1), 15-23
42. *Agenți activi de suprafață, Determinarea valorii pH-ului soluțiilor sau dispersiilor* (Nr. 5.SR EN ISO 1262), **2004**
43. *PH-metrie. Determinarea electrometrică a pH-ului soluțiilor apoase* (Nr. 8619/3-90), **1990**
44. *Săpunuri. Determinarea apei și a substanțelor volatile. Metoda prin uscare în etuvă* SR:ISO Nr. 672: **1996**
45. *Animal and vegetables oils and fats. Determination of the peroxide index.* SR: EN ISO Nr. 3960 **2017**
46. *Animal and vegetable fats and oils—Determination of acid value and acidity.* SR: EN ISO Nr. 660, **2020**
47. *Determination of total free alkali in soaps* (SR:ISO: Nr. 684) **1996**
48. *Analysis of soaps—Determination of total alkali content and total fatty matter content* (Nr. SR ISO 685), **2020**
49. L. M. Dascalu (Rusu); M. Moldovan; D. Prodan; I. Ciotlăuș; R. Carpa; R. Ene; S. Sava; R. Chifor; M. E. Badea; *Studia UBB Chemia*, **2020**, LXV, (2), 57-67
50. R.M. Atlas, *Handbook of Microbiological Media*, 4th edition, CRC Press, New York **2010**
51. R. Carpa; *Biotehnologii în Industria Cosmetică. Lucrări Practice*. Ed. Presa Universitară Clujeană, Cluj-Napoca, România, **2020**
52. *Cosmetics—Microbiology—Microbiological limits* (ISO Nr. 17516) **2014**

EX VIVO EXPERIMENTAL AND SPECTROSCOPIC ANALYSIS OF URINARY STONE DISSOLUTION BY EL-MAATYA SPRING WATER: A MULTI-ANALYTICAL APPROACH

Hichem HAFFAR^a, Asma CHETOUANI^{b,*} ,
Souhir IZOUNTAR^c and Fatima Zohra BEZGHOUD^c

ABSTRACT. El-Maatya spring water, sourced from Algeria, is locally esteemed for its therapeutic attributes and has undergone scientific scrutiny to evaluate its litholytic potential on urinary calculi. Thorough physicochemical and microbiological assessments were performed to analyze its composition and ensure its safety. The microbiological evaluation yielded excellent results, demonstrating an absence of coliforms, *E. coli*, and *streptococci*, thereby affirming the water's sanitary integrity. Spectroscopic techniques, including UV and FTIR, were employed to ascertain the composition of the urinary stones, primarily consisting of calcium oxalate and uric acid. *Ex vivo* dissolution experiments indicated a markedly elevated rate of mass loss in uric acid stones when compared to calcium oxalate stones, which exhibited negligible solubility—underscoring the selective efficacy of the water. Microscopic examinations revealed significant morphological changes in the structure of the calculi following exposure. Finally, a survey involving 241 participants corroborated the favorable perception of El-Maatya water regarding urinary health, thereby reinforcing its traditional utilization.

Keywords: *El-Maatya water, urolithiasis, dissolution, uric acid, calcium oxalate*

^a Laboratory of Inorganic Materials LIM, Faculty of Sciences, University of M'sila, Algeria. PO Box 166 Ichebilia, 28000 M'sila, Algeria.

^b Laboratory of Multiphasic Polymeric Material (LMPMP)s, Faculty of Technology, University Ferhat Abbas of Setif 1, 19000.

^c Process Engineering Department, Faculty of Technology, University Ferhat Abbas of Setif 1, 19000.

* Corresponding author: asmachetouani@univ-setif.dz



INTRODUCTION

Nephrolithiasis is a common condition in men that leads to kidney stones mostly made of calcium oxalate. It is linked to metabolic problems and an imbalance in the pH of the urine [1, 2]. Urinary lithiasis creates crystalline concretions, blocking urine flow [3]. Urolithiasis, a kidney or bladder stone-producing condition, is gaining prevalence and requiring medication to alleviate pain and naturally expel stones [4, 5]. Pathogenic theories include precipitation and crystallization, nucleation, and suppression of inhibitory mechanisms [6]. Common drugs like allopurinol, citrate, cystone, and thiazide diuretics are used to prevent and treat the condition, but they don't always work because it can happen again and have bad side effects [5]. Among these, citrate lowers the formation of calcium stones by connecting to calcium and stopping the crystallization of calcium oxalate and calcium phosphate [7]. As a consequence, urolithiasis can lead to pyonephrosis and hydronephrosis, especially in individuals with type 2 diabetes and obesity [8, 9].

The consumption of spring water offers numerous health advantages [10]. Several water springs with specific mineral compositions can help prevent urolithiasis. For example, Fiuggi Water reduces urinary parameters such as calcium, phosphate, and uric acid [11], while Cerelia Water increases urinary pH and citrate excretion [12], and Serebryanny Klyuch Water reduces calcium oxalate deposits [13].

Excess minerals in drinking water, including magnesium [14], calcium, sulfates, and fluorides, are essential in preventing urinary calculi, which are primarily calcium oxalate-based [15]. Prevention relies on hydration [16], calcium consumption [17], and a balanced diet [18]. Mineral waters are effective in treating illnesses like renal lithiasis, with minimal stone development risks if medical advice is followed [6]. Environmental factors, such as climate, socio-economic status, and dietary habits, influence the use of thermomineral waters in cryotherapy for various ailments [19, 16]. Long-term use of hydrogen-rich water lowers high uric acid levels and uric acid stones [20], while alkaline water raises the body's ability to get rid of uric acid and use purines [21, 22]. Alkalinization of urine to a pH between 6.5 and 7.0 effectively dissolves uric acid stones and helps prevent the formation of calcium oxalate stones [15, 23].

The study by Karagülle et al. found that using bicarbonate-rich mineral water can prevent recurrent calcium oxalate urolithiasis by enhancing urinary pH, citrate and magnesium excretion, and decreasing calcium oxalate supersaturation [24]. Uric acid stones, the second most prevalent type of renal stones [25], can be managed with oral pharmacological treatment through urine alkalinization [23]. Diluting urine stops crystal-forming substances like oxalate and calcium from forming in the urinary tract. This lowers the

saturation of kidney stone-forming substances and raises the calcium oxalate nucleation threshold [26]. In addition, different minerals commonly present in natural waters, such as calcite, magnesian calcite, aragonite, halite, and sylvite, exhibit variable solubility in aqueous environments, which can influence alkalization processes and, consequently, the solubility of urinary calculi [27, 28].

In Algeria, many studies on urolithiasis have been done, looking at how the chemical makeup of urinary calculi changes depending on where the patients live, their age, and their gender [29, 30]. Further research has investigated the impact of plant extracts from Algeria on stone dissolution [31-33], as well as the impacts of thermal spring water from various locations in the western region of the country [34, 15].

This study aims to assess the physicochemical and microbiological effects of spring water from El-Maatya in the Sétif province. We focus on evaluating the dissolution of urinary calculi retrieved from patients following surgical intervention using this water.

We are conducting a statistical analysis to assess public awareness and attitudes of this water, considering variables such as age and gender.

RESULTS AND DISCUSSION

Analysis Of El-Maatya water

Physicochemical tests

The findings derived from volumetric dosing and spectroscopic analysis are encapsulated in **Table 1**. It is observed that the conductivity measurement is approximately 1764 $\mu\text{S}/\text{cm}$, which remains within the acceptable limit (2800 $\mu\text{S}/\text{cm}$) for potable water according to Algerian standards, but is higher than the conductivity values of spring waters reported by Ennaghra [10]. This elevation may be attributable to an augmented concentration of dissolved ions, such as minerals and salts, present in this water. The mineral concentrations align with the established standards detailed in the table, with the exception of sodium, nitrates, bicarbonates, and the total alkaline titer, which are significantly heightened relative to the normative values. This elevation can be elucidated for each parameter as follows:

The water analyzed in our study has a sodium concentration greater than 200 mg/L, as well as a bicarbonate content exceeding 600 mg/L, thus classifying it among '*waters with sodium*' and '*waters with bicarbonates*' according to the classification of the European Directive 2009/54/EC [35].

Bicarbonate-rich mineral waters, such as those analyzed in our study, possess alkaline properties that provide several health benefits, including improved digestion, enhanced diuresis, and reduced bone resorption. Additionally, these waters could play a role in regulating cardiometabolic risks and in urinary alkalization, which favors the dissolution of kidney stones [35]. Specifically, bicarbonate-rich waters like Cerelia water have been shown to increase urinary pH and citrate excretion, making the urinary environment less conducive to the formation of both uric acid and calcium stones [12, 36]. Moreover, experimental studies indicate that alkaline mineral water can reduce oxidative stress and inflammation, offering further protection against kidney stone formation [36].

In our research, the nitrate concentration slightly exceeded the prescribed threshold, indicating a potential environmental impact, especially from anthropogenic activities such as agriculture or urban development, as highlighted in previous studies [16, 37]. The nitrate contamination in the water of Dar Bentata, as reported by Amara-Rekkab (2023) [16], aligns with our observations and points to the risks posed by agricultural runoff. Nitrates in drinking water primarily result from sources like nitrogen-based fertilizers, improper waste disposal, and untreated wastewater discharge, which contribute to contamination of groundwater, a key drinking water source in many regions [38-40]. Research in various regions, such as the Poyang Lake Plain and the North East Alluvial Plains of Bihar, shows that agricultural practices, particularly the excessive use of fertilizers, are significant contributors to elevated nitrate levels [38, 39].

In relation to the pollution parameters, we distinctly noted the minimal concentrations of ammonium, nitrite, and phosphate compounds, recorded at 0.03 mg/L, 0.03 mg/L, and 0.02 mg/L, respectively, which substantiates the lack of contamination or pollution in this water, thereby favorably impacting our study. Iron is an essential micronutrient, closely involved in haemoglobin synthesis and oxygen transport. According to the World Health Organization [41], the recommended daily intake of iron for adults ranges from 10 to 50 mg. The total iron concentration measured in El-Maatya water (0.02 g/L, i.e., 20 mg/L) remains below the average daily requirement, indicating that this water may slightly but positively contribute to daily iron intake without posing any toxicological risk.

Table 1. Results of physicochemical parameters

Parameters		Algerian standard
Physicochemical parameters		
pH	7.62	6.5-9
Temperature (°C)	23.6	25
Electrical conductivity ($\mu\text{S}/\text{cm}$)	1764	2800
Turbidity (NTU)	1.17	5
TDS (mg/L)	902	1500
Global mineralization		
Calcium (mg/L)	44	200
Magnesium (mg/L)	17.01	150
Chloride (mg/L)	76.68	500
Nitrates (mg/L)	67	50
Total hardness (°F)	18	50
Sodium (mg/L)	390	200
Potassium (mg/L)	1.5	12
Bicarbonate (mg/L)	671	610
Sulfate (mg/L)	230	400
Complete alkaline title (°F)	55	50
Pollution parameters		
Ammonium (mg/L)	0.03	0.5
Nitrites (mg/L)	0.03	0.2
Phosphates (mg/L)	0.02	0.5
Heavy metals		
Total iron (mg/L)	0.02	0.3

Bacteriological analyses

These bacteriological findings entirely correspond to those published by Ennaghra *et al.* 2024 [10], which indicate 0 CFU/100 mL for *total coliforms*, *Escherichia coli*, and *fecal streptococci*. Every tested parameter was negative, hence ensuring the great microbiological quality of El-Maatya water.

Analysis of urinary calculi

Dissolution test

After about three hours, we observed that stone **2** found in El-Maatya (**M**) water began to dissolve, and the others after one day, while those in the negative and positive control groups remained unchanged. After one day, the stones in the El-Maatya group were completely dissociated (**Figure 1a**).

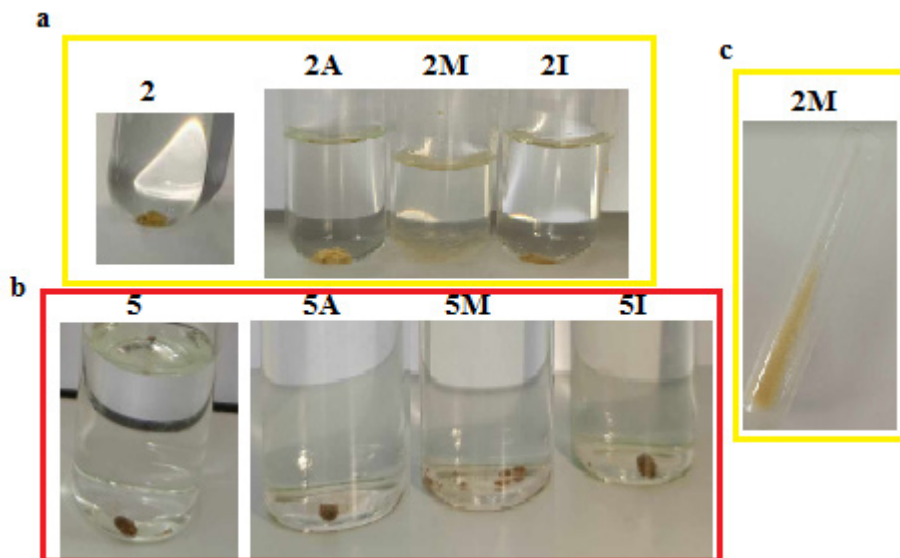


Figure 1. Photographs showing the dissolution of stones 2 **(a)** and 5 **(b)** in the three media (A, I, and M), and the precipitate of stone 2M **(c)** after one month of observation.

Some urinary stones found in the citrate group showed a slight dissolution, while the mineral water remained a negative control (unchanged) **(Figure 1b)**. After one month, the previous observations remained the same. Note: no dissolution but very fine powders obtained as a precipitate **(Figure 1c)**.

Monitoring the dissolution of urinary calculi

In order to gain a better understanding of the inhibitory effect of El-Maatya **(M)** water, this method is based on monitoring the loss of mass of urinary calculi under the effect of different media over an incubation period of 3 weeks. The dissolution rates, calculated as a percentage, are shown in **Figure 2**. These results show that :

- The dissolution kinetics appear to be different for each incubation medium.
- A slight variation in mass loss was observed during the first 7 hours, especially in the case of calculus number 5.
- Calculus number 2 dissolved easily from the start of immersion and reached 90% dissolution on day 23.
- No variation was observed when mineral water (I) was used as the medium.
- After 15 days, dissolution began in the sodium citrate medium (A) with a dissolution rate that was very low.

- Calculus number 4 is made up of several layers (in the form of a dragée). It looks completely different from the others. After one day, the first outer layer of the 4M stone dissociated and its color began to lighten. However, for calculus 4A and 4I, no change was observed (neither loss of mass nor dissolution of the outer layer).
- According to the results obtained, the size and weight of the stone had no impact on the dissolution test. Calculi 2 and 5, which are large, were solubilized, whereas calculus **4A** was not. So it's the environment that plays a decisive role.
- El-Maatya (**M**) water proved to be the best medium for stone dissolution. The dissolution rates for 2M, 3M, 4M, and 5M stones are 90.28%, 76%, 73.15%, and 21.18%, respectively. Calcium oxalate is known to be slightly more difficult to dissolve than uric acid, which is why the dissolution rate of stone No. 5 is the lowest compared with the others.
- When comparing this *ex vivo* dissolution test using plant extracts, they found that dissolution continued until the eighth week [31].

The in vitro and physicochemical effects of El-Maatya water

Our *in vitro* analyses showed that uric acid and calcium oxalate stones dissolved on contact with the spring water tested. These results should be interpreted in the light of the physico-chemical properties of this water, in particular its pH of 7.6, its high concentration of bicarbonates, its high total alkaline titre (55°F) and its sodium content, which exceeds Algerian standards.

High concentrations of sodium and bicarbonates can have an impact on the dissolution of kidney stones, in particular by influencing the alkalinisation of urine and thus promoting the dissolution of certain types of stone, as observed in our *in vitro* tests. This observation is in line with the study by Alsinnawi et al, who reported complete dissolution of stones in 39% of patients treated with sodium bicarbonate alone, with urinary pH maintained above 7 for around 9 weeks [42].

Despite epidemiological evidence indicating that elevated sodium intake correlates with an increased likelihood of urinary stone formation [43], our *ex vivo* investigations demonstrate that the sodium-rich spring water examined exhibits a noteworthy capacity for stone dissolution. This seemingly paradoxical finding may be elucidated through intricate physico-chemical processes associated with the diverse array of minerals contained within the water, particularly emphasizing the buffering effect rendered by bicarbonate and the pronounced alkalinity. These findings imply that the litholytic properties of water are not exclusively contingent upon its sodium concentration, but rather also depend on its comprehensive ionic equilibrium, which warrants further investigation.

The dissolution rate of urinary calculi in different media over 23 days is shown in **Figure 2**.

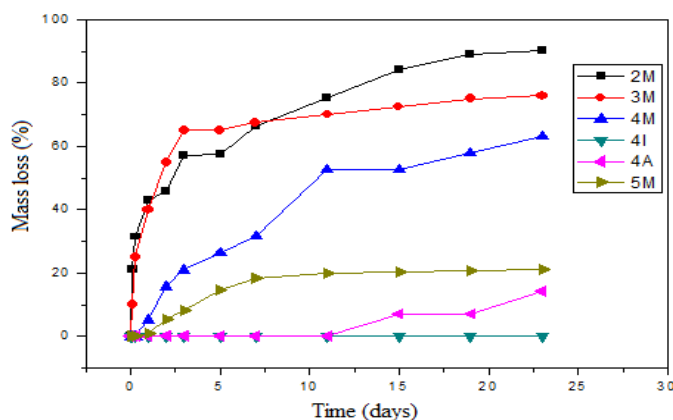


Figure 2. Evolution of mass loss over time for the different media.

a. Variation in pH

The pH of El-Maatya water is more basic than that of sodium citrate and mineral water, with a value of 7.95 ± 0.01 . During the incubation of urinary calculi, the pH of the media varied with time, gradually increasing to reach values of 8.65, then stabilizing at the end, whether in M, I, or A (**Figure 3**).

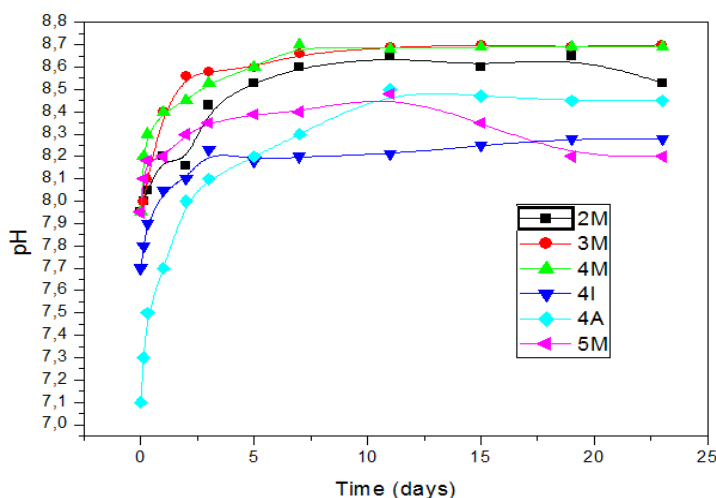


Figure 3. Variation in pH as a function of time.

b. Variation in stone size

Figure 4 and **5** illustrate the evolution of urinary stone size over time, showing a remarkable reduction for the **2M** stone, which decreased from 20 mm to 9 mm. For the **3M** stone, the size was reduced by approximately half. The size of the **4M** stone changed slightly, from 13 to 5 mm.

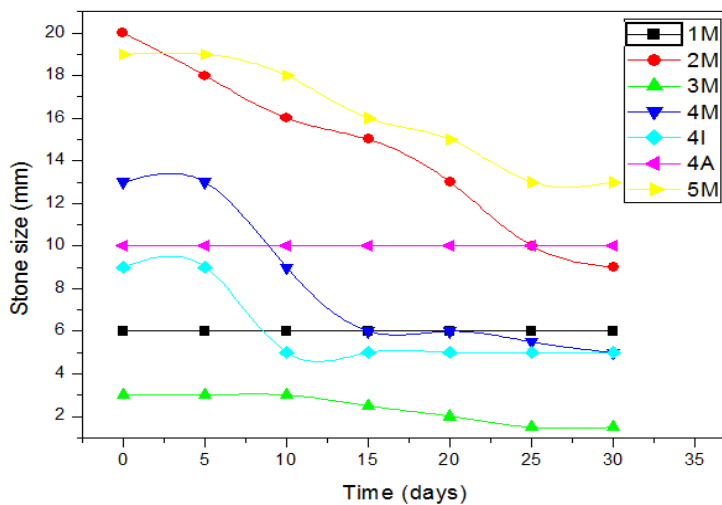
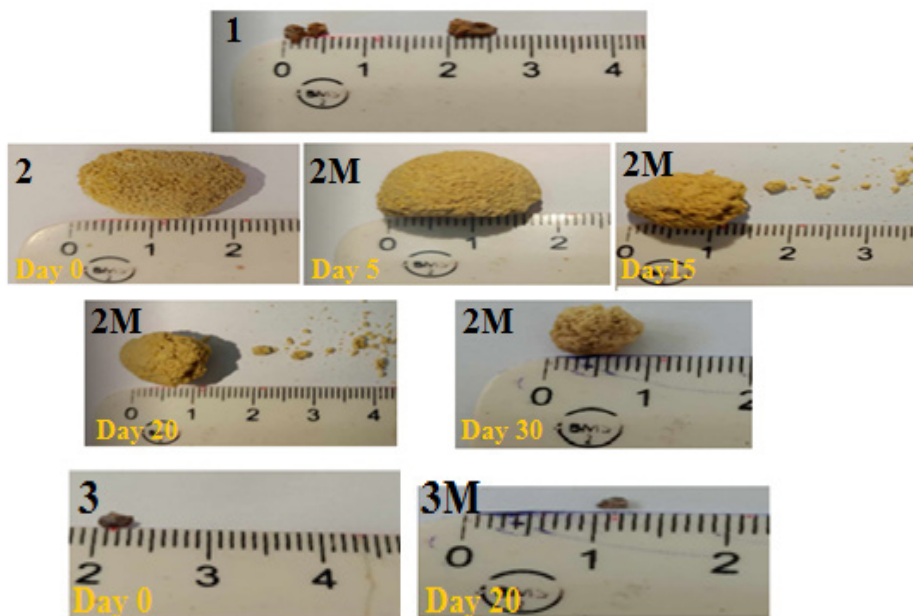


Figure 4. Variation in the size of urinary stones as a function of time.



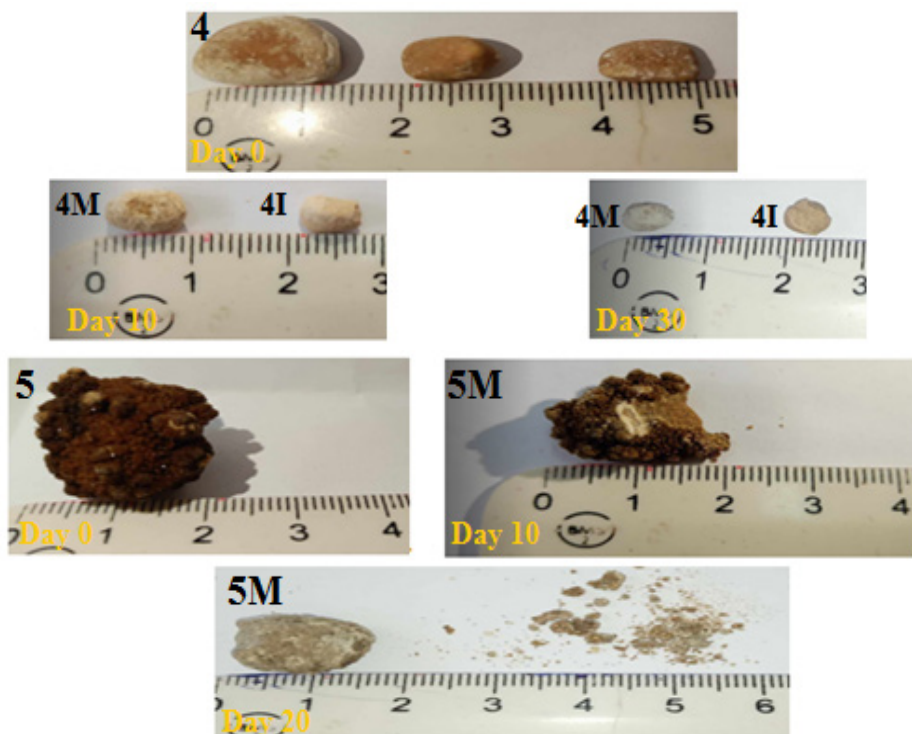


Figure 5. Changes in the size of urinary calculi over time.

Study by UV-VIS spectroscopy

a. Study conducted on El-Maatya water (M)

The UV spectrum (**Figure 6**) shows two characteristic bands at 215 nm and 280 nm, typical of uric acid [44], observed for urinary calculi numbers **1**, **2**, **3** and **4**. Furthermore, two additional bands at 350 nm and 400 nm are observed in the UV spectrum corresponding to urinary stone number **2**. The first is probably related to impurities, and the second band could be correlated to the yellow colour obtained (**Figure 7**) during the immersion of urinary calculus number **2**. This additional band at 400 nm suggests the presence of other compounds in the stone, such as dyes or other chemical substances in addition to uric acid. It is also possible that the presence of bilirubin or bilirubin derivatives contributes to the yellow colouration, particularly in the case of liver problems.

EX VIVO EXPERIMENTAL AND SPECTROSCOPIC ANALYSIS OF URINARY STONE DISSOLUTION
BY EL-MAATYA SPRING WATER: A MULTI-ANALYTICAL APPROACH

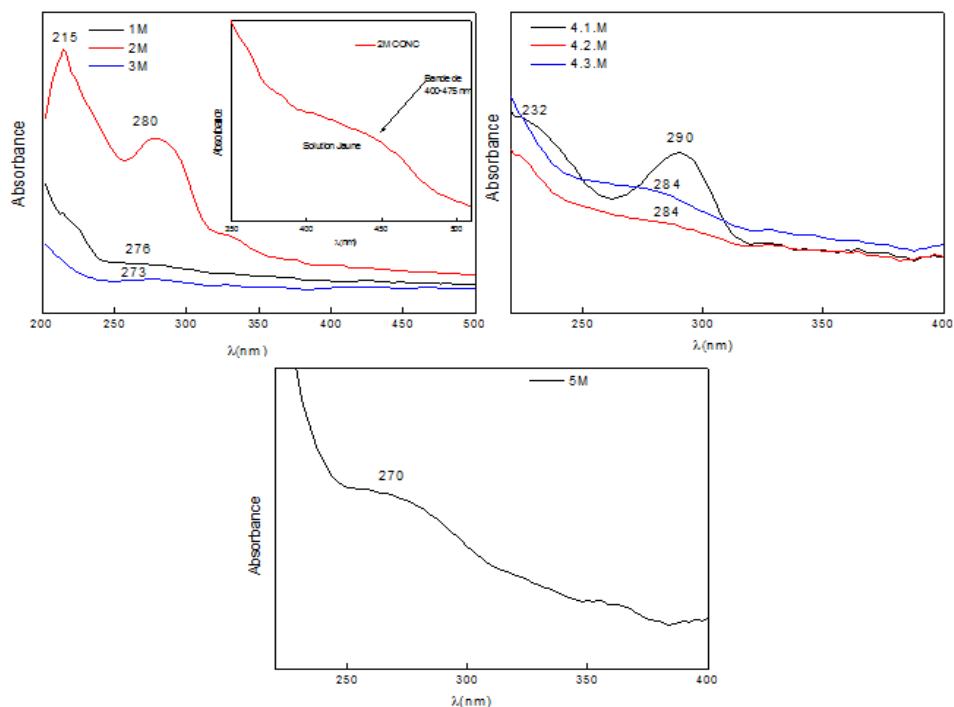


Figure 6. UV spectrum of M water after 24 hours of dissolution of urinary calculi numbers 1, 2, 3, and 4.1, 4.2, and 4.3 corresponding to uric acid and urinary stone number 5 corresponding to calcium oxalate.

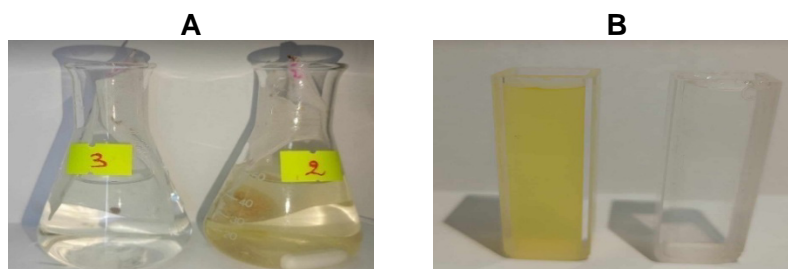


Figure 7. Representation of Erlenmeyer flasks (A) and UV-Vis cuvettes (B) containing M water after 24 hours of dissolution of urinary calculi (samples 3 and 2), showing the color change.

The UV spectrum corresponding to urinary calculus number 5 shows a single characteristic band at 270 nm, typical of calcium oxalate [45]. This absorption band at 270 nm is consistent with the presence of calcium oxalate, a common compound in kidney stones. The absence of other significant bands

in the spectrum suggests a relative purity of the sample analyzed, highlighting mainly the presence of CaC_2O_4 . *It should be noted that a yellow color similar to that observed for calculi number 2 is obtained, but no absorbance in the visible range is observed.*

b. Study using sodium citrate (A)

The study carried out with sodium citrate **(A)** reveals that the UV spectra of urinary calculi placed in this medium, compared with those in El-Maatya water **(M)**, show a shift of the bands towards higher wavelengths (*bathochrome effect*) with a difference in λ_{max} between 2 nm and 20 nm (**Figure 8**). For example, the band at 215 nm in the case of **2M** is shifted to 236 nm, and a further shifting from 280 nm to 290 nm is observed. These observations could be attributed to the difference in pH and ionic strength of the salts present in El-Maatya water, which differ significantly from sodium citrate. Another observation concerns the presence of two characteristic dual-chromophore bands linked to uric acid in the spectrum of sodium citrate, whereas in the spectrum of El-Maatya water a single chromophore is generally observed, particularly in the cases of **3M**, **4.2M**, and **4.3M**.

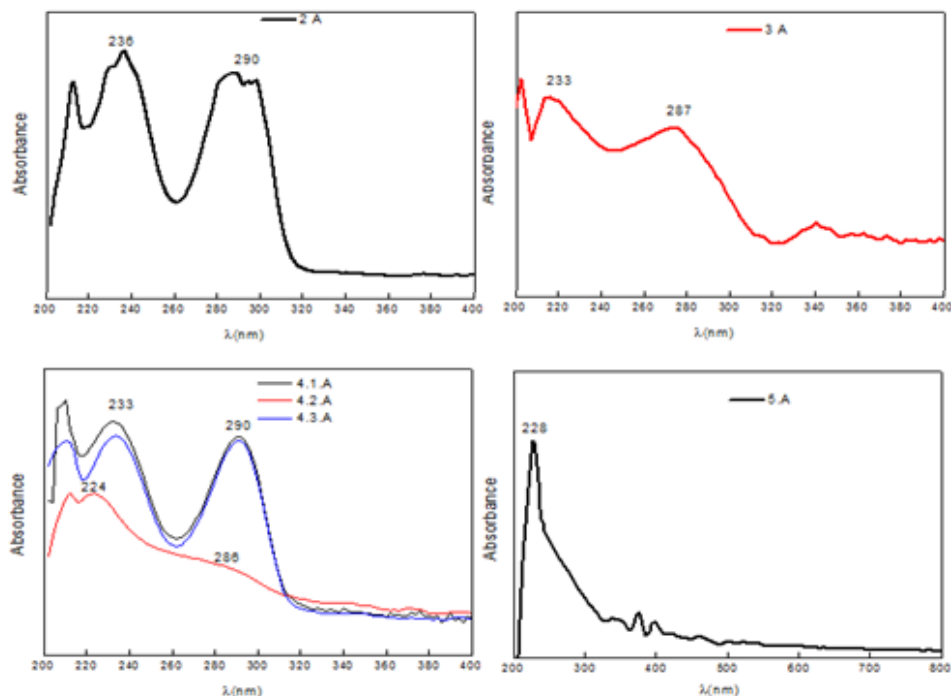


Figure 8. UV spectrum in sodium citrate after 24 hours of dissolution of urinary calculi number **2**, **3**, and **4.1**, **4.2**, **4.3**, and **5** corresponding to uric acid.

Contrary to the previous interpretation, we observe a decrease in λ_{\max} of the CaC_2O_4 characteristic band of urinary calculus N°5 (**Figure 6**). It is of the order of 270 nm in **M** water and 228 nm in **A** water, corresponding to a *hypsochromic effect*

c. Study using mineral water (I)

The UV spectra corresponding to mineral water (**I**) are not clear when compared with those of citrate (**A**) and El-Maatya (**M**). In addition, this water was unable to dissolve the stones, so no changes were apparent after treatment.

Infrared spectroscopy

Identification of the components of urinary calculi is essential to provide information on the aetiological factors responsible for their formation, making therapy and prevention possible. Morphological examination combined with infrared spectroscopy can provide useful information about their chemical composition.

a. Urinary calculi N° 1, 2, 3, and 4 (4-1; 4-2 and 4-3)

After visual analysis of the peaks obtained in the infrared vibration spectra of urinary calculi **1, 2, 3, and 4**, we were able to determine that they were all of the same type, i.e., uric acid.

The salt form of uric acid most commonly found in urinary calculi is the anhydrous form; it has a characteristic infrared spectrum that is easily recognized by the presence of an N-H distortion vibration in the 1637 - 1624 cm^{-1} frequency region. However, Mujahid et al. have suggested that this elongation vibration is linked to the C=O group [46].

Numerous N-H elongation bands are observed in the 3600 to 2600 cm^{-1} range, as well as other bands attributed to hydrogen bonds (OH). A band at 1588 cm^{-1} , attributed to carbonyl deformation of the conjugated amide, is absent. In agreement with Sekkom et al., C-C elongation appears at 1449 cm^{-1} (**Figure 9a**) and 1410 cm^{-1} (**Figure 9b**) due to the hypsochromic effect of the amide and carbonyl groups [47].

The peaks observed at [1449-1410 cm^{-1}] and 1109 cm^{-1} are due to O-H deformation and C-O elongation, respectively. The C-N elongation and deformation vibrations appear in the frequency region 1021 - 1000 cm^{-1} and at 858 cm^{-1} , respectively [48].

b. Urinary stone No. 05

After analysis and close examination of the peaks in the spectrum shown in **Figure 10**, we concluded that this urinary calculus is a calcium oxalate.

Pure calcium oxalate monohydrate was characterized by five bands: The absorption band observed at 3500 - 3021 cm^{-1} is due to the elongation

vibration of the O-H function, which is in agreement with Sekkoum et al. [47]. Two strong absorbances at 1651 and 1322 cm^{-1} correspond to the C=O and C-O elongations, respectively [49].

According to Asyana et al. [48], two bands at 771 and 667 cm^{-1} correspond, respectively, to the deformation of C-H bonds and the out-of-plane deformation of O-H bonds. In-plane deformation of the O-C bond appears at 514 cm^{-1} (**Figure 10**).

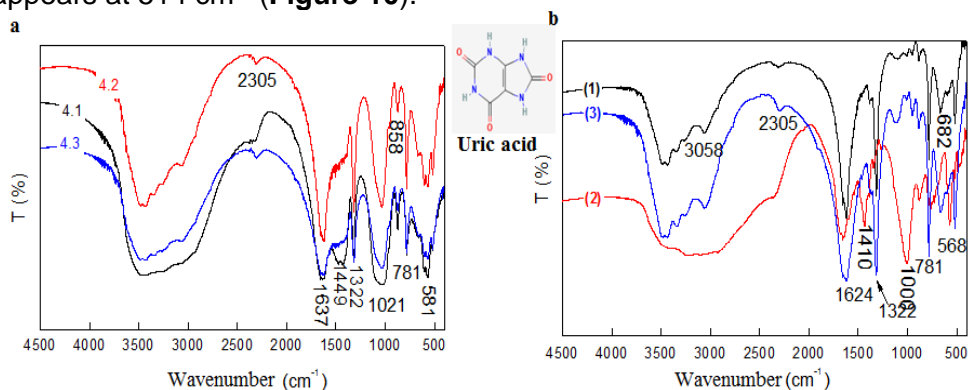


Figure 9. Infrared spectra of urinary stones number 4 (a) and 1, 2, and 3 (b) corresponding to uric acid.

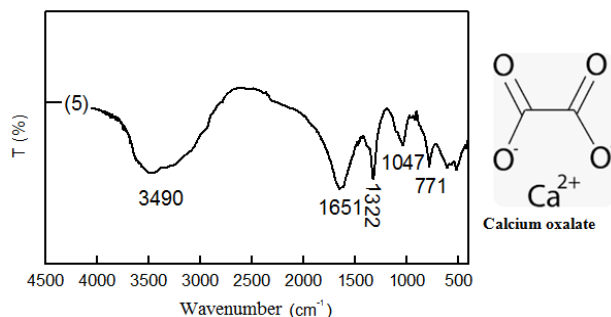
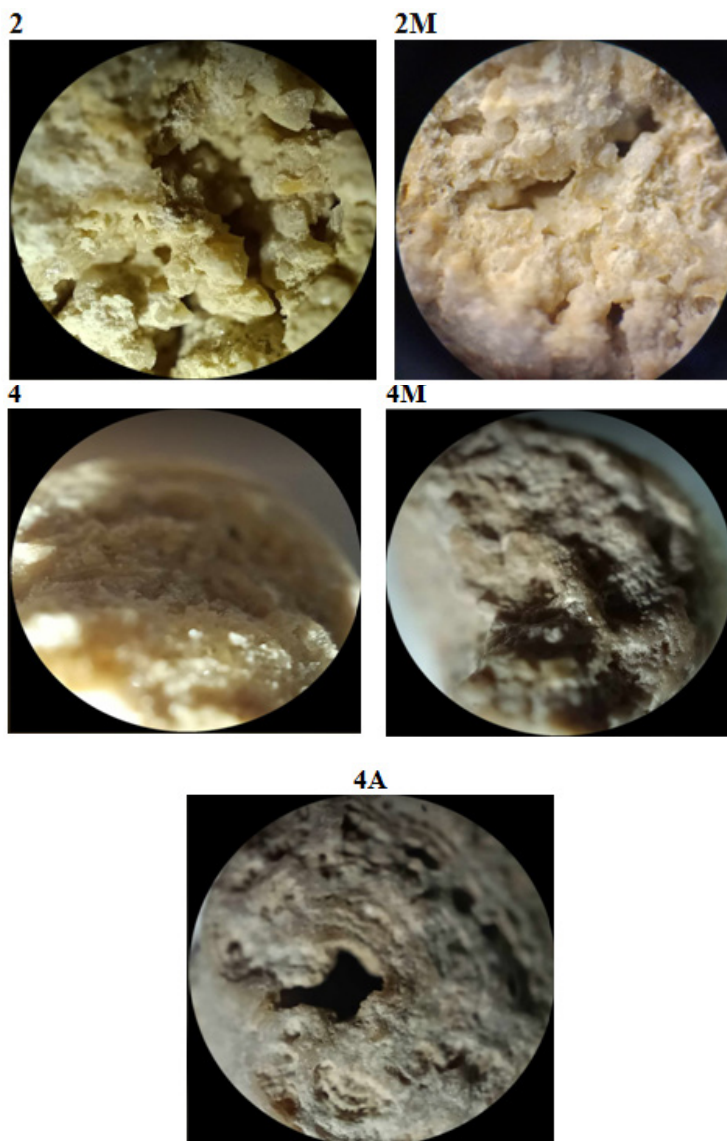


Figure 10. Infrared spectrum of urinary stone number 5 corresponding to calcium oxalate.

Light microscopic examination

Microscopic examination of the peripheral layers of the stone can be essential in identifying its morphological type and the metabolic disorder responsible for its nucleation or growth process. In addition, comparing the urinary calculus before and after a dissolution treatment allows morphological changes to be highlighted (**Figure 11**).

Figure 11 depicts the microscopic morphology of kidney stones before and after treatment, revealing a significant difference. Stone 5 had a brilliance, both microscopically and macroscopically, that has since disappeared. On a macroscopic scale, the color of calculus 4 shifted to light gray when the outer layer of lithiasis disappeared. On a microscopic scale, we see the same change, confirming the transformation. The similar phenomenon is seen with urinary stone 2.



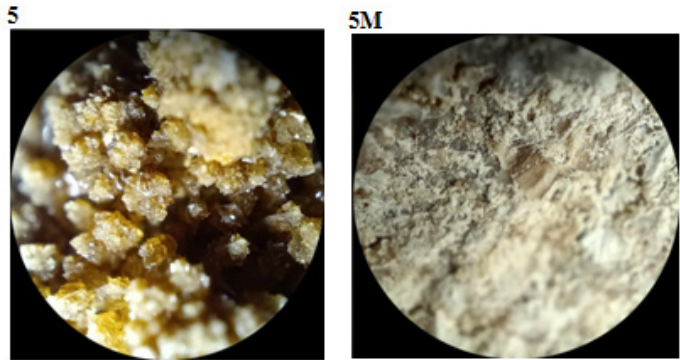


Figure 11. Optical microscope image of stones 2, 4, and 5 before and after treatment at 20X scale.

The disappearance of the brightness of stone 5 after treatment probably indicates a change in its chemical composition, suggesting dissolution or a change to a less bright and more brittle crystalline phase. In addition, the change in color of stone 4 to light gray, associated with the disappearance of its outer layer, suggests a significant alteration in its structure, perhaps due to the action of the treatment.

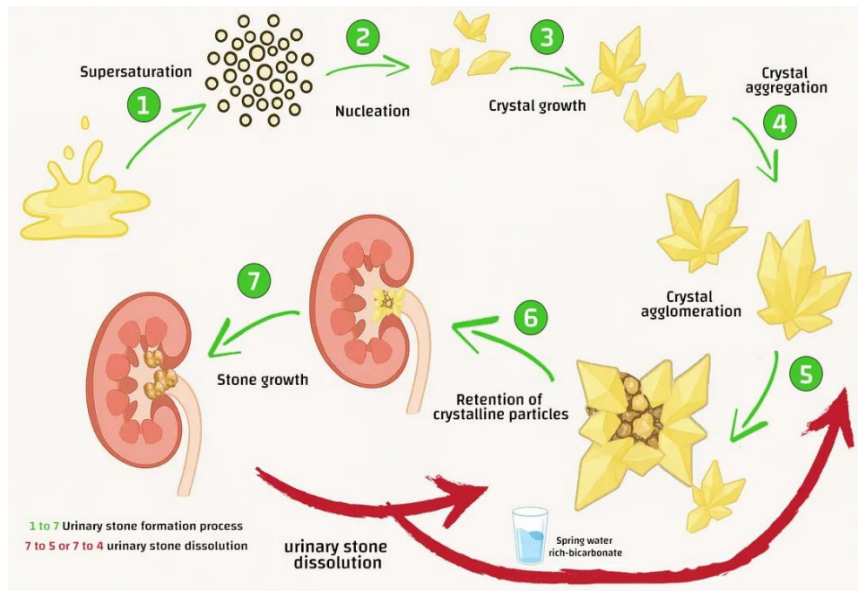


Figure 12. Proposed mechanism of urinary stone dissolution by spring water.

These changes suggest possible mechanisms of action (**Figure 12**) of the treatment on kidney stones but would require further study to be confirmed.

Survey on the use of El-Maatya water

241 people responded to the survey on the use of El-Maatya water. Of these, 76% were women and 23.7% men.

The majority of respondents were young people aged between 20 and 40, and 82.6% were university graduates. Participants came from various wilayas, in particular 70.12% from Sétif, 6.64% from Borj Bouaririj, 4.56% from Algeria, 3.73% from Mila, 1.66% Skikda, 1.24% Tlemcen, 0.83% Boumerdes and Oum Bouaki, and 0.41% from Batna, Djelfa, Bejaia, Jijel, Blida, Tiaret, Khenchela, Guelma, and Mascara

Only 40.7% of respondents were familiar with El-Maatya water. Of these, 26.1% said that the water is used mainly for cooking, making it easier to cook chickpeas and white beans. A further 5.4% use it for cosmetic purposes and 21.7% for medical treatments. Among the respondents, 38.6% suffer personally from lithiasis or have relatives who do and use El-Maatya water as a treatment. Of these, 9.5% consult a urologist during their water treatment. A further 13% combine the water with other medicines under the guidance of their general practitioner.

17.4% of participants reported negative effects of this water, such as brittle bones, frequent urination, and the risk of abortion in pregnant women.

In addition, 43.2% knew of other waters used to treat urinary lithiasis, including:

29 people knew of Maa Zdim, 10 in Ain Bouglez, 9 in Borj Bouaririj, 7 in Ain Ben Tata (Tlemcen), 3 in Nguauas (Batna), 5 in Ouled Yalass, 2 in Algeria, and 1 in Annaba.

Opinions differ on the taste of the water. 22 people say it is tasteless, 4.98% find it bitter, 36.1% describe it as concentrated water, and 36.93% don't know what it tastes like.

The majority strongly recommend the use of this water.

Future investigations should include clinical trials on voluntary subjects to assess the dissolution dynamics of urinary stones through periodic CT scans. Such studies would provide direct evidence of the curative efficacy of El-Maatya water and support its potential medical application in urolithiasis prevention and treatment.

CONCLUSIONS

El Maatya's water has favorable physicochemical and microbiological characteristics for healthy consumption, although certain mineral values, such as sodium, nitrates, bicarbonates, and total alkalinity, exceed standard norms.

The high concentrations of some minerals, such as sodium, can be attributed to the geology of the area of this spring and to other environmental factors.

Microbiological tests show a total absence of *coliforms*, *E. coli*, and *streptococci*, guaranteeing good sanitary quality.

Dissolution tests indicate that this water can be effective in dissolving certain types of urinary stones, mainly those composed of uric acid (bands at 215 nm and 280 nm), but is less effective for calcium oxalate stones (band at 270 nm).

The type of urinary stone (uric acid and calcium oxalate) was identified by UV and infrared spectroscopy based on the presence of chromophores and associated functional groups.

Light microscopic analysis confirmed a complete change in the morphology of the stones, both microscopically and macroscopically.

The survey of the local population, based on a sample of 241 people, shows that the water is well accepted and used for its perceived benefits, despite some potential drawbacks linked to the high concentrations of certain minerals.

Future studies should focus on a detailed mineralogical analysis of El-Maatya water using XRD and optical microscopy, as well as on correlating its mineral composition with the nutritional and metabolic needs of the local population.

EXPERIMENTAL SECTION

Material

The following reagents were used in the practical session:

Sodium citrate tribasic dihydrate (Biochem, purity $\geq 99\%$); distilled water; Ifri mineral water; El-Maatya spring water; sodium hydroxide (NaOH), pellets (Sigma-Aldrich, purity $\geq 98\%$); sodium salicylate (Sigma-Aldrich, purity $\geq 99\%$); sulphuric acid (H_2SO_4 , Sigma-Aldrich, 95–98%); silver nitrate (AgNO_3 , Sigma-Aldrich, purity $\geq 99.8\%$); potassium chromate (K_2CrO_4 , Sigma-Aldrich, purity $\geq 99\%$); hydroxylamine hydrochloride ($\text{NH}_2\text{OH}\cdot\text{HCl}$, Sigma-Aldrich, purity $\geq 98\%$); hydrochloric acid (HCl, Sigma-Aldrich, 37%). Other reagents required for the titrimetric determinations were used according to the ISO standards cited in Table 2.

Analysis of El-Maatya water

The water of El-Maatya, also known as Ain Al-Shifa, is located in the village of El-Maatya, in the commune of Draa Kbila, to the north of the province of Sétif, Algeria (Google Maps – Plus Code: C234+7X). This well was dug in 2001, and a spring structure was built for it in 2002.

The water sampling was conducted in May 2024 at the designated source, utilizing sterile containers that were subsequently stored in a cooler maintained at a temperature of 4°C. Following this, the samples were transported to the laboratory for comprehensive analysis. We performed both physicochemical and microbiological assessments of El-Maatya water at the ADE (Algérienne des Eaux) facility located in Sétif.

Physicochemical analyses

For the physicochemical parameters, an electrochemical approach was employed to assess the physical parameters, including pH, temperature, electrical conductivity, and turbidity, using benchtop instruments from HACH (USA): a pH meter (HACH, benchtop type), a conductivity meter (HACH, benchtop type), and a turbidity meter (Model 2100N, HACH, USA).

For the chemical parameters, volumetric methods were applied to determine chloride, calcium, total hardness, and alkalimetric titre, using standard glassware (burette, pipette, conical flask, and beaker).

Spectrophotometric methods were employed for the determination of nitrate, nitrite, ammonium, phosphate, sulfate, and total iron using a molecular absorption spectrophotometer (HACH DR 6000, USA). Sodium and potassium concentrations were measured using a flame photometer (Jenway, UK).

Table 2. Physicochemical water analysis methods

Parameters	References to the analytical method
Analysis by spectroscopic methods	
Nitrates (NO_3^-)	T 90-012, NF-August1975
Nitrite (NO_2^-)	ISO 6777, 1 st edition, August 1984
Ammonium (NH_4^+)	ISO 7150, 1 st edition, 1984
Phosphates (PO_4^{3-})	ISO 6878, 1 st edition, 1998
Sulfates (SO_4^{2-})	Rodier [50]
Total iron	ISO 6332, 1 st edition, August 1994
Sodium (Na^+) and Potassium (K^+)	ISO 9964, 3 rd edition, 1993
electrochemical method	
Conductivity	ISO 7888, May 1985
pH	ISO 1052-3-2008
turbidity measurements	ISO 7027-1-1999
Analysis by volumetric assay	
Chlorides (Cl^-)	ISO 9297 T90014, 1989
Calcium (Ca^{2+})	ISO 6058, 1 st edition, june 1984
Total Hardness (T.H.)	ISO 6059, 1 st edition, 1984
Complete Alkaline Titration (C.A.T.)	ISO 9963, 1 st February 1996

All spectrometric and volumetric measurements were performed according to the standard methods summarized in Table 2, with sulfate content determined spectrophotometrically using a calibration curve (solutions 0–7) and absorbance measured at 420 nm after addition of BaCl₂, following Rodier [50].

Bacteriological analysis

Bacteriological analyses were carried out in accordance with ISO 9308-1 and ISO 7899-2, by filtering 100 mL of El-Maatya water through a 0.45 µm membrane, followed by inoculation on Tergitol TTC agar for coliforms and *Escherichia coli*, and Slanetz and Bartley agar for *fecal streptococci*. Incubation was performed at 36 ± 2 °C for 21 ± 3 hours for *coliforms* and *E. coli*, and at 44 ± 4 hours for *intestinal enterococci*. Characteristic colonies were confirmed by subculturing on *Brilliant Green Bile Lactose (BGBL)* and tryptophan broths and BEA agar, in accordance with ISO 8199.

Urinary stone analysis

The monitoring of stones dissolution

In this method, we monitored the effect of the different media *ex-vivo* by following the variation in mass of natural stones from immersion to three weeks [33]. Calculi were collected from various patients suffering from urinary lithiasis, with weights ranging from 2 to 350 mg. Three media were chosen: El-Maatya water (M), sodium citrate (A) as a positive control and mineral water (I) as a negative control.

The urinary stones were placed in porous bags made of woven fiber, then in eight Erlenmeyer flasks containing 25 mL of different media.

Table 3 displays the urinary calculus contents and the corresponding media for each Erlenmeyer flask. The effectiveness of the various media is indicated by the percentage of dissolution [51], determined using the following formula :

$$a\% = \frac{w_{initial} - w_{final}}{w_{initial}} 100$$

Where a% is the dissolution rate of the urinary stone and $w_{initial}$ and w_{final} are the stone weights before and after incubation in the different solutions.

Table 3. Characteristics of each Erlenmeyer flask used with its corresponding contents: flask number, number of the urinary calculus, and volume of the medium.

Erlenmeyer N°	1	2	3	4	5	6	7	8
Medium	M	A	M	M	M	A	I	M
Stone N°	01	01	02	03	04-1	04-2	04-3	05
Volume (mL)	25	25	50	25	25	25	25	50

At each time interval, the stones were sampled, dried, and weighed to study mass loss. At the same time, pH values were measured by a pH meter in the liquid media.

Note: We analyzed calculus N°01 by infrared and UV spectroscopy only because the solubility test did not work (in our opinion, calculus N°1 was fixed by formalin (formaldehyde) for an anapathological study).

Solubility test

Given that the urinary calculi available to us are unique, we planned to take three small pieces of each calculus to test their dissolution in a 5 ml volume of three different media (El-Maatya water: M, mineral water as a negative control: I, and sodium citrate as a positive control: A).

Ultraviolet analysis

After one day of immersion, 0.2 mL was withdrawn from each medium containing the stones. The samples were diluted and transferred into a UV cell for chromophore analysis. The measurements were performed using a UV–Vis spectrophotometer (Unicam 300, England).

Infrared analysis

Seven pellets were prepared using a mixture of 98% KBr and 2% of the powdered stones (samples 1–5). The infrared spectra were recorded using a Fourier-transform infrared spectrophotometer (Shimadzu IR Affinity-NF, Japan) within the mid-infrared range of 4000–400 cm⁻¹.

Qualitative analysis of urinary calculi using an optical microscope

The study was carried out on small pieces of urinary calculi N° 2, 4, and 5 before and after treatment with M water, using an optical microscope (20X magnification). The microscope used is from the brand Optika.

Survey on the water from the el-maatya region (draa kebila commune) for the treatment of urinary and kidney stones

Responses were collected via Google Forms on this site: https://docs.google.com/forms/d/12QRw4E_QDOGQt-H88zs9LrVALaHzDKdGuCnIIHWIM1U/edit?usp=sharing, as well as by paper questionnaires asking people questions and ticking their answers.

The survey was carried out taking into account various criteria, such as *the gender of the participants, the taste of El-Maatya water, the region of origin, age, level of education, and the perceived effects of water*. These aspects made it possible to analyse the perceptions and uses of water within the population.

ACKNOWLEDGEMENTS

The authors would like to thank the Laboratoire Public de l'Algérienne des Eaux, Unité Sétif, for performing the physicochemical and microbiological analyses of the El-Maatya spring water. Their technical support and expertise contributed significantly to the quality of this research.

REFERENCES

1. R. W. Schrier; *The patient with kidney stones*. In: Schrier RW (ed) *Manual of Nephrology*, 7th ed.; Lippincott Williams & Wilkins, Philadelphia, **2009**, pp. 83–103
2. R. Manglik; *Kidney stones*. In: *EduGorilla Prep Experts* (ed) *Neuroendocrinology*; EduGorilla Publication, **2024**, pp 1333–1335
3. W. Khitri; N. Lachgueur; A. Tasfaout; A. Lardjam; A. Khalfa; *Rev. Ethnoécologie*, **2016**, 9.
4. A. L. O'Kell; D. C. Grant; S. R. Khan ; *Urolithiasis*, **2017**, 45(4), 329–336.
5. S. Ahmed; M. M. Hasan; H. Khan; Z. A. Mahmood; S. Patel; *Biomed. Pharmacother.*, **2018**, 107, 272–281.
6. L. Irsay; E. Bordinc; M. Borda; R. Ungur; V. Ciortea; I. Onac; *Balneo Res. J.*, **2014**, 5(1), 37–43
7. S. Doizi, J. Letendre, K. Bensalah, O. Traxer; *Prog. Urol.*, **2013**, 23(16), 1312–1317.
8. K. Bishop; T. Momah; J. Ricks; *Prim. Care*, **2020**, 47(4), 661–671.
9. R. Terkeltaub; *Clinical features of gout*. In: *Terkeltaub R (ed) Gout and Other Crystal Arthropathies*. Elsevier, Philadelphia, **2011**, pp. 110–119.
10. N. Ennaghra; Z. E. Boudjellab; *Afr. J. Biol. Sci.*, **2024**, 6(16), 1783–1795.
11. F. Di Silverio; A. R. D'Angelo; *Arch. Ital. Urol. Androl.*, **1994**, 66(5), 253–258.
12. A. Bertaccini; M. Borghesi ; *Arch. Ital. Urol. Androl.*, **2009**, 81(3), 192–194.
13. Y. F. Lobanov; A. Y. Zharikov; Y. F. Zverev; L. A. Strozenko; A. S. Kalnitsky; N. M. Mikheeva; *Med. Sovet.*, **2023**, 13, 238–244.
14. F. Bouhezila; T. Bouchene; K. Dellil; F. Z. Saadat; *1st Int. Semin. Biol. Physiol. Pathophysiol. (ISBPP)*, **2023**.

15. H.M. Djellouli; S. Taleb; D. Harrache-Chettouh; S. Djaroud; *Santé*, **2005**, 15(2), 109–112.
16. A. Amara-Rekkab; *Sci. J. King Faisal Univ. Basic Appl. Sci.*, **2023**, 24(2), 26–30
17. A. L. Rodgers; *Urol. Int.*, **1997**, 58(2), 93–99.
18. S. Lewandowski; A. L. Rodgers; *Clin. Chim. Acta.*, **2004**, 345(1–2), 17–34.
19. F. Abbassene; A. Maizia; N. Messaoudi; L. Bendahmane; H. Boukharouba; M. Daudon; A. Addou; *Tunis Med.*, **2020**, 98(5), 396–403.
20. F. Wu; J. Ma; J. Xue; X. Jiang; J. Liu; J. Zhang; Y. Xue; B. Liu; S. Qin; *Heliyon*, **2024**, 10(16), e36401.
21. N. Takahashi; Y. Ohtsuka; *Onsen Kenkyu*, **2004**, 67(2), 79–86.
22. Y. Nishida; *J. Jpn. Soc. Balneol Climatol Phys. Med.*, **1970**, 98–131.
23. A. Mousavi; R. Takele; B. Limbrick; K. N. Thaker; K. B. Scotland; *Soc. Int. Uro. J.*, **2024**, 5(4), 284–299.
24. O. Karagülle; U. Smorag; F. Candir; G. Gundermann; U. Jonas; A. J. Becker; A. Gehrke; C. Gutenbrunner; *World J. Urol.*, **2007**, 25, 315–323
25. E. Paul; P. Sasikumar; S. Gomathi; A. Abhishek; G. S. Selvam; Recombinant lactic acid bacteria secreting OxdC as a novel therapeutic tool for the prevention of kidney stone disease. In: Grumezescu AM (ed) Multifunctional systems for combined delivery, biosensing and diagnostics. Elsevier, Amsterdam, 2017, pp. 327–345.
26. S. J. M. Stoots; M. M. E.L. Henderickx; G. M. Kamphuis; *Cent. Eur. J. Urol.*, **2024**, 77, 494–506.
27. S.E. Avram; C. Mandiuc; I. Petean; L.B. Tudoran; G. Borodi; *Studia UBB Chemia.*, **2025**, 70(3), 35–53.
28. S.E. Avram; L.B. Tudoran; G. Borodi; I. Petean; *Water*, **2025**, 17, 2892.
29. K. Sekkoum; H. M. Djellouli; N. Belkboukhari; S. Taleb; A. Cheriti; *Ann. Sci. Technol.*, **2012**, 4(1), 1–8
30. Z. Djelloul; A. Djelloul; A. Bedjaoui; Z. Kaid-Omar; A. Attar; M. Daudon; A. Addou; *Prog. Urol.*, **2006**, 16(3), 328–335.
31. H. Haffar; A. Chetouani; *Rev. Agr. Acad.*, **2024**, 7(2), 106–126.
32. N. Benahmed; A. Cheriti; *Egypt. J. Chem.* **2025**, 1-13
33. B. Hannache; *La lithiase urinaire : épidémiologie, rôle des éléments traces et des plantes médicinales*. Dissertation, Université Paris Sud – Paris XI. **2014**, pp. 1-102
34. I. Djaafri; K. Seghir; V. Vallès; L. Barbiéro; *Earth*, **2024**, 5(2), 214–227.
35. S. Quattrini; B. Pampaloni; M. L. Brandi; *Clin. Cases Miner. Bone Metab.*, **2017**, 13(3), 173–180.
36. L. Liu; C. Lin; X. Li; Y. Cheng; R. Wang; C. Luo; X. Zhao; Z. Jiang; *Evid. Based Complement Alternat. Med.*, **2023**, 1-10
37. W. Weber; S. Kub; *Environ. Sci. Eur.*, **2022**, 34(1), 34-53.
38. H. Shi; Y. Du; Y. Xiong; Y. Deng; Q. Li; *Sci. Total Environ.*, **2024**, 173-283
39. A. Kumar; S. K. Singh; S. K. Meena; S. K. Sinha; L. Rana; *Int. J. Environ. Clim. Change*, **2024**, 14(3), 17–31.

40. Y. Sailaukhanuly; S. Azat; M. Kunarbekova; A. D. Tovassarov; K. Toshtay; Z. T. Tauanov; L. Carlsen; R. Berndtsson; *Int. J. Environ. Res. Public Health*, **2023**, 21(1), 2101-0055
41. Guidelines for drinking-water quality: 4th edition incorporating the first and second addenda [Internet]. Geneva: World Health Organization; 2022.
42. M. Alsinnawi; Z. Maan; G. Rix; *J. Clin. Urol.*, **2016**, 9, 268–273.
43. B. Afsar; M. C. Kiremit; A. A. Sag; K. Tarim; O. Acar; T. Esen; Y. Solak; A. Covic; M. Kanbay; *Eur. J. Intern. Med.*, **2016**, 35, 16–24.
44. T. J. Lin; K. T. Yen; C. F. Chen; S. T. Yan; K. W. Su; Y. L. Chiang; *Sensors (Basel)*, **2022**, 22(8), 2208-3009
45. K. H. Ko; Y. Kim; H. M. Park; Y. H. Cha; T. S. Kim; L. Lee; G. Lim; J. Han; K. H. Ko; D. Y. Jeong; *Appl. Phys. B*, **2015**, 120(2), 233–238.
46. A. Mujahid; A. I. Khan; A. Afzal; T. Hussain; M. H. Raza; A. T. Shah; W. U. Zaman; *Appl. Nanosci.*, **2015**, 5, 527–534.
47. K. Sekkoum; A. Cheriti; S. Taleb; N. Belboukhari; *Arab. J. Chem.*, **2016**, 9(3),330–334.
48. V. Asyana; F. Haryanto; L. Fitri; T. Ridwan; F. Anwary; H. Soekersi; *J. Phys. Conf. Ser.*, **2016**, 694,012-051.
49. R. M. Silverstein RM; G. C. Bassler; *J. Chem. Educ.*, **1962**, 39(11), 546.
50. J. Rodier, Analyse de l'eau.: 8th ed.,Paris, **1996** ; P214
51. F. Meiouet; S. El Kabbaj; M. Daudon; *Prog. Urol.*, **2011**, 21(1), 40–47.

EXPERIMENTAL DESIGN-BASED OPTIMIZATION APPROACHES IN UPLC METHOD DEVELOPMENT: SIMULTANEOUS QUANTITATIVE ESTIMATION OF SULFADIAZINE AND TRIMETHOPRIM IN A COMBINED VETERINARY FORMULATION

Zehra Ceren ERTEKİN^a, Erdal DİNÇ^{a,*}

ABSTRACT. This study reports a comparative application of three different experimental designs to develop ultra-performance liquid chromatography (UPLC) methods for simultaneous quantification of sulfadiazine and trimethoprim in veterinary tablets. The effects of column temperature, buffer ratio, and flow rate on chromatographic response were systematically evaluated by response surface methodology using full factorial design (FFD), Box–Behnken design (BBD), and central composite design (CCD). Full quadratic models were constructed and evaluated for each design, using statistical parameters and studying the response surface plots. Then, optimal conditions providing efficient peak resolution in shortest runtime were calculated, and experimentally confirmed. FFD and BBD produced nearly identical optimal conditions, while CCD yielded conditions with shorter run time and sufficient resolution. The optimal conditions were determined from two experimental design methods: the first set from FFD and BBD (collectively referred to as FFD/BBD-UPLC), and the second set from CCD (referred to as CCD-UPLC). Both sets of conditions underwent system suitability tests and were validated for linearity, limits of detection and quantification, precision, accuracy, and specificity. Recoveries for sulfadiazine and trimethoprim were within 99.3–100.5% with relative standard deviations less than 1.8%. The developed methods were successfully applied to commercial veterinary tablet analysis, with statistically comparable assay results in accordance with the label claims for both drugs.

Keywords: UPLC, optimization, experimental design, sulfadiazine, trimethoprim, pharmaceutical analysis

^a Ankara University, Faculty of Pharmacy, Department of Analytical Chemistry, Emniyet Mah. Dogol Cd. 06560, Yenimahalle, Ankara, Türkiye

* Corresponding author: dinc@ankara.edu.tr



INTRODUCTION

Veterinary drug formulations, especially those intended for food-producing animals, play a critical role in ensuring both animal health and food safety. These formulations must demonstrate the intended therapeutic efficacy and comply with regulatory requirements to minimize the risk of drug residues in animal-derived food products and to help control the development of antimicrobial resistance [1]. Fixed-dose combinations, such as sulfadiazine (SDZ) and trimethoprim (TMP), are commonly used in veterinary medicine due to their synergistic antibacterial effects. SDZ and TMP inhibit sequential steps in bacterial folate synthesis, resulting in selective and enhanced and selective bactericidal activity, reduced resistance development, and broad antimicrobial coverage [2].

Literature survey reveals that the simultaneous determination of SDZ and TMP in pharmaceutical preparations has been carried out by chemometrics-assisted spectrophotometric methods [3-5] thin-layer chromatography [6], capillary zone electrophoresis [7, 8] and HPLC [9, 10]. The development of fast, feasible, accurate, and reproducible analytical methods that serve as alternatives to existing ones have always been important for pharmaceutical industry, for both human and veterinary drugs. Ultra-performance liquid chromatography (UPLC) offers a modern, high-efficiency alternative to HPLC with reduced run times and improved resolution, making it highly suitable for simultaneous analysis of combination drugs. However, the full benefits of UPLC can only be realized when chromatographic conditions are carefully optimized.

Optimization in analytical chemistry, particularly in chromatographic method development, is critical to achieve selectivity, sensitivity, feasibility, and efficiency. Traditional one-variable-at-a-time optimization is labor-intensive and often fail to detect interactions between variables. Response surface methodology (RSM) has emerged as a rational, statistically robust strategy for optimization in many fields including pharmaceuticals, engineering, and food sciences. RSM is based on fitting a polynomial equation to experimental data using mathematical and statistical techniques. It enables simultaneous evaluation of multiple experimental factors, the construction of predictive models, and the determination of optimal factor levels to achieve the best system performance [11, 12].

In response surface methodology, it is necessary to select an experimental design that defines which experiments will be conducted. Experimental designs for first-order models are typically used for screening purposes or when curvature is not expected in the response surface [13]. However, in order to model the interaction of factors, curvatures, and critical

response points such as maxima or minima, experimental designs with at least three levels are required. Such designs are able to fit full quadratic models which allow to predict the optimal levels of experimental factors that yield the best response [11, 14]. The choice of experimental design directly influences the number of required experiments, the quality of the fitted model, and the accuracy of the predicted optimum. Among the most commonly employed RSM designs are full factorial design (FFD), Box–Behnken design (BBD), and central composite design (CCD). FFD is a cubic design which includes all possible combinations of factor levels. It enables detailed exploration of all factor interactions but becomes resource-intensive with increasing number of factors. BBD is more economical, requiring fewer runs and avoiding extreme factor levels, making it preferable when the corner points in the design space may be operationally difficult. CCD includes axial points, which may introduce challenges under extreme experimental conditions but offers superior predictive capabilities and greater flexibility in exploring the design space [15, 16].

While each of these designs has theoretical and statistical advantages, comparative studies evaluating their practical outcomes in chromatographic optimization remain limited. Such comparisons are valuable for guiding method developers in selecting the most appropriate design based on analytical performance, resource demands, and optimization success.

This study aimed to compare FFD, BBD, and CCD designs for optimizing a UPLC method for the simultaneous quantification of SDZ and TMP in veterinary tablet formulations. As it is important have an efficient resolution in a short analysis time in pharmaceutical chromatographic analyses, a chromatographic response function that ensures sufficient resolution between peaks, narrow peak width and short analysis time was used as response. Using this response as the optimization criterion, each design was assessed for its ability to produce efficient, fast, and high-resolution chromatographic conditions. The optimal conditions obtained from each design were validated and compared in terms of analytical performance and practical suitability for the quantitative determination of SDZ and TMP in veterinary tablet samples.

RESULTS AND DISCUSSION

Response surface methodology offers a powerful alternative to conventional one-variable-at-a-time optimization in various fields including science, technology, and industry. It involves several critical decisions that collectively influence the quality and the performance of a predictive model that would be used for a defined purpose. The key steps include (1) selecting

relevant factors and their levels, ensuring they cover the experimental space of interest; (2) identifying measurable responses that align with the optimization objectives; (3) choosing an appropriate experimental design and carrying out the experiments; (4) employing a suitable fitting technique (e.g., linear regression, polynomial models, or machine learning algorithms) to model the system's behavior; and (5) applying an optimization strategy (such as grid-search, derivative functions, or gradient-based methods). Each step impacts the model's accuracy, interpretability, generalizability, and predictive performance, which overall affect the outcome as the optimal conditions and the optimal response [11].

The focus of this work was the third step, selecting the optimal design for response surface methodology. Quadratic models, which are needed to find an optimum response of a system, can be estimated using full factorial designs with three or more levels for each factor, but these designs require a high number of runs. More efficient designs, such as CCD and BBD, are generally preferred due to the reduced number of runs. The choice of design depends on desired precision, the nature of the design space, and experimental constraints such as the number of experiments and available resources, often the most critical consideration. BBD is preferred if fewer runs are needed and avoiding extreme points is desirable [17, 18]. On the other hand, CCD is the most widely used design because it has better predictive power and can be a good choice after a factorial screening design when converting the screening phase into an RSM by adding central and axial points into the design [19, 20]. In this work, we compared the most common RSM designs to evaluate their practical performance to choose the best set of experimental conditions for optimal response. Throughout the all RSM procedure a chromatographic response function developed by Rakić et al. [21] was used as the dependent variable. This function abbreviated as CRF is calculated by measuring various parameters such as retention times, peak widths, height of the peaks, height of the valleys (in case of overlapping peaks), and elution time. It typically decreases with narrow peak widths, shorter analysis time, and sufficient resolution between the peaks. Therefore, the optimal chromatographic settings are characterized by the lowest CRF values. Previous works indicated CRF was a suitable response for UPLC method development, achieving efficient chromatographic separation in a short run time [22-25].

Development of Chromatographic Method by Experimental Design

In this work, some preliminary experiments were conducted instead of a factorial screening step because most UPLC factors affecting the chromatographic response were predictable from our experience with UPLC

analyses. Categorical factors such as column type and mobile phase composition (organic solvent and buffer type) were determined prior to the experimental design process. A mixture of HCOOH-HCOONa buffer and methanol was found suitable on the C18 column to observe significant shifts in the retention times of both drugs with the variations in the ratio of methanol and buffer. Potential factors, namely, concentration, pH and ratio of the buffer in mobile phase, column temperature, and flow rate were tested to observe if they have an apparent effect on the retention times. A change in the concentration of the buffer (from 20 mM to 100 mM) did not affect the elution times, and 20 mM was chosen to reduce the possibility of salt precipitation. The pH of the buffer did not change the retention times of the drugs; however, pH 4.4 had a significantly lower solvent peak. Hence, the pH of the buffer was excluded as a factor from the design, and 20 mM pH 4.4 sodium formate buffer was used during the remaining experiments. Column temperature, buffer ratio, and flow rate were selected as factors x_1 , x_2 , and x_3 , respectively, as they showed observable changes in chromatographic behavior.

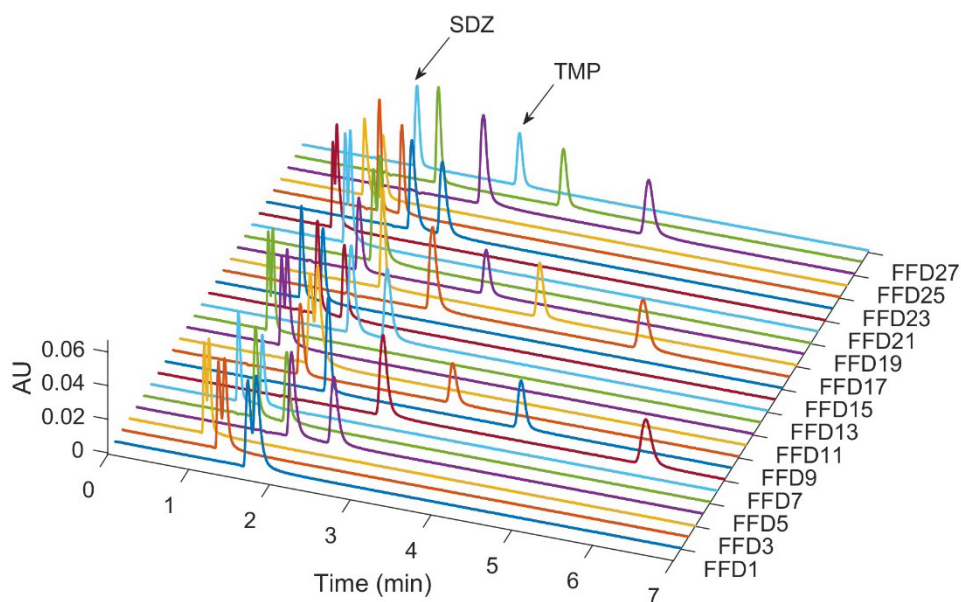
A common design space was needed to compare FFD, BBD, and CCD so we aimed to use standardized factor levels (-1, 0, +1) across all three designs. The levels of factors for FFD, BBD, and CCD were systematically determined based on preliminary screening work and critical instrumental constraints such as UPLC backpressure and run time, ensuring the experimental design covered the widest possible chromatographic design space. The objective was to define a range where the chromatographic behavior of the peaks spanned from maximum separation with the constraint of a maximum 7-minute run time to minimal separation, which is near-complete overlapping of the peaks. Specifically, a low column temperature (30 °C), high buffer ratio (78.0 %) and low flow rate (0.16 mL/min) was defined as the maximum separation conditions. The maximum overlap conditions were defined as high column temperature (50 °C), low buffer ratio (52.0 %) and high flow rate (0.28 mL/min). These values were considered as -1 and +1 factor levels, and central point of the values were defined as 0 level, as listed in Table 1. The value of the axial point was calculated using the formula $\alpha = 2^{k/4} = 2^{3/4} \approx 1.682$ to obtain a rotatable CCD. Table 1 depicts the factor levels used in all three designs.

Design matrices of FFD, BBD and CCD were generated according to the factor levels in Table 1, and they are provided in [supplementary material](#). The number of experiments were calculated using the formulas 3^k for FFD, $2k \times (k - 1) + 1 + n_0$ for BBD and $2^k + (2k + 1) + n_0$ for CCD, where k is the number of factors and n_0 is the number of replicate in the center point (0, 0, 0), which was 3 and 5 for BBD and CCD, respectively. In the end, three different design matrices containing 27, 15, and 20 experimental runs were generated for FFD, BBD, and CCD, respectively.

Table 1. Factors and their corresponding levels used in FFD, BBD, and CCD

	x_1	x_2	x_3
Level	Column temp (°C)	Buffer (%)	Flow rate (mL/min)
$-\alpha$	23.2	43.1	0.12
-1	30.0	52.0	0.16
0	40.0	65.0	0.22
$+1$	50.0	78.0	0.28
$+\alpha$	56.8	86.9	0.32

All experimental runs in three different design matrices were performed by injecting a standard solution of 20 µg/mL SDZ and 20 µg/mL TMP, by detection at 245 nm. Figure 1 illustrates the chromatograms from 27 runs required by the FFD. Figure 2 and 3, depict the chromatograms recorded during the application of BBD and CCD, respectively. Data from these chromatograms were used to calculate the CRF response for each run. Table S1, Table S2, and Table S3 in the supplementary material list the experimentally measured responses at each run.

**Figure 1.** Illustration of 27 chromatograms obtained from FFD design matrix

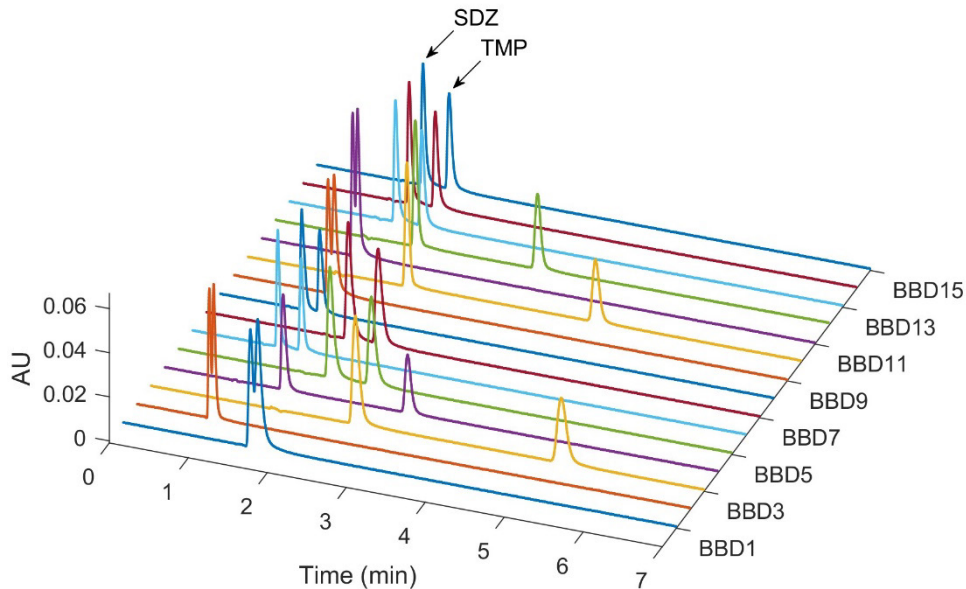


Figure 2. Illustration of 15 chromatograms obtained from BBD design matrix

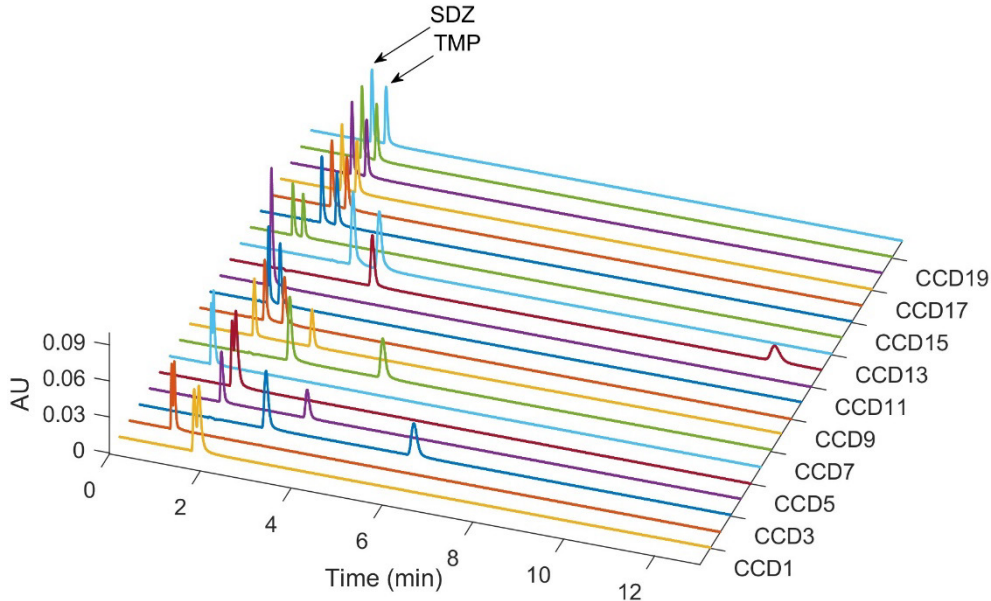


Figure 3. Illustration of 20 chromatograms obtained from CCD design matrix

For each design, a full quadratic model containing three variables (x_1 , x_2 , x_3), their squared terms and the binary interactions was constructed to the experimental data using least squares regression. A representative model is given as

$$\hat{y} = \beta_0 + \beta_1 x_1 + \beta_2 x_2 + \beta_3 x_3 + \beta_{11} x_1^2 + \beta_{22} x_2^2 + \beta_{33} x_3^2 + \beta_{12} x_1 x_2 + \beta_{13} x_1 x_3 + \beta_{23} x_2 x_3$$

where x_1 , x_2 , and x_3 represent the variables, β_0 is the intercept, β_1 , β_2 , and β_3 are the linear terms, β_{11} , β_{22} , and β_{33} are the quadratic terms, β_{12} , β_{13} , and β_{23} are the interaction terms.

Table 2 presents the estimated coefficients (β), t-test statistics, and p-values for three quadratic regression models corresponding to FFD, BBD, and CCD, highlighting the statistical significance of linear, quadratic, and interaction effects ($p < 0.05$).

Table 2. Estimated coefficients, t-test statistics, and p-values for three quadratic regression models obtained from FFD, BBD and CCD

term	FFD		BBD		CCD	
	estimate	p-value	estimate	p-value	estimate	p-value
β_0	2.394	1.94×10^{-38}	2.457	2.10×10^{-13}	2.183	2.29×10^{-29}
β_1	0.028	1.74×10^{-11}	0.028	8.83×10^{-05}	0.098	1.18×10^{-17}
β_2	-0.753	1.39×10^{-35}	-0.694	1.01×10^{-11}	-1.705	4.48×10^{-30}
β_3	-0.230	7.73×10^{-27}	-0.244	1.88×10^{-09}	-0.402	8.41×10^{-24}
β_{11}	-0.013	7.44×10^{-4}	-0.073	5.46×10^{-06}	0.058	1.54×10^{-15}
β_{22}	0.914	5.8×10^{-33}	0.829	2.87×10^{-11}	2.125	3.77×10^{-31}
β_{33}	0.161	3.73×10^{-20}	0.148	1.59×10^{-07}	0.148	1.36×10^{-19}
β_{12}	-0.094	9.05×10^{-19}	0.010	3.78×10^{-02}	-0.374	2.52×10^{-22}
β_{13}	0.006	1.12×10^{-2}	0.022	1.35×10^{-03}	0.003	6.55×10^{-3}
β_{23}	0.080	1.55×10^{-17}	0.144	1.47×10^{-07}	0.069	5.69×10^{-15}

The quadratic models detailed in Table 2 were used to plot the response surface and contour plots. These figures illustrate the interaction of each pair of selected factors, enabling the visualization of their combined effects on CRF in two dimensions within the design space. As there are three pairs in each model, three plots were generated for each design, namely FFD, BBD, and CCD, presented in Figure S1, Figure S2, and Figure S3,

respectively in [supplementary material](#). The response surfaces of the same factor pair obtained by different designs have similar features, but the greater design space of CCD reveals more curvatures. One may utilize these plots to choose an acceptable region of factor levels that would result in a desirable response. However, it is also possible to predict the optimal levels of factors that would result in the best possible response by using the models. Indeed, in this work, the optimal levels of variables minimizing the CRF were computed using the models given in Table 2. Table 3 summarizes the optimal values for each factor, using the models obtained by FFD, BBD, and CCD. As can be seen in this table, the values obtained by FFD and BBD are very similar—or even identical. In order to compare the optimal conditions obtained by different designs, a mixture of SDZ and TMP was injected into the UPLC system with 10 replications using the conditions given in Table 3. A representative chromatogram from each condition is presented in Figure 4. When these chromatograms are examined, there is almost no difference between FFD and BBD in terms of resolution, peak width and analysis time. However, the optimal conditions determined using CCD resulted in a shorter analysis time with a slightly lower but still sufficient resolution.

Table 3. The optimal chromatographic conditions obtained by FFD, BBD, and CCD

	Factor	FFD	BBD	CCD
x_1	Column temperature (°C)	38.5	39.3	44.9
x_2	Buffer (%)	69.9	69.7	70.5
x_3	Flow rate (mL/min)	0.26	0.26	0.30

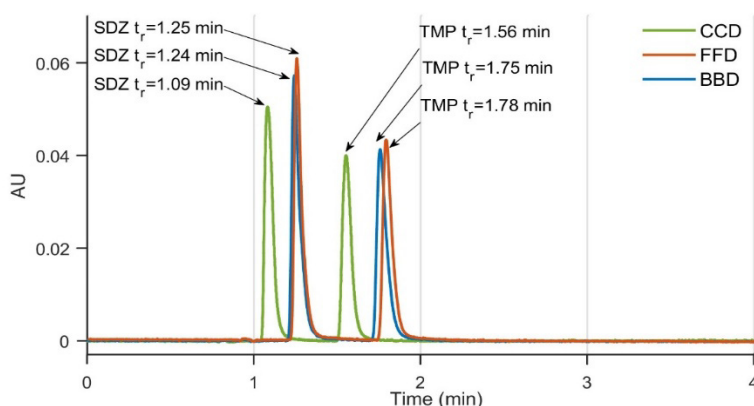


Figure 4. Chromatograms obtained with optimal conditions calculated from FFD, BBD and CCD.

In order to perform a more rational comparison of optimal conditions obtained by different designs, CRF values calculated from ten chromatograms were compared statistically. Statistical comparison of CRF values obtained from FFD design versus BBD and CCD design was performed using F-test and Student's t-test. As presented in supplementary material Table S4, the average CRF values obtained by FFD, BBD and CCD were calculated as 2.4142, 2.4282 and 2.0314, respectively.

The difference between CRF values obtained by FFD and BBD was not statistically significant at a significance level of 0.05, which is also observed visually Figure 4. FFD and BBD cover the same design space, but unlike BBD, FFD includes the corner points. It is evident that BBD has more statistical efficiency compared to other designs, meaning it requires fewer experiments and has the same exploratory power. Hence, it was concluded that BBD might be a better choice than FFD for optimization purposes.

However, CRF values obtained by CCD were found to be statistically different from FFD ($p=0.05$). The smaller response obtained by CCD indicated that using CCD enabled reaching a smaller CRF value; hence, it outperformed FFD and BBD, possibly due to the greater design space. Indeed, the optimal flow rate predicted by CCD was 0.30 mL/min, which was out of the range of factor levels of FFD and BBD.

FFD provided a comprehensive evaluation of the system, but require a high number of experimental runs (27), making it the least efficient option for complex optimizations. BBD was the most statistically efficient design in the range of -1 and +1 design space. It required significantly fewer runs (15) than FFD while yielding a statistically similar optimal CRF value (2.4282 vs. 2.4142), demonstrating equal modeling power within the factor cube. However, BBD is limited by its inability to explore the corners of the design space. In contrast, the CCD, despite requiring more runs (20) than BBD, offered the superior optimal solution, by covering a greater design space using the axial points. This expanded range allowed the model to predict an optimal flow rate (0.30 mL/min) outside the -1 and +1 limits, which resulted in a statistically lower CRF value (2.0314). Consequently, the CCD was the most effective method for this specific optimization, as its broader domain allowed it to locate a more favorable true minimum for the response surface.

The implementation of experimental design-based optimization of chromatographic methods aligns strongly with the principles of green analytical chemistry [26]. This approach serves as an efficient tool to reduce the environmental impact of analytical method development by conserving energy, reducing solvent consumption, and decreasing the number of experimental trials. Statistical experimental designs such as FFD, BBD, and CCD help to find the real optimal conditions by maximizing the information gained with a

pre-defined number of experiments, as opposed to the classical one variable at a time approach [27]. Reducing the number of experimental trials results in a significant reduction in solvent and reagent consumption, aligning with green chemistry's principle of waste prevention, thereby reducing hazards to both the environment and human health. Furthermore, the final optimal conditions predicted by RSM, such as the shortest analysis time obtained by CCD design in this work, would minimize solvent and energy consumption during the routine application of the UPLC method.

We also aimed to compare the analytical performance of each optimal condition for the simultaneous quantification of SDZ and TMP in commercial samples. Since the chromatographic conditions obtained using FFD and BBD designs were not significantly different, the average of the optimal conditions derived from these two designs was employed for the quantitative analysis of SDZ and TMP. This chromatographic method, with a column temperature of 38.9 °C, 69.8 % buffer, and a 0.26 mL/min flow rate, was called the FFD/BBD-UPLC method and resulted in retention times of 1.24 min and 1.77 min for SDZ and TMP, respectively. In contrast, the chromatographic conditions obtained from the CCD design differed from those of the other two designs. To enable comparison of analytical results, a second UPLC method using these CCD-derived conditions with a column temperature of 44.9 °C, 70.5 % buffer and 0.30 mL/min flow rate was referred to as the CCD-UPLC method, with retention times of 1.07 and 1.54 for SDZ and TMP, respectively.

Application of Optimized Methods for the Quantitative Analysis

Two different UPLC methods were developed using different designs by RSM approach, aimed for implementation in the quantitative analysis of SDZ and TMP in veterinary tablet samples. For this aim, the calibration set of analytes were prepared as explained in Section "Preparation of Standard Solutions", and were injected into the UPLC system using two different methods, FFD/BBD-UPLC and CCD-UPLC. Calibration and prediction steps were performed at the detection wavelength of 267 nm and 230 nm for SDZ and TMP, respectively. The chromatograms of the calibration set recorded at 267 and 230 nm by the application of FFD/BBD-UPLC method are illustrated in Figure 5(I)a and Figure 5 (I)b, respectively. Figure 5 (II)a and Figure 5 (II)b depict the chromatograms of the calibration set detected at 267 and 230 nm, respectively.

The peak areas of SDZ and TMP were calculated from the UPLC chromatograms recorded at 267 nm for SDZ and 230 nm for TMP, for both UPLC methods (See Figure 5). The linear regression between the peak area

and concentration for each substance was modelled using the least squares approach. Detection wavelengths, linear ranges and statistical data of regression analysis were summarized in Table 4. As can be seen here, the statistical parameters of FFD/BBD-UPLC and CCD-UPLC methods were similar. The determination of SDZ and TMP in both validation and commercial tablet samples was performed using the linear regression equations shown in Table 4.

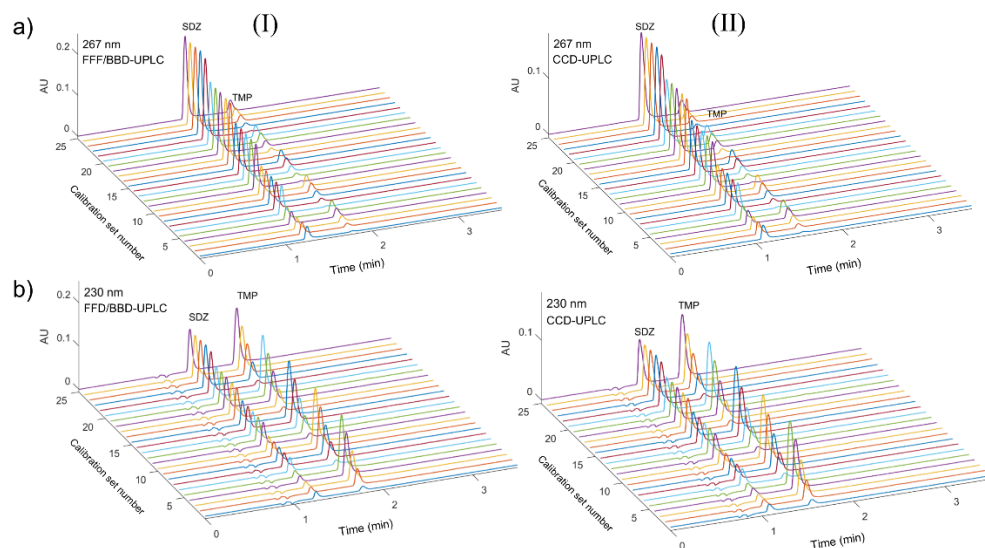


Figure 5. Chromatograms of the calibration set recorded at **a)** 267 nm for the determination of SDZ and **b)** 230 nm for the determination of TMP, obtained by the application of **(I)** FFD/BBD-UPLC and **(II)** CCD-UPLC methods

Table 4. Regression analysis results of SDZ and TMP during the application of FFD/BBD-UPLC and CCD-UPLC methods

	FFD/BBD-UPLC		CCD-UPLC	
	SDZ	TMP	SDZ	TMP
Detection wavelength (nm)	267	230	267	230
Linear range ($\mu\text{g/mL}$)	6-38	2-26	6-38	2-26
Slope	2.847	3.111	2.495	2.748
Intercept	-1.151	0.473	-1.016	0.269
Correlation coefficient	0.9992	0.9997	0.9991	0.9998
Standard error of slope	0.024	0.016	0.022	0.012
Standard error of intercept	0.604	0.259	0.539	0.204
Standard error of correlation coefficient	1.382	0.672	1.233	0.528
Limit of detection ($\mu\text{g/mL}$)	0.70	0.28	0.71	0.24
Limit of quantitation ($\mu\text{g/mL}$)	2.12	0.83	2.16	0.74

Validation of the optimized methods

Prior to analytical validation experiments, system suitability tests were carried out to evaluate the suitability and effectiveness of the optimized chromatographic methods. A standard solution containing 20 µg/mL SDZ and 20 µg/mL TMP was injected 10 times into UPLC and system suitability parameters were calculated using the Waters Empower2 software. The average values of these parameters, reported in Table 5, were found to be suitable for continuing the validation procedures.

Table 4. Regression analysis results of SDZ and TMP during the application of FFD/BBD-UPLC and CCD-UPLC methods

	FFD/BBD-UPLC		CCD-UPLC		Recommended
	SDZ	TMP	SDZ	TMP	
Retention time (min)	1.24	1.77	1.07	1.54	
Capacity factor (k')	1.07	1.95	1.15	2.08	k' > 1
Resolution (R)	-	6.13	-	4.67	R > 2
Tailing factor (T)	1.58	1.45	1.64	1.46	T < 2
Theoretical plate number (N)	4140	5598	2480	4111	N > 2000
RSD of retention time	0.11	0.10	0.19	0.13	RSD < 1
RSD of peak area	0.89	1.15	0.97	1.17	RSD < 1

RSD: relative standard deviation

For both FFD/BBD-UPLC and CCD-UPLC methods, linearity and high correlation coefficients were reported in the working concentration ranges of SDZ and TMP. Limit of detection and limit of quantification values were calculated using the standard deviation of the intercept and slope values of calibration equations, given in Table 4. As can be seen in Table 4, the values for both drugs obtained from the FFD/BBD-UPLC and CCD-UPLC methods were very similar, all compatible with the working ranges and serving the intended purpose of the methods.

The accuracy and precision of the optimized UPLC methods were evaluated by recovery studies of binary synthetic mixtures. A test set of 11 binary mixtures was analyzed by FFD/BBD-UPLC and CCD-UPLC methods, and their analysis results were reported in Table S5 in [supplementary material](#). The mean and standard deviation values of SDZ recoveries were reported to be 100.16% with 1.31 using FFD/BBD-UPLC method and 100.54% with 1.06 using CCD-UPLC method. On the other hand, mean

recovery with standard deviation values of TMP were reported to be 99.30% with 1.79 and 100.36% with 1.74 using FFD/BBD-UPLC and CCD-UPLC methods, respectively.

Another approach to assess accuracy and precision was the application of FFD/BBD-UPLC and CCD-UPLC methods to the analysis of inter-day and intra-day samples. Standard mixture solutions at three concentration levels (80%, 100%, and 120% of test level) were analyzed three times on the same day and on three consecutive days. The analysis results, along with recovery, standard deviation, relative standard deviation and relative standard error values are listed in Table S6 in [supplementary material](#). These results indicated that the optimized UPLC methods gave accurate and precise results with good reproducibility.

Specificity/selectivity of the optimized methods was evaluated by the standard addition technique. The standard addition samples, which were prepared in triplicate as described in section “Preparation of Standard Solutions”, were analyzed by FFD/BBD-UPLC and CCD-UPLC methods. The added recover and relative standard deviation were calculated as shown in Table 6.

Table 6. Analysis results of standard addition samples by the application of FFD/BBD-UPLC and CCD-UPLC techniques

		Added		Found		Recovery (%)		RSD	
		SDZ	TMP	SDZ	TMP	SDZ	TMP	SDZ	TMP
FFD/ BBD- UPLC	Tablet +	10	5	10.09	4.94	101.0	98.8	0.19	0.19
	Tablet +	15	12	14.98	12.06	99.9	100.5	0.06	0.20
	Tablet +	20	19	20.25	19.21	101.2	101.1	0.05	0.18
CCD- UPLC	Tablet +	10	5	10.15	4.99	101.5	99.7	0.30	0.16
	Tablet +	15	12	14.81	11.93	98.7	99.4	0.12	0.03
	Tablet +	20	19	20.27	19.46	101.3	102.4	0.10	0.16

RSD: Relative standard deviation

Overall, both UPLC methods, optimized using distinct experimental designs, demonstrated comparable and acceptable analytical performance across all validation parameters.

Analysis of commercial tablet samples by the optimized methods

Following the validation procedures, FFD/BBD-UPLC and CCD-UPLC methods were applied for the quantitative estimation of SDZ and TMP in commercial tablet samples. The tablet solutions mentioned in “2.4. Preparation of Commercial Sample Set” were injected into UPLC instruments under the optimized conditions of FFD/BBD-UPLC and CCD-UPLC methods. The stacked chromatograms of the commercial sample set obtained by the FFD/BBD-UPLC method are shown in Figure 6(I)a (267 nm) and Figure 6(I)b (230 nm). Figure 6(II)a and Figure 6(II)b depict the chromatograms of the commercial samples set obtained by the application of CCD-UPLC method for determination of SDZ at 267 nm and for TMP at 230 nm.

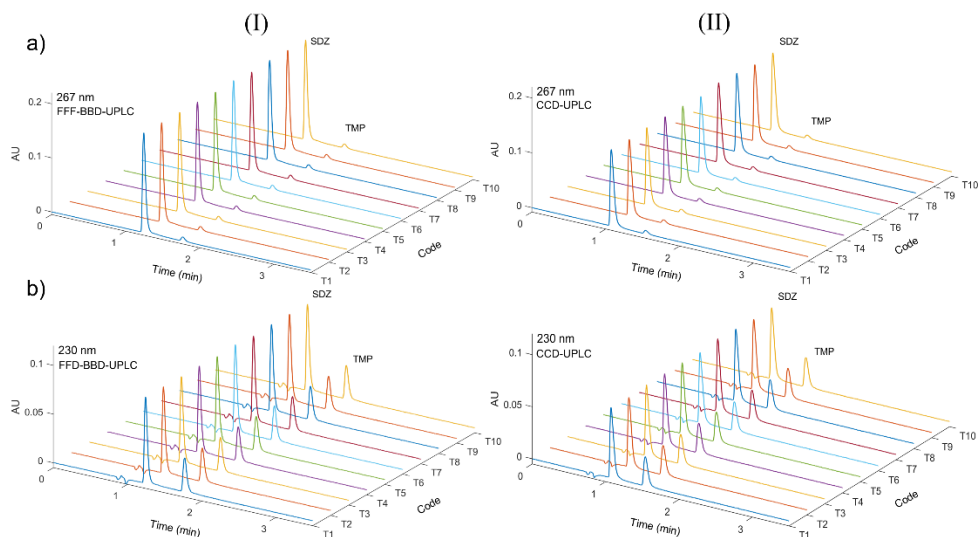


Figure 6. Chromatograms of the commercial sample set recorded at **a)** 267 nm for the assay of SDZ and **b)** 230 nm for the assay of TMP, obtained by the application of **(I)** FFD/BBD-UPLC and **(II)** CCD-UPLC methods

The peak areas in these chromatograms and calibration equations given in Table 4 were used to calculate the concentration of SDZ and TMP in the commercial sample set. Corresponding amounts of SDZ and TMP per tablet were computed as listed in Table 7. The average assay results were 997.60 mg/tablet and 1002.38 mg/tablet for SDZ, and 197.46 mg/tablet and 197.76 mg/tablet for TMP, both in accordance with the manufacturer's declaration. Relative standard deviation and relative error values were

smaller than 2% for both drugs using the optimized methods. The assay results from two different methods were statistically compared using F-test and Student's t-test, each applied at a significance level of 0.05, and were found to be comparable. Both UPLC methods successfully achieved accurate and reliable determination of SDZ and TMP in tablets for veterinary use.

Table 7. Assay results of commercial tablet samples obtained by FFD/BBD-UPLC and CCD-UPLC.

Code	FFD/BBD-UPLC		CCD-UPLC	
	SDZ (mg/tablet)	TMP (mg/tablet)	SDZ (mg/tablet)	TMP (mg/tablet)
T1	993.1	198.0	1000.7	201.1
T2	1013.1	196.3	986.5	193.5
T3	988.6	192.5	998.9	195.0
T4	988.1	200.4	1012.5	201.1
T5	992.9	200.2	1002.6	201.7
T6	986.5	201.5	991.4	193.3
T7	1010.4	192.4	1018.5	194.7
T8	1002.8	196.0	1015.9	201.2
T9	994.3	200.4	998.5	201.5
T10	1006.2	196.8	998.4	194.5
Mean	997.6	197.5	1002.4	197.8
SD	9.74	3.27	10.34	3.80
RSD	0.98	1.65	1.03	1.92
SE	3.08	1.03	3.27	1.20
RE	-0.24	-1.27	0.24	-1.12
CI	991.6-1003.6	195.4-199.5	996.0-1008.8	195.4-200.1
F-test	1.13	1.35	F-tabulated: 3.18	
t-test	1.11	0.25	t-tabulated: 2.26	

Label claim: SDZ:1000 mg/tablet, TMP: 200 mg/tablet

SD: Standard deviation

RSD: Relative standard deviation

SE: Standard error

RE: Relative error

CI: confidence interval (p=0.05)

CONCLUSIONS

This study explores the selection of experimental design matrices (FFD, BBD, and CCD) during response surface methodology to optimize UPLC conditions for the simultaneous quantification of sulfadiazine and trimethoprim in commercial tablets for veterinary use. The comparative performance of FFD, BBD, and CCD for UPLC optimization was studied with standardized factor levels. All designs provided successful models with significant effects on the response, and optimal conditions provided satisfactory outcomes for efficient and fast chromatographic analysis. CCD performed better factor exploration, possibly due to broader design space with the inclusion of axial points, resulting in chromatographic conditions with shorter analysis time while maintaining desirable resolution between the peaks. Application of FFD and BBD gave rise to very similar, if not the same, optimal conditions, confirming the efficiency of BBD for UPLC optimization. These results indicate CCD may be preferred for UPLC optimization when the resources permit, while BBD is a viable alternative for constrained settings. As three different designs resulted in two different optimal chromatographic conditions, each were validated and applied to quantitative analysis of SDZ and TMP in tablets. They showed good analytical performance during the validation studies, and achieved assay results that were statistically comparable and consistent with the labeled content. The optimized UPLC methods were found suitable for quality control of SDZ and TMP in veterinary tablet formulations and may be extended to other drug combinations with similar challenges.

EXPERIMENTAL SECTION

Chemical and reagents

Sulfadiazine (99.35 %) and trimethoprim (99.55 %) standard materials were purchased from Alfa Aesar (USA). Gradient grade methanol was procured from Sigma-Aldrich, (USA), and ultrapure water was obtained from a Milli-Q water purification system (Millipore, USA). Formic acid (98%-100%, d=1.22g/mL) and NaOH (≥98%) were of ACS reagent grade and were supplied by Sigma-Aldrich (USA) and Riedel-de Haën (Germany), respectively. Biotrin Tablet, containing 1000 mg sulfadiazine and 200 mg trimethoprim per tablet, was produced by Ceva Animal Health Inc. and was procured from a veterinary clinic in Ankara, Türkiye.

Instrumentation, Chromatographic Conditions, and Software

Chromatographic studies were performed using an ACQUITY UPLC H-Class system (Waters, USA) equipped with a quaternary pump, a cooling autosampler, a temperature-controlled column compartment with pre-heater, and a photodiode array detector. All chromatographic work was carried out on a Waters UPLC BEH C₁₈ 100 mm (130Å, 1.7 µm, 2.1 mm) column.

The temperature of the autosampler was maintained at 15 °C, the solvent of injected samples was a mixture of methanol and water (50:50, v/v). Detection of sulfadiazine and trimethoprim was performed at 267 nm and 230 nm, respectively, with an injection volume of 1 µL. Different ratios of methanol and sodium formate buffer were used as mobile phase during the experimental design and optimization steps. The remaining chromatographic parameters were determined using different experimental designs via RSM, as explained in the section Results and Discussion. All samples were filtered through nylon syringe filters (0.2 µm) before injection. The inorganic component of the mobile phase was filtered through a cellulose nitrate membrane of 0.2 µm.

Empower2 software (Waters, USA) was used to control the UPLC instrument and chromatographic data collection. The generation of the experimental design matrices, response surface modelling, optimization, as well as calibration models and quantification were performed by concurrent use of Microsoft Excel (Microsoft, USA) and Matlab (MathWorks, USA). Figures were plotted in Matlab (MathWorks, USA).

Preparation of Standard Solutions

A mixture of ultrapure water and gradient grade methanol (50:50, v/v) was prepared previously and was used as solvent for all the standard and sample solutions. Individual stock solutions of sulfadiazine and trimethoprim were prepared by dissolving 20 mg and 10 mg of standard material in a 100 mL solvent mixture by manual shaking, and ultrasonication for 5 minutes. Standard solutions for calibration and validation were prepared by mixing and diluting the appropriate amounts of stock solutions.

The calibration set was planned using a factorial design of 5² (5 levels with equal steps and 2 analytes) within the working range of 6-38 µg/mL for sulfadiazine and 2-26 µg/mL for trimethoprim.

Three sets of analytical validation samples were prepared in a similar manner, by mixing and diluting required volumes. The first set, called binary synthetic mixture was used to assess the accuracy and the precision of the methods. The binary synthetic mixture set consisted of 11 solutions with different concentration of drugs from the calibration set, as given in Table S5 in supplementary material.

The second validation set consisted of intra-day and inter-day samples, that were freshly prepared at three different concentration levels: 80% (20 µg/mL SDZ + 4 µg/mL TMP), 100% (25 µg/mL SDZ + 5 µg/mL TMP), and 120% (30 µg/mL SDZ + 6 µg/mL TMP) of the specified test concentration and analyzed both on the same day and on three consecutive days to assess repeatability and intermediate precision.

The last set of validation samples, named standard addition samples, was prepared in triplicates to evaluate the effect of excipients in the solid dosage form and to evaluate the selectivity of the method. Three concentration levels of standards (10, 15, and 20 µg/mL for SDZ and 5, 12, and 19 µg/mL for TMP) were spiked into a tablet solution at a fixed volume (theoretically containing 15 µg/mL SDZ + 3 µg/mL TMP, according to the label claim). An extra tablet solution, without adding the standards, was prepared to calculate the added recovery values based on the hypothetically added amount.

Preparation of Commercial Sample Set

Three Biotrin tablets for veterinary use were weighed on an analytical balance and finely powdered in a mortar. A quantity of powder equivalent to 1/10 of a tablet by mass was transferred and diluted to 100 mL. After mixing the contents of the volumetric flask in an ultrasonic bath for 15 minutes followed by 15 minutes of magnetic stirring, the solution was filtered through a 0.2 µm nylon membrane syringe filter. This filtrate was further diluted to ensure SDZ and TMP concentrations fell within their working ranges. This process was repeated 10 times to obtain the commercial sample set.

SUPPLEMENTARY MATERIAL

The supplementary material for this article has been uploaded to Zenodo and is available at: <https://doi.org/10.5281/zenodo.17937817>.

ACKNOWLEDGMENTS





This work was conducted in the Chemometrics Laboratory of the Faculty of Pharmacy, with support from Ankara University Scientific Research Fund (Project No. 10A3336001).

REFERENCES

1. C. M. Lathers; *J. Clin. Pharmacol.*, **2001**, 41: 595–599.
2. S. H. Zinner; K. H. Mayer; *Sulfonamides and Trimethoprim*, in *Mandell, Douglas, and Bennett's Principles and Practice of Infectious Diseases*, 8th ed.; R. Dolin and M.J. Blaser, Eds.; Saunders: Philadelphia, USA, **2015**. pp. 410–418.
3. A. Espinosa-Mansilla; F. Salinas; I. De Orbe Paya; *Anal. Chim. Acta*, **1995**, 313: 103–112.

4. A. M. Galvez; J. V. G. Mateo; J. Martínez Calatayud; *Journal of Pharmaceutical and Biomedical Analysis*, **2002**, 30: 535–545.
5. Ş. E. Hişmioğulları; E. Yarsan; E. Dinç; *J. Anim. Vet. Adv.*, **2010**, 9: 857–861.
6. F. Khattab; S. Riad; M. Rezk; H. Marzouk; *J. Planar. Chromatogr. - Mod. TLC*, **2014**, 27: 113–119.
7. D. Zou; X. Wu; G. Nan; *Chinese Pharmaceutical Journal*, **1998**, 33: 106–108.
8. L. Y. Fan; H. L. Chen; X. G. Chen; Z. D. Hu; *J. Sep. Sci.*, **2003**, 26: 1376–1382.
9. M. Iyer; M. Honrao; S. Y. Gabhe; *Indian Drugs*, **1994**, 31: 497–499.
10. J. Shao; F. F. Mao; X. D. Tu; *Yao xue xue bao = Acta pharmaceutica Sinica*, **1992**, 27: 375–380.
11. M. A. Bezerra; R. E. Santelli; E. P. Oliveira; L. S. Villar; L. A. Escaleira; *Talanta*, **2008**, 76: 965–977.
12. E. Dinç; *Chemometric strategies in chromatographic analysis of pharmaceuticals*, in *Chemometrics in Chromatography*, 1st ed.; Ł. Komsta, Y. Vander Heyden, and J. Sherma, Eds.; CRC Press: Boca Raton, **2018**. pp. 381–414.
13. G. Hanrahan; K. Lu; *Crit. Rev. Anal. Chem.*, **2006**, 36: 141–151.
14. R. G. Brereton; *Experimental Design*, in *Chemometrics: Data Analysis for the Laboratory and Chemical Plant*, 2nd ed. John Wiley & Sons: Wiltshire, England, **2003**. pp. 15–117.
15. D. C. Montgomery; *Design and Analysis of Experiments*. 8th Ed. ed. **2013**: John Wiley & Sons.
16. R. H. Myers; D. C. Montgomery; C. M. Anderson-Cook; *Response Surface Methodology: Process and Product Optimization Using Designed Experiments*. 3rd ed. Wiley series in probability and statistics. **2009**, Hoboken, N.J.: Wiley. xiii, 680 p.
17. S. Atila Karaca; N. Rashidova; A. Uğur; D. Yenicali Uğur; *Chemical Papers*, **2020**, 74: 1541–1549.
18. S. Aliyeva; S. Atila Karaca; A. Uğur; A. G. Dal Poğan; D. Yenicali Uğur; *Chemical Papers*, **2020**, 74: 4443–4451.
19. E. R. V. Almeida; A. S. Melo; A. S. Lima; V. A. Lemos; G. S. Oliveira; C. F. Cletche; A. S. Souza; M. A. Bezerra; *Food Chemistry*, **2025**, 480: 143849.
20. Z. Zhang; B. Xiaofeng. *Comparison About the Three Central Composite Designs with Simulation*. in *2009 International Conference on Advanced Computer Control*. **2009**.
21. T. Rakić; B. Jančić Stojanović; A. Malenović; D. Ivanović; M. Medenica; *Talanta*, **2012**, 98: 54–61.
22. T. Rakić; B. J. Stojanović; M. Jovanović; A. Malenović; D. Ivanović; M. Medenica; *Anal. Lett.*, **2013**, 46: 1198–1212.
23. E. Dinç; Z. C. Ertekin; G. Rouhani; *J. Liq. Chromatogr. Related Technol.*, **2015**, 38: 970–976.
24. E. Büker; E. Dinç; *J. Chromatogr. Sci.*, **2017**, 55: 154–161.
25. N. Ünal; E. Dinç; *Food Anal. Methods*, **2025**, 18: 1255–1268.
26. M. Tobiszewski; A. Mechlińska; J. Namiesnik; *Chem. Soc. Rev.*, **2010**, 39: 2869–2878.
27. N. Nakov; J. Acevska; K. Brezovska; Z. Kavrakovski; A. Dimitrovska; *Green strategies toward eco-friendly HPLC methods in pharma analysis*, in *High Performance Liquid Chromatography-Recent Advances and Applications*, 1st ed.; O. Núñez, et al., Eds.; IntechOpen: London, **2023**.

EFFECT OF ELEVATED CONCENTRATIONS OF CADMIUM ON HEAVY METAL(OID)S CONTENT, ANTIOXIDANT ACTIVITY AND CONTENT OF ROSMARINIC ACID OF LEMON BALM (*MELISSA OFFICINALIS* L.)

Denis MITOV^{a*} , Stefan PETROVIĆ^a , Katarina MILENKOVIĆ^a ,
Jelena MRMOŠANIN^a , Biljana ARSIĆ^a ,
Aleksandra PAVLOVIĆ^a , Snežana TOŠIĆ^a 

ABSTRACT. Lemon balm (*Melissa officinalis* L.) is a well-established medicinal plant prized for its rich content of bioactive compounds. This study explored how artificial cadmium (Cd) contamination of soil affects the accumulation of heavy metal(oid)s, antioxidant activity, and the concentration of rosmarinic acid in lemon balm. At a soil Cd level of 20 mg/kg, plant growth was reduced, while the concentrations of most other elements, antioxidant activity, total phenolics, and flavonoids decreased, and the rosmarinic acid content increased slightly. In contrast, lower Cd levels (5 and 10 mg/kg) led to a modest increase in antioxidant activity and phenolic content. Cadmium accumulation in the aerial parts exceeded the WHO limit for medicinal plants. Although minor improvements in antioxidant properties were observed at lower Cd levels, and rosmarinic acid increased at 20 mg/kg, the health risks associated with Cd accumulation remain a concern. Therefore, monitoring Cd content in lemon balm grown on contaminated soils is essential to ensure its safe medicinal use.

Keywords: lemon balm, cadmium, soil pollution, rosmarinic acid, antioxidant activity

INTRODUCTION

Medicinal plants and their preparations are increasingly used today. In recent years, with the rapid flow of information thanks to the internet and media, it has become increasingly common to hear about the harmful effects

^a Faculty of Sciences and Mathematics, University of Niš, Serbia.

* Corresponding author: denis.mitov@pmf.edu.rs



of commercially available drugs. Consequently, people are turning more and more to the use of plants for treating various illnesses. The popularity of medicinal plants and herbal preparations is related to the fact that they are very accessible to humans, they have a relatively low price, as well as the fact that people around the world believe that their use, even if it does not result in the desired therapeutic effect, cannot lead to any unwanted side effects [1]. One of the problems that arises in the use of medicinal plants is the accumulation of heavy metal(oid)s in the parts of the plant used for preparing various preparations. For example, an analysis of medicinal herbs in Poland found an increased concentration of Cd [2], as well as an increased concentration of Cd in samples of thyme and chamomile in Spain [3].

Soil pollution with heavy metal(oid)s is one of the most important environmental problems today. Heavy metal(oid)s are naturally present in the soil. However, their increased concentrations in the soil are primarily the result of various human activities such as mining, smelting, disposal of industrial wastes, use of wastewater for irrigation, application of fertilisers and pesticides, etc. [4]. Unlike organic pollutants, heavy metal(oid)s are not biodegradable, so they are accumulated in the environment [5]. Plants growing in polluted soil can absorb heavy metal(oid)s, and if these plants are consumed by people or animals, the heavy metal(oid)s can have a harmful effect on them. For example, Cd and cadmium compounds are human carcinogens. Upon entering the human body, Cd is effectively retained and accumulates over a person's lifetime. Cadmium primarily hurts the kidneys, especially on the proximal tubular cells, which are its leading accumulation site. Cadmium also has an adverse effect on human bones, while increased exposure to Cd can disrupt normal lung function and lead to lung cancer [6,7].

Lemon balm (*Melissa officinalis* L.) is a perennial herbaceous plant originating from southern Europe and is now cultivated worldwide. The plant has a lemon-like scent and has been used for various purposes throughout the centuries. In medicinal applications, lemon balm leaves are used, which are collected just before flowering, or the essential oil obtained by steam distillation from fresh lemon balm shoots. Lemon balm is a good source of antioxidants and contains significant amounts of phenolic compounds. Lemon balm leaves contain flavonoid glycosides (quercitrin, rhamnocitrin, apigenin, and luteolin derivatives), phenolic acids, catechin tannins, triterpene compounds, and rosmarinic acid. The main components of the essential oil are the monoterpene aldehydes citral (geranial and neral). Important constituents of lemon balm essential oil also include geraniol, citronellol, linalool, geranyl acetate, β -caryophyllene, and β -caryophyllene oxide [8,9]. Lemon balm has antimicrobial, antispasmodic, antiviral, mildly sedative, and antithyroid effects. The leaf and essential oil are used in the form of infusions, extracts, and tinctures for

mild insomnia. Due to its pleasant aroma, lemon balm essential oil is also used in the perfume and food industries. Additionally, various lemon balm extracts and essential oils can be used for the treatment of herpes simplex viruses [9,10].

A large number of studies on the topic of heavy metal(oid)s and medicinal plants emphasise the significance of researching the effects of soil pollution with heavy metal(oid)s on medicinal plants. For example there are studies about lemon balm, marigold etc. that investigate effect of soil pollution with heavy metal(oid)s on content of heavy metal(oid)s in these plants [11-13]. Also some studies investigate effect of soil pollution with heavy metal(oid)s on antioxidant activity and content of phenolic compounds in plants [14,15].

As lemon balm is one of the most commonly used medicinal plants worldwide, this study aims to investigate the impact of soil pollution with Cd on the heavy metal(oid)s content of lemon balm. Lemon balm is a good source of antioxidants, so another goal of this study is to examine the effects of soil pollution with Cd on the antioxidant activity of lemon balm extract, the content of total phenols, total flavonoids, as well as the content of rosmarinic acid, as one of the main bioactive components which is responsible for the medicinal properties of lemon balm.

RESULTS AND DISCUSSION

The soil used in this pot experiment was sampled in the vicinity of the city of Niš, Serbia, from a location where no agro-technical practices had been applied for many years to minimise the impact of these effects on the growth of lemon balm. The soil, belonging to the type silty clay loam, was sampled at a depth of about 20 cm, air-dried for three weeks, ground, and sieved. The obtained soil was mixed with special substrate Hawita Professional in a 1:1 (%v/v) ratio to improve soil quality. To create Cd-contaminated soil, the soil was treated with a solution of $\text{Cd}(\text{NO}_3)_2 \times 4\text{H}_2\text{O}$ in amounts to achieve soil with added Cd concentrations of 5, 10, and 20 mg/kg, and then mixed to ensure the Cd content in the soil was as uniform as possible. The artificial contaminated soil was placed in plastic pots with a diameter of 22 cm and then left to equilibrate, with daily mixing of the soil. After one month, four 3-week-old lemon balm seedlings (purchased from the Institute 'Dr. Josif Pancic', Belgrade) were planted in each pot. The pots were kept outdoors so that the conditions under which the lemon balm grew (temperature, sun exposure, humidity) were as close as possible to those in nature, and as much as possible the same for all pots from June to August (about seven weeks), after which the lemon balm was harvested, with the roots separated from

the above-ground parts, *i.e.*, the shoots. The height of the plants was measured, and all plant material was air-dried (indoors, on paper, covered with paper) until just before the analysis. To ensure sufficient quantities of material for the necessary analyses, each unit of the model system was replicated twice (two pots). Prior to analysis, the plant material and soil were combined into a single, representative sample for each unit of the model system. Labels on pots are Cd-0 for the referent pot, Cd-5, Cd-10, and Cd-20 for pots where Cd is added in amounts of 5, 10, and 20 mg Cd/kg of soil, respectively. Labels -S, -R, and -Sh represent soil, root and shoot samples, respectively.

To assess the potential effect of added Cd on the growth of lemon balm, the height of the plant was measured, and the results are presented in Figure 1 as the average length of all plants (four plants per pot) within a treatment. With the increase in Cd concentration in the soil, plant's height decreases. The results of the one-way ANOVA indicate that there is no statistically significant difference in the height of the plant between the uncontaminated soil and the soil treatments with 5 mg/kg and 10 mg/kg.

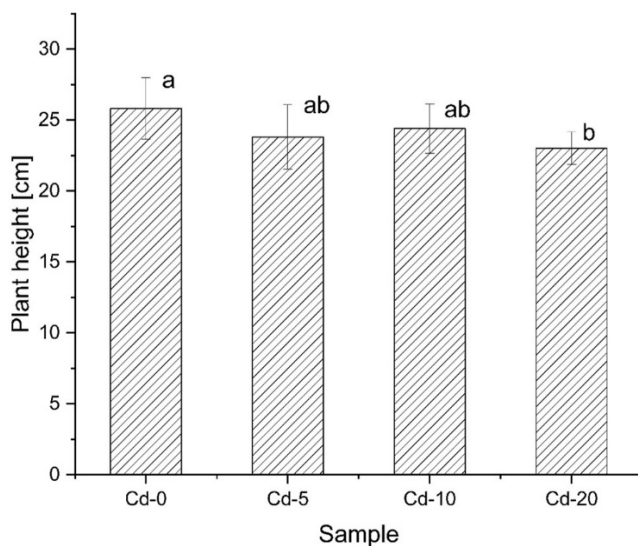


Figure 1. Effect of soil pollution with Cd on lemon balm plant height. *Vertical bar* represents standard deviation of mean height of eight plants per treatment. Bars marked with the same letter are not significantly different, according to the statistical test ($\alpha = 0.05$)

A statistically significant difference is observed in the case of Cd addition at 20 mg/kg compared to uncontaminated soil. Namely, Cd, as a non-essential metal, has a toxic effect on plants at higher concentrations, which occurs through the induction of oxidative stress, changes in the permeability and integrity of the cell membrane, reactions with sulfhydryl groups, or the replacement of essential metals in enzymes and proteins [16].

The same effect of Cd on the height of lemon balm was observed by Kilic and Kilic [13]. They also concluded that increased Cd concentration in the soil leads to decreased essential oil content in the leaves. In the case of soil pollution with a quantity of 30 mg Cd/kg, the essential oil content decreased by as much as 97% compared to lemon balm grown on uncontaminated soil. The same negative impact of Cd was noted in the case of sorghum [17]. However, literature data also indicate that an increase in Cd concentration in the soil leads to an increase in coriander height at lower Cd concentrations, followed by a decrease at higher Cd concentrations [18].

The pH of the used soil was 6.8, and the electrical conductivity was 0.48 mS/cm. In a study of the pH values of various soil samples in the Niš area, the pH ranged from 7.26 to 10.24, while conductivity levels were between 0.12 and 0.88 mS/cm, which is consistent with the obtained results [19].

Concentrations of analysed elements in soil samples are presented in Table 1. Among the analysed elements, Fe is the most abundant, while Cd is the least abundant. The content of all analysed elements is below the Maximum Allowed Concentration (MAC) [20]. The addition of Cd as nitrate salt to the soil resulted in an increase in the concentration of Cd in the soil to such an extent that the concentration of Cd was always higher than the MAC value (3 mg/kg): for the sample Cd-5-S by 1.97 times, for Cd-10-S by 4.08 times, and for Cd-20-S by 8.5 times.

Concentrations of analysed elements in roots and shoots are presented in Tables 2 and 3, respectively. In the roots of the lemon balm, the highest concentrations of Fe were found, while Pb and As, as non-essential and potentially toxic elements, were the least present. Soil contamination with Cd leads to an increase in Cd concentration in the roots. In the shoots of lemon balm, the order of the most abundant elements among the analysed ones is Fe > Zn > Mn > Cu, while Cd, As, Pb, and Cr are present in much lower amounts. This is consistent with the fact that the first-mentioned elements are essential metals necessary for plant growth, whereas the others are non-essential elements, some of them potentially toxic.

Table 1. Contents of elements \pm SD (mg/kg of sample, dry mass) in soil samples

Element	Sample			
	Cd-0-S	Cd-5-S	Cd-10-S	Cd-20-S
As	8.9 \pm 0.1	8.8 \pm 0.2	8.18 \pm 0.06	8.8 \pm 0.3
Cd	0.77 \pm 0.01	5.90 \pm 0.06	12.26 \pm 0.02	25.5 \pm 0.2
Cr	39.5 \pm 0.3	42 \pm 2	37.7 \pm 0.3	38.3 \pm 0.4
Cu	23.8 \pm 0.2	23.1 \pm 0.9	23.5 \pm 0.2	23.9 \pm 0.3
Fe	14400 \pm 70	14930 \pm 20	13300 \pm 100	13960 \pm 80
Mn	372 \pm 4	379.2 \pm 0.9	332 \pm 4	377.5 \pm 0.6
Pb	23.45 \pm 0.09	24.0 \pm 0.3	21.89 \pm 0.07	23.28 \pm 0.09
Zn	27.0 \pm 0.2	28.31 \pm 0.09	25.39 \pm 0.05	26.37 \pm 0.06

Table 2. Contents of elements \pm SD (mg/kg of sample, dry mass) in root samples

Element	Sample			
	Cd-0-R	Cd-5-R	Cd-10-R	Cd-20-R
As	1.0 \pm 0.2	1.24 \pm 0.06	1.18 \pm 0.05	1.36 \pm 0.04
Cd	0.19 \pm 0.01	12.78 \pm 0.09	50.8 \pm 0.2	72.2 \pm 0.2
Cr	5.00 \pm 0.03	6.37 \pm 0.06	5.18 \pm 0.02	6.27 \pm 0.03
Cu	10.75 \pm 0.08	9.7 \pm 0.1	15.20 \pm 0.08	15.40 \pm 0.03
Fe	2150 \pm 10	2721 \pm 4	2170 \pm 30	2797 \pm 5
Mn	38.6 \pm 0.2	38.8 \pm 0.2	30.0 \pm 0.3	43.0 \pm 0.4
Pb	2.50 \pm 0.06	2.87 \pm 0.04	2.499 \pm 0.008	3.02 \pm 0.03
Zn	28.26 \pm 0.09	39.4 \pm 0.2	40.9 \pm 0.3	42.8 \pm 0.3

Contamination of the soil with Cd resulted in a noticeable increase in the concentration of Zn and Cu in the roots (51% and 43%, respectively), a slightly lower increase in the case of As, Cr and Fe, and the least in the case of Mn and Pb. Increase of Pb and Cu content in roots of lemon balm under increasing concentration of Cd in soil was also observed previously [11]. Adamczyk-Szabela et al. [21] observed that the uptake of Zn in the root of lemon balm is inversely proportional to the concentration of Cd in the soil. The increase in the concentration of Cd in the soil also resulted in an increase in the concentration of Cd in the above-ground part of the plants. A similar

effect was observed by Arsenov et al. [22] in parsley and celery. The application of solutions of Cu to the soil also resulted in an increase in Cu concentration in the roots and above-ground parts of wheat [23].

Table 3. Contents of elements \pm SD (mg/kg of sample, dry mass) in shoot samples

Element	Sample			
	Cd-0-Sh	Cd-5-Sh	Cd-10-Sh	Cd-20-Sh
As	0.50 \pm 0.05	0.44 \pm 0.05	0.21 \pm 0.02	0.25 \pm 0.03
Cd	0.09 \pm 0.01	1.483 \pm 0.001	1.736 \pm 0.008	2.178 \pm 0.007
Cr	4.178 \pm 0.008	9.088 \pm 0.007	18.1 \pm 0.2	1.27 \pm 0.05
Cu	10.54 \pm 0.01	11.71 \pm 0.03	12.9 \pm 0.2	10.9 \pm 0.2
Fe	882 \pm 3	920 \pm 10	345 \pm 2	253 \pm 3
Mn	30.1 \pm 0.2	29.5 \pm 0.2	33.7 \pm 0.3	12.3 \pm 0.2
Pb	0.83 \pm 0.03	0.67 \pm 0.03	1.24 \pm 0.04	0.20 \pm 0.04
Zn	39.0 \pm 0.3	40.1 \pm 0.3	55.2 \pm 0.4	37.5 \pm 0.3

An increase in the concentration of Cd in the soil was reflected differently in the concentrations of other elements in shoots. It is evident that at a Cd concentration of 20 mg/kg, the content of most other elements significantly decreases (As, Cr, Fe, Mn, Pb). Also, it is interesting to note that lower concentrations of added Cd (5 or 10 mg/kg) even enhance the uptake of some elements in shoots (Cr, Cu, Fe, Mn, Zn) probably as a defence mechanism of the plant. The increase in the concentration of Cd in the soil (20 mg/kg) also resulted in a decrease in Zn concentration in the above-ground part of lemon balm, as noted by Adamczyk-Szabela et al. [21]. In case of marigold [12] increase in Cd concentration in the soil led to a reduction of Zn content in marigold leaves and an increase in Zn content in the petals. The content of Cd in the above-ground part of the lemon balm in the reference sample is below some national limits for toxic metals in herbal medicines and products, as well as the WHO recommendations (0.3 mg/kg) [24], while in samples where the soil was artificially contaminated with Cd, this concentration was exceeded. This indicates that using lemon balm grown in soil contaminated with significant amounts of Cd could pose a potential health risk to users.

In order to assess the ability of a plant species to uptake, accumulate, and translocate heavy metal(oid)s, the following factors were calculated: BCF-Biological Concentration Factor as the ratio of element

concentration in root and soil; MR-Mobility Ratio as the ratio of element concentration in the above-ground part and the soil; TF-Translocation Factor as the ratio of element concentration in the above-ground part and the root and EF-Enrichment Factor as the ratio of element concentration in the plant part (root or shoot) from contaminated and control soil. The results obtained for Cd are presented in Table 4.

Table 4. Biological coefficients (factors) for assessing the potential of lemon balm according to the accumulation and translocation of Cd

Sample	BCF	MR	TF	EF _{root}	EF _{shoot}
Cd-0	0.25	0.12	0.40	/	/
Cd-5	2.16	0.25	0.12	66	16
Cd-10	4.15	0.14	0.03	263	18
Cd-20	2.83	0.08	0.03	373	23

From the values of BCF and EFs, it can be concluded that the lemon balm can uptake and accumulate Cd and the lemon balm from polluted areas can be harmful to consumers of this medicinal plant. Of the other determined elements, only Zn shows good accumulation in the roots (BCF 1.04-1.62), good accumulation in the above-ground part (MR 1.42-2.18) as well as good translocation through plant parts (TF 1.02-1.38). A slightly more pronounced accumulation in the roots is observed in the case of Cu (BCF up to 0.65), unlike other elements with BCF values no higher than 0.2. Additionally, Cu with MR values ranging from 0.44 to 0.55 exhibits a slightly better accumulation of the tested elements in shoots, unlike other elements with MR values ranging from 0.01 for Pb to 0.48 for Cr. Cr, Cu and Mn show a slightly more pronounced translocation from the roots to the aerial part.

Hierarchical cluster analysis (Ward's method with squared Euclidean distance) on standardized data was used to group analysed elements according to their similarities of uptake by lemon balm shoots and roots (Figure 2.). Arsenic, iron, and lead form a single cluster because the fact that soil doping with Cd at a concentration of 20 mg/kg results in the highest concentrations of these elements in the root and the lowest concentrations in the aerial part. Manganese appears as a separate cluster, connected to the cluster formed by As, Fe, and Pb, but its concentration in the root is the lowest at the 10 mg/kg treatment, unlike As, Fe, and Pb. Chrome and zinc form one cluster because their content in the aerial part is much higher when the soil is doped at 10 mg/kg compared to other treatments. Cadmium and copper form a separate cluster, which indicate a possible

similarities in the mechanisms of uptake and translocation of these two elements in the lemon balm grown under such conditions. Certainly, the dendrogram shows the specifics of this plant species in the context of uptake and translocation of the examined elements from the roots to the aerial part.

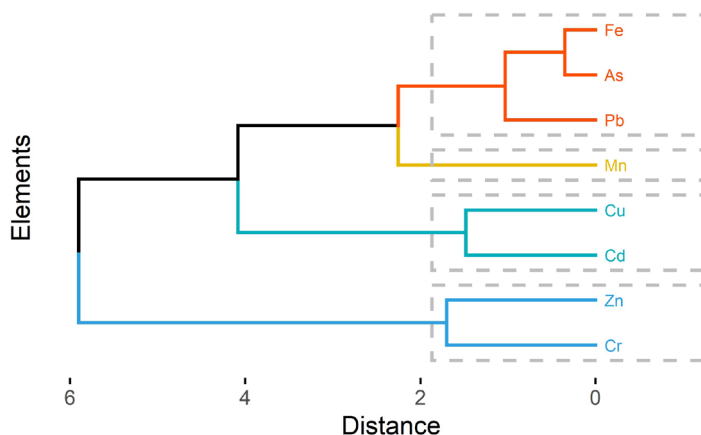


Figure 2. Hierarchical cluster analysis of analysed elements in lemon balm roots and shoots

The results of determining the total phenolic content (TPC), total flavonoid content (TFC), rosmarinic acid content, and antioxidant activities are shown in Table 5.

Table 5. The total phenolic content, the total flavonoid content, the rosmarinic acid content and antioxidant activities

Sample	TPC [mg/g gallic acid eq.]	TFC [mg/g catechin eq.]	Rosmarinic acid [mg/g]	DPPH [μmol/g trolox eq.]
Cd-0-Sh	69 ± 3 ^a	78 ± 2 ^a	26.9 ± 0.1 ^b	380 ± 20 ^{ab}
Cd-5-Sh	70 ± 1 ^a	76 ± 2 ^a	26.2 ± 0.2 ^b	390 ± 20 ^{ab}
Cd-10-Sh	74 ± 3 ^a	77 ± 2 ^a	26.0 ± 0.1 ^b	440 ± 30 ^a
Cd-20-Sh	65 ± 3 ^a	70.1 ± 0.4 ^b	31.4 ± 0.3 ^a	330 ± 20 ^b

*The contents of elements marked with the same letter for two or more samples within one column do not statistically differ significantly ($\alpha=0.05$).

The one-way ANOVA results show: there is no statistically significant difference between all samples with regard to TPC; TFC noticeably decreases at Cd concentration of 20 mg/kg; antioxidant activity increases with the increase in Cd concentration up to a concentration of 20 mg/kg, when it noticeably decreases; the content of rosmarinic acid apparently does not depend on the concentration of Cd until a concentration of 20 mg/kg when it increase significantly. Adamczyk-Szabela et al. [21] noticed that the addition of Cd to the soil (1 mg/kg and 6 mg/kg) led to an increase in total phenols content in lemon balm. Similar effects were observed in beans [25], in chamomile grown in Hoagland's solution with the addition of Ni, where TPC first decreased at the lowest Ni concentration and then increased [26] and in the species *Drimia elata* where treatment with Cd at 2 mg/kg led to an increase in TPC, but at 5 and 10 mg/kg treatments, a decrease was observed [27]. In coriander, increasing the concentration of Cd in the soil in the same amounts as in this study led to an increase in total phenols, with the highest total phenol content observed in the 20 mg/kg soil treatment, while soil contamination with Pb at 100 mg/kg first led to a decrease in TPC, and at treatments of 200 and 400 mg/kg, an increase in total phenol content was observed [18]. Analysis of corn leaves for total phenols content [28] shows that soil contamination with Cd, Cu, and Pb leads to an increase in total phenols compared to the reference unit. In case of basil (*Ocimum basilicum* L.), increased Cd content in the soil resulted in higher TPC and TFC up to amount of 100 mg/kg Cd in soil and then further increase of Cd content in soil results in TPC and TFC decrease [14]. In the species *Erica andevalensis*, increasing the concentration of Cd in the soil initially did not have a significant effect on total phenolic compounds. However, at the 5 mg/kg soil treatment, a maximum was reached. Then at the 50 mg/kg soil treatment, total phenols decreased again, which may be explained as that Cd in higher concentrations in soil inhibits some methabolics paths which have impact of synthesis of phenolics compounds The total flavonoid content increased with the increase in Cd concentration in the soil but at a concentration of 50 mg/kg, there was a slight decrease in flavonoid content [15].

A similar increase in flavonoid content was observed in beans [25]. In chamomile, where the effect of Ni on flavonoid content was studied, the initial increase in Ni concentration led to a decrease in flavonoid content, followed by an increase with further Ni concentration increases [26]. In *Drimia elata*, soil treatment with 2 mg/kg of Cd led to a slight increase in total flavonoid content [27]. However, higher concentrations of 5 mg/kg and 10 mg/kg caused a significant reduction in flavonoids. Similar trends were observed in *Gynura procumbens* [29] and *Gynura pseudochina* [30].

Since lemon balm is a good source of antioxidants responsible for its medicinal properties, it is crucial to assess the impact of soil contamination with Cd on its antioxidant activity. With the increase in Cd concentration in the soil, the antioxidant activity increased up to 10 mg/kg Cd in the soil. Although the antioxidant activity increased, which could potentially enhance the medicinal properties of lemon balm, the problem is that at such Cd concentrations in the soil, the lemon balm absorbs Cd in its aerial parts in amounts exceeding the allowable limits for medicinal plants, which may pose a risk of Cd toxicity to people using lemon balm grown in Cd-contaminated soil. When the soil was treated with 20 mg/kg Cd, there was a decrease in the antioxidant activity of lemon balm. A similar effect of soil contamination was observed in basil [31].

Rosmarinic acid is one of the most important phenolic compounds in lemon balm, known for its various medicinal effects, including the treatment of herpes simplex virus [32]. The initial increase in Cd concentration in the soil led to a decrease in the content of rosmarinic acid. However, when the soil was treated with 20 mg/kg Cd, the concentration of rosmarinic acid increased. However, since at this Cd concentration in the soil the amount of Cd in the aerial part of lemon balm exceeds the permissible levels, the use of lemon balm grown in contaminated soil, even though the rosmarinic acid content increased, is not recommended due to the high Cd content.

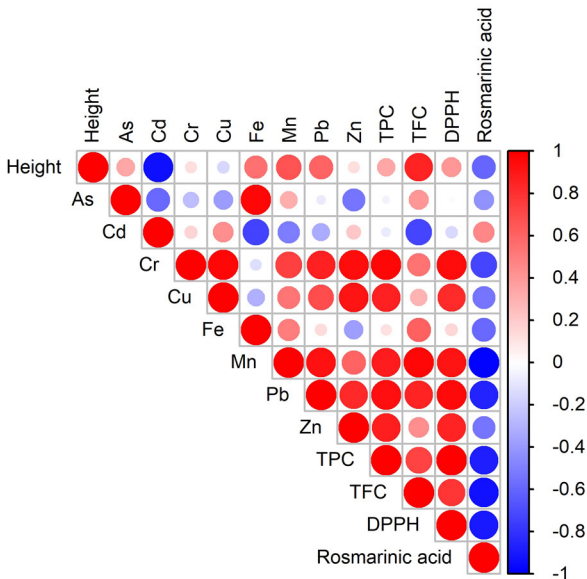


Figure 3. Correlation matrix (Pearson correlation)

A similar effect of Cd on the rosmarinic acid content was observed in *Abelmoschus esculentus* L. grown under hydroponic conditions, where the addition of 50 mg/l Cd led to a decrease in rosmarinic acid content, while at 100 mg/l Cd, there was an increase in rosmarinic acid content [33].

In order to see relationship between analysed items in lemon balm shoots correlation matrix with Pearson correlation coefficients are performed and results are presented on Figure 3.

As shown in Figure 3. Cd content is negatively correlated with most of the analysed parameters. Higher concentrations of Cd in shoots of lemon balm are strongly correlated negatively with lemon balm height and most of the other determined elements. It's interesting that there is some small positive correlation between Cd concentration in shoots and rosmarinic acid concentration. Also, there is a high positive correlation between DPPH, TPC and TFC, which is expected because phenolic compounds are the main bioactive compounds with antioxidant activity.

CONCLUSIONS

Soil pollution with Cd negatively affects lemon balm growth by reducing plant height. Lemon balm grown on Cd-contaminated soil may pose a risk to human health, as the concentration of Cd in aerial parts exceeds the WHO-recommended limits for medicinal plants. Cadmium affects both total phenolic content (TPC) and total flavonoid content (TFC), with low concentrations promoting an increase, while higher levels cause a decline. At a concentration of 20 mg/kg Cd, antioxidant activity decreases despite an increase in rosmarinic acid content. Based on BCF and enrichment factors, lemon balm shows the ability to uptake and accumulate Cd, especially in shoots, which reinforces concerns about its safety when grown in polluted soils. Among other elements, only Zn showed efficient accumulation and translocation (BCF, MR, and TF > 1), while Cu and Cr demonstrated moderate accumulation and mobility. Future research should focus on monitoring of Cd transfer into herbal preparations and exploring methods to reduce Cd uptake for safe medicinal use, as well as methods to increase uptake for potential phytoremediation applications.

EXPERIMENTAL SECTION

Analysis of soil pH and electric conductivity of soil

Approximately 10 g of dry soil was weighed and transferred into a 100 ml Erlenmeyer flask. Then, 10 ml of deionised water was added, and the mixture was shaken for one hour on a shaker. Afterwards, the liquid was carefully decanted,

and the pH value was measured using a pH meter (Hanna Instruments, USA) and the electrical conductivity was measured using a conductometer (Hanna Instruments, USA) [34].

Analysis of heavy metal(oid)s content in soil and plant samples

The content of heavy metal(oid)s was determined using optical emission spectrometry with inductively coupled plasma (ICP-OES, iCAP 6300 Duo, Thermo Scientific, Cambridge, UK). The preparation of samples was performed using microwave digestion (ETHOS EASY, Milestone, Bergamo, Italy). The EPA3051a method, provided in the instrument's application note, was used for soil sample preparation. Approximately 0.5 g of soil was weighed and transferred into teflon vessels. To each vessel, 9 ml of concentrated nitric acid and 3 ml of concentrated hydrochloric acid were added. The digestion program was as follows: within 20 minutes, a temperature of 180 °C was reached and then maintained for 10 minutes. After 20 minutes of cooling, the contents were quantitatively transferred to a 50 ml volumetric flask and diluted to the mark with deionised water [35]. Approximately 0.35 g of plant material (root and above-ground part) was weighed, placed and transferred into vessels. Then, 3 ml of concentrated hydrogen peroxide and 5 ml of concentrated nitric acid were added. The digestion program was as follows: within 20 minutes, a temperature of 190 °C was reached and then maintained for 10 minutes. After digestion, the contents of the vessels were transferred to a 25 ml volumetric flask and diluted to the mark with deionised water [36]. Concentrations of eight heavy metal(oid)s (As, Cd, Cr, Pb, Mn, Cu, Zn, Fe) are determined by the ICP-OES method of external calibration curve. Working wavelengths were selected considering the relative intensity of emission, presence of spectral interferences, corrected peak (signal-to-background ratios) under the following instruments parameters: 1150 W (generator RF power), 50 rpm (peristaltic pump speed), 100 rpm (flushing pump speed), 12 L/min (cooling gas flow), 0.5 L/min (auxiliary gas flow), 0.5 L/min (nebulization gas flow), 5 s (pump stabilization time), 30 s (sample uptake delay), axial direction plasma observation and three trials for each measurement. Selected wavelengths, correlation coefficient (r), limits of detection ($LOD=3\sigma/m$) and limits of quantitation ($LOQ=10\sigma/m$), where σ is standard deviation of blank and m is slope of the calibration line, are presented in Table 6. The satisfactory relative standard deviation of the reproducibility of the sample preparation by microwave digestion (a sample of the aerial part of the plant untreated with Cd prepared six times) ranges from 2.21% for Mn to 5.90% for Cd, except for As with a value of 14.72%.

Table 6. Wavelengths, correlation coefficients, limits of detection, and limits of quantification for determined elements

Element	Wavelength [nm]	r	LOD [mg/kg]	LOQ [mg/kg]
As	189.042	0.999990	0.1307	0.3960
Cd	214.438	0.999958	0.0055	0.0183
Cr	267.716	0.999924	0.0605	0.2016
Cu	324.754	0.999997	0.0592	0.1974
Fe	259.940	0.999859	0.0972	0.3241
Mn	257.610	0.999992	0.0054	0.0182
Pb	220.353	0.999983	0.2220	0.7400
Zn	202.548	0.999823	0.0087	0.0291

Analysis of total phenolics, total flavonoids, antioxidant activity and rosmarinic acid content

Approximately 0.5 g of dried plant material was weighed and placed in an Erlenmeyer flask. To each flask, 50 ml of 70% methanol was added, and then the flasks were placed on a shaker for extraction, which was carried out for 2 hours at room temperature. After that, the liquid extract was separated from the solid residue by centrifugation in plastic tubes at 3000 rpm for ten minutes. The extract was then filtered through 0.45-micron microfilters and stored in a refrigerator until analysis.

The total polyphenol content (TPC) in the above-ground part of lemon balm was analysed using the Folin-Ciocalteu method. A 0.1 ml portion of the extract, prepared as described above, was transferred to a 10 ml volumetric flask. Next, 0.5 ml of Folin-Ciocalteu reagent was added, and after 5 minutes, 2 ml of saturated Na₂CO₃ solution was added. The flask was filled with deionised water to reach a total volume of 10 ml and left in the dark for 30 minutes. The absorbance was then recorded at 760 nm using a UV-VIS PerkinElmer Lambda 15 spectrometer, with deionised water serving as the blank. For calibration, standards of gallic acid solutions were prepared by adding 0.5 ml of Folin-Ciocalteu reagent and 2 ml of saturated Na₂CO₃ solution to a properly weighted amount of gallic acid, adjusting the volume with deionised water to achieve final concentrations ranging from 1 to 9 µg/ml. After 30 minutes in the dark, the absorbance of the standards was measured, and a calibration curve was generated: $A = 0.04385 + 0.10517C_{\text{gallic acid}}$ [37,38]. The total polyphenol content of the extracts was expressed as milligrams of gallic acid equivalents per gram of dry lemon balm sample (mg GAE/g).

For the determination of total flavonoids content (TFC), a 0.1 ml portion of the lemon balm extract was placed into a 10 ml volumetric flask, followed by the addition of 0.3 ml of 5% NaNO₂. After 5 minutes, 1.5 ml of an AlCl₃ solution was added, and 5 minutes later, 2 ml of 1M NaOH was added. The flask was brought to a final volume of 10 ml with deionised water. Absorbance was measured at 510 nm, using deionised water as a blank. A calibration curve was established using catechin working solutions (1–10 mg/l) prepared from a 0.5 mg/ml stock solution. The curve demonstrated linearity, following the equation $A = 0.03612 + 0.00491C_{(\text{catechin})}$. Using this equation, the total flavonoid content was determined and expressed as milligrams of catechin equivalents per gram of dry sample (mg CE/g) [39].

To prepare the sample, 0.5 mL of the extract was diluted to 50 ml using 70% (v/v) methanol. Antioxidant activity was assessed using the DPPH method, as outlined by Brand-Williams et al. [40], with slight modifications. A DPPH solution at a concentration of 1×10^{-4} mol/l in methanol was prepared. From this diluted DPPH solution, 5.0 ml was transferred to a 10 ml volumetric flask, and 0.5 ml of the diluted extract was added. The flask was then filled up with methanol to a final volume of 10 ml. After 30 minutes, the colour change of the DPPH radical was measured spectrophotometrically at 520 nm. A calibration curve was established using Trolox solutions, based on the reduction in absorbance, which represented the DPPH radical scavenging activity. The antioxidant activity of the samples was expressed as micromols of trolox equivalents per gram of dry lemon balm ($\mu\text{molTE/g}$).

To determine the content of rosmarinic acid, the method by Mašković et al. [41] with some modifications was used (Agilent 1200 system, Agilent Technologies, Santa Clara, CA, USA). The analytical column employed was a Zorbax Eclipse XDBC18 column (5 μm , 4.6×150 mm, Agilent Technologies, Santa Clara, CA, USA). The mobile phase was delivered at a constant flow rate of 0.8 ml/min over a total run time of 40 minutes. Solvent A consisted of 5% formic acid in deionised water, while Solvent B was composed of 5% formic acid in 80% acetonitrile. The gradient program was as follows: 0% B for the first 10 minutes, increasing to 25% B from 10 to 20 minutes, 25–40% B between 20 and 30 minutes, 40–70% B from 30 to 35 minutes, and 70–80% B during the final 5 minutes of the analysis.

Statistical analysis

Statistical analysis is performed using R. The normality of obtained values is tested with the Kolmogorov-Smirnov test. For correlation between elements in shoots, the corrplot package was used, for hierarchical clustering the factoextra and dentextend packages were used and for one-way ANOVA

and Tukey posthoc test, the dplyr and multcompView packages were used. For making graphs OriginLab and R were used.

ACKNOWLEDGMENTS

The authors gratefully acknowledge funding support from the Ministry of Education, Science and Technological Development of the Republic of Serbia (Project No. 451-03-136/2025-03/ 200124 and Project No. 451-03-137/2025-03/200124).

REFERENCES

1. S. Arpadjan, G. Çelik, S. Taşkesen and Ş. Güçer, *Food Chem. Toxicol.*, **2008**, *46*, 2871–2875.
2. P. Kalny, Z. Fijałek, A. Daszczuk and P. Ostapczuk, *Sci. Total Environ.*, **2007**, *381*, 99–104.
3. M. C. Martín-Domingo, A. Pla, A. F. Hernández, P. Olmedo, A. Navas-Acien, D. Lozano-Paniagua and F. Gil, *J. Food Compos. Anal.*, **2017**, *60*, 81–89.
4. S. Dubey, M. Shri, A. Gupta, V. Rani and D. Chakrabarty, *Environ. Chem. Lett.*, **2018**, *16*, 1169–1192.
5. N. Sarwar, M. Imran, M. R. Shaheen, W. Ishaq, A. Kamran, A. Matloob, A. Rehim and S. Hussain, *Chemosphere*, **2017**, *171*, 710–721.
6. A. Bernard, *Indian J. Med. Res.*, **2008**, *128*, 557–564.
7. S. Martin and W. Griswold, *Environ. Sci. Technol. briefs citizens*, **2009**, *15*, 1–6.
8. A. Chevallier; *The Encyclopedia of Medicinal Plants*; DK Pub.: New York, USA ; Boston (Dist. Houghton Mifflin), **1996**; pp. 111–112
9. N. Kovačević, *Osnovi farmakognozije*, Altera, Belgrade, Serbia, **2004**.
10. P. Schnitzler, A. Schuhmacher, A. Astani and J. Reichling, *Phytomedicine*, **2008**, *15*, 734–740.
11. D. Adamczyk-Szabela, K. Lisowska, Z. Romanowska-Duda and W. M. Wolf, *Sci. Rep.*, **2020**, *10*, 1–10.
12. N. K. Moustakas, A. Akoumianaki-Ioannidou and P. E. Barouchas, *Aust. J. Crop Sci.*, **2011**, *5*, 277–282.
13. S. Kilic and M. Kilic, *Appl. Ecol. Environ. Res.*, **2017**, *15*, 1653–1669.
14. S. Đogić, N. Džubur, E. Karalija and A. Parić, *Acta Agric. Serbica*, **2017**, *22*, 57–65.
15. B. Márquez-García, M. Á. Fernández-Recamales and F. Córdoba, *J. Bot.*, **2012**, *2012*, 1–6.
16. G. DalCorso, in *Plants and Heavy Metals*, ed. A. Furini, Springer, Dordrecht, **2012**, pp. 1–25.

17. M. J. Hassan, M. A. Raza, S. U. Rehman, N. Ansar, H. Gitari, I. Khan, M. Wajid, M. Ahmed, G. A. Shah, Y. Peng and Z. Li, *Plants*, **2020**, 9, 1575.
18. B. Fattahi, K. Arzani, M. K. Souiri and M. Barzegar, *Ind. Crops Prod.*, **2021**, 171, 113979.
19. J. S. Nikolić, V. D. Mitić, M. V. Dimitrijević, M. D. Ilić, S. A. Ćirić and V. P. Stankov Jovanović, *Chem. Naissensis*, **2019**, 2, 114–137.
20. R. of Serbia, Regulation on allowed quantities of hazardous and harmful substances in soil and water for irrigation and methods of their testing, **1994**.
21. D. Adamczyk-Szabela, E. Chrześcijańska, P. Zielenkiewicz and W. M. Wolf, *Molecules*, **2023**, 28, 2642.
22. D. Arsenov, M. Župunski, S. Pajević, M. Borišev, N. Nikolić and N. Mimica-Dukić, *Environ. Geochem. Health*, **2021**, 43, 2927–2943.
23. O. Culicov, A. Stegarescu, M. L. Soran, I. Lung, O. Opreș, A. Ciorîță and P. Nekhoroshkov, *Molecules*, **2022**, 27, 4835.
24. W. H. O. (WHO), *WHO guidelines for assessing quality of herbal medicines with reference to contaminants and residues*, Geneva, **2007**.
25. K. Benhabiles Ait El Hocine, Y. Bellout and F. Amghar, *Appl. Ecol. Environ. Res.*, **2020**, 18, 3757–3774.
26. J. Kováčik, B. Klejdus and M. Bačkor, *J. Plant Physiol.*, **2009**, 166, 1460–1464.
27. A. Okem, C. Southway, W. A. Stirk, R. A. Street, J. F. Finnie and J. Van Staden, *South African J. Bot.*, **2015**, 98, 142–147.
28. D. Kisa, M. Elmastaş, L. Öztürk and Ö. Kayır, *Appl. Biol. Chem.*, **2016**, 59, 813–820.
29. A. M. H. Ibrahim, J. S. Quick, R. Kaya, J. Grandgirard, D. Poinot, L. Krespi, J. P. Nénon, A. M. Cortesero, A. U. Islam, A. K. Chhabra, S. S. Dhanda, R. Munjal, I. J. Biosci, S. Shaukat, A. S. Khan, M. Hussain, M. Kashif, N. Ahmad, S. U. Rehman, M. Bilal, R. M. Rana, M. N. Tahir, M. K. N. Shah, H. Ayalew, G. Yan, P. Bala, H. Lalmia and C. College, *Crop Pasture Sci.*, **2017**, 2, 291–296.
30. B. Mongkhonsin, W. Nakbanpote, A. Hokura, N. Nuengchamnong and S. Maneechai, *Plant Physiol. Biochem.*, **2016**, 109, 549–560.
31. K. Korkmaz, Ö. Ertürk, M. Ç. Ayvaz, M. M. Özcan, M. Akgün, A. Kirli and D. O. Alver, *Indian J. Pharm. Educ. Res.*, **2018**, 52, S108–S114.
32. M. Petersen and M. S. J. Simmonds, *Phytochemistry*, **2003**, 62, 121–125.
33. A. Mousavi, L. Pourakbar, S. Siavash Moghaddam and J. Popovic-Djordjevic, *J. Environ. Chem. Eng.*, **2021**, 9, 105456.
34. R. O. Miller and D. E. Kissel, *Soil Sci. Soc. Am. J.*, **2010**, 74, 310–316.
35. USEPA, *Method 3051A: Microwave assisted acid digestion of sediments, sludges, soils, and oils*, Washington (DC), **2007**.
36. K. Milenković, J. Mrmošanin, S. Petrović, D. Mitov, B. Zlatković, J. Mutić, D. Kostić, S. Tošić and A. Pavlović, *Not. Bot. Horti Agrobot. Cluj-Napoca*, **2024**, 52, 1–21.
37. P. Stratil, B. Klejdus and V. Kubáň, *J. Agric. Food Chem.*, **2006**, 54, 607–616.
38. D. Huang, O. U. Boxin and R. L. Prior, *J. Agric. Food Chem.*, **2005**, 53, 1841–1856.

39. R. F. V. De Souza and W. F. De Giovanni, *Spectrochim. Acta - Part A Mol. Biomol. Spectrosc.*, **2005**, *61*, 1985–1990.
40. W. Brand-Williams, M. E. Cuvelier and C. Berset, *LWT - Food Sci. Technol.*, **1995**, *28*, 25–30.
41. P. Mašković, V. Veličković, M. Mitić, S. Đurović, Z. Zeković, M. Radojković, A. Cvetanović, J. Švarc-Gajić and J. Vujić, *Ind. Crops Prod.*, **2017**, *109*, 875–881.

HPLC/DAD ANALYSIS OF VITAMIN C AND ANTIOXIDANT CAPACITY DETERMINATION OF *VITIS VINIFERA* L. GRAPES DURING RIPENING

Nicoleta MATEI^a, Semaghiul BIRGHILA^{a,*}, Simona DOBRINAS^a,
Elena Carmen LUPU^b, Antoanela POPESCU^b

ABSTRACT. This study aims to determine the vitamin C (ascorbic acid, AA) content and antioxidant capacity in five varieties of grapes (skin, pulp and seeds). A simple, fast and sensitive High-Performance Liquid Chromatography/Diode Array Detection (HPLC-DAD) method was used for the determination of ascorbic acid in grapes (*Vitis vinifera* L.) samples from Murfatlar vineyard. Total antioxidant capacity was determined through photochemiluminescence method as ACL (Antioxidant capacity of lipid soluble substances). The LOD was 0.40 µg/mL for the HPLC-DAD method. The advantages of the method are using of small amounts of samples and reagents, short analysis time and minimum steps for sample preparation. Antioxidant capacity of *Vitis vinifera* L. grapes alcoholic extract ranged between 0.02 and 7.42 mmoles equivalent TROLOX/100g product. After statistical analysis (ANOVA), a significant correlation between the ascorbic acid concentration and the antioxidant capacity was observed in peel, pulp, and seeds during ripening. Due to the high content of ascorbic acid and antioxidant capacity, future analysis should focus on the determination of other bioactive substances in grapes.

Keywords: Ascorbic acid, grapes, peel, pulp, seed, HPLC-DAD, antioxidant capacity

^a Ovidius University of Constanta, Faculty of Applied Sciences and Engineering, Department of Chemistry and Chemical Engineering, 124 Mamaia Blvd., RO-900527, Constanta, Romania, nmatei@univ-ovidius.ro, sbirghila@univ-ovidius.ro, sdorbinas@univ-ovidius.ro

^b Ovidius University of Constanta, Faculty of Pharmacy, 6 Câpitan Aviator Al. Şerbănescu Street, Constanta, Romania 900470, clupu@univ-ovidius.ro, antoanela.popescu@univ-ovidius.ro

* Corresponding author: sbirghila@univ-ovidius.ro



INTRODUCTION

The grapes are cultivated all over the world and the most important species is *Vitis vinifera* L. from Europe and from which are derived all major varieties of table grapes and wine. The grapes contain a lot of nutrients, especially polyphenols, which are important due to their role as natural antioxidants [1]. Antioxidants are used in the prevention and treatment of cancer [2], inflammatory [3,4], cardiovascular [5,6] and neurodegenerative diseases [7-10]. There are also trace elements (reducing and oxidizing agents) essential for carrying out the chemical reactions required for cell multiplication (Se, Ni, Cr, I, Zn, Cu, Mn, F, V, Co) which give the grape some original nutritional qualities. Its content is enriched with many organic acids found in grape berries (malic, tartaric, citric, isocitric, ascorbic, caffeic, oxalic, succinic, lactic, fumaric, etc.), water (80% of the fresh fruit weight) and inorganic compounds (K^+ , Na^+ , Ca^{2+} , Mg^{2+} , Fe^{2+} , SO_4^{2-} , PO_4^{3-}) [11].

One interesting point with grapes is that they accumulate very low levels of ascorbic acid, in comparison with other fruits. This may be due to the fact that grape berry tissues transform AA to tartaric acid. The level varies depending on the maturity degree of grapes. Ascorbic acid (more abundant in the grape berries exposed to sunlight) varies between 4 and 10 mg/100g [11-15].

Also, the grapes contain fats (0.16 g/100g), proteins (0.72 g/100g), carbohydrates (17 g/100g), vitamins (especially B complex which is well represented by vitamins B_1 – 0.069 mg/100g, B_3 – 0.188 mg/100g and B_5 – 0.05 mg/100g) [11]. In fact, fruits are an excellent type of food characterized by a low content of calories and a high amount of antioxidant substances, which are able to prevent a wide range of diseases. Therefore, fruits represent a major source of antioxidants. The content of phytochemical substances is influenced by numerous factors such as ripening time, genotype, cultivation techniques, and climatic conditions. Maturity stages are another important factor that influences the compositional quality of the fruit. During fruit ripening, several biochemical, physiological and structural modifications happen, and these changes determine the fruit quality attributes. In fact, harvesting at the proper maturity stage is essential for optimum quality and often for the maintenance of this quality after harvest and storage [16].

There is a controversial debate in the literature about the influence of ascorbic acid on the antioxidant capacity of fruits or vegetables. It is also known that fruits generally contain more antioxidants and most of these proved to be phenolic compounds and anthocyanins [16].

Many analytical methods [17-23] have been proposed for the determination of AA in different fruits: peroxidase-mimetic colorimetric biosensors [24], a food-grade Fe β Cyclodextrin nanozymes [25] or a smartphone-

based colorimetric sensor using Zn/Co bimetallic organic framework-derived nanozymes [26]. However, the preferred method by far for analyzing AA is HPLC with ultraviolet (UV) or diode array (DAD) detection [27-32].

There are many methods (*in vitro* and *in vivo*) to determine antioxidant capacity: TEAC determination, seric malondialdehyde determination and low and total seric glutathione determination [33-39]. In this paper total antioxidant capacity of grape aqua-alcoholic solution was estimated using Chemiluminescence method in lipid samples (ACL), according to Analytic Jena procedure, Germany, using PHOTOCHEM coupled to PC apparatus [40-42].

The grapes varieties studied in this paper were from Murfatlar village. Harvested grapes in vineyard Murfatlar were used to obtain local Romanian wine, a sort of wine that has won many medals in international competitions [43]. In relation to the importance of phytochemicals and antioxidant power concerning the functional aspect of grape fruits, the aim of this work was to evaluate the changes of vitamin C content and antioxidant capacity during ripening. ANOVA, Tukey post hoc test and Pearson correlation (r) analysis were performed to assess the relationship between ascorbic acid content and antioxidant capacity across different ripening stages.

RESULTS AND DISCUSSION

Ascorbic acid has multiple biological functions, and it is believed that the role of AA in disease prevention is due to its ability to scavenge free radicals in the biological systems [17]. Despite the fact that the grapes contain a small amount of AA, this gives the grape some original nutritional qualities such as microelements and the other antioxidants.

For ascorbic acid determination, the procedure described by ASRO, SR EN 14130 [44] was optimized under laboratory conditions. First, to determine the wavelength detection, a sample of ascorbic acid solution, with a concentration of 0.4 mg/mL, was injected in the HPLC-DAD. The absorption spectrum was recorded against the blank (mobile phase), in a 1 cm cuvette, figure 1.

Under the described chromatographic (HPLC-DAD) conditions, ascorbic acid was eluted at 6.54 ± 0.01 min, (Figure 2).

For the linearity and limit of detection, solutions of the standards of six different concentrations were analyzed and the calibration curves ($y = a + bx$) were constructed by plotting the peak area ratios (y) of analyte versus the respective concentrations. Figure 3 shows the calibration curve performed within the working range: 0.5- 15 $\mu\text{g/mL}$.

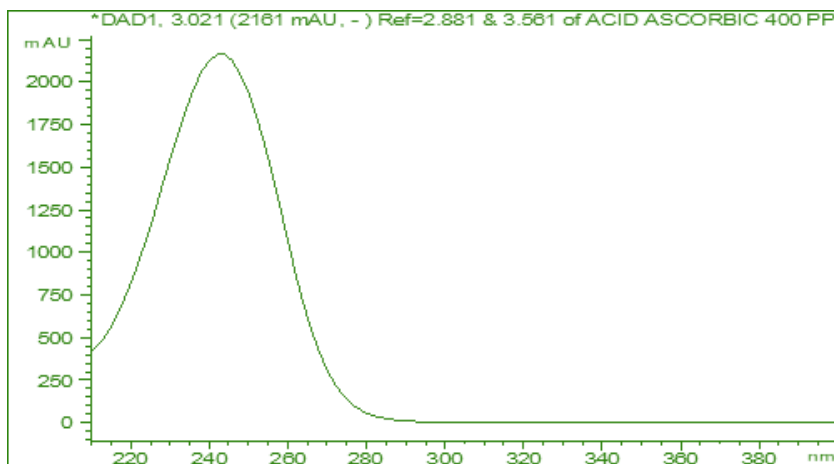


Figure 1. The absorption spectrum of standard ascorbic acid solution

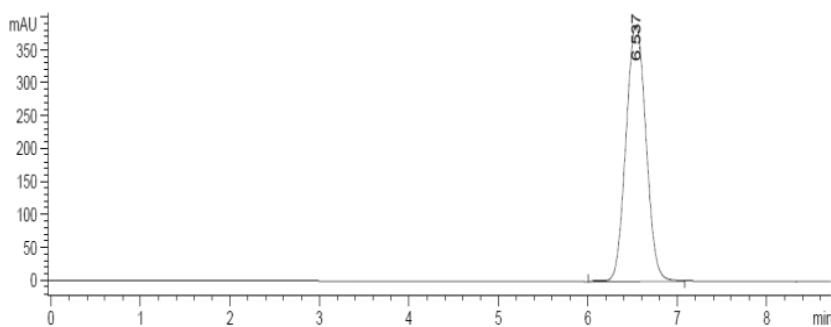


Figure 2. The chromatogram of standard ascorbic acid solution of concentration 15 µg/mL

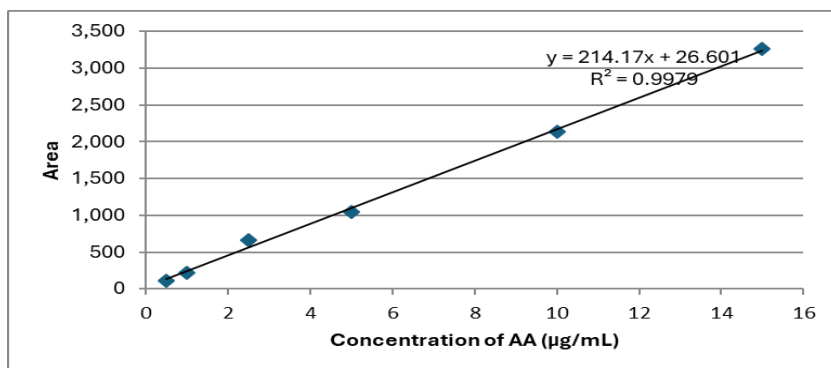


Figure 3. Calibration curve for AA determination within the working range: 0.5- 15 µg /mL

The linear dynamic range and the limit of detection (LOD) of the HPLC-DAD method were determined. It was observed a good linearity of the method response in the 0.5-15 µg/mL concentration range with $R^2 = 0.9979$. The equation curve registered was: $A = 214.2c - 26.6$. The LOD was 0.40 µg/mL for the HPLC with DAD detection. 6.54±0.01 min (values are given as means ± standard deviations (n = 3)) of the retention time was also registered.

For the precision of the method, every sample solution of the same concentration on the calibration curve was injected at least three times to determine the relative standard deviation (RSD) values for peak areas. The RSD values for peak areas ranged from 0.77% to 1.59% for standard solutions of ascorbic acid. The obtained RSD values (below 5%) presented in Table 1 indicated an excellent repeatability and precision of the proposed method [45].

The concentration of ascorbic acid was determined in five varieties of grape (*Vitis vinifera L.*) samples from Murfatlar vineyard (Murfatlar village, Constanta) using HPLC-DAD.

Table 1. The relative standard deviation (RSD) values for peak areas

Acid ascorbic concentration (µg/ mL)	RSD% (Area)
0.5	1.37
1	1.59
2.5	1.04
5	1.18
10	0.98
15	0.77

A typical chromatogram of a pulp white grape sample is shown in Figure 4. The concentration of ascorbic acid was determined in three different parts of the grape: peel, pulp and seed which were collected during ripening, at the beginning of the ripening period (unripe), in the middle (almost ripe) and before the harvest (ripe).

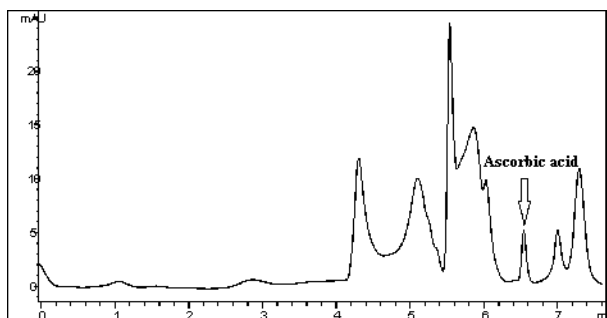


Figure 4. Representative HPLC-DAD chromatogram for a variety of white grape pulp sample

The results of the analyzed samples were summarized in figure 5.

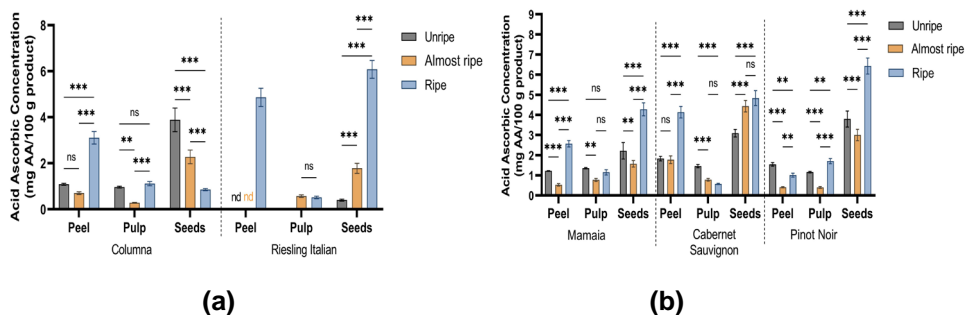


Figure 5. The acid ascorbic content of grapes on three different dates of ripening period: (a) White grapes (Columna, Riesling Italian). (b) Red grapes (Mamaia, Cabernet Sauvignon, Pinot Noir).

Bars show mean \pm standard deviation ($n = 3$ replicates, nd: not detected). Pairwise differences among ripening stages within *Vitis Vinifera* varieties \times vegetal material were tested by two-way ANOVA with Tukey post-hoc test (ns: $p \geq 0.05$; * $p < 0.05$; ** $p < 0.01$; *** $p < 0.001$).

The highest content of ascorbic acid was found in seeds from most of the varieties (white and red grapes) while the lowest content was found in the pulp (between 0 and 4.13 mgAA/100g) of the grapes samples. The peel contains amounts of ascorbic acid ranging from 0 to 4.86 mgAA/100g whereas in the seeds the concentration reaches up to 6.43 mgAA/100g product. The results obtained in ripe grapes for vitamin C are comparable to those obtained by High Performance Liquid Chromatography/Electrospray Ionization-Mass Spectrometry [46].

Statistical analysis (Figure 5) confirmed that these differences were significant for most comparisons across ripening stages ($p < 0.05$), particularly in seeds and peel, while in pulp the variation with maturity was generally not significant.

The antioxidants capacities (mmoles equivalent TROLOX/100 g vegetal product) of white and red grapes on three different dates of the ripening period from Murfatlar vineyard were presented in figure 6 and were estimated using the Chemiluminescence method in lipid samples (ACL).

The antioxidant capacity of grape samples varied both with the type of vegetal material and the ripening stage. In white grape cultivars (Figure 6 (a)), the highest antioxidant capacity was consistently recorded in the seeds, reaching values above 6 mmol Trolox equivalents/100 g product in the ripe stage, whereas the peel and pulp exhibited markedly lower activities, often

below 2 mmol Trolox equivalents/100 g. A similar trend was observed in red grape cultivars (Figure 6 (b)), where the seeds showed the most pronounced antioxidant capacity, with significant increases during ripening ($p < 0.001$), while the pulp remained the poorest source of antioxidants across all stages.

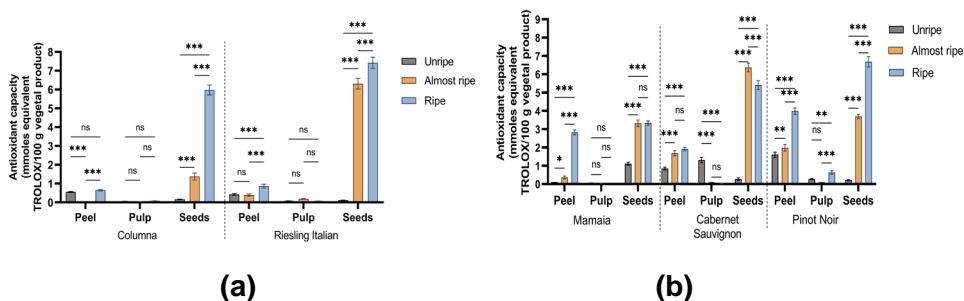


Figure 6. The antioxidant capacity of grapes at three different dates of ripening period: (a) White grapes (Columna, Riesling Italian). (b) Red grapes (Mamaia, Cabernet Sauvignon, Pinot Noir).

Bars show mean \pm standard deviation ($n = 3$ replicates, nd: not detected). Pairwise differences among ripening stages within *Vitis Vinifera* varieties \times vegetal material were tested by two-way ANOVA with Tukey post-hoc test (ns: $p \geq 0.05$; * $p < 0.05$; ** $p < 0.01$; *** $p < 0.001$).

It was found that the antioxidant activity of grapes not only depends on the content of ascorbic acid, but also on other bioactive compounds. In the analysed samples, the antioxidant capacity was generally higher in those with increased ascorbic acid content, both in white and red grape varieties. Therefore, a significant correlation between the ascorbic acid concentration and the antioxidant capacity was observed in peel, pulp, and seeds during ripening (Figures 7, 8), which is in agreement with the findings of Aldina Kesic et al. [33].

In white grapes, the correlation between ascorbic acid content and antioxidant capacity is consistently strong throughout berry development, although the direction of association varied depending on the vegetal material. In the unripe stage, highly significant and very strong positive correlations were observed across all vegetal materials, with r values ranging between 0.955 and 0.959. At the almost ripe stage, ascorbic acid showed a very strong positive correlation with antioxidant capacity in the pulp ($r = 0.960$), a very strong negative correlation in the peel ($r = -0.989$), and a weak, non-significant association in the seeds ($r = -0.338$). In the ripe stage, ascorbic acid was very strongly and positively correlated with antioxidant capacity in the peel and seeds ($r = 0.924 - 0.983$), whereas in the pulp it was very strongly and negatively correlated ($r = -0.977$).

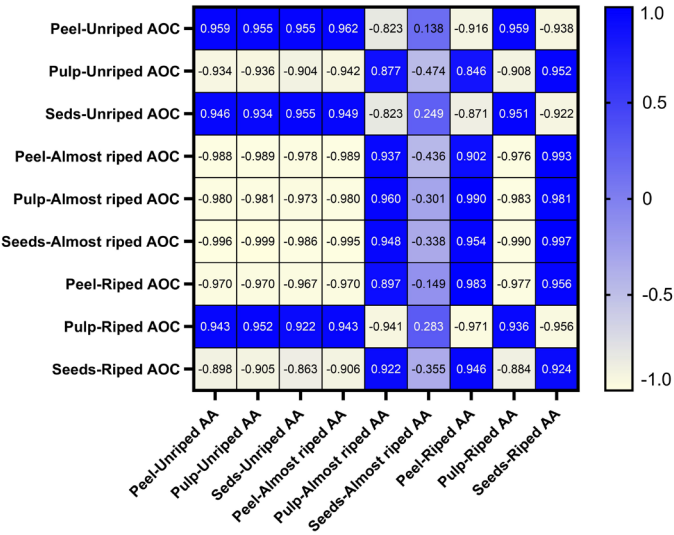


Figure 7. Heatmap for correlation between between the acid ascorbic acid content and antioxidant capacity in the peel, pulp and seed of ripe grape for white grapes. Blue indicates strong positive correlations ($r = 1$), while yellow signifies strong negative correlations ($r = -1$). $|r| > 0.811$ statistically significant at $p < 0.05$.

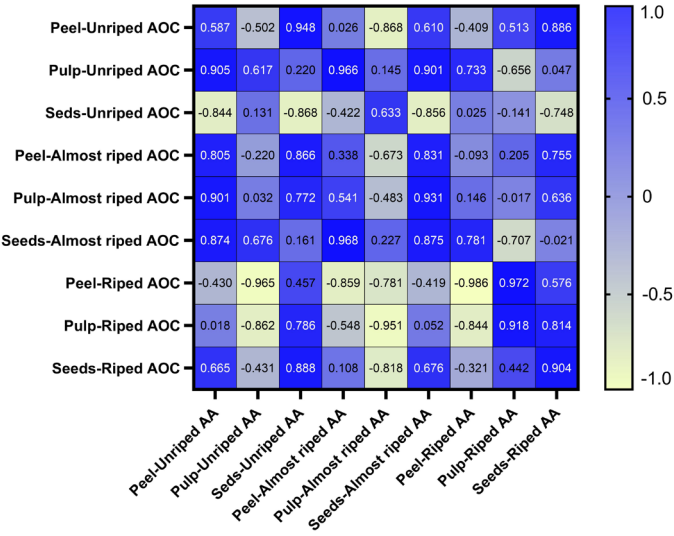


Figure 8. Heatmap for correlation between between the acid ascorbic acid content and antioxidant capacity in the peel, pulp and seed of ripe grape for red grapes. Blue indicates strong positive correlations ($r = 1$), while yellow signifies strong negative correlations ($r = -1$). $|r| > 0.602$ statistically significant at $p < 0.05$.

In red grapes, the correlation between ascorbic acid content and antioxidant capacity varied depending on the vegetal material and the ripening stage. In the unripe stage, the correlation was weak and not statistically significant in the peel and pulp ($r = 0.587-0.617$), whereas in the seeds it was very strong and highly significant, but negative ($r = -0.868$). At the almost ripe stage, ascorbic acid showed weak and non-significant correlations with antioxidant capacity in the peel ($r = 0.338$) and pulp ($r = -0.483$), while in the seeds it was very strongly and positively correlated ($r = 0.875$). In the ripe stage, ascorbic acid was very strongly and negatively correlated with antioxidant capacity in the peel ($r = -0.986$), whereas in the pulp and seeds it was very strongly and positively correlated ($r = 0.904-0.918$).

It can be observed that the ascorbic acid concentration and the antioxidant capacity in grapes increased during the ripening process. But Tavarini et al (2008) reported that the accumulation of AA during ripening depends on the type of fruit and that when fruits become overripe, the ascorbic acid content declines with the degradation of fruit tissues. They found that the AA content increased with ripening in apricot, peach and papaya, but decreased in apple and mango [16]. Similarly, our results showed an increase in ascorbic acid content with grape ripening.

According to literature data, the antioxidant capacity is generally higher in seeds compared to the peel of grapes. Lachman et al. analyzed grapes from five vineyards in the Czech Republic and found average antioxidant capacity values of 6.27% in peel and 27.21% in seeds, based on 25 samples [48]. This aligns with our findings, where seeds consistently exhibited higher antioxidant activity than peel, showing that seeds represent the major contributors to the antioxidant potential of grapes.

CONCLUSIONS

The parameters of HPLC-DAD method for the determination of ascorbic acid in samples of grapes were developed for linearity, precision and for low detection limits values, as well. The method provides a rapid and sensitive means of determining ascorbic acid in grape samples from Murfatlar vineyard. The method described is very simple, involves little sample preparation, small amounts of sample and reagents and is fast since the total analysis time does not exceed 10 minutes. The results obtained using the HPLC-DAD method are comparable to the results obtained by other researchers.

The ascorbic acid and the antioxidant capacity of grapes depend on the varieties of grapes and on the harvesting time. It can observe that the ascorbic acid concentration and antioxidant capacity in grapes increased with ripening grapes. A significant correlation between the ascorbic acid concentration and the antioxidant capacity was observed in peel, pulp, and seeds during ripening.

EXPERIMENTAL SECTION

Materials

Standard of ascorbic acid was purchased from Merck (Darmstadt, Germany). HPLC-grade methanol, acetic acid, metaphosphoric acid and trisodium phosphate were purchased from Fluka (Buchs, Switzerland). All chemicals were of analytical grade (purity > 98%) and were used without further purification. 6-hydroxy-2,5,7,8-tetramethylchroman-2-carboxylic acid, as standard substance TROLOX, was purchased from Merck.

All the solutions were made up of ultrapure water from a Milli-Q Elix3 system. Solvents were filtered through 0.2- μ m membranes (Millipore, Bedford, MA, USA) and degassed before use.

Standard solution

The stock solution of ascorbic acid was prepared at a concentration of 1mg/mL by weighing accurately the appropriate mass using a Metler Toledo analytical balance (± 0.0001 g accuracy). The stock solution was diluted with acidified water for the preparation of working solutions in a concentration range from 0.5 to 15 μ g/mL ascorbic acid that were stored in the dark at a temperature of 4^o C. Standard substance TROLOX, a derivative of vitamin E, is Hoffman-LaRoche's trade name for 6-hydroxy-2,5,7,8-tetramethylchroman-2-carboxylic acid and was used for the antioxidant capacity. This standard solution was diluted to prepare plot calibration curve for 6 concentrations (0.5, 1, 1.5, 2, 2.5 and 3 nmols TROLOX).

SAMPLES PREPARATION

Samples

The methods were applied to the analysis of real samples including five grape varieties from Murfatlar vineyard (Murfatlar town, Constanta country) collected during the ripening period. Three red grape varieties: Pinot Noir, Cabernet Sauvignon and Mamaia and two white grape varieties: Columna, Riesling Italian were chosen for analysis. The grapes were carefully separated into peel, pulp and seeds; they peeled them with the help of a scalpel.

Acid Ascorbic determination

For the chromatographic determinations, extraction was performed on the day of analysis, by homogenizing (using a Bosh blender) three fruit portions of 5 g each. Thus, three biological replicates were obtained. The homogenized material (peel, pulp or seeds) was dissolved in 25 mL of metaphosphoric acid 20 g/L in a volumetric flask. Samples were adjusted to pH 2.5 to 2.8 with trisodium phosphate 200g/L. The homogenate was sonicated by a Bransonic cleaner and then centrifuged at 4 °C and 5000 rpm for 10 min, using a Hettich Universal 320 centrifuge (Andreas Hettich GmbH & Co. KG). The supernatant was filtered through 0.45-µm filters (Chromafil Xtra PTFE-45/25 particle size of 0.45 µm), The samples were kept in dark colored vials and analyzed immediately after extraction.

Antioxidant capacity determination

For the antioxidant capacity, 5 g of homogenized dried material (peel, pulp or seeds) was left in contact with 50 mL methanol 98% in brown recipients in the dark in order to obtain the extracts. The mixture was strongly shaken three times every day. After seven days of contact time 5 mL alcoholic extract, previously filtered, were collected in glass recipients and stored at 4 °C. 5 µL, 10 µL or 20 µL of samples were analyzed after extraction. For determination each extract was diluted with ethanol.

INSTRUMENTATION

HPLC-DAD analysis

The identification and quantification of ascorbic acid was carried out using an HPLC Agilent 1200 system with the following components: quaternary pump, DAD, thermostat, degassing system, autosampler. The autosampler temperature was set to 4 °C. The separation of the analyte was carried out on a Zorbax XDB C18, 250 mm × 4.6 mm; 5 µm column (Phenomenex, SUA). The mobile phase consisted of (A – 95 %) 0.1% acetic acid in HPLC-grade water and (B – 5 %) methanol, eluted in isocratic conditions. The injected volume sample was 20 µL at a flow rate of 0.25 mL min⁻¹. Detection using a DAD was performed at a specific wavelength of 245 nm for ascorbic acid [44]. The analysis time was 10 minutes. The results were obtained by comparison with the standard. The results were the mean values from three replicates of the same sample.

Antioxidant capacity analysis

The total antioxidant activity of grapes aqua-alcoholic solution was estimated using the Chemiluminescence method in lipid samples (ACL). This was performed according to Analytic Jena procedure, Germany, using PHOTOCHEM coupled to PC apparatus [28]. The extern source of light was represented by a Hg lamp carried with phosphorus, with highest energy at the wavelength $\lambda = 351$ nm and the free radicals source was H_2O_2 . The antioxidant activity was calculated using the calibration curve and was expressed as Trolox equivalents. This reaction takes place in the presence of a light quant registered by the detector (photomultiplier) [40-42]. The results were expressed in units of TROLOX (mmols).

Statistical analysis

All experiments were carried out in triplicate, and the results are expressed as mean \pm standard deviation (SD). Prior to inferential analyses, the normality of data distribution was assessed using the Shapiro–Wilk test. The statistical analysis was conducted with GraphPad Prism software (GraphPad Software, San Diego, CA, USA). Differences between samples were evaluated by two-way analysis of variance (ANOVA), followed by Tukey post hoc test, with statistical significance set at $p < 0.05$. In addition, the Pearson correlation (r) analysis was performed to assess the relationship between the ascorbic acid content and the antioxidant capacity across different ripening stages.

REFERENCES

1. L. P. Leong; G. Shui, *Food Chem.*, **2002**, 76, 69–75.
2. D. Feskanich; R. G. Ziegler; D. S. Michaud; E. L. Giovannucci; F. E. Speizer; W. C. Willett; G. A. Colditz, *J Natl Cancer Inst.*, **2000**, 92, 1812–1823.
3. A. D. Haegele; C. Gillette; C. O'Neill; P. Wolfe; J. Heimendinger; S. Sedlacek; H. J. Thompson, *Cancer Epidemiol. Biomark. Prev.*, **2000**, 9, 421–425.
4. K. B. Michels; E. Giovannucci; J. K. Joshipura; B. A. Rosner; M. J. Stampfer; C. S. Fuchs; G. A. Colditz; F. E. Speizer; W. C. Willett, *J Natl Cancer Inst.*, **2000**, 92, 1740–1752.
5. A. Sabra; T. Neticadan; C. Wijekoon, *Food Chem X*, **2021**, 12, 100149.
6. H. Wang, *Polymers*, **2025**, 17 (6), 750.
7. A. Ahmad; H. Ahsan, *J. Immunoass. Immunochem.*, **2020**, 41, 257–271.
8. H. Wang, *Expert Rev. Mol. Med.*, **2023**, 25, e24.
9. J. E. Klaunig, *Curr. Pharm. Des.*, **2018**, 24, 4771–4778.

10. V. Sosa; T. Moliné; R. Somoza; R. Paciucci; H. Kondoh; M.E. LLeonart, *Ageing Res. Rev.*, **2013**, 12, 376–390.
11. L. A. Terry, *Health-promoting Properties of Fruit and Vegetables*, Editura CAB International North, America, **2011**, pp.154.
12. C. Tardea, *Chimia si analiza vinului*. Editura Ion Ionescu de la Brad. București, Romania, **2007**, pp. 514.
13. C. Dani; L. S. Oliboni; R. Vanderlinde; D. Bonatto; M. Salvador; J. A. P. Henriques, *Food Chem. Toxicol.*, **2007**, 45, 2574-2580.
14. China Food Composition 2002, compiled by Institute of Nutrition and Food Safety, China CDC. Beijing: Peking University Medical Press, **2002**, pp. 82
15. B. Farida; R. Djamai; Y. Cadot, *J. Int. Sci. Vigne Vin.*, **2014**, 48, 153-162.
16. S. Tavarini; E. Degl'Innocenti; D. Remorini; R. Massai; L. Guidi; *Food Chem.*, **2008**, 107, 282-288.
17. N. Matei; S. Dobrinas; G. L. Radu; *Ovidius Univ. Ann. Chem.*, **2012**, 23, (2), 174-179.
18. N. Matei; S. Birghila; S. Dobrinas; P. Capota; *Acta Chim. Slov.*, **2004**, 51, 169-175.
19. N. Matei; V. Magearu; S. Birghila; S. Dobrinas; *Rev. Chi.*, **2004**, 55 (5), 294-296.
20. V. K. Gupta; R. Jain; K. Radhapyari; N. Jadon; S. Agarwal; *Anal. Biochem.*, **2011**, 408, 179–196.
21. V. Raghu; P. Kalpana; K. Srinivasan; *J. Food Compos. Anal.*, **2007**, 20, 529–533.
22. M. C. Yebra-Biurrun; R. M. Cespon-Romero; P. Bermejo-Barrera; *Mikrochim. Acta*, **1997**, 126, 53-58.
23. R. Zuo; S. Zhou; Y. Zuo; Y. Deng, *Food Chem.*, **2015**, 182, 242-245.
24. X. Han; J. Zhou; Y. Li; Y. Zhao; Y. Li; Y. Hua; T. Dong; F. Chai; *Food Chem.*, **2025**, 479, 143727.
25. J. Li; J. Zhang; X. Yang; A. Kong; N. Wang; J. Tang; X. Yu; *Food Chem.*, **2025**, 466, 2025, 142158.
26. M. Liang; Z. Han; M. Li; Y. Shen; Z. Liu; X. Geng; X. Li; Y. Cao; H. Shi; X. Li; S. He; P. Liu; *J. Food Compos. Anal.*, **2025**, 141, 2025, 107334.
27. R. Engel; L. Abrankó; E. Stefanovits-Bányai; P. Fodor; *Acta Aliment.*, **2010**, 39 (1), 48–58.
28. L. Novakova; P. Solich; D. Solichova; *Trends Anal. Chem.*, **2008**, 27, 10, 942-958.
29. I. Mato; S. Suarez-Luque; J.F. Huidobro; *Food Res. Int. I*, **2005**, 38, 1175–1188.
30. R. M. Uckoo; G.K. Jayaprakasha; S.D. Nelson; B.S. Patil; *Talanta*, **2011**, 83, 948–954
31. R. N. AlKaraki; S. K. Tarawneh; R. R. Haddadin; R. Aqil; R. M. Alkasasbeh; *Results Chem.*, **2024**, 10, 101701.
32. A. Wojdyło; Á. A. Carbonell-Barrachina; P. Legua; F. Hernández; *Food Chem.*, **2016**, 201, 307-314.

33. B. Kiss; D. S. Popa; G. Crisan; M. Bojita; F. Loghin F; *Farmacia*, **2009**, 57 (4), 432-441.
34. R. Ferreira Oliveira; C. Amorim Camara; M. F. Agrab; T. M. Sarmiento Silva; *Nat. Prod. Commun.*, **2012**, 12, 1597-1600.
35. A. Kowalczyk; I. Biskup; I. Fecka, *Nat. Prod. Commun.*, **2012**, 12, 1631-1634.
36. W. M. Nuzul; H. Wan Salleh; F. Ahmad, K. Heng Yen; H. Mohd Sirat; *Nat. Prod. Commun.*, **2012**, 12, 1659-1662.
37. G. Szabo; E. Csiki; Á.-F. Szoke; N. Muntean, *Studia UBB Chemia*, LXVII, **2022**, 3, 7-16.
38. A. A. Adehuwa-Olabode; A. Sautreanu; L. Vlase, A.-M. Vlase, D. Muntean, *Studia UBB Chemia*, LXVII, **2022**, 3, 17-35.
39. L. David; B. Moldovan; *Studia UBB Chemia*, LXVII, **2022**, 3, 37-44.
40. <http://analitica.inycom.es/es-es/>.
41. G. Stanciu; C. Chirila; S. Dobrinás; T. Negreanu-Pirjol; *Rev. Chim. (Bucharest)*, **2010**, 61 (1), 41-44.
42. A. Popescu; T. Negreanu – Pirjol; C. Rosca; M. Arcus; L. Bucur; V. Istudor *Ovidius Univ. Ann. Che.*, **2011**, 22, 62-66.
43. <http://www.murfatlar.com/site/>
44. ASRO Standard Roman, SR EN 14130. *Produse alimentare, Determinarea vitaminei C prin HPLC, Comitetul European de Standardizare*, **2003**.
45. I. G. Tanase; G. L. Radu; A. Pana; M. Buleandra; *Validarea metodelor analitice, Principii teoretice si studii de caz*, Ed. Printech, Bucuresti, Romania, **2007**, pp. 111.
46. N. Matei; G. L. Radu; G. Truica; S. Eremia; S. Dobrinás; G. Stanciu; A. Popescu; *Anal. Meth.*, **2013**, 5 (18), 4675-4679.
47. A. Kesic; M. Mazalovic; A. Crnkic; B. Catovic; S. Handzidedic; G. Dragosevic; *Eur. J. Sci. Res.*, **2009**, 32, 95-101.
48. J. Lachman; M. Sulc; K. Faitova; V. Pivec; *Int. J. Wine Res.*, **2009**, 1, 101-121.

A NEW HPLC METHOD APPROACH FOR THE QUANTIFICATION OF QUERCETIN IN SEVEN DIFFERENT ANATOLIAN PLANT EXTRACTS

Aysun DİNÇEL^{a*}, Murat KÜRŞAT^b, İbrahim Seyda URAS^c,
Belma KONUKLUGİL^d

ABSTRACT. The use of natural antioxidants, especially phenolic compounds derived from foods and plants, has been extensively investigated in the context of preventive and therapeutic medicine. Quercetin, a flavonoid of the flavonol class, exhibits multiple health-promoting properties, including antioxidant, antimicrobial, and antifungal activities. The present study aimed to quantify quercetin in seven plant species native to Türkiye: *Zosima absinthifolia*, *Anarrhinum orientale*, *Fumaria asepalae*, *Ferulago stellata*, *Salvia pseudeuphratica*, *Rhabdosciadium microcalycinum*, and *Diplotaenia cachrydifolia*. A novel reversed-phase HPLC-DAD method was developed for the determination of quercetin in these plant extracts and subsequently validated in accordance with ICH guidelines. The method demonstrated linearity over the concentration range of 0.4–1.2 µg/mL ($r^2 > 0.999$), with mean recovery values ranging from 96.5% to 98.3%. All validation parameters were evaluated and confirmed in accordance with ICH guidelines, demonstrating the method's reliability for quantifying quercetin in plant matrices.

Keywords: *Zosima absinthifolia*, *Anarrhinum orientale*, *Fumaria asepalae*, *Ferulago stellata*, *Salvia pseudeuphratica*, *Rhabdosciadium microcalycinum*, *Diplotaenia cachrydifolia*, Quercetin, HPLC, Validation

^a Department of Analytical Chemistry, Faculty of Pharmacy, Lokman Hekim University, Ankara, Türkiye

^b Department of Biology, Faculty of Science and Arts, Bitlis Eren University, Bitlis, Türkiye

^c Department of Pharmacognosy, Faculty of Pharmacy, Ağrı Ibrahim Cecen University, Ağrı, Türkiye

^d Department of Pharmacognosy, Faculty of Pharmacy, Lokman Hekim University, Ankara, Türkiye

* Corresponding author: aysun.dincel@lokmanhekim.edu.tr



INTRODUCTION

Flavonoids are low molecular mass plant secondary metabolites that can serve as plant growth promoters or inhibitors by mediating plant-microbe interactions. Various external variables also influence the formation of these metabolites. Developmental factors alter the initiation and differentiation of plant parts responsible for secondary metabolite synthesis and quantity. Many factors also play a role in altering the biosynthesis of these metabolites (such as region, height, soil structure, climate, and growing conditions) [1, 2].

There are differences in the chemical structure of flavonoids depending on the degree of hydroxylation and polymerization, as well as structural classes, other conjugations, and substitutions. Flavonoids can be classified into many subclasses comprising flavonols (e.g., quercetin and kaempferol); flavonols constitute a subclass of flavonoids characterized by the presence of a ketone functional group [3], flavones (e.g., apigenin and flavones), isoflavonoids, flavanones (e.g., flavanone and hesperetin), catechins, anthocyanidins, and isoflavones. There are various studies and publications on the effectiveness of flavonoids against free radicals and their use in treatment. Flavonoids, characterized by their structural diversity and widespread occurrence in plants, confer numerous health benefits, including potent antioxidant, anti-inflammatory, antibacterial, anti-ageing, and metabolic disease-modulating properties. Emerging evidence also highlights their potential in preventing cardiovascular disorders. Diets rich in flavonoids have been linked to improved endothelial function, lower blood pressure, and a reduced risk of atherosclerosis. Specific flavonoids, such as quercetin and catechins, have been shown to regulate nitric oxide production, thereby promoting vasodilation and enhancing blood flow, which are crucial for maintaining cardiovascular health. Beyond their cardiovascular effects, flavonoids may exert neuroprotective actions by alleviating oxidative stress and inflammation, key mechanisms involved in the development of neurodegenerative conditions, including Alzheimer's and Parkinson's diseases [4-7].

Quercetin, a plant pigment, is classified as a plant secondary metabolite of flavonoids and grouped under flavonols. It is widely present in tea and onions. Additionally, its antioxidant properties were well known. Quercetin exhibits a broad spectrum of potential health-promoting effects in humans. Clinical investigations have been carried out in specific contexts, such as its role in lowering blood pressure [8]. A substantial body of *in vitro* and *in vivo* animal research has explored its antioxidant capacity [8].

Furthermore, both experimental models and cell-based studies have demonstrated its antiallergic and anti-asthmatic activities. In addition, extensive *in vitro* and *in vivo* evidence supports the anticancer properties of quercetin [9]. In addition to its antioxidant properties, it also provides numerous

medical benefits, including anticancer, antiviral, anti-diabetic, anti-inflammatory, and antitumor effects. Quercetin is a yellow, crystalline powder; despite its general insolubility, it is slightly soluble in alcohol, for instance, ethanol [10-12].

In this study, *Zosima absinthifolia*, *Anarrhinum orientale*, *Fumaria asepalae*, *Ferulago stellata*, *Salvia pseudeuphratica*, *Rhabdosciadium microcalycinum*, and *Diplotaenia cachrydifolia* were studied for the determination of quercetin content. All plants were collected from different areas of Türkiye. Previous studies on *Zosima absinthifolia* and *Salvia pseudeuphratica* have demonstrated remarkable antioxidant and anticholinesterase activities [13, 14]. *Anarrhinum orientale* is recognized as a medicinal plant and exhibits antimicrobial properties [15]. Previous studies have shown that *Fumaria asepalae* has antifungal and antibacterial properties [16]. *Diplotaenia cachrydifolia* and *Rhabdosciadium microcalycinum* are endemic species [14] and are known as medicinal plants [12].

In light of the significant health-promoting properties of quercetin, the present study aimed to quantify its content in seven plant species and to assess those with the highest levels for potential applications in dietary supplements or as sources of bioactive compounds.

To date, no studies have quantified quercetin in these plant species, highlighting a critical gap in the literature and underscoring the need to evaluate their potential as sources of this bioactive compound.

A simple and selective chromatographic method was developed for the quantification of quercetin. Validation parameters for the developed method were also studied according to the International Council for Harmonisation of Technical Requirements for Pharmaceuticals for Human Use (ICH) requirements for specificity, accuracy, linearity, and precision (ICH) [17, 18].

RESULTS AND DISCUSSION

Analytical procedure

Concentrations of quercetin in the plant extract samples were measured by using high-performance liquid chromatography with a diode array detector (HPLC-DAD) system. A new and simple chromatographic method was developed for the quantitative analysis of quercetin. Each solution was injected into the HPLC system in duplicate, and the mean peak area was calculated.

Validation studies

Specificity

There was no interfering peak at the intended separation in the analytical technique.

Linearity

The new chromatographic method was developed and applied for the quantification of quercetin in plant extract. The calibration curve was drawn using concentrations of 0.4, 0.6, 0.8, 1.0, 1.1, and 1.2 µg/mL ($r^2 > 0.999$), as shown in Table 1.

Table 1. Calibration curve parameters (n=6)

	Slope	Intercept	r^2	Slope RSD	Intercept RSD	Residual sum of squares
$y = ax + b$	19251.33	-2808.6	0.99914	0.848	0.751	4.0

RSD: Relative Standard Deviation

LOD and LOQ

The LOD and LOQ values were found to be 0.1 µg/mL and 0.4 µg/mL, respectively.

System suitability test

At least two of these criteria are required for the acceptability of system suitability for the developed method. The values obtained meet the accepted criteria of a tailing factor ≤ 1.5 and a theoretical number of plates > 2000 , and the system was found to be suitable for analyzing the targeted substance [19].

Accuracy and precision

The mean recovery values were found in the range of 96.5% and 98.3%. For precision studies, the intra-day and inter-day variations were carried out for 0.6, 1.0, and 1.2 µg/mL. The results of the method throughout the linear range, the highest RSD value for six replicate sample analyses, were 1.12% for intra-day precision studies and 1.28% for inter-day precision studies, which are less than 2.0% [17, 18]. The acceptability criteria specified that accuracy should be within 85–115% of the nominal values, and precision should demonstrate a relative standard deviation (RSD) of not more than 15% (**Table 2**).

Table 2. Inter-day and intra-day accuracy and precision results (n=6)

	Inter-day			Intra-day		
Added (µg/mL)	0.6	1.0	1.2	0.6	1.0	1.2
Found, \bar{x} µg/mL	0.59	0.97	1.17	0.59	0.97	1.19
Precision; RSD (%)	1.28	1.01	0.69	1.12	0.94	0.47
Recovery (%)	98.3	96.5	97.8	98.6	96.8	98.2

\bar{x} : Mean value, RSD: Relative Standard Deviation.

A NEW HPLC METHOD APPROACH FOR THE QUANTIFICATION OF QUERCETIN IN SEVEN
DIFFERENT ANATOLIAN PLANT EXTRACTS

The peak of quercetin was well separated from the other interfering peaks, and good resolution was achieved. Figure 1 shows the chromatogram of a quercetin-free plant extract obtained from *Salvia pseudoeuphratica*. Figure 2 also shows a plant extract (obtained from *Fumaria asepalae*) chromatogram that contains 0.808 mg/g of quercetin. There was no interference around the quercetin peak. The retention times for the quercetin peak were found as 6.27 ± 0.008 min (Mean \pm Standard Deviation). **Table 3** gives the results of quantified quercetin concentrations from the different plant extracts.

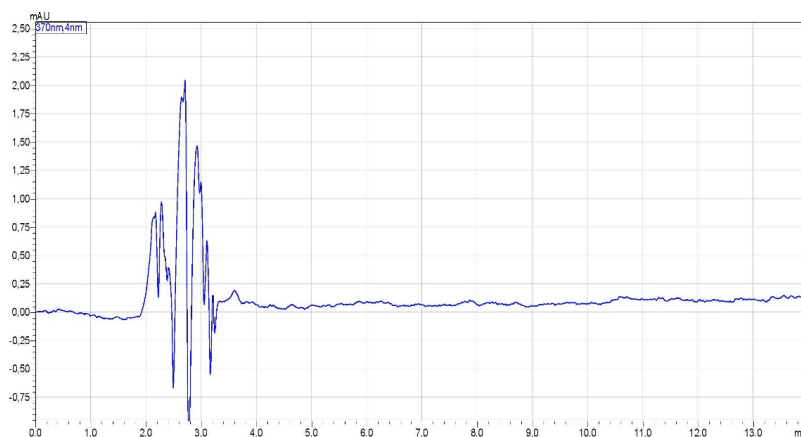


Figure 1. Chromatogram of the quercetin-free plant extract
(*Salvia pseudoeuphratica*)

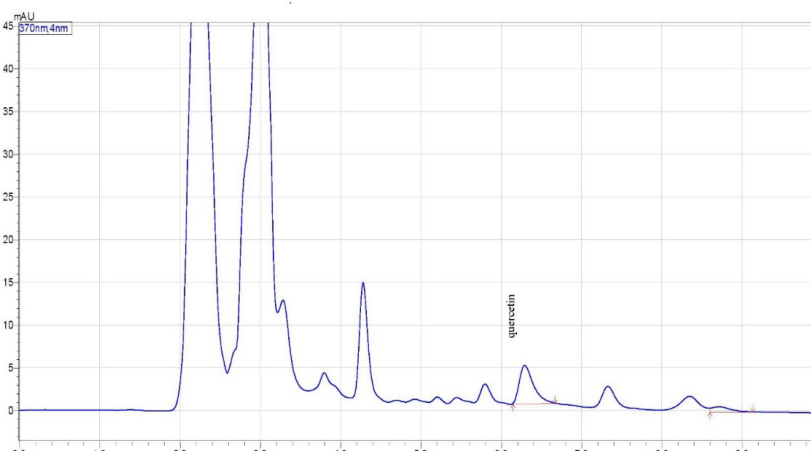


Figure 2. Chromatogram of plant extract (*Fumaria asepalae*)
containing 0.808 mg/g of quercetin

There are several methods for the determination of quercetin in plants. The developed method is superior according to the used mobile phases and short retention time. The chromatographic system used is an isocratic elution, and complex and gradient mobile phase mixtures were not used for the quantitation of quercetin. In the literature, studies have reported quercetin sensitivity at the mg/g level or as molarity. The developed method is more sensitive and selective compared to other methods, especially in terms of LOD and LOQ values (0.1 µg/mL and 0.4 µg/mL) [20-22]. For the plant extracts studied, quercetin content could not be determined in two of them. Among the analyzed samples, *Fumaria asepal*a exhibited the highest quercetin concentration (0.807 mg/g extract), which was approximately 13 times greater than that of the most dilute sample (*Ferulago stellata*). The extracts of *Anarrhinum orientale* and *Rhabdosciadium microcalycinum* showed nearly identical quercetin concentrations (**Table 3**).

Table 3. Quercetin from the plant extract (n=6)

Plant	Calculated concentration (mg/g extract) ± SD
<i>Zosima absinthifolia</i>	0.197 ± 0.03
<i>Anarrhinum orientale</i>	0.118 ± 0.001
<i>Fumaria asepal</i> a	0.808± 0.019
<i>Ferulago stellata</i>	0.063 ± 0.003
<i>Salvia pseudeuphratica</i>	Not determined
<i>Rhabdosciadium microcalycinum</i>	0.105 ± 0.002
<i>Diplotaenia cachrydifolia</i>	Not determined

SD: Standard Deviation

CONCLUSION

In the present study, a new, simple, accurate, and precise reversed-phase HPLC-DAD method was developed and validated for the determination of quercetin in accordance with guidelines of the International Conference on Harmonization (ICH). This method was applied easily for the quantification of quercetin in plant extracts. In this study, seven different plant extracts obtained from different areas of Türkiye were studied by using this novel chromatographic method. Studied plants have also not been analyzed for the quercetin content before. This study gives a new approach for the identification of these seven plants.

EXPERIMENTAL SECTION

Chemicals and reagents

Analytical standard of Quercetin was purchased from Merck, (Darmstadt, Germany). Acetonitrile (HPLC grade, CARLO ERBA, Italy), methanol (HPLC grade, CARLO ERBA, Italy), and NaH₂PO₄ (Sigma-Aldrich, USA) were purchased. Quercetin stock solution was prepared with ethanol at 1 mg/mL, and the solution to be used in the analysis was prepared daily by diluting the stock solutions with an ethanol: water (1:1, v/v) mixture to the desired concentration values. Stock solutions were stored at -20 °C for only 1 week.

Plant Materials

Murat Kürşat collected and identified every plant from various parts of Türkiye in 2020. In September, *Diplotaenia cachrydifolia* Boiss. was collected at a height of 2250 meters on Karz Mountain in Bitlis. In September, *Rhabdosciadium microcalycinum* Hand.-Mazz. and *Ferulago stellata* Boiss. were collected at a height of 1750 meters on Kambos Mountain in Bitlis, in August, *Anarrhinum orientale* Benth. was collected at a height of 1600 meters on Kambos Mountain in Bitlis. In May, *Zosima absinthifolia* (Vent.) Link and *Fumaria asepala* were collected from the Baskil region of Elazığ. The plant *Salvia pseudeuphratica* Rech.f. was collected from Keban, Elazığ, in July. Bitlis Eren University has voucher specimens for every plant.

Plant extraction

50 g of dried plant material was obtained from each plant. Coarsely ground part of each plant was extracted with methanol at room temperature. The extraction procedure was carried out four times for each plant, and all plants were extracted with 1 L of freshly added methanol for 12 hours using a magnetic stirrer. At the end of the extraction studies, four extracts of solvent content were pooled. The pooled methanol phase evaporated with a rotary evaporator, and the dry crude extracts were obtained. Extracts of *Zosima absinthifolia*, *Anarrhinum orientale*, *Fumaria asepala*, *Ferulago stellata*, *Salvia pseudeuphratica*, *Rhabdosciadium microcalycinum*, and *Diplotaenia cachrydifolia* were studied for the application of a new chromatographic method.

Extract analysis procedure

Samples were accurately weighed using an analytical balance (Ohaus, USA), approximately 0.05 g, into the 15 mL Falcon tube and dissolved

with 10 mL of HPLC-grade methanol. The mixtures were sonicated in an ultrasonic bath for 30 min. Then the mixtures were stirred for 30 min with a magnetic stirrer. The mixtures were diluted with HPLC-grade methanol ten times or not according to the sample content. After the dissolving procedure, solutions were filtered by a 0.22 μm PTFE syringe filter, and then 10 μL of an aliquot was injected into the HPLC system. This procedure was repeated twice for each sample.

Instrumentation and chromatographic conditions

The chromatographic system consisted of a Shimadzu liquid chromatograph system (LC-2030 2D Plus Prominence-I), 10 μL injection loop, an autosampler, a Diode Array Detector, and a system controller using CLASS-VP 5.0 (Shimadzu, Kyoto, Japan). The separation was achieved by XBridge, C18 (250 x 4.6 mm (I.D.), particle size 5 μm) analytical column (The column temperature was 20 $^{\circ}\text{C}$) (Waters, Milford, MA, USA). The mobile phase consisted of 20 mM NaH_2PO_4 (pH=4.16) and acetonitrile (65:35; (v/v)) in isocratic mode, and the detector wavelength was set to 370 nm. A 10 μL aliquot of the sample solution was injected into the HPLC system at a flow rate of 1.1 mL/min. For preparing all solutions, type 1 water (Simplicity 185 Water System, Millipore Corp., Bedford, MA, USA) was used. The mobile phase was filtered through a membrane filter (pore diameter of 0.45 μm) and kept in an ultrasonic bath for 15 min to remove the soluble gases.

Validation studies

Specificity

Selectivity was tested after the injection of drug-free plant extract and the mobile phase injection.

Linearity

Linearity studies were conducted using standard solutions prepared by quantitative dilution of the stock solution. In this method, a calibration curve was constructed by plotting the concentration values against the peak area of quercetin. The slope, intercept, and correlation coefficient of the calibration curve ($y = ax + b$) were calculated.

LOD and LOQ

The limit of detection (LOD) was calculated as the signal-to-noise (S/N) ratio of 3:1 ($n=6$), and the limit of quantification (LOQ) value was calculated as the signal-to-noise (S/N) ratio of 10:1 ($n=6$) for standard solution analyses.

System suitability test

System suitability tests were performed using 1 µg/mL quercetin, and the results were evaluated based on retention time, injection repeatability, capacity factor, tailing factor, and the theoretical number of plates. The values obtained must meet the accepted criteria for good separations: capacity factor (k') values between 1 and 10, tailing factor ≤ 1.5, and theoretical number of plates > 2000.

Accuracy and Precision

For accuracy analyses, recovery values were calculated for six repeated analyses (for 1 µg/mL of quercetin) by using spiking of a drug-free plant extract sample. For the reproducibility of the method, three concentration values in the linear range were analyzed at six replicates. For accuracy and precision values, relative standard deviation (RSD) values were calculated and evaluated [17, 18].

REFERENCES

1. B. Sultana; F. Anwar; *Food Chemistry*, **2008**, 10, 879-884
2. I. Del Valle; T. M. Webster; H. Y. Cheng; J. E. Thies; A. Kessler; M. K. Miller; Z. T. Ball; K. R. MacKenzie; C. A. Masiello; J. J. Silberg; J. Lehmann; *Science advances*, **2020**, 6(5), eaax8254.
3. A. N. Panche; A. D. Diwan; S. R. Chandra; *Journal of nutritional science*, **2016**, 5, e47.
4. A. N. Panche; A. D. Diwan; S. R. Chandra; *J. Nutr. Sci.*, **2016**, 5, e47.
5. S. Tang; B. Wang; X. Liu; W. Xi; Y. Yue; X. Tan; J. Bai; L. Huang; *Food Frontiers*, **2025**, 6, 218-247.
6. A. Roy; A. Khan; I. Ahmad; S. Alghamdi; B. S. Rajab; A. O. Babalghith; M. Y. Alshahrani; S. Islam; M. R. Islam; *Biomed. Res. Int.*, **2022**, 5445291.
7. B. A. Owona; W. A. Abia; P. F. Moundipa; *Int. Immunopharmacol.*, **2020**, 84, 106498.
8. K. J. Meyers; J. L. Rudolf; A. E. Mitchell; *J. Agric. Food Chem.*, **2008**, 56, 830-836.
9. J. Lu; D. M. Wu; Y. L. Zheng; *J. Pathol.*, **2010**, 222, 199-212.
10. R. Balestrini; C. Brunetti; M. Cammareri; S. Caretto; V. Cavallaro; E. Cominelli; M. De Palma; T. Docimo; G. Giovino; S. Grandillo; F. Locatelli; *Int. J. Mol. Sci.*, **2021**, 22, 2887
11. D. Hoxha; B. Bauer; G. Stefkov; G. Hoxha; *Macedonian Pharmaceutical Bulletin*, **2022**, 68(2), 3-5
12. L. Nohutçu; M. Tunçtürk; R. Tunçtürk; *Yüzüncü Yıl Üniversitesi Fen Bilimleri Enstitüsü Dergisi*, **2019**, 24(2), 142-151

13. S. Karakaya; M. Koca; S. Yılmaz; K. Yıldırım; N. Pınar; B. Demirci; M. Brestic; O. Sytar; *Molecules*, **2019**, 24(4), 722
14. M.K. Erdogan; R. Gundogdu; Y. Yapar; I.H. Gecibesler; M. Kirici; L. Behcet; B. Tuzun; P. Taslimi; *ChemistrySelect*, **2022**, 7(17), e202200400
15. M. Kakar; M.U. Amin; S. Alghamdi; M.U.K. Sahibzada; N. Ahmad; N. Ullah; *Evidence-Based Complementary and Alternative Medicine*, **2020**, 3903682
16. S. Khamtache-Abderrahim; M. Lequart-Pillon; E. Gontier; I. Gaillard; S. Pilard; D. Mathiron; H. Djoudad-Kadji; F. Maiza-Benabdesselam; *Industrial Crops and Products*, **2016**, 94, 1001-1008
17. ICH, **2014**. Harmonized Tripartite Guideline, Validation of analytical procedures: Text and Methodology Q2(R1), ICH Steering Committee, <https://database.ich.org/sites/default/files/Q2%28R1%29%20Guideline.pdf>. (accessed 30 January 2025)
18. ICH, **2022**. Harmonized Tripartite Guideline, on validation of analytical procedures Q2(R2), ICH Steering Committee, https://database.ich.org/sites/default/files/ICH_Q2-R2_Document_Step2_Guideline_2022_0324.pdf. (accessed 30 January 2025)
19. The United States Pharmacopoeia (USP), **2000**, 24th revision, Easton, Rand Mc Nally Taunton.
20. K. Hui Mian; S. Mohamed; *J. Agric. Food Chem.* **2001**, 49, 3106-3112
21. C. Gang; Z. Hongwei; Y. Jiannong; *Analytica Chimica Acta*, **2000**, 423, 69-76.
22. Y. Wang; J. Cao; J.H. Weng; S. Zeng; *Journal of pharmaceutical and biomedical analysis*, **2005**, 39(1-2), 328–333.

ANTIOXIDANT, ANTI-HAEMOLYTIC ACTIVITY, VITAMIN AND ELEMENT PROFILE OF *RHAMNUS CORNIFOLIUS*

Ahmet BAKIR^{a*}, Mehtap BAKIR^b, Suat EKİN^a,
Mehmet FIRAT^c

ABSTRACT. The antioxidant, antiradical, and anti-hemolytic activities of the methanol extract of *Rhamnus cornifolius* leaves were investigated, along with the determination of element and vitamin levels in the dried plant material. Element analyses were determined by ICP-OES dry ashing, vitamins by HPLC, vitamin C, total phenolic, flavonoid, antioxidant capacity, DPPH[•], ABTS^{•+} and anti-haemolytic activity spectrophotometrically. Total phenolic, flavonoid and antioxidant capacities of the plant were measured as 4.482 ± 0.159 mg GA/g, 27.420 ± 2.551 mg QE/g and 41.795 ± 18.506 mM AA/g, while retinol, α -tocopherol, phylloquinone and ascorbic acid as 0.2167 ± 0.019 , 4.313 ± 0.685 , 0.5622 ± 0.09 μ mol/kg and 403.631 ± 8.682 mg 100/g. IC₅₀ values of DPPH[•], ABTS^{•+} and anti-haemolytic assays were determined as 33.974 ± 1.918 (BHT = IC₅₀ 26.979 ± 1.116), 58.197 ± 1.826 (trolox = IC₅₀ 27.854 ± 1.352) and 68.51 ± 5.33 (trolox = IC₅₀ 44.040 ± 0.290) μ g/mL, respectively. According to the results of this study, it was determined that the vitamin and element content of the plant was at high level, ABTS^{•+} and DPPH[•] tests showed a promising antioxidant power. These findings represent the first report in the literature, and the plant's composition was evaluated as a basis for future in vivo studies.

Keywords: *Rhamnus cornifolius*, methanol extract, antioxidant, element, vitamin, anti-haemolytic activity

INTRODUCTION

There are many definitions of medicinal and aromatic plants in the literature. According to the Food and Agriculture Organisation of the United Nations (FAO), medicinal and aromatic plants are defined as plants that provide

^a Van Yuzuncu Yil University, Department of Chemistry, Faculty of Science, 65800, Van, Türkiye

^b Van Yuzuncu Yil University, Başkale Vocational School, Organic Agriculture, 65800, Van, Türkiye

^c Van Yuzuncu Yil University, Department of Biology, Faculty of Education, 65800, Van, Türkiye

* Corresponding author: ahmetbakir@yyu.edu.tr



medicine to people to prevent diseases, maintain health and treat ailments [1]. At least 8000 phenolic substances of different amounts and qualities have been identified so far in the structure of plants [2]. These compounds play an important role in destroying or inhibiting free radicals. Thus, they increase the body's resistance to cell damage and prevent unwanted oxidation products [3].

Vitamins are compounds that are essential for performing some special cellular events other than proteins, lipids and carbohydrates which are macronutrients and are needed at trace levels in the organism [4]. Vitamins have been found to have important roles in reactions involving free radicals, electron transport and membrane biochemical strengthening [5]. Fat-soluble vitamins A, D, E and K do not need to be taken frequently when they are stored in the liver and fat [6]. However, for this, it is necessary to take these vitamin elements necessary for tissues with appropriate nutrition.

Dietary minerals, which are not included in the term vitamins but support health, are essential nutrients for the body [7]. Functioning as catalytic cofactors of enzymes, the roles and functions of these elements are extremely diverse and vital. They are useful for plant growth, development and yield [8]. They interact directly with free radical formation and free radical scavengers. Maintaining the integrity of the cell membrane depends on a protection or repair mechanism that can neutralise oxidative reactions [9]. Even minor deficiencies in vitamins and minerals can lead to serious health issues, though they often go unnoticed until they become severe [7]. Preventing this unfavourable situation is possible with an appropriate diet.

Hakkari Province, located in the Eastern Anatolia Region of Turkey, has different ecological and climatic characteristics, high mountains and a wide range of endemic plant diversity as a result of the plant flora spread over a very large area. *Rhamnus Cornifolius Boiss. & Hoh.* belongs to the *Rhamnaceae* family and is generally distributed in Northern Iraq, South-Western Iran and Hakkari Province in Turkey. *R. cornifolius* is one of 22 *Rhamnus* species growing naturally in Turkey [10].

What makes these plant species valuable are the yellow coloured dyes contained in their fruits. These colouring substances are flavonoids and partly anthroquinones. Anthroquinones are organic compounds found in some plants. They are used as dyes, pigments and also for medicinal purposes. The plant has been traditionally used for its antioxidant and anti-inflammatory effects in the treatment of constipation related to liver diseases [11]. Numerous studies, both past and ongoing, have investigated the potential of plant-derived phytochemicals in the prevention of diseases such as cardiovascular disorders, cancer, and osteoporosis. [12,13].

The aim of this study was to investigate the antioxidant, antiradical properties, bioelements and vitamin content of the methanol extract of the leaf part of *R. cornifolius* growing in Hakkari province of Turkey, which has a rich flora,

by various methods. For this purpose, total phenolic, flavonoid and antioxidant capacity of the plant and vitamin A, E, K and C contents were determined. DPPH[•], ABTS^{•+} and phenylhydrazine radical scavenging capacity and element levels were also determined.

RESULTS AND DISCUSSION

Total antioxidant capacity, total phenolic and total flavonoid content, DPPH[•], ABTS^{•+} and anti-haemolytic activity levels were measured to determine the antioxidant properties of the methanol extract of *R. cornifolius* leaves. In addition, the levels of vitamins A, E, K and C and elements (K, Na, Ba, V, Ti, Cr, Cu, Sr, As, Se, Cd, Pb, Mo, Fe, Mn, Al, Zn, Co) of *R. cornifolius* were determined and all results are shown in Table 1 and Table 2.

Table 1. Vitamins A, E, K and C, total phenolic and flavonoid content, total antioxidant capacity, element (Ba, V, Ti, Cr, Cu, Sr, As, Se, Cd, Pb, Mo, Fe, Mn, Al, Zn, Co, K and Na) levels of *R. cornifolius*.

Parameters	<i>Rhamnus cornifolius</i> ($\bar{X} \pm \text{SEM}$)
Retinol (μmol/kg)	0.2167 ± 0.0190
α-tocopherol (μmol/kg)	4.3130 ± 0.6850
Phylloquinone (μmol/kg)	0.5622 ± 0.0900
Vitamin C (mg 100/g)	403.6310 ± 8.6820
Total phenolic content (mg GAE/g)	4.4820 ± 0.1590
Total flavonoid content (mg QE/g)	27.4200 ± 2.5510
Total antioxidant capacity (mM A.A/g)	41.7950 ± 18.5060
Ba (μmol/kg)	18.6250 ± 0.6090
V (μmol/kg)	5.8710 ± 0.0740
Ti (μmol/kg)	19.3550 ± 0.4620
Cr (μmol/kg)	3.5240 ± 0.6650
Cu (μmol/kg)	9.1210 ± 0.4550
Sr (mmol/kg)	0.0443 ± 0.0015
As (μmol/kg)	0.5240 ± 0.0550
Se (μmol/kg)	1.0650 ± 0.0360
Cd (μmol/kg)	0.0720 ± 0.0058
Pb (μmol/kg)	0.4490 ± 0.1600
Mo (μmol/kg)	0.0448 ± 0.0200
Fe (mmol/kg)	0.6850 ± 0.0132
Mn (μmol/kg)	142.8090 ± 4.3980
Al (μmol/kg)	6.6964 ± 0.3500
Zn (μmol/kg)	24.6830 ± 1.6380
Co (μmol/kg)	17.5250 ± 0.0125
K (mmol/kg)	3.0010 ± 0.0041
Na (mmol/kg)	1.8940 ± 0.1540

Values are expressed as mean ± standard error of the mean ($\bar{X} \pm \text{SEM}$).

Table 2. Values of % inhibition and IC₅₀ (µg/mL) in methanol extracts of leaf of *R. cornifolius* compared with a positive controls.

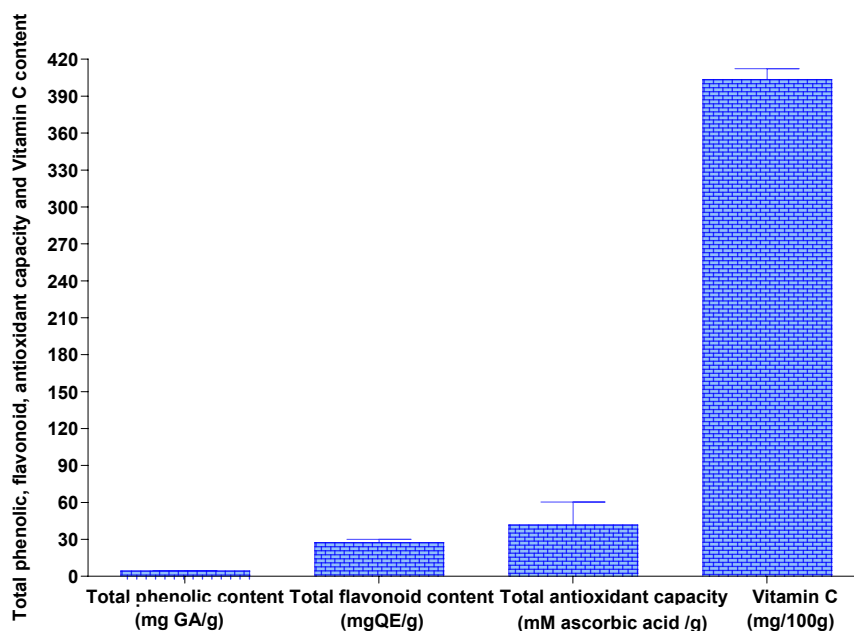
Control		% Inhibition $\bar{X} \pm \text{SEM}$	IC ₅₀ (µg/mL) $\bar{X} \pm \text{SEM}$
DPPH*		65.339 ± 0.443	33.974 ± 1.918
		74.792 ± 0.764	26.979 ± 1.116
ABTS**	BHT	89.333 ± 2.571	58.197 ± 1.826
		95.493 ± 0.849	27.854 ± 1.352
	Trolox		
PhNHNH ₂		71.560 ± 2.390	68.510 ± 5.330
	Trolox	58.220 ± 0.310	44.040 ± 0.290

Values are expressed as mean ± standard error of the mean ($\bar{X} \pm \text{SEM}$). Samples were carried out in triplicate. DPPH*: 2,2-diphenyl-1-picrylhydrazyl; ABTS**: (2,2'-azinobis (3-ethylbenzothiazoline-6-sulfonic acid)); PhNHNH₂: Phenylhydrazine.

DPPH: $y = 6E-05x^2 + 0.1286x + 45.514$; ABTS: $y = -0.0002x^2 + 0.5555x + 16.444$;

PhNHNH₂: $y = -15.18\ln(x) + 114.52$

Total phenolic, flavonoid, antioxidant capacity and vitamin C content of the plant methanol extract were calculated with the help of standard graphs and shown in Figure 1.

**Figure 1.** Total phenolic, flavonoid, total antioxidant capacity and vitamin C content of *R. cornifolius*.

Comparison with positive controls (BHT and trolox) was performed to determine the scavenging of radicals (DPPH[•], ABTS^{•+}) and haemolysis (PhNHNH₂) of the plant methanol extract. The % inhibition, % haemolysis and IC₅₀ values calculated after DPPH[•]/BHT, ABTS^{•+}/trolox and PhNHNH₂/trolox comparisons were determined and shown in Figure 2, Figure 3.

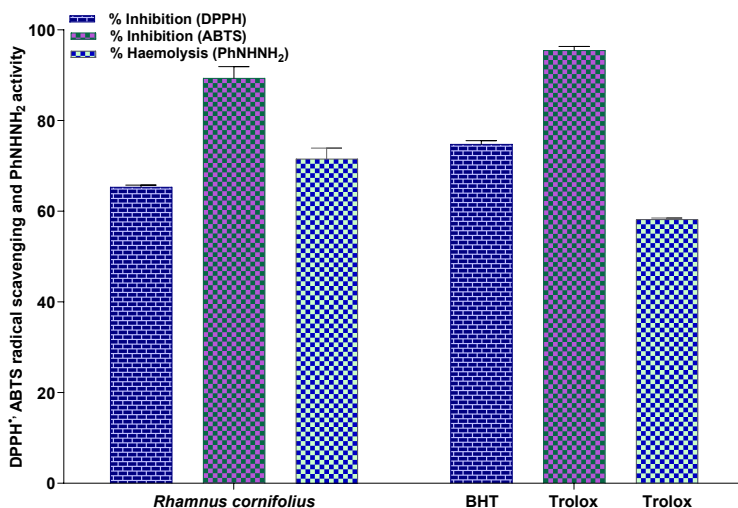


Figure 2. % inhibition values of BHT and Trolox used in comparison with DPPH, ABTS and anti-hemolytic activity of *R. cornifolius*

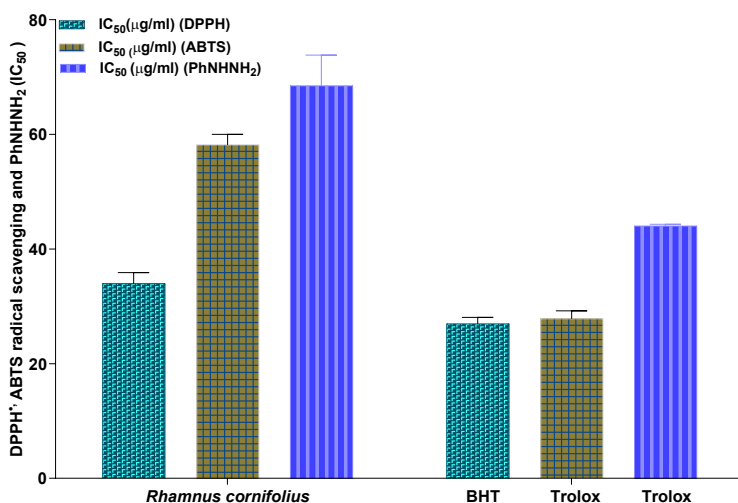


Figure 3. IC₅₀ values of BHT and Trolox used in comparison with DPPH, ABTS and anti-hemolytic activity of *R. cornifolius*

The element content of the dry leaves of *R. cornifolius* was determined and all the determined amounts are expressed in Figure 4, Figure 5 and Figure 6.

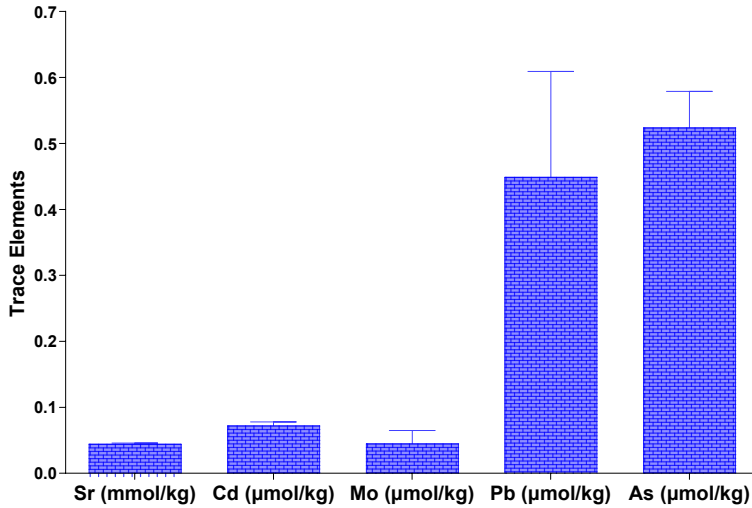


Figure 4. Trace element (Sr, Cd, Mo, Pb, As) levels of dry leaf parts of *R. cornifolius*.

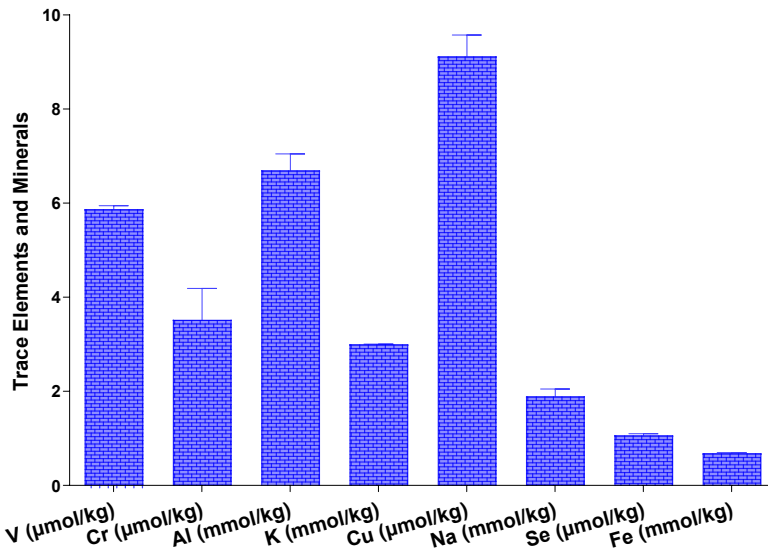


Figure 5. Element (V, Cr, Al, Cu, Se, Fe, K and Na) levels of *R. cornifolius* ry leaf parts.

ANTIOXIDANT, ANTI-HAEMOLYTIC ACTIVITY, VITAMIN AND ELEMENT PROFILE OF
RHAMNUS CORNIFOLIUS

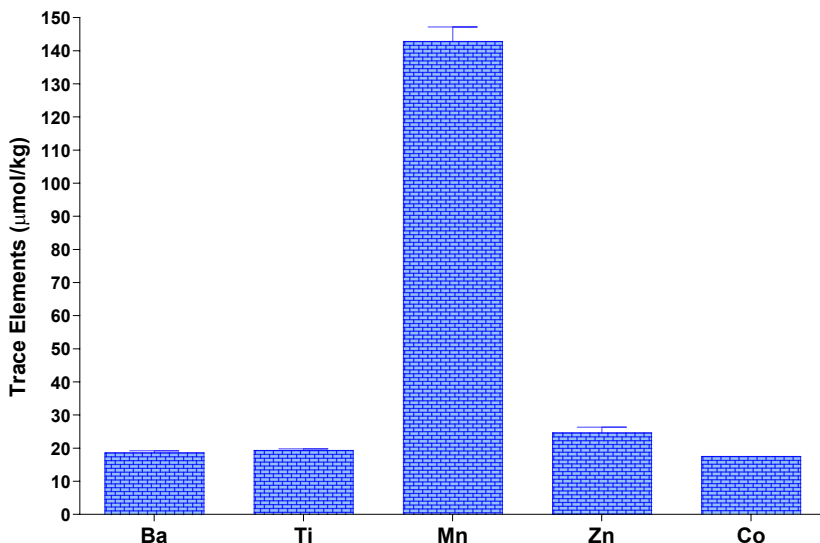


Figure 6. Element (Ba, Ti, Mn, Zn, Co) levels of *R. cornifolius* dry leaf parts.

Since vitamins are not produced in appropriate amounts by bodily metabolic processes, they must be taken in the diet at the necessary and sufficient level [7]. According to the World Health Organisation (WHO) data, 2 billion people face micronutrient deficiency. This deficiency partly includes vitamins A, D and various B vitamins and essential minerals [14]. Vitamin C, which is included in the subgroup of vitamins, shows antioxidant properties by minimising the damage caused by free radicals to cells. On the other hand, this vitamin, which is a common dietary supplement, is also a prerequisite for the production of collagen, the conversion of iron into a form that is easily absorbed in the intestines and the synthesis of the hormone serotonin, which is secreted for the regular functioning of the immune system [6]. The antioxidant properties of α -tocopherol, the most common form of vitamin E, are well known. This property is mainly due to the accepted idea that it terminates the chain reactions resulting from peroxy radicals caused by free radicals [15]. Recent studies on the effect of vitamin K in combination with vitamin C on anti-cancer activity are of great interest [16]. The K_1 form of this vitamin, phyloquinone, is found in green leafy vegetables.

In this study, the amounts of vitamins A, E, K and C in the dried leaves of *R. cornifolius* were determined. The level of vitamin C included in the study was 403.631 ± 8.682 mg 100/g. Vitamins A, E and K levels were determined as 0.2167 ± 0.019 μ mol/kg, 4.313 ± 0.685 μ mol/kg and 0.5622 ± 0.09

$\mu\text{mol/kg}$, respectively and all values are given in Table 1. No studies on vitamins A, E and K of both *Rhamnaceae* family and *R. cornifolius* species were found. This is the first report of these vitamin values for *R. cornifolius* and therefore it is considered to be an important reference for future studies.

On the other hand, the values of vitamin C in the methanol extract of the leaves of *R. frangula* and *R. kurdica*, two species close to *R. cornifolius* in previous studies, were 85/63 mg 100/g, 5.937 ± 5.53 mg 100/g and 14.06 ± 1.07 μg 100/mg, respectively [17,18]. When the vitamin C content of *R. cornifolius*, *R. frangula* and *R. kurdica* were compared, it was found that the vitamin C value was higher in *R. cornifolius*. Considering the vitamin values in *R. cornifolius* as a whole, the presence of vitamins A, E and K is important and the high vitamin C value shows that this plant is a good source of vitamins.

Flavonoids, phenolic acids and phenolic compounds, even in the polyphenol class, are the most frequently encountered groups in plant contents [19]. Flavonoids are of particular interest due to their multiple roles in plants and their effects on human health [20,21]. Phenolic compounds are powerful and natural antioxidants that play an important role in destroying or inhibiting free radicals. Thus, they increase the body's resistance to cell damage and prevent lipid peroxidation [3,22].

In this study, total phenolic, total flavonoid content and total antioxidant capacity of *R. cornifolius* were determined. Total phenolic content was calculated from gallic acid standard curve graph, total flavonoid content was calculated using quercetin curve and antioxidant capacity was calculated according to ascorbic acid standard graph. Total phenolic, flavonoid and antioxidant amounts were found to be 4.482 ± 0.159 mg GAE/g, 27.420 ± 2.551 mg QE/g and 41.795 ± 18.506 mM AA/g, respectively and the results are shown in Table 1. When the literature was examined, the total phenolic value in the methanol extract of *R. alaternus* leaves, which is close to the plant, contains 77.8 mg GAE/g and this value is higher than the value observed in our study [23]. In another study, TPC value in 60% EtOH extract of *R. prinoides* stems was determined as 228.21 ± 13 mg GAE/g [24].

There is a balance between the presence of minerals and trace elements and metabolic reactions. The energy balance necessary for the survival of any organism (plant or human) is largely determined by the values of these minerals and trace elements [25,26]. Trace elements form complex structures with proteins, enzymes and carbohydrates to participate in biochemical reactions. Antioxidant enzymes require elements such as copper, zinc, iron and selenium for optimum catalytic activity [27,28].

The daily amount of trace elements required for the body is between 15-80 μg . Despite the small amount of trace elements in the human body, they are essential for the continuity of many important physiological functions

in the organism. They function as cofactors in the structure of some enzymes, participate in the structure of bone, teeth and many organic substances, maintain acid-base balance in metabolic reactions, transport processes of gases during immunity and respiration, participate in membrane structures and regulate the functional pathways of neurons [29,30].

In this study, when the element level of *R. cornifolius* plant was analysed, it was determined that it had the content and shown in Table 1, $18.625 \pm 0.609 \mu\text{mol/kg}$ ($5.7401 \pm 2.5416 \text{ mg/kg}$) Ba, $5.871 \pm 0.074 \mu\text{mol/kg}$ ($0.2991 \pm 0.0038 \text{ mg/kg}$) V, $19.355 \pm 0.462 \mu\text{mol/kg}$ ($0.9275 \pm 0.0221 \text{ mg/kg}$) Ti, $3.524 \pm 0.665 \mu\text{mol/kg}$ ($0.1832 \pm 0.0346 \text{ mg/kg}$) Cr, $9.121 \pm 0.455 \mu\text{mol/kg}$ ($0.5796 \pm 0.0289 \text{ mg/kg}$) Cu, $0.0443 \pm 0.0015 \text{ mmol/kg}$ ($0.0039 \pm 0.0001 \text{ mg/kg}$) Sr, $0.524 \pm 0.055 \mu\text{mol/kg}$ ($0.0393 \pm 0.0041 \text{ mg/kg}$) As, $1.065 \pm 0.036 \mu\text{mol/kg}$ ($0.0841 \pm 0.0028 \text{ mg/kg}$) Se, $0.072 \pm 0.0058 \mu\text{mol/kg}$ ($0.0081 \pm 0.0007 \text{ mg/kg}$) Cd, $0.449 \pm 0.160 \mu\text{mol/kg}$ ($0.0930 \pm 0.0332 \text{ mg/kg}$) Pb, $0.0448 \pm 0.02 \mu\text{mol/kg}$ ($0.0043 \pm 0.0019 \text{ mg/kg}$) Mo, $0.685 \pm 0.0132 \text{ mmol/kg}$ ($38.2552 \pm 0.7372 \text{ mg/kg}$) Fe, $142.809 \pm 4.398 \mu\text{mol/kg}$ ($7.8456 \pm 0.2416 \text{ mg/kg}$) Mn, $6.6964 \pm 0.350 \mu\text{mol/kg}$ ($0.1628 \pm 0.0085 \text{ mg/kg}$) Al, $24.683 \pm 1.638 \mu\text{mol/kg}$ ($1.6135 \pm 0.1071 \text{ mg/kg}$) Zn, $17.525 \pm 0.0125 \mu\text{mol/kg}$ ($1.0328 \pm 0.0007 \text{ mg/kg}$) Co, $3.001 \pm 0.00412 \text{ mmol/kg}$ ($117.3451 \pm 0.1611 \text{ mg/kg}$) K ve $1.894 \pm 0.154 \text{ mmol/kg}$ ($43.5427 \pm 3.5404 \text{ mg/kg}$) Na.

When the elemental and mineral levels of *R. cornifolius* were compared, it was determined that $\text{K} > \text{Na} > \text{Fe} > \text{Sr} > \text{Mn} > \text{Zn} > \text{Ti} > \text{Ba} > \text{Co} > \text{Cu} > \text{Al} > \text{V} > \text{Cr} > \text{Se} > \text{As} > \text{Pb} > \text{Cd} > \text{Mo}$. Considering these results, it was determined that besides macro elements such as K and Na, the most critical and important trace elements such as Fe, Mn, Zn, Co, Cu, V, Cr, Se and Mo were also present. When the literature was examined, some elemental analyses of *Rhamnus prinoides*, which is close to the plant we used in the study, were found as follows. The results were $129.90 \pm 1.572 \text{ mg/kg}$ K, $2.60 \pm 0.520 \text{ mg/kg}$ Na, $28.311 \pm 1.263 \text{ mg/kg}$ Cu, $10.267 \pm 0.467 \text{ mg/kg}$ Mn, $1.487 \pm 0.0231 \text{ mg/kg}$ Cr, $0.022 \pm 0.0076 \text{ mg/kg}$ Cd, $8.1 \pm 1.153 \text{ mg/kg}$ Fe and $10.177 \pm 0.0643 \text{ mg/kg}$ Zn [31]. When *R. cornifolius* and *R. prinoides* plants were compared, it was determined that *R. cornifolius* had rich and different elemental content, although the elemental values of *R. prinoides* were higher.

DPPH[•] and ABTS^{•+} are common methods based on spectrophotometric determination used to evaluate the antioxidant potential of foods and phenolics in vitro [32]. In these methods, the reduction that occurs between a radical and a substance that can give hydrogen (H⁺) atom results in a decrease in absorbance. This result emphasises the relationship between antioxidant and free radical. The total antioxidant capacity of the methanol extract prepared to evaluate the antioxidant activity of *R. cornifolius* was determined by these methods. One of the most important signs in these methods is IC₅₀ value.

IC₅₀ (mg/mL) measurement was evaluated by analysing the relationship between antioxidants and radical concentration and spectrophotometric monitoring of their absorbance [33].

The scavenging power of *R. cornifolius* methanol extract against DPPH[•] and ABTS^{•+} radicals was compared with synthetic antioxidants BHT and trolox. The highest % inhibition value for DPPH[•] radical was found to be 65.339 ± 0.443 and 74.792 ± 0.764 for BHT and shown in Table 2. IC₅₀, decreaseing with 50% the initial DPPH concentration. Lower IC₅₀ values indicatee higher antioxidant potential. [34]. IC₅₀ value of 33.974 ± 1.918 µg/mL for *R. cornifolius* and 26.979 ± 1.116 µg /mL for BHT were recorded and given in Table 2. From these results, it was found that the % inhibition value of the plant was low compared to BHT, but the IC₅₀ value was high and in this case it was less effective than BHT in scavenging DPPH[•] radical. Methanol extract of the plant showed significant antioxidant activity by DPPH[•] method. In previous studies, the IC₅₀ values for DPPH[•] were 21.04 ± 1.35 and 11.82 ± 1.06 µg/mL and for BHT were 19.50 ± 1.06 and 19.30 ± 1.06 µg/mL in *R. kurdica* and *R. pallasii subsp. sintenisii* plants, respectively [17,11].

In our study, the scavenging capacity of the methanol extract of *R. cornifolius* on ABTS^{•+}, a stable radical, was determined and compared with trolox, a water-soluble analogue of vitamin E. The highest % inhibition value of the plant on ABTS^{•+} radical was found to be 89.333 ± 2.571 and 95.493 ± 0.849 for trolox. The lower the IC₅₀ value, the higher the radical reducing activity. The IC₅₀ value was calculated and the values of 50% inhibition of ABTS^{•+} radical were measured as 58.197 ± 1.826 µg/mL for the plant and 27.854 ± 1.352 µg/mL for trolox and all results are shown in Table 2. Trolox is a powerful synthetic antioxidant. Although the plant showed a lower percentage of inhibition, the IC₅₀ value was higher than trolox, which can be concluded that it is less effective in scavenging ABTS^{•+} radical.

In previous studies, the ABTS^{•+} radical scavenging activity of *R. prinoides*, a species close to the plant we studied, was compared with BHT and trolox. IC₅₀ values in these results were measured as 0.596 ± 0.005 µg/mL for the plant, 0.059 ± 0.003 µg/mL and 0.041 ± 0.002 µg/mL for BHT and trolox, respectively [24]. Although the plant extract was high in terms of IC₅₀ values against synthetic antioxidants BHT and trolox, it can be said that polyphenols containing active H⁺ atom donors in the plant exhibit strong antioxidant properties in capturing these radicals.

Phenylhydrazine (PHZ) is used as an anaemia inducing agent in laboratory animals [35]. The toxic effect of PHZ for the body is associated with its effect on red blood cells (RBC). The main function of RBCs is to carry oxygen to cells. PHZ causes anaemia by decreasing the number of RBCs and consequently the haemoglobin level and packed cell volume (PVC) [36].

In this study, anti-haemolytic activity values were determined for both the methanol extract of the plant leaf and trolox, which was used for comparison. For this, the highest inhibition values were measured as 71.56 ± 2.39 for phenylhydrazine and 58.22 ± 0.31 for trolox. On the other hand, the IC₅₀ values for phenylhydrazine and trolox were measured as 68.51 ± 5.33 µg/mL and 58.22 ± 0.31 µg/mL, respectively, and these values are shown in Table 2. In terms of anti-haemolytic activity, *R. cornifolius* extract showed weak values against trolox. However, the molecular diversity of antioxidant substances may always prevent the formation of a positive or linear relationship. Therefore, different methods should be used to make accurate judgements about antioxidant capacities in plants. In previous studies, a slight increase was found in the extracts of the leaves of *R. alaternus*, a neighbouring plant, at a concentration of 50 mg/mL [37]. When the plants were compared, it was concluded that *R. cornifolius* showed higher haemolytic power.

CONCLUSIONS

In this study, it is important that the results analysed in the methanol extract of the leaves of *R. cornifolius* are the first and in this respect, it is important to be included in the literature. On the other hand, the determination of vitamin A, E and K values only in this study in the *Rhamnaceae* family, which contains a very large number of species, has a different importance. The variety and richness of macromineral (K and Na) and micromineral (Fe, Mn, Zn, Co, Cu, V, Cr, Se and Mo) content, which are necessary to maintain optimal health and growth, indicate that it will be consumed as food. In this study, it was concluded that vitamin C (ascorbic acid), total phenolic content, flavonoid content and total antioxidant potential of the plant were at sufficient level and these results of the plant will be recorded and will constitute a reference for further studies. Our analysis of the plant extract's antiradical properties revealed its effectiveness in countering radical attacks, with ABTS•⁺ and DPPH• assays confirming strong antioxidant capacity (IC₅₀ = µg/mL). These results comprehensively demonstrated that *R. cornifolius* is a good source of natural polyphenols, provides important parameters for further studies and will be a potential candidate for future in vivo studies.

EXPERIMENTAL SECTION

Plant collection location and preparation

R. cornifolius Boiss. Hoh: Turkey. C9 Hakkari: Yüksekova, Oremar region, Sat mountains, Herduav locality, 1320 m, 37°22'41", 44°10'08", 7 July 2018, M. Fırat & A. Bakır. Species identification of the plant was made

by Dr. Mehmet FIRAT and specimen vouchers were deposited to the herbarium with the code number 34042 (VHLF).

The leaf and characteristic appearance of *R. cornifolius* are given in Figure 7. The leaf part of the plant was used in the study. The flowering period was selected as the most effective time to obtain the maximum yield of the plant leaf. The leaves of the plant were dried in a cool place without light for three weeks. After drying, the leaves were ground to a fine powder in a plant grinder and stored in glass bottles for analyses.



Figure 7. Characteristic images of *R. cornifolius*. a) general view of the plant, b) leaf view of the plant

Preparation and analysis of methanol extract of plant leaves

For the preparation of MeOH extract of the plant extract, the method of Cai *et al.* [38] was modified and adapted to this study. An appropriate amount (20 g) of dry plant leaves, previously pulverised in a plant grinder and stored in glass bottles, was weighed and transferred to a coloured bottle and MeOH at 80% concentration was added. The plant leaf, which was kept away from light, was subjected to extraction at 30°C for 36 h in a water bath with stirrer. Then centrifuged at 4500 rpm for 15 min and filtered with suitable filter paper (Whatman No. 1). MeOH in the filtrate was extracted under reduced pressure at 40°C using a rotary evaporator and removed. Finally, the crude extracts were lyophilised in a -65°C refrigerator until dry and stored in the dark at +4°C for further analysis. The yield of methanol extracts obtained from the leaf of *R. cornifolius* was measured as 28.97% according to the formula below.

$$\% \text{ yield} = \frac{\text{Weight of the crude (g)}}{\text{Weight of the dried } R.\text{cornifolius} \text{ powder used for extraction (g)}}$$

Determination of element content

The element content of *R. cornifolius* leaves was determined by dry digestion method [39]. According to this method, 1 g of *R. cornifolius* leaf samples were placed in porcelain crucibles and 2 ml of ethanol+sulfuric acid was added. For the results to be reliable, 3 replicates were performed. Initially, the muffle furnace was set at 250°C and gradually increased (by 50°C per hour) to 550°C.

The purpose of doing this is to heat the samples in a controlled manner and not to damage the elements in them. The samples made in porcelain crucibles were placed in the muffle furnace, which reached a temperature of 250°C. When the oven temperature reached 550°C, the samples were trapped in the muffle furnace until the next day. 5 mL HCl was added to the cooled samples. After the samples were filtered with blue band filter paper, they were removed from the muffle furnace, subjected to a series of procedures and prepared for analysis using Inductively coupled plasma (ICP) and optical emission spectrometry (OES) [Brand of the device: thermo scientific; model: ICAP6300DOU] and inductively coupled plasma (ICP) and mass spectrometry (MS) [Brand of the device: Thermo scientific; model: X II series].

Determination of total phenolic content

The total phenolic content in the extract of *R. cornifolius* was measured spectrophotometrically after some modifications in the FCR method [40]. To the leaf extract samples of the plant prepared by dilution with MeOH, 300 µl of 2% sodium carbonate, 100 µl of FCR marker were added and incubated at room temperature for 2 hours. The absorbance of the samples was read at 765 nm. A standard curve was prepared using different concentrations of gallic acid solutions. Results were reported in milligrams of gallic acid equivalent (GAE) per gram of dried extract (mg GAE/g).

Determination of total flavanoid content

Flavonoid content of *R. cornifolius* extract was determined using aluminium nitrate method [41,42]. First, 500 µL of the diluted methanol extract stock solution was taken. Then, 100 µL of CH₃COOK, 100 µL of Al(NO₃)₃, and 4600 µL of ethanol were added sequentially. The solutions were then vortexed and incubated at room temperature for 45 minutes. Finally, the absorbances were read against the control sample at 415 nm wavelength. Flavonoid concentration was calculated by plotting quercetin (QE) and the total flavonoid content of the samples was reported as quercetin equivalent (mg QE/g).

Determination of total antioxidant capacity

The aim is based on the reduction of acidic Mo-VI to Mo-V by a series of reactions to form the green coloured phosphate/Mo(V) compound at acidic pH [43]. Different concentrations of the plant MeOH extract were prepared. 200 µL of these samples were taken and 0.2 L of marker solution [600 mM H₂SO₄ + 28 mM Na₂HPO₄ + 4 mM (NH₄)₂MoO₄] was added, followed by 2 h in a water bath previously set at 100 °C. The samples were removed from the water bath and allowed to stand at room temperature. The samples were read against the control sample at 695 nm wavelength. Total antioxidant capacity was calculated by drawing ascorbic acid standard graph and total antioxidant capacity of the samples was given as mM ascorbic acid/g.

Determination of DPPH[•] radical scavenging activity

In the study, free radical scavenging activities of MeOH extracts of the plant were determined using DPPH[•] [44,45]. In order to determine the free radical scavenging activity of the prepared extracts by using DPPH 'total antioxidant potential' measurement method, 2 mg/mL stock extract solution was diluted with MeOH and prepared in different concentrations. DPPH[•] system follows a stable radical generating procedure. In order to determine the scavenging activity of this radical, 4000 µl of 0.04 mg/mL DPPH[•] solution was added to the solutions of different concentrations prepared by dilution with MeOH and incubated at appropriate temperature for 45 min. Absorbance readings were made at 517 nm. Absorbance values of the prepared samples were expressed against the control. BHT, a synthetic antioxidant, was used as a control against the sample. Antiradical activity was determined from the formula below [46].

$$\text{Inhibition (\%)} = \left\{ \frac{A_{\text{Blank}} - A_{\text{Sample}}}{A_{\text{Blank}}} \right\} \times 100$$

Using the above % inhibition formula, the plant extraction concentrations were calculated as IC₅₀ (The micromolar concentration required to inhibit half of the radical formed in any given situation is µg/mL.) [47,48].

Determination of ABTS^{•+} radical scavenging activity

ABTS^{•+} radical is produced by the reaction of ABTS^{•+} with an oxidising species. Sodium persulfate was used in our study. Firstly, ABTS^{•+} (0.002 M) and K₂S₂O₈ (2.45 mM) solutions were mixed to prepare the reactive radical. This mixture was incubated in a dark place for 13-16 hours. 1800 µL of ABTS^{•+}

reagent was added to each of the test samples (200 μ L) and measured at 734 nm after 2 h in the dark room. Plant methanol extract was carried out by modifying the method described by [49,50]. Trolox was used as synthetic antioxidant. The active power of ABTS^{•+}, a redox radical, was calculated from the following formula [51].

$$\text{Inhibition (\%)} = \left\{ \frac{A_{\text{Blank}} - A_{\text{Sample}}}{A_{\text{Blank}}} \right\} \times 100$$

Haematological parameter analysis

The radical scavenging activity of *R. cornifolius* leaf extract after haemolysis of erythrocytes with phenylhydrazine (PHZ) was determined according to this method [52]. Briefly, 1 mL PHZ, 0.1 mL 20% PCV, 1.850 mL buffer were added to samples prepared from different concentrations of methanol extract of *R. cornifolius* leaves. 37°C for 1 hour and then centrifuged at 4000 rpm for 10 minutes. After transferring the supernatant to other tubes, the absorbance at 540 nm was read against the control sample. The results were compared with trolox.

Determining vitamin C content

Vitamin C content in *R. cornifolius* dry leaves was determined by spectrophotometric device at 521 nm wavelength. The first step in the determination of vitamin C content was to add 2 mL of HPO₃ and 0.5% oxalic acid to 1 g samples (3 replicates) and centrifuge at 5000 rpm for 5 min. After centrifugation, 2000 μ L of the filtrate was taken, 1-2 drops of thiourea and 500 μ L of 2,4-dinitrophenylhydrazine (2,4-DNFH) were added and taken in a water bath at 100°C. After the water bath, sulfuric acid solution was added slowly. The tubes prepared at room temperature were vortexed for 5 min. Absorbic acid concentrations of the samples were calculated using the calibration graph obtained [53,54].

Vitamin A, E and K analyses

Standard solution and calibration

Retinol, α -tocopherol and phyloquinone stock solutions were prepared at 500 μ g/mL. To prepare the standard solution, the stock solutions were diluted with methanol accordingly. Linear regression analysis of the peak area versus standard solution concentrations was used to calculate the calibration.

Vitamin extraction process

The amounts of retinol, α -tocopherol and phyloquinone in *R. cornifolius* leaves were determined by modifying the studies of [55,56]. Weighed 4000 mg of dried and shade ground plant leaf samples were extracted with n-hexane and EtOH. BHT (0.02%) was added to the prepared samples, mixed at the appropriate time and then kept in the dark for 30 hours. Then centrifuged at +4°C and 5000 rpm for 15 min.

The clear solution in the resulting phase was filtered using filter paper and 500 μ L of n-hexane was added. Finally, it was left to dry under nitrogen gas (at 37°C). Immediately after the drying process was completed, the remaining part was dissolved in 250 μ L of MeOH+C₄H₈O (tetrahydrofuran) (98%) and made ready for analysis.

Chromatographic conditions

Vitamin retinol, α -tocopherol and phyloquinone analyses were performed on a GI Science C₁₈ reversed phase high performance liquid chromatography column (250 x 4.6 mm ID), MeOH (80 ml) + tetrahydrofuran (20 ml) mobile phase, 1500 μ L/min flow rate at 24°C. HPLC - applications were performed for retinol (325 nm), α -tocopherol (290 nm) and phyloquinone (248 nm) in 0.1 mL volumes in dark coloured vials in a tray autosampler (-10°C) using a PDA array detector. Chromatographic values of vitamins are shown in figure 8. Also chromatographic analysis measurements were performed by isocratic elution (40°C), a separation technique of HPLC.

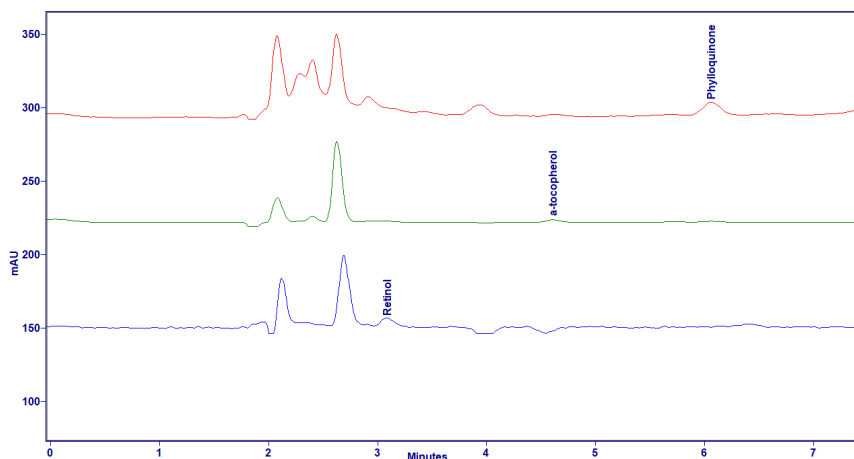


Figure 8. HPLC chromatogram of retinol, α -tocopherol, and phyloquinone at 325, 290, and 248 nm

Statistics data

The data of the measurement results are expressed as mean and mean standard error ($X \pm \text{SEM}$). Group graphs are also expressed in the same way ($X \pm \text{SEM}$). Nonlinear regression analysis was used to find the IC_{50} measurement data. The measurements are presented in three replicates.

Running head: ANTIOXIDANT, ANTI-HAEMOLYTIC ACTIVITY OF *R. CORNIFOLIUS*

ACKNOWLEDGMENT

This study was supported by TÜBİTAK-BİDEP as 2209-A University Students Research Project (2023/2 period).

REFERENCES

1. M. Elaine; *FAO Diversification Booklet*, Rome, **2011**, pp.1-63
2. H. Yıldız; T. Baysal; *J. Food Eng.*; **2003**, 7, 29-35
3. F. Shahidi; M. Naczki; CRC Press Google Schola, **2003**, 2, 221-226
4. R. F. Denise; *Lippincott Visual Explanation Workbooks Biochemistry*, İstanbul, **2019**, pp.399-410
5. H. Aysun; *J. Ankara Uni. Faculty of Phar.*, **2009**, 38, 233-255
6. O. O.Sinbad; A. A. Folorunsho; O. L. Olabisi; O. A. Ayoola; E.J.Temitope; *J. Food Sci. Nutri. Res.*, **2019**, 2, 214-235
7. V. V. Sugandhi; R. Pangen; L. K. Vora; S. Poudel; S.Nangare; S. Jagwani; V. Patravale; *Food Sci. Nutri.*, **2024**, 12, 48-83
8. H. Kaur; H. Kaur; H.Kaur; Srivastava, S; *Plant Growth Regulation*, **2023**, 100, 219-236
9. K.L.Manda; A.L.Bhatia; *Cell Bio. Toxi.*, **2003**, 19, 367-372
10. A. Ünal; O. Tolga; E. Özgür; F. Mehmet; A. Necmi; *General Directorate of Forestry Publications*, Ankara, 2014, pp. 248-271
11. S. Mahmoodi; A.Taleghani; R. Akbari; M. Mokaber-Esfahani; *Arabian J. Che.*, **2022**, 15, 103924
12. C. M. Hasler; *J. Nut.*, **2002**, 132, 3772-3781
13. T. Coşkun; *J. Paedi. Child Health*, **2005**, 48, 61-84
14. I. Darnton-Hill; *Current Develop. Nut.*, **2019**, 3, nzz075
15. M.G.Traber; J. Atkinson; *Free Rad. Bio. Med.*, **2007**, 43, 4-15
16. D. Ivanova; Z. Zhelev; P. Getsov; B. Nikolova; I. Aoki; T. Higashi; R.Bakalova; *Redox Biol.*, **2018**, 16, 352-358
17. M. B. Gholivand; M. Piryaee; *African J. Biotec.*, **2014**, 13
18. M. Azadbakht; L. Moezi; S. M. H. Tabaei; *J. Maz. Uni. Med. Sci.*, **2015**, 24, 292-306

19. D. V. Ratnam; D. D. Ankola; V. Bhardwaj; D. K. Sahana; M. R. Kumar; *J. Cont. Rel.*, **2006**, 113, 189-207
20. R. Nicolas; M. Phillip; W. K. Judith; *Lotus Japonicus Handbook*, Springer, Dordrecht. **2005**, pp. 349-354
21. B. Ahmet; E. Suat; F. Mehmet; *Kah. Sütçü İmam Uni. J. Agri. Nat.* **2023**, 26, 966-976
22. A. Eyad; G. Ş. İhsan; İ. B. Halil; *J. Tekirdag Agri. Faculty*, **2024**, 21, 81-93
23. A. Samira; M. Chaima; B. Mohammed; H. Hamada; *Herba Polonica*, **2023**, 69, 15-28
24. C. Gui-lin; M. M. Fredrick; X. Yong-bing; S. Flora Didii; H. Guang-Wan; G. M ing-Quan; *Pharmaceuticals*, **2020**, 13, 55
25. W. J. Miller; *J. Dairy Sci.*, **1975**, 58, 1549-60
26. A. Abdolla-Ali; E. Suat; B. Ahmet; Y. Damla; *Inter. J. Sec. Meta.*, **2022**, 9, 194-207
27. B. L. Rameshwar; A. Abdullatif; S. N. Prem; M. Alice Babu; B. I. Abdulla; D. Hussein; *J. Trace Ele. Exp. Med.*, **2002**, 15, 57-66
28. C. Kalpana; V. P. Menon; *Tox. Mech. Meth.*, **2004**, 14, 339-343
29. H. V. Kobla; S. L. Volpe; *Food Sci. Nut.*, **2000**, 40, 291-308
30. C. L. Henry; *Nutrition*, **2004**, 20, 632-644
31. A. Nagari; A. Abebaw; *Sci, Tech. and Arts Res. J.*, **2013**, 2, 20-26
32. F. Anna; K. Dae-Ok; C., Sank-Jin; I. K. Song; C. K. Ock; *J. Food Comp. Analis.*, **2011**, 24, 1043-1048
33. O. Malgorzata; L. D. Anadrzej; *Chem. Papers*, **2018**, 72, 393-400
34. W. Brand-Williams; M. E. Cuvelier; C. L. W. T. Berset; *LWT-Food Sci. Tech.*, **1995**, 28, 25-30
35. G. Pitchaiah; K. Sravani; C. Vasanthi; S. K. Siva; K. Navyaja; V. K. Priya; *IJEP J.*, **2015**, 5, 91-95
36. S., Pooja; K. Y. Navneet; S. Poonam; F. W. Bansode; R.K. Singh; *Inter. J. Basic App. Med. Sci.*, **2012**, 2, 86-91
37. C. M Tarik; H. Farah; B., Ouhiba; G. Imane; *Bulletin de la Soc. Roy. des Sci. Liège*, **2020**, 89, 1-14
38. C. Yizhong; L. Qiong; S., Mei; C., Harold; *Life Sci.*, **2004**, 74, 2157-2184
39. Z. Mester; R. Sturgeon; *Sample Preparation For Trace Element Analysis*, Elsevier, Amsterdam, **2003**, pp. 520
40. N. Gamez-Meza; J. A. Noriega-Rodriguez; L.A. Medina-Juarez; J. Ortega-Garcia; R. Cazarez-Casanova; O. Argulo-Guerreo; *J. American Oil Chem. Soci.*, **1999**, 76: 1445-1447
41. Y. K. Park; M. H. Koo; M. Ikegaki; J.K. Arq. de Bio. Tech., **1997**, 40, 97-106
42. J. L. Lamasion; A. Carnat; C. Petitjean; *Anna. Pharma. Fran.*, **1990**, 48, 335-340
43. P. Pilar; P. Manuel; A. Miguel; *Anal. Bioche.*, **1999**, 269, 337-341
44. K. J. Andrew; S. J. Richard; *J. Ethno.*, **1997**, 56, 103-108
45. C. Muriel; H. Kurt; P. Olivier; D.Wahjo; *Helvetica Chimica Acta*, **1997**, 80, 1144-1152
46. D. Pin-Der; T. Yang-Ying; Y. Gow-Chin; *LWT-Food Sci. Tech.*, **1999**, 32, 269-277
47. M. Burits; K. Asres; F. Bucar; *Phy. Res.*, **2001**, 15, 103-108

ANTIOXIDANT, ANTI-HAEMOLYTIC ACTIVITY, VITAMIN AND ELEMENT PROFILE OF
RHAMNUS CORNIFOLIUS

48. S. C. Robert; C.R. Jeri; *Bio. Pharma.*, **1987**, 36, 1457–1460
49. R. Roberta; P. Nicoletta; P. Anna; P. Ananth; Y. Min; R. Catherine; *Free Rad. Biology and Med.*, **1999**, 26, 1231-1237
50. M. J. Nicholas; R. Catherine; D. J. Michael; G. Vimala; M., Anthony; *Clinical Sci.*, **1993**, 84, 407-412
51. B. A, Marino; Ca Antonio; A. Manuel; *Food chemistry*, **2001**; 73, 239-244
52. A. Valenzuela; H. Rios; G. Neiman, G; *Experientia*, **1977**; 33, 962-963
53. M. A.Brewster; CU, Mosby Comp., St. Lovis USA, 1984, pp. 656-685
54. N. A. Golubkina; O. V. Prudnik; *J. Anal. Che. of the USSR.* **1989**, 44, 1091-1100
55. A. S. Iman; B. Grisellhi; and E. Inaam; *J. Food Comp. Anal.*, **2006**, 19, 167-175
56. S, Ahmet; K. Yasar; K. Fikret; S. Senem; *J. Integrative Plant Biology*, **2005**; 47, 487-493

RP-HPLC AND HPTLC-BASED PHYTOCHEMICAL STUDIES OF ENDEMIC *NEPETA CADMEA* BOISS. AND ITS EFFECTS ON CARBOHYDRATE DIGESTIVE ENZYMES

Selin KALENDER^a, Alper GÖKBULUT^{b,*}, Burçin ÖZÜPEK^c,
Sultan PEKACAR^c, Didem Deliorman ORHAN^c

ABSTRACT. This study investigated the *in vitro* inhibitory potential of the methanol extract of the aerial parts of *Nepeta cadmea* on α -glucosidase and α -amylase, which are known as key enzymes related to type 2 diabetes mellitus. To determine the active constituents of the endemic Lamiaceae plant, validated RP-HPLC and HPTLC techniques were used. The methanol extract demonstrated moderate and dose-dependent inhibitory activity, with inhibition rates of $43.57 \pm 4.32\%$ against α -glucosidase at 2 mg/mL and $36.74 \pm 7.23\%$ against α -amylase at 1 mg/mL. Phytochemical analysis revealed that rosmarinic acid (0.6290 ± 0.0095 g/100g dw) was the predominant phenolic compound, followed by chlorogenic acid (0.0429 ± 0.0012 g/100g dw) and caffeic acid (0.0027 ± 0.0002 g/100g dw). These findings suggest that this endemic Lamiaceae plant may have potential as a natural therapeutic agent for managing diabetes mellitus. Further studies are warranted to explore its mechanisms of action and to evaluate its efficacy in clinical settings.

Keywords: α -amylase, α -glucosidase, RP-HPLC, HPTLC, *Nepeta cadmea*

INTRODUCTION

The genus *Nepeta* L. (Lamiaceae) is known to comprise approximately 250 species worldwide. Reports indicate the distribution of *Nepeta* species across Southwest and Central Asia, North America, North Africa, Europe,

^a Sivas Provincial Health Directorate, Public Hospitals Services Presidency, Örtülüpınar Mahallesi, İnönü Boulevard No: 55, State Hospital, Sivas, Türkiye

^b Department of Pharmacognosy, Faculty of Pharmacy, Ankara University, Ankara, Türkiye

^c Department of Pharmacognosy, Faculty of Pharmacy, Gazi University, Ankara, Türkiye

* Corresponding author: gokbulut@pharmacy.ankara.edu.tr



and the Mediterranean regions. In Türkiye, this genus contains a total of 39 species and 50 taxa, 19 of which are endemic [1, 2]. As with most members of the Lamiaceae family, many *Nepeta* species have been traditionally used for colds, stomach aches, and as stimulants. Some *Nepeta* species are also traditionally used as diuretics, sudorific agents, cough suppressants, antispasmodic agents, asthma treatments, antipyretics, and sedatives; for nervous disorders and depression; as spices; and in herbal teas [2, 3]. Numerous studies on *Nepeta* species have revealed that these plants contain terpenoid compounds such as monoterpenes, sesquiterpenes, diterpenes, triterpenes, and phenolic compounds in addition to nepetalactones and their glycosidic forms. Due to their pleasant aroma and generally high monoterpene content, these plants yield highly valued essential oils. Terpenoids and flavonoids are the dominant components in the chemical composition of the *Nepeta* genus [4, 5]. *Nepeta cadmea* Boiss., a species of the *Nepeta* genus, is known in Turkish as “honaz pisikotu” and is endemic to Türkiye. *N. cadmea* is a perennial herbaceous species rich in essential oils [2, 6, 7]. Phytochemicals found in *N. cadmea* include 4 α ,7 α ,7 α -nepetalactone; 1,5,9-epideoxyloganic acid; (*E*)-rosmarinic acid; eugenyl β -D-glucopyranoside; eugenyl-O- β -apiofuranosyl-(1 \rightarrow 6)-O- β -glucopyranoside; lariciresinol 4'-O- β -D-glucopyranoside; guloside (corcoyonoside C); icaraside B2 and icaraside B2 [8, 9].

Diabetes mellitus (DM) is a common metabolic disease worldwide, and type 2 diabetes (T2DM), in particular, is characterized by insulin resistance and persistently high blood glucose levels. In patients with T2DM, postprandial hyperglycemia is associated with impaired starch digestion, a process in which the enzymes α -glucosidase and α -amylase play key roles. Inhibition of these enzymes is being investigated as an effective therapeutic strategy to regulate blood sugar levels and manage diabetes [10]. Among *Nepeta* species, a 70% ethanol extract of *N. cataria* L. was found to have a moderate inhibitory effect on enzymes responsible for carbohydrate hydrolysis. The literature has reported that the methanol extract of *N. hindostana* (B. Heyne ex Roth) Haines exhibits a significant antidiabetic effect in a streptozotocin-induced diabetes model [11-13].

The aim of this study was to perform qualitative and quantitative analyses of the methanol extract obtained from the aerial parts of *N. cadmea* for phenolic compounds. For this purpose, a Reversed-Phase High-Performance Liquid Chromatography (RP-HPLC) method was developed to determine the amounts of the main compounds in the plant extract. Furthermore, High-Performance Thin-Layer Chromatography (HPTLC) analysis was performed to identify the active ingredient groups contained in the methanol extract of the plant, thus strengthening the specificity of the study. Another important objective of this study was to test the *in vitro* antidiabetic potential of *N. cadmea*. In

this context, the potential antidiabetic effects of the plant were evaluated by testing its α -glucosidase and α -amylase inhibitory activities, which play an effective role in regulating blood glucose levels and managing diabetes.

RESULTS AND DISCUSSION

Studies on *Nepeta* species have focused primarily on their essential oil components. In this study, which investigated the antidiabetic potential of an extract prepared with methanol from the aerial parts of *N. cadmea* collected from the Denizli region, α -glucosidase and α -amylase enzymes were used. Furthermore, qualitative and quantitative analyses of the phenolic compounds in the extract were performed using RP-HPLC, and TLC screening of phenolic compounds was conducted, and the HPTLC technique was applied for the first time for this species.

As a result of these studies, the highest inhibition of the α -glucosidase enzyme by *N. cadmea* methanol extract was $43.57 \pm 4.32\%$ at a concentration of 2 mg/ml. The inhibition value of the reference compound, acarbose, at the same concentration was 100%. The highest inhibition of the α -amylase enzyme by *N. cadmea* methanol extract was $36.74 \pm 7.23\%$ at a concentration of 1 mg/ml (Table 1). Accordingly, *N. cadmea* methanol extract can be considered a moderate α -glucosidase and α -amylase inhibitor. In their 2019 study, Sarikurkcü and colleagues (2019) investigated the α -glucosidase and α -amylase inhibitory activity of extracts prepared using methanol via Soxhlet extraction from the aerial parts of *N. cadmea*. The study concluded that the inhibitory activity of *N. cadmea* on α -glucosidase and α -amylase was found to be 2.02 and 0.24 mmol ACEs/g extract, respectively ($p < 0.01$). These results demonstrated that the plant extract has a weak inhibitory effect on both enzymes [5]. Considering the differences between our research and the 2019 study by Sarikurkcü et al., to the best of our knowledge this study is the first HPTLC-based phenolic profile identification for *N. cadmea*, and rosmarinic acid is addressed as the major compound in the methanol extract. Also, the determination of moderate and dose-dependent inhibitory activity of α -glucosidase is important for the originality of the study.

In another study conducted by Sarikurkcü et al. (2018) the α -glucosidase and α -amylase inhibitory activities of the essential oil obtained from the aerial parts of *N. cadmea* were investigated. The study results showed that the inhibitory activity of *N. cadmea* essential oil on α -glucosidase (IC_{50} : 5.93 ± 0.18 mg/mL) was very low compared to acarbose (IC_{50} : 0.99 ± 0.01 mg/mL), while its inhibitory value on α -amylase (IC_{50} : 1.35 ± 0.02 mg/mL) was very similar to that of acarbose (IC_{50} : 1.33 ± 0.01 mg/mL). The findings indicated that the essential oil was highly effective on α -amylase [14].

Table 1. Inhibitory activity of *N. cadmea* methanol extract on α -glucosidase and α -amylase enzymes

Samples	Concentration (mg/ml)	Inhibition % \pm S.D.	
		α -Glucosidase	α -Amylase
<i>N. cadmea</i> extract	0.5	n.a.	n.a.
<i>N. cadmea</i> extract	1	17.14 \pm 2.18***	36.74 \pm 7.23***
<i>N. cadmea</i> extract	2	43.57 \pm 4.32***	n.a.
Acarbose	0.5	100 \pm 0.00***	n.a.
Acarbose	1	99.86 \pm 0.24***	78.88 \pm 8.53***
Acarbose	2	100 \pm 0.00***	100 \pm 0.00***

-.: No activity (n.a.), S.D.: Standard Deviation, ***p<0.001

(compared with acarbose values at the same concentration)

In this study, in addition to RP-HPLC assay, TLC, and HPTLC techniques were also used for the phytochemical analysis of *N. cadmea*. Based on the available literature, HPTLC analysis was performed for the first time on this species (Figures 1 and 2). The phenolic profile of the *N. cadmea* methanol extract was determined by RP-HPLC targeting the following compounds: gallic acid, chlorogenic acid, caffeic acid, sinapic acid, ellagic acid, protocatechuic acid, *p*-coumaric acid, ferulic acid, rosmarinic acid, rutin, luteolin-7-glucoside, quercetin, luteolin, apigenin, and kaempferol (Figures 3 and 4). In addition, quantitative analyses were carried out specifically for rosmarinic acid, chlorogenic acid, and caffeic acid. The validation parameters of the quantitatively analyzed compounds are presented in Table 2. The study revealed that the plant contained significant amounts of rosmarinic acid, chlorogenic acid, and caffeic acid. According to the quantitative determination results, the rosmarinic acid, chlorogenic acid, and caffeic acid rates in the plant were determined as 0.6290 \pm 0.0095 g/100g dw, 0.0429 \pm 0.0012 g/100g dw, and 0.0027 \pm 0.0002 g/100g dw, respectively (Table 3).

Kaska and colleagues (2018) carried out phytochemical analysis of ethanol extract prepared from aerial parts of *N. cadmea* using RP-HPLC. The study reported that the ethanol extract was rich in chlorogenic acid (1050.74 μ g/g) and caffeic acid (3683.34 μ g/g) [7]. In another study where the phytochemical content of *N. cadmea* was evaluated using the RP-HPLC technique, it was found that the amounts of chlorogenic acid (3.30 \pm 0.12 mg/g) and caffeic acid (0.47 \pm 0.03 mg/g) were high, but the plant did not contain rosmarinic acid [5]. RP-HPLC analysis indicated that methanol extracts of flowers, leaves, and roots of *N. humilis*, another *Nepeta* species, contained only rosmarinic acid. It has been reported that the flower extract

has the highest rosmarinic acid content (0.397 ± 0.01 g/100 g dry weight) [15]. These results indicated that the levels of chlorogenic acid and caffeic acid detected in our study were lower, while rosmarinic acid levels were higher, compared to previous studies. These differences may be attributed to various environmental and methodological factors, such as the extraction technique used, the type of solvent, the geographical region where the plant was collected, the time of collection, and seasonal factors. Our RP-HPLC analysis identified rosmarinic acid, previously reported by Takeda et al. (1998) [9], to be the main compound isolated from *N. cadmea*. Furthermore, a study by Ngo and Chua (2018) [16], revealed that rosmarinic acid exhibited high inhibitory activity, particularly against the α -glucosidase enzyme, making it a promising natural candidate for the treatment of type 2 diabetes. In the literature, chlorogenic acid, caffeic acid, and rosmarinic acid compounds found in *N. cadmea* have been reported to have inhibitory effects on α -glucosidase and α -amylase enzymes [17-20]. In our study, the methanol extract of the aerial parts of *N. cadmea* had moderate α -glucosidase and α -amylase inhibitory activity, suggesting that these phenolic compounds may exhibit inhibitory effects alone or through a synergistic interaction. In particular, the potential of rosmarinic acid, both alone and in combination with other phenolics, has led to the idea that this molecule should be considered an important phytochemical candidate for antidiabetic activity.

Table 2. r^2 , LOD, LOQ values, mean area, SD, and % RSD data for chlorogenic acid, caffeic acid, and rosmarinic acid

Compound	Standard curve	r^2	LOD (mg/L)	LOQ (mg/L)	Mean area, n= 9	SD	%RSD
Chlorogenic acid	$y = 22083x - 6.4807$	0.9999	0.112	0.370	7.35	0.1309	1.78
Caffeic acid	$y = 56891x + 30.81$	0.9996	0.021	0.069	5.13	0.0997	1.94
Rosmarinic acid	$y = 28820x - 26.234$	0.9999	0.073	0.240	130.79	0.1572	1.95

Table 3. The content of phenolic compounds in *N. cadmea* aerial parts (g/100 g dry weight of the plant)

Compound	<i>N. cadmea</i>
Chlorogenic acid	0.0429 ± 0.0012
Caffeic acid	0.0027 ± 0.0002
Rosmarinic acid	0.6290 ± 0.0095

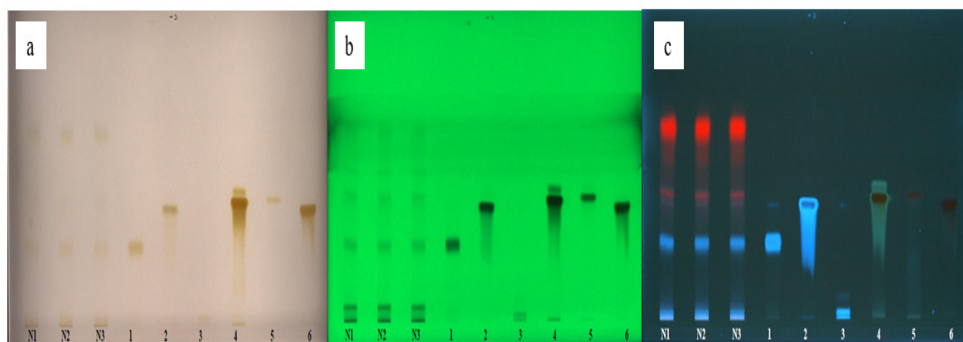


Figure 1. HPTLC chromatograms of the methanol extract of the aerial parts of *N. cadmea* and standard compounds in the solvent system Toluene: Ethyl Acetate: Formic Acid (5:4:1), visualized under a) daylight, b) UV 254 nm, c) UV 366 nm (N1, N2, N3: Extract; 1: Rosmarinic Acid, 2: Caffeic Acid, 3: Chlorogenic Acid, 4: Quercetin, 5: Apigenin, 6: Luteolin)

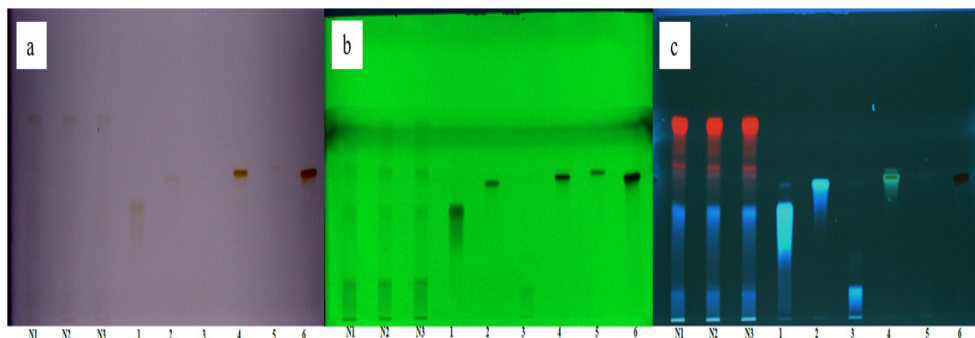


Figure 2. HPTLC chromatograms of the methanol extract of the aerial parts of *N. cadmea* and standard compounds in the solvent system Chloroform: Ethyl Acetate: Acetone: Formic Acid (4:3:2:1), visualized under a) daylight, b) UV 254 nm, and c) UV 366 nm (N1, N2, N3: Extract; 1: Rosmarinic Acid, 2: Caffeic Acid, 3: Chlorogenic Acid, 4: Quercetin, 5: Apigenin, 6: Luteolin)

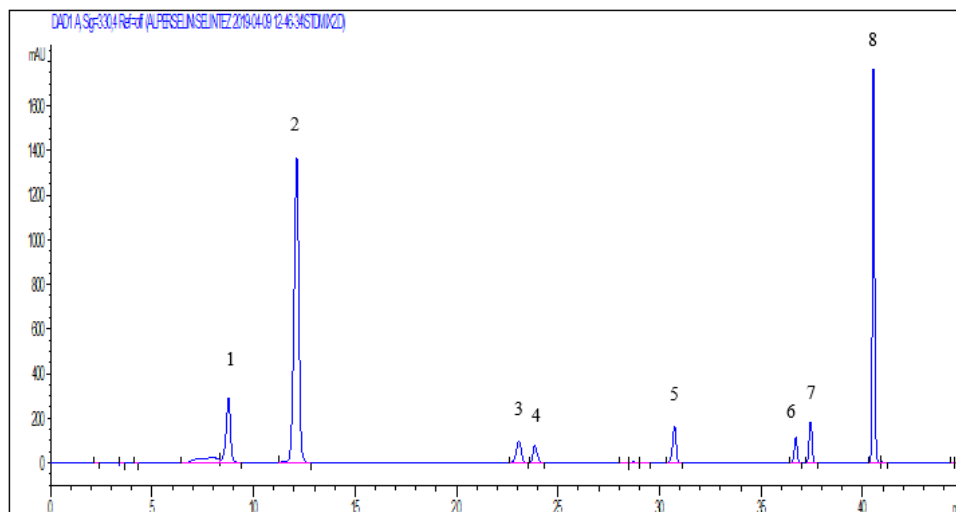


Figure 3. RP-HPLC chromatogram of some standard compounds at 330 nm (in order: chlorogenic acid (1), caffeic acid (2), rutin (3), ellagic acid (4), rosmarinic acid (5), quercetin (6), luteolin (7), apigenin (8))

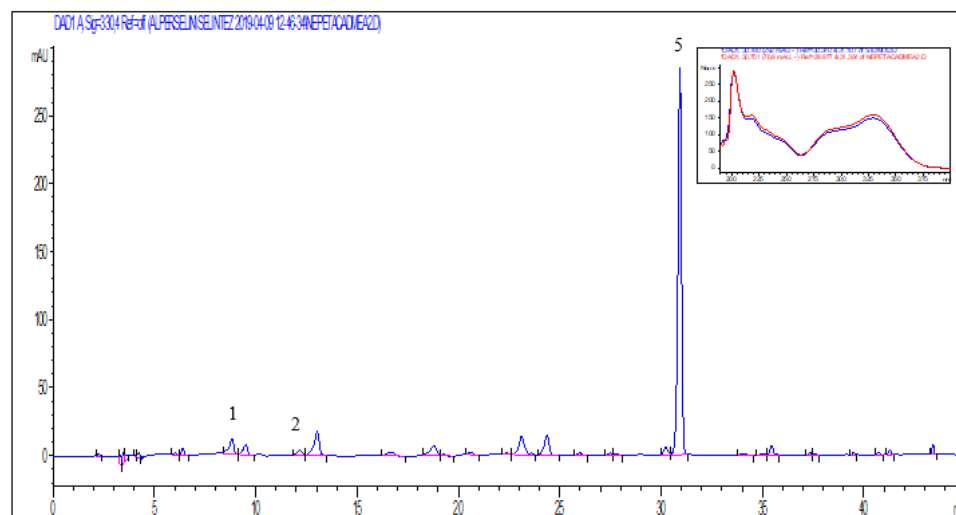


Figure 4. RP-HPLC chromatogram of the methanol extract of the aerial parts of *N. cadmea* at 330 nm, chlorogenic acid (1), caffeic acid (2), rosmarinic acid (5) and overlaid UV spectra of standard rosmarinic acid and the rosmarinic acid detected in the extract

CONCLUSIONS

In this study, the *in vitro* antidiabetic potential of a methanol extract of *N. cadmea* aerial parts was determined to have a moderate inhibitory effect, compared to acarbose, on the enzyme α -glucosidase, which plays a role in carbohydrate digestion. Both RP-HPLC and HPTLC analyses provided detailed characterization of the plant's phenolic compound content, revealing rosmarinic acid as the main component, followed by chlorogenic and caffeic acids. The higher inhibitory effect observed in this study, compared to previous studies, may be due to the synergistic effect of the phenolic compounds present in the extract, especially rosmarinic acid. This study represents the first application of HPTLC to *N. cadmea*, introducing an innovative analytical approach that enhances the accuracy and reproducibility of phytochemical profiling. In conclusion, this study provided a more detailed characterization of the phytochemical structure of *N. cadmea* and showed that the plant can be considered a natural resource that could lead to different *in vitro* and *in vivo* studies for the management of postprandial hyperglycemia in type 2 diabetes mellitus.

EXPERIMENTAL SECTION

Plant material

N. cadmea was collected in its flowering stage from Denizli Kızılcabölük, Turkey. Voucher specimen has been deposited in the Herbarium of Ankara University Faculty of Pharmacy under the herbarium code of AEF 28879. The plant was identified by Prof. Dr. Mehmet Çiçek from Pamukkale University and Assoc. Prof. Dr. Gülderen Yılmaz from Ankara University.

Preparation of extract and standards

Dried and milled aerial parts of the plant were extracted twice with methanol using a magnetic stirrer for 4 h (50 °C, 600 rpm). The filtered extracts were combined, and methanol (MeOH) was completely evaporated by a rotary evaporator (Buchi-R200). The yield of the extract was 14.235%. Phenolic compounds were purchased from Sigma (Germany): apigenin (A3145), caffeic acid (C0625), chlorogenic acid (C3878), ellagic acid (E2250), ferulic acid (128708), gallic acid (G7384), kaempferol (K0133), luteolin (L9283), luteolin-7-glucoside (49968), p-coumaric acid (C9008), protocatechuic acid (03930590), quercetin (Q4951), rosmarinic acid (536954), rutin (R5143), and sinapic acid (D7927).

Assay for α -amylase inhibitory activity

The α -amylase inhibitory activity of the methanol extract of *N. cadmea* was determined by the method of Ali et al. (2006) [21]. Porcine pancreatic α -amylase type VI (EC 3.2.1.1, Sigma) was dissolved in distilled water. As substrate solution, potato starch (0.5%, w/v) in phosphate buffer (pH 6.9) was used. Experiments were carried out with three replicates. The reaction was initiated by the addition of the enzyme solution. Then the tubes were incubated at 37 °C for 3 min. After the addition of substrate, the tubes were incubated at 37 °C for 5 min. Then, DNS (3,5-dinitrosalicylic acid) colour reagent solution was added to the mixture and put into an 85 °C heater. After 15 min, distilled water was added to the tubes, and the tubes were cooled. Absorbances of the mixtures were read at 540 nm. Acarbose was used as the positive control. Maltose formed as a result of starch hydrolysis was calculated using the maltose calibration equation, and then the inhibition percentage was determined [21].

Assay for α -glucosidase inhibitory activity

α -Glucosidase type IV enzyme (Sigma Co., St. Louis, USA) was dissolved in phosphate buffer (0.5 M, pH 6.5). The enzyme solution, extracts, and pure compounds were preincubated in a 96-well microtiter plate for 15 min at 37 °C. After that, the substrate solution [*p*-nitrophenyl- α -D-glucopyranoside (NPG), Sigma] was added. The mixture was incubated for 35 min at 37 °C. The increase in the absorption at 405 nm due to the hydrolysis of NPG by α -glucosidase was measured by VersaMax ELISA microtiter plate reader [22]. Acarbose (Bayer Group, Turkey), a potent α -glucosidase inhibitor, was used as a positive control. The inhibition percentage (%) was calculated by the equation: Inhibition % = $[(A_{\text{Control}} - A_{\text{Sample}}) / A_{\text{Control}}] \times 100$.

Phytochemical Analysis

TLC and HPTLC analysis

Prior to HPTLC experiments, TLC trials were performed using various solvent systems to find the most efficient method for the optimum separation of the phenolic compounds: Toluene-ethyl acetate-formic acid (5:4:1, v/v/v), Toluene-ethyl acetate-formic acid (8.5:1.5:0.1, v/v/v), Chloroform-ethyl acetate-acetone-formic acid (4:3:2:1, v/v/v/v), Ethyl acetate-water: formic acid (15:1:1, v/v/v), Ethyl acetate-water-formic acid-acetic acid (100:27:11:11, v/v/v/v), Ethyl acetate-methanol-water (100:16.5:13.5, v/v/v/v). The extracts were applied three times, and standards were applied as rosmarinic acid, caffeic acid, chlorogenic acid, quercetin, apigenin, and luteolin.

Following the determination of the suitable solvent system/s, HPTLC analysis was done using a Camag HPTLC system. Five microliters of the samples were sprayed in the form of 8 mm bands with an Automatic TLC Sampler 4 (ATS 4, CAMAG, Switzerland) onto pre-coated HPTLC glass plates (20 x 10 cm, Si 60 F254, Merck). The distance from the left side and the lower edge was 15 mm and 8 mm, respectively. Linear ascending development was carried out with an Automatic Developing Chamber 2 (ADC 2, CAMAG, Switzerland). Toluene-ethyl acetate-formic acid (5:4:1, v/v/v) and Chloroform-ethyl acetate-acetone-formic acid (4:3:2:1, v/v/v/v) were used as mobile phases. Relative humidity was not controlled. The twin through chamber was saturated for 20 minutes with 25 mL of the mobile phase before development. Ten milliliters of the same mixture were used for development. Plates were air-dried before and after development by ADC2. Documentation of the plates was performed by Reprostar 3 (CAMAG, Switzerland) at 366nm, 254 nm, and daylight. The extracts were applied three times, and the standards were used in the following order: rosmarinic acid, caffeic acid, chlorogenic acid, quercetin, apigenin, and luteolin [23, 24].

RP-HPLC-DAD analysis

Chromatographic assay of phenolic compounds was done using a previously validated HPLC-DAD method [25]. An Agilent 1260 Series HPLC system equipped with a quaternary pump, an auto-sampler, a column oven, and a diode-array UV/VIS detector was utilized. Data analysis was performed using Agilent Chemstation. The separation was made on ACE 5 μ C18 (250 x 4.60 mm) column. The mobile phase was a mixture of trifluoroacetic acid 0.1% in water (solution A), trifluoroacetic acid 0.1% in methanol (solution B), and trifluoroacetic acid 0.1% in acetonitrile (solution C). The composition of the gradient was (A:B:C), 80:12:8 at 0 min, 75:15:10 at 8 min, 70:18:12 at 16 min, 65:20:15 at 24 min, 50:35:15 at 32 min, 25:60:15 at 40 min, and 80:12:8 at 45 min. The duration between runs was 2 min. The injection volume was 10 μ L for each standard and sample solution. The detection UV wavelength was set at 230, 330, 360, 340, and 280 nm, and the column temperature was set to 30 °C. For the qualitative and quantitative analysis of phenolic compounds by HPLC, some phenolic compounds that are likely to be present in the plant were used as standards. These compounds include gallic acid, chlorogenic acid, caffeic acid, sinapic acid, ellagic acid, protocatechuic acid, *p*-coumaric acid, ferulic acid, rosmarinic acid, rutin, luteolin-7-glucoside, quercetin, luteolin, apigenin, and kaempferol. Quantification was performed by measuring at 330 nm for chlorogenic acid, caffeic acid, and rosmarinic acid using a photo-diode array detector. Quantitative determinations of chlorogenic acid, caffeic acid, and rosmarinic acid were performed, and

the validation parameters such as the coefficient of determination (r^2), limits of detection (LOD) and quantification (LOQ), mean area values (\bar{x}), standard deviation (SD), and percentage relative standard deviation (%RSD) were calculated.

Statistical Analysis

All experiments were performed in triplicate, and data are expressed as the mean \pm standard deviation (S.D.). Statistical evaluations, including linear regression, were carried out using Microsoft Excel and GraphPad InStat software. Statistical significance was determined at $p < 0.05$ (* $p < 0.05$, ** $p < 0.01$, *** $p < 0.001$).

ACKNOWLEDGMENTS


We would like to express our gratitude to Prof. Dr. Mehmet Çiçek and Assoc. Prof. Dr. Gülderem Yılmaz for their assistance in the collection and identification of the plant.

REFERENCES

1. T. Dirmenci; *Nepeta*. In *Türkiye Bitkileri Listesi (Damarlı Bitkiler)*; Güner, A., Aslan, S., Ekim, T., Vural, M., Babaç, M. T., Eds.; Nezahat Gökyiğit Botanik Bahçesi ve Flora Araştırmaları Derneği Yayını: İstanbul, Türkiye, **2012**; pp. 564-568. ISBN 978-605-60425-7-7.
2. G. Yılmaz; G. Öztürk; M. Çiçek; B. Demirci; *Int. J. Second. Metab.*, **2020**, 7(1), 28-34.
3. T. Baytop; *Türkiye’de Bitkiler ile Tedavi, Geçmişte ve Bugün*, 2nd ed.; Nobel Tıp Kitabevleri: İstanbul, Türkiye, **1999**; pp. 480. ISBN 975-420-0211.
4. C. Formisano; D. Rigano; F. Senatore; *Chem. Biodivers.*, **2011**, 8(10), 1783-1818.
5. C. Sarikurkcu; M. Eskici; A. Karanfil; B. Tepe; *S. Afr. J. Bot.*, **2019**, 120, 298-301.
6. T. Dirmenci; *BAÜ Fen Bil. Enst. Derg.*, **2003**, 5(2), 38-46.
7. A. Kaska; N. Deniz; M. Çiçek; R. Mammadov; *J. Food Sci.*, **2018**, 83(6), 1552-1559.
8. K. H. C. Baser; B. Demircakmak; A. Altintas; H. Duman; *J. Essent. Oil Res.*, **1998**, 10(3), 327-328.
9. Y. Takeda; Y. Oiso; T. Masuda; G. Honda; H. Otsuka; E. Sezik; E. Yesilada; *Phytochemistry*, **1998**, 49(3), 787-791.
10. T. P. Lam; N. V. N. Tran; L. H. D. Pham; N. V. T. Lai; B. T. N. Dang; N. L. N. Truong; T. D. Tran; *Nat. Prod. Bioprospect.*, **2024**, 14(1), 4.

11. A. M. M. Naguib; M. E. Ebrahim; H. F. Aly; H. M. Metawaa; A. H. Mahmoud; E. A. Mahmoud; F. M. Ebrahim; *Nat. Prod. Res.*, **2012**, 26(23), 2196-2198.
12. S. Devi; R. Singh; *Int. J. Pharm. Pharm. Sci.*, **2016**, 8(7), 330-335.
13. A. Sharma; R. Cooper; G. Bhardwaj; D. S. Cannoo; *J. Ethnopharmacol.*, **2021**, 268, 113679.
14. C. Sarikurkcü; O. Ceylan; S. Targan; S. Ć. Zeljković; *Ind. Crops Prod.*, **2018**, 125, 5–8.
15. A. Gökbulut; G. Yilmaz; *J. Res. Pharm.*, **2020**, 24(6), 901-907.
16. Y. L. Ngo; L. S. Chua; *Curr. Enz. Inhib.*, **2018**, 14(2), 97-103.
17. P. P. McCue; K. Shetty; *Asia Pac. J. Clin. Nutr.*, **2004**, 13(1).
18. G. Oboh; O. M. Agunloye; S. A. Adefegha; A. J. Akinyemi; A. O. Ademiluyi; *J. Basic Clin. Physiol. Pharmacol.*, **2015**, 26(2), 165-170.
19. N. Cardullo; G. Floresta; A. Rescifina; V. Muccilli; C. Tringali; *Bioorg. Chem.*, **2021**, 117, 105458.
20. K. S. Tshiyoyo; M. J. Bester; J. C. Serem; Z. Apostolides; *J. Mol. Struct.*, **2022**, 1266, 133492.
21. H. Ali; P. J. Houghton; A. Soumyanath; *J. Ethnopharmacol.*, **2006**, 107(3), 449-455.
22. S. H. Lam; J. M. Chen; C. J. Kang; C. H. Chen; S. S. Lee; *Phytochemistry*, **2008**, 69(5), 1173-1178.
23. A. Gökbulut; *Turk. J. Pharm. Sci.*, **2016**, 13(2), 159-166.
24. A. Gökbulut; *Curr. Anal. Chem.*, **2021**, 17(9), 1252-1259.
25. A. Gökbulut; *Trop. J. Pharm. Res.*, **2015**, 14(10), 1871–1877.

HYDRAULIC MODELING AND OPTIMIZATION OF THE OIL GATHERING NETWORK IN THE PERIPHERAL FIELD RAMA–RAA NORTH, HASSI MESSAOU D (ALGERIA)

Ourdia AMZAL^a, Ahmed Salah Eddine MEDDOUR^a , Farid SOUAS^{a*} ,
Radia AKSOUH^a , Abdelhamid SAFRI^a

ABSTRACT. This study presents the hydraulic modeling and optimization of the RAMA and RAA crude oil gathering network in Algeria's Hassi Messaoud oil field to enhance production efficiency and ensure stable field performance. A digital network model was developed using PIPESIM to simulate multiphase flow behavior from the wellheads to the Early Production Facility (EPF). The model calibration showed strong agreement between simulated and measured pressures, with deviations below 7%, confirming its reliability. Simulation results revealed several oversized flowlines with velocities below the recommended 1–5 m/s range and an undersized line (MFD BEKEN) exhibiting excessive velocities and pressure losses above 0.85 bar/km. To address these issues, the impact of integrating 11 new wells was evaluated, showing increase in line and manifold pressures. An optimization study was subsequently conducted by adjusting pipeline diameters and adding new flowlines in compliance with API design standards. The optimized configuration improved velocity distribution and reduced erosion risks, ensuring safer and more efficient network operation across the RAMA–RAA fields.

Keywords: crude oil, flow behavior, hydraulic modeling, PIPESIM, RAMA–RAA fields, pipeline optimization.

INTRODUCTION

Crude oil remains the dominant source of global energy, contributing approximately 37% of the world's total energy supply [1]. It plays a critical role in economic growth and industrial development, serving as the base for

^a LEGHYD Laboratory, Faculty of Civil Engineering, University of Science and Technology Houari Boumediene (USTHB), Bab Ezzouar, Alger, Algeria

* Corresponding author: fa.souas@gmail.com, farid.souas@usthb.edu.dz



producing transportation fuels and a wide range of petrochemical products such as solvents, polymers, and intermediates [2]. Despite global efforts toward energy diversification, crude oil will continue to be an essential raw material in the foreseeable future. Light crude oils, such as Algeria's Saharan blend, are highly valued due to their low density, low sulfur and asphaltene content, and low viscosity, which make them relatively easier to transport.

Algeria is a key oil and gas producer with vast hydrocarbon reserves that are central to its national economy. Most of the country's petroleum resources are located in the southeastern Saharan region, particularly in large fields such as Hassi Messaoud. The oil and gas sector is dominated by the national company Sonatrach, which is responsible for both exploration and production. In an effort to boost overall output, Sonatrach has expanded operations to nearby satellite fields, including the RAMA-RAA field. However, the exploitation of this field presents operational challenges due to the long distances between wells and surface treatment facilities. Crude oil from RAMA-RAA is transported to the recently developed RAMA-2 Early Production Facilities (EPF) for initial processing and stabilization.

Nevertheless, several issues persist throughout the production and transportation chain. One of the most critical concerns is the deposition of asphaltenes and other heavy components, which can occur in various parts of the system, including near-wellbore regions, tubing, separators, and pipelines [3]. Recent studies on Algerian crude oils have also highlighted complex flow behavior driven by compositional variability and aging effects, particularly the distinctions between fresh crude and sludge deposits, which further complicate transportation and handling [4–6].

Crude oil is a complex mixture of hydrocarbons including aromatics, resins, and asphaltenes, resulting in non-Newtonian flow behavior under certain conditions. These suspended particles increase the risk of fouling and deposition along infrastructure, reducing energy efficiency and increasing operational costs [7]. Transporting crude oil through pipelines, especially over long distances, is particularly affected by changes in temperature, pressure, and composition. To better understand and mitigate these challenges, numerous researchers have studied the flow behavior of non-Newtonian fluids in different pipeline configurations. For example, Das et al. [8] investigated non-Newtonian flow through bends, while Trallero [9] focused on oil–water flow in horizontal pipes. Hansen [10] developed phenomenological models for multiphase flow in gravity separators, and Bannwart [11] explored core annular oil–water flow regimes. Bandyopadhyay and Das [12] proposed empirical correlations for pressure drop and flow resistance in different pipeline components. In addition, Rudman and Blackburn [13] applied direct numerical simulation (DNS) methods

to analyze the transport of non-Newtonian fluids, offering valuable insights into turbulent flow dynamics and supporting the design of more efficient pipeline systems.

The primary objective of this study is to develop and calibrate a reliable hydraulic model of the RAMA–RAA oil gathering network in Hassi Messaoud (Algeria) using PIPESIM, in order to identify operational inefficiencies and propose optimized pipeline configurations. This work is crucial for improving flow assurance, reducing pressure losses and erosion risks, and ensuring safe, stable, and efficient production. The optimized network serves as a practical framework for future well integration and development planning, contributing to enhanced field performance and long-term asset integrity.

This study contributes a calibrated hydraulic model of the RAMA–RAA gathering system and applies an integrated calibration–optimization workflow to diagnose velocity imbalance, evaluate erosion risk, and propose diameter and routing modifications tailored to long-distance multiphase networks.

RESULTS AND DISCUSSION

After developing the gathering network model, flow simulations were performed in PIPESIM to evaluate the hydraulic behavior of the system from the wellheads to the EPF. This analysis provided a clear overview of the flow regimes and helped identify sections prone to excessive pressure losses, corrosion, or erosion.

Model calibration was then conducted to ensure agreement between simulated and measured data. The process aimed to minimize the deviation between the measured pressure (P_{pm}) and the simulated pressure (P_{pc}), following the criterion:

$$\text{Relative deviation} = \frac{|P_{pm} - P_{pc}|}{P_{pm}} \leq 7\% \quad (1)$$

The 7% acceptance threshold was selected as a conservative limit consistent with typical field gauge uncertainty and standard practice in preliminary network-model calibration.

Parameter tuning primarily involved adjusting the gas–oil ratio, pipe roughness, and the choice of flow correlation. The Beggs & Brill correlation [14] provided the best match between calculated and observed pressures. Figure 1 illustrates the calibration results, showing that all relative deviations between measured and simulated pressures are within the acceptable 7% range, confirming that the developed network model is well matched and accurately represents actual field conditions.

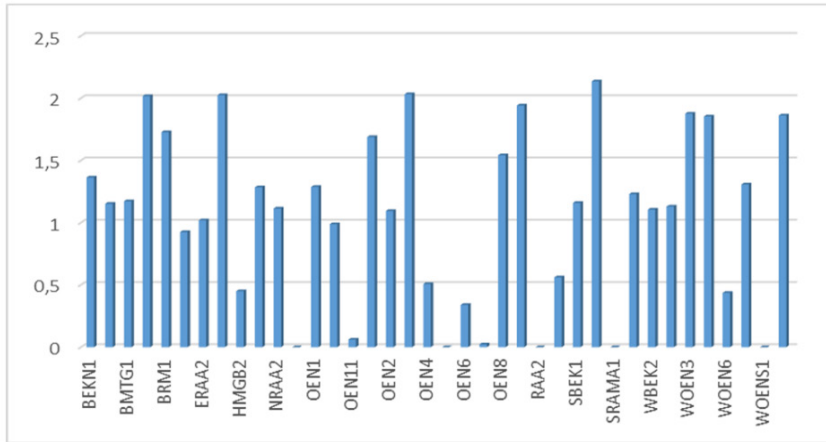


Figure 1. Model calibration result

Table 1. Results of the simulation of the existing network

Start	Gradient P (bar/km)	Mixture velocity Vm [1-5] m/s
JCT OEN	0.6	0.52
MFD BEKN	1.14	8.86
MFD OEN-M1	0.51	0.73
MFD OEN-M4	1.64	0.07
MFD OEN-M5	0.3	0.94
BEKN-1	0.93	0.09
BMTG-1	1.253	0.31
BMTG-2	2.038	0.83
ERAA-2	0.786	0.51
HMGB-2	0.783	0.81
NRAA-1	2	0.03
NRAA-2	0.044	0.14
OEN-1	11.80	0.69
OEN-10	0.337	0.06
OEN-11	0.665	0.98
OEN-12	0.495	0.68
OEN-6	0.563	0.82
OEN-7	0.4	0.66
OEN-9	0.337	0.97
RAA-5	0.948	0.5
SBEK-1	1.475	0.75
SOEN-1	1.395	0.03
WOEN-4	1.350	0.35
WOEN-7	12.500	0.49
ZMD-1	1.075	0.04

HYDRAULIC MODELING AND OPTIMIZATION OF THE OIL GATHERING NETWORK IN THE PERIPHERAL FIELD RAMA-RAA NORTH, HASSI MESSAOUD (ALGERIA)

The calibrated model was subsequently used to analyze the hydraulic performance of the existing network. The results, summarized in Table 1, indicate that several flowlines are oversized as reflected by flow velocities below the recommended range of 1–5m/s, whereas the MFD BEKN line exhibits velocities exceeding acceptable limits, suggesting undersizing. In addition, many wells display pressure gradients greater than 0.85 bar/km, implying excessive head losses and potential operational inefficiencies. Overall, the simulation demonstrates that although the network performs satisfactorily, certain sections would benefit from resizing or optimization to improve flow distribution and minimize the risks of erosion or deposition.

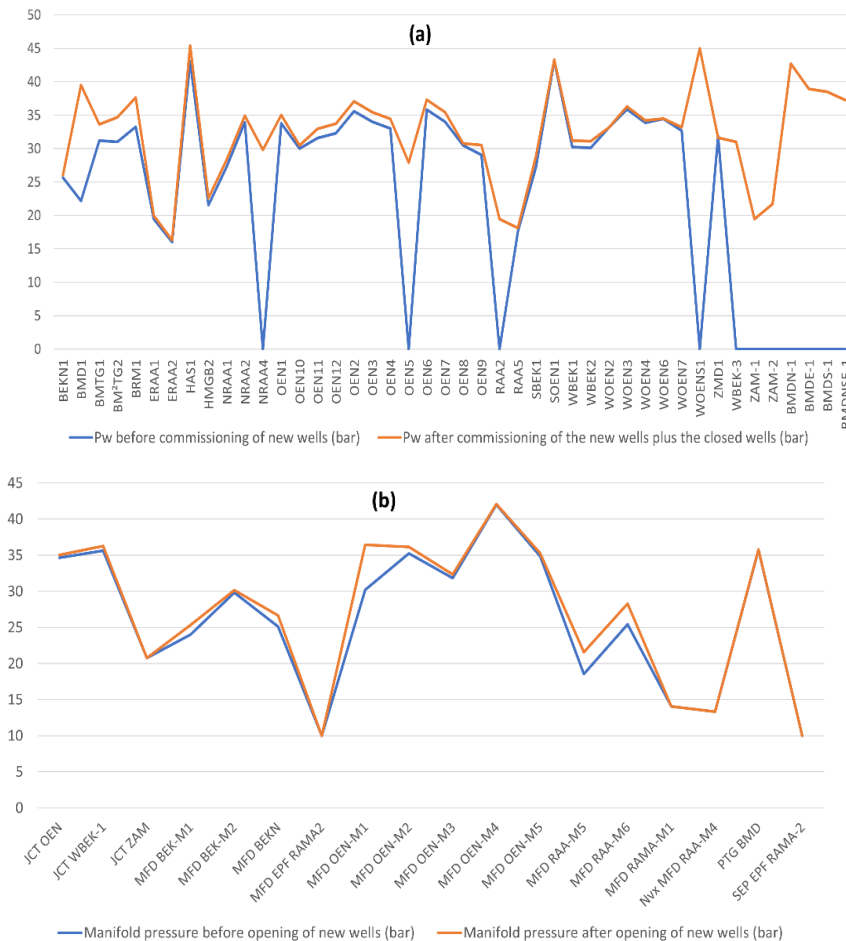


Figure 2. Comparison between current pressures and those after commissioning of new wells for (a) flowlines and (b) manifolds

In order to address the problem of oversized and undersized flowlines, additional wells were opened, including NRAA-4, OEN-5, RAA-5, and WOENS-1. Moreover, new wells currently under drilling — BMDE-1, BMDN-1, BMDS-1, and BMDNSE-1 — were considered in the simulation. The production parameters of BMD-1 were assumed to represent these new wells, with estimated values of $Q = 10 \text{ m}^3/\text{h}$, gas-oil ratio (GOR) = $250 \text{ sm}^3/\text{sm}^3$, and temperature = 26°C . In addition, the wells WBEK-3, ZAM-1, and ZAM-2 were included with the following estimated parameters:

- WBEK-3: $Q = 8 \text{ m}^3/\text{h}$, GOR = $200 \text{ sm}^3/\text{sm}^3$, $T = 28^\circ\text{C}$
- ZAM-1: $Q = 7 \text{ m}^3/\text{h}$, GOR = $100 \text{ sm}^3/\text{sm}^3$, $T = 45^\circ\text{C}$
- ZAM-2: $Q = 10 \text{ m}^3/\text{h}$, GOR = $120 \text{ sm}^3/\text{sm}^3$, $T = 30^\circ\text{C}$

The parameters for future wells were estimated from analog wells in the same reservoir units and from historical production of the most representative existing producer (BMD-1). These values were provided by the operating company (EP SONATRACH) as planning assumptions.

Figure 2a presents the comparison between the current flowline pressures and those obtained after the commissioning of the new wells (BMDE-1, BMDN-1, BMDS-1, BMDNSE-1, ZAM-1, WBEK-3, ZAM-2). The analysis indicates that the flowline pressures were readjusted following the start-up of these wells, demonstrating an adaptation of the network to the evolving production conditions of the field. Figure 2b shows the comparison between current and post-commissioning manifold pressures. The simulation results reveal noticeable variations in manifold pressures after the integration of the new wells. Overall, it can be concluded that the commissioning of additional wells led to an increase in pipeline pressures for several existing producers. This rise in P_p may negatively affect the production performance of some wells, highlighting the need for network optimization to maintain stable and efficient operations.

To assess the impact of commissioning new wells on the RAMA and RAA gathering network, a new simulation scenario was developed, focusing on the analysis of mixture flow velocities. The Erosion Velocity Ratio (EVR), defined as the ratio between the actual flow velocity and the critical erosion velocity, was calculated to evaluate the risk of erosion. According to industry standards, the EVR value should remain below 70% to avoid potential erosion problems. An EVR threshold of 0.7 was adopted as a conservative screening limit commonly used in industry erosion-risk assessments (e.g., API RP 14E guidelines [15]).

The simulation of the RAMA–RAA gathering system after the commissioning of the 11 new wells showed that 33 flowlines are oversized (highlighted in yellow in Table 2) and three pipelines are undersized (highlighted in red in Table 2). Based on these findings, an optimization study was carried

out to adjust the line diameters and, where necessary, to propose the installation of additional pipelines. These modifications aim to ensure that the network complies with API design standards.

Table 2. Analysis of mixture velocity results

Name	System pressure loss (bar)	Mixture velocity at inlet (m/s)	Mixture velocity at outlet (m/s)	Maximum erosion velocity ratio (%)
BEKN-1	0.93	0.08	0.09	0.87
BMD-1	3.80	1.65	1.98	18.27
BMDE-1	3.21	0.72	0.87	8.60
BMDN-1	7.01	0.65	0.87	8.60
BMDS-1	2.80	0.74	0.87	8.60
BMDSE-1	1.57	0.78	0.87	8.59
BMTG-1	3.82	0.23	0.28	3.44
BMTG-2	4.88	0.60	0.76	7.84
BRM-1	2.41	0.82	0.95	11.10
ERAA-1	0.42	1.06	1.11	9.67
ERAA-2	2.26	0.43	0.53	5.05
HAS-1	20.03	0.04	0.06	0.98
HMGB-2	1.85	0.66	0.77	9.53
JCT OEN_MFD OEN-M3	2.78	0.45	0.49	5.92
JCT WBEK-1_MFD BEK-M1	11.60	0.60	0.97	9.08
JCT ZAM_MFD RAMA-M1	6.70	1.67	2.44	22.71
MFD BEK-M1_MFD EPF RAMA2	14.02	3.27	7.59	47.70
MFD BEK-M2_MFD BEK-M1	5.77	1.92	2.38	20.94
MFD BEKN_MFD EPF RAMA2	15.10	3.96	9.55	62.29
MFD OEN-M1_MFD BEKN	5.09	0.56	0.69	7.50
MFD OEN-M2_MFD BEK-M1	11.22	2.76	4.05	40.26
MFD OEN-M3_MFD BEKN	6.74	2.22	2.80	28.57
MFD OEN-M4_JCT OEN	7.36	0.05	0.06	1.00
MFD OEN-M5_MFD OEN-M3	3.00	0.82	0.90	11.05
MFD RAA-M5_Nvx MFD RAA-M4	5.19	0.54	0.73	8.03
MFD RAA-M6_MFD RAA-M5	6.98	0.13	0.17	3.36
MFD RAMA-M1_MFD EPF RAMA2	4.04	1.09	1.49	11.92
NRAA-1	0.45	0.03	0.03	0.59
NRAA-2	0.17	0.13	0.14	3.07
NRAA4	4.43	0.05	0.06	1.17
Nvx MFD RAA-M4_MFD EPF RAMA2	3.34	0.76	1.00	9.12
OEN-1	0.60	0.61	0.67	7.98
OEN-10	1.28	0.06	0.06	1.25
OEN-11	1.13	0.88	0.94	11.22
OEN-12	1.88	0.58	0.65	8.10
OEN-2	5.21	0.90	1.11	12.27
OEN-3	3.62	1.08	1.33	14.51
OEN-4	2.59	0.79	0.94	10.43

Name	System pressure loss (bar)	Mixture velocity at inlet (m/s)	Mixture velocity at outlet (m/s)	Maximum erosion velocity ratio (%)
OEN-5	2.83	0.95	1.13	10.97
OEN-6	2.43	0.69	0.79	9.99
OEN-7	0.61	0.59	0.63	8.26
OEN-8	5.68	1.64	2.13	20.27
OEN-9	0.33	0.88	0.92	10.27
PTG BMD MFD EPF RAMA2	25.69	3.14	10.95	56.79
RAA-2	6.09	0.09	0.13	1.05
RAA-5	5.78	0.05	0.06	0.77
SBEK-1	7.82	0.50	0.70	7.32
SOEN-1	5.58	0.03	0.03	0.61
WBEK-3	1.22	0.74	0.83	8.23
WOEN-2	2.72	1.10	1.28	13.45
WOEN-3	2.45	1.25	1.43	16.86
WOEN-4	4.45	0.27	0.33	4.59
WOEN-6	1.01	1.38	1.44	15.83
WOEN-7	6.33	0.37	0.47	6.90
WOENS-1	9.95	0.11	0.14	1.91
ZAM-1	6.27	0.56	0.82	7.22
ZAM2	0.93	0.81	0.90	9.18
ZMD-1	0.86	0.07	0.04	1.69

The optimization objective was to minimize pressure imbalance and reduce the maximum Erosion Velocity Ratio (EVR) across the network. Constraints included feasible multiphase velocities (1–5m/s), available commercial pipe diameters, and preservation of the existing network topology. Each candidate design was evaluated using the calibrated PIPESIM model.

Table 3. Current and modified pipeline diameters

Name	Current diameter	Optimized diameter
BEKN-1	6"	4"
BMDE-1	6"	4"
BMDN-1	6"	4"
BMDS-1	6"	4"
BMDSE-1	6"	4"
BMTG-1	6"	4"
BMTG-2	6"	4"
ERAA-2	6"	4"
HAS-1	6"	4"
HMGB-2	6"	4"
JCT OEN MFD OEN-M3	6"	4"
MFD BEK-M1 MFD EPF RAMA2	12"	14"

HYDRAULIC MODELING AND OPTIMIZATION OF THE OIL GATHERING NETWORK
IN THE PERIPHERAL FIELD RAMA-RAA NORTH, HASSI MESSAOUD (ALGERIA)

Name	Current diameter	Optimized diameter
MFD BEKN MFD EPF RAMA2	12"	14"
MFD OEN-M1 MFD BEKN	8"	6"
MFD OEN-M4 JCT OEN	8"	6"
MFD RAA-M5 Nvx MFD RAA-M4	10"	6"
MFD RAA-M6 MFD RAA-M5	8"	6"
NRAA-1	8"	6"
NRAA-2	6"	4"
NRAA4	6"	4"
OEN-1	6"	4"
OEN-10	6"	4"
OEN-12	6"	4"
OEN-6	6"	4"
OEN-7	6"	4"
PTG BMD MFD EPF RAMA2	8"	10"
RAA-2	6"	4"
RAA-5	6"	4"
SBEK-1	6"	4"
SOEN-1	6"	4"
WBEK-3	6"	4"
WOEN-4	6"	4"
WOEN-7	6"	4"
WOENS-1	6"	4"
ZAM-1	6"	4"
ZMD-1	6"	4"

The newly proposed diameters, illustrated in Table 3, were incorporated into the previously calibrated model, and the network was re-simulated to validate the selected values. The updated results, summarized in Table 4 and illustrated in figure 3, demonstrate a clear improvement in flow velocity distribution across the network, confirming the effectiveness of the proposed design modifications.

Table 4. Optimization results of the RAMA & RAA network

Name	System pressure loss (bar)	Mixture velocity at outlet (m/s)	Maximum erosion velocity ratio (%)
BEKN-1	0.85	1.91	11.02
BMD-1	3.87	3.12	13.60
BMDE-1	2.99	1.96	12.63
BMDN-1	6.99	3.09	12.62
BMDS-1	4.74	3.09	12.62
BMDSE-1	3.27	3.08	12.62

Name	System pressure loss (bar)	Mixture velocity at outlet (m/s)	Maximum erosion velocity ratio (%)
BMTG-1	3.46	1.25	8.75
BMTG-2	6.05	1.97	10.38
BRM-1	2.36	1.04	8.96
ERAA-1	0.45	1.10	10.66
ERAA-2	2.42	1.21	10.55
HAS-1	19.78	1.15	6.39
HMGB-2	1.85	1.08	8.07
JCT OEN_MFD OEN-M3	2.69	1.10	8.98
JCT WBEK-1_MFD BEK-M1	10.96	1.14	11.61
JCT ZAM_MFD RAMA-M1	6.70	2.44	10.74
MFD BEK-M1_MFD EPF RAMA2	10.31	4.23	15.92
MFD BEK-M2_MFD BEK-M1	5.83	2.81	12.35
MFD BEKN_MFD EPF RAMA2	10.65	4.84	15.34
MFD OEN-M1_MFD BEKN	5.78	1.45	10.17
MFD OEN-M2_MFD BEK-M1	11.81	4.77	10.92
MFD OEN-M3_MFD BEKN	6.69	3.39	10.78
MFD OEN-M4_JCT OEN	7.24	1.28	6.72
MFD OEN-M5_MFD OEN-M3	2.95	1.05	8.80
MFD RAA-M5_Nvx MFD RAA-M4	8.23	2.00	9.11
MFD RAA-M6_MFD RAA-M5	1.01	1.58	4.42
MFD RAMA-M1_MFD EPF RAMA2	4.04	1.49	12.54
NRAA-1	2.45	1.10	4.39
NRAA-2	1.69	1.31	4.40
NRAA4	4.51	1.12	4.77
Nvx MFD RAA-M4_MFD EPF RAMA2	3.34	1.00	11.03
OEN-1	1.38	1.73	8.94
OEN-10	1.28	1.57	5.01
OEN-11	1.11	1.09	9.03
OEN-12	4.78	1.72	8.70
OEN-2	5.05	1.29	9.75
OEN-3	3.56	1.55	9.89
OEN-4	2.52	1.10	9.76
OEN-5	2.76	1.37	11.38
OEN-6	5.92	2.05	8.46
OEN-7	1.35	1.64	8.19
OEN-8	5.93	2.58	11.56
OEN-9	0.33	1.05	9.61

HYDRAULIC MODELING AND OPTIMIZATION OF THE OIL GATHERING NETWORK
IN THE PERIPHERAL FIELD RAMA-RAA NORTH, HASSI MESSAOUD (ALGERIA)

Name	System pressure loss (bar)	Mixture velocity at outlet (m/s)	Maximum erosion velocity ratio (%)
PTG BMD_MFD EPF RAMA2	12.81	3.96	19.30
RAA-2	5.60	1.12	12.39
RAA-5	5.69	1.12	7.17
SBEK-1	8.62	1.88	10.43
SOEN-1	5.55	1.08	5.65
WBEK-1	0.04	0.69	9.01
WBEK-2	3.93	1.65	11.96
WBEK-3	1.93	2.15	10.80
WOEN-2	2.64	1.49	10.24
WOEN-3	2.42	1.57	8.88
WOEN-4	4.45	0.82	7.49
WOEN-6	0.97	1.58	9.55
WOEN-7	8.08	1.16	7.11
WOENS-1	9.22	1.35	7.73
ZAM-1	8.79	1.85	11.29
ZAM2	0.93	0.90	9.83
ZMD-1	0.89	1.04	4.37

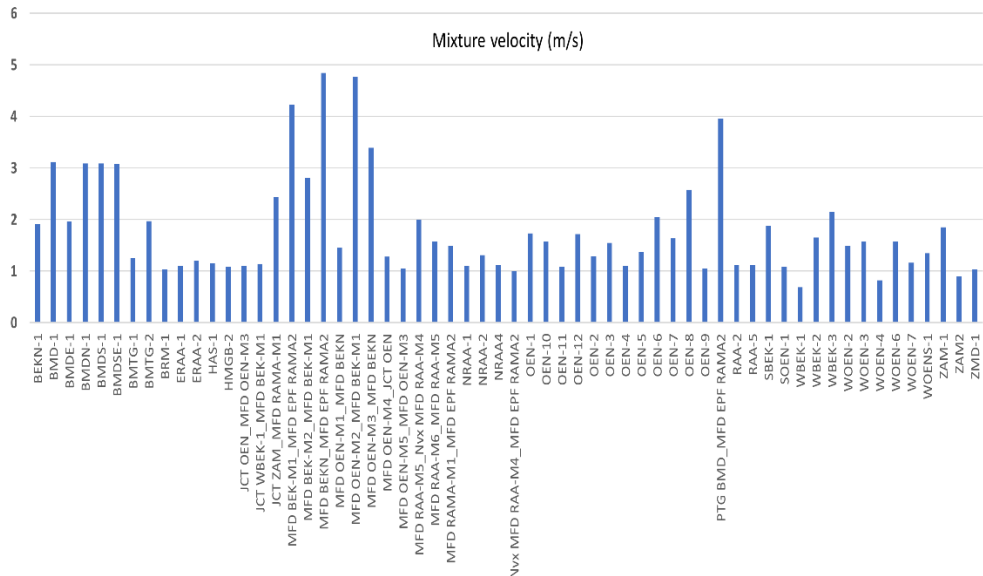


Figure 3. Histogram of mixture velocities after network optimization

While the optimized configuration performs well under the modeled conditions, it is important to recognize the practical limitations of the simulation approach.

The model is steady-state and does not capture transient thermal effects or short-term variations in flow behavior. These simplifications may slightly affect absolute pressure and velocity predictions when applied to real operating conditions. In practice, operational factors such as startup, shut-in, temperature fluctuations, and variations in (GOR) can produce temporary deviations from the steady-state baseline; however, these fluctuations occur around the modeled equilibrium, and therefore the relative optimization trends and the recommended network configuration remain valid.

CONCLUSIONS

The hydraulic modeling and optimization of the RAMA and RAA gathering network provided a comprehensive understanding of the system's flow behavior and performance. The calibration of the PIPESIM model demonstrated a strong agreement between simulated and measured pressures, with deviations below 7%, confirming the reliability of the constructed network model.

The initial analysis revealed several oversized and undersized flowlines, resulting in suboptimal flow velocities and high-pressure gradients in certain sections. The commissioning of new wells and the corresponding simulations highlighted an overall increase in pipeline and manifold pressures, emphasizing the importance of network reconfiguration to maintain balanced production.

Subsequent optimization efforts, including the adjustment of pipeline diameters and the integration of new flowlines, led to a more uniform velocity distribution across the network. The improved results, consistent with API design standards, confirm the technical soundness of the proposed modifications.

Overall, the optimized RAMA–RAA network model ensures safer operation, reduced erosion risk, and enhanced production efficiency, serving as a reliable framework for future development planning and well tie-in scenarios in the field.

EXPERIMENTAL SECTION

The modeling of the oil collection network for the RAMA and RAA fields was carried out using the PIPESIM 2022 software. This methodology describes the data acquisition, modeling procedure, and simulation steps performed to analyze flow behavior and optimize network performance.

Field Description and Data Collection

The RAMA and RAA production fields comprise 38 oil wells, of which 4 wells are shut-in. The total production of the active wells is approximately 407.9 m³/h of crude oil and 1.223.920 sm³/d of gas, transported to the EPF (Early Production Facility) RAMA-2 through a 109.5 km gathering network of various diameters. The main input data used for network modeling include well production parameters, pipeline geometry, collector characteristics, and fluid properties.

Reservoir Fluid Properties

The physical properties of the produced fluids are as follows: oil with a density of 43° API, gas with a density of 0.83, and water with a density of 1.02. The parameters measured during well testing include oil flow rate, gas flow rate, head and pipe pressures, temperature, and water cut (WC). The following relations are used to define two key parameters:

$$GOR = \frac{Q_g}{Q_h} \quad (2)$$

$$WC = \frac{Q_w}{Q_w + Q_h} \times 100 \quad (3)$$

where: Q_g is the gas flow rate. Q_h is the oil flow rate. and Q_w is the water flow rate.

Well Test Data

Table 5 presents the latest gauge data from the producing wells in the RAMA–RAA fields.

Table 5. Latest well gauge data

N°	Well	GOR	Qh (sm ³ /h)	Watercut (%)	T (C°)
01	BEKN1	155.21	0.9	0	35
02	BMD1	307.25	15	0	32
03	BMTG1	170	4.2	0	25
04	BMTG2	1941	8.1	29.67	29
05	BRM1	160.34	13.3	0	29
06	ERAA1	153.65	8.7	0	40
07	ERAA2	90.36	5.3	0	32
08	HAS1	81.85	1.8	0	40

OURDIA AMZAL, AHMED SALAH EDDINE MEDDOUR, FARID SOUAS,
RADIA AKSOUH, ABDELHAMID SAFRI

N°	Well	GOR	Qh (sm ³ /h)	Watercut (%)	T (C°)
09	HMGB2	74.75	13.3	0	32
10	NRAA1	19.5	2.8	0	45
11	NRAA2	20	8.4	0	37
12	NRAA4	27	2.9	0	29
13	OEN1	143.32	9.9	0	30
14	OEN10	33.6	3.1	0	36
15	OEN11	134.53	14.1	0	40
16	OEN12	121.89	10.7	0	35
17	OEN2	161.49	13.9	0	35
18	OEN3	167.76	16.1	0	25
19	OEN4	161.82	11.8	0	25
20	OEN5	168.1	10.8	0	30
21	OEN6	128.71	13.4	0	32
22	OEN7	121.58	11.5	0	32
23	OEN8	174.9	19.5	0	36
24	OEN9	152.66	11.8	0	30
25	RAA2	75.32	0.9	0	36
26	RAA5	96.5	1.1	57	25
27	SBEK1	136.46	8	0	26
28	SOEN1	39.39	1.3	0	33
29	SRAMA1	219	0.5	0	36
30	WBEK1	173.13	8.6	0	30
31	WBEK2	259.4	10.7	0	30
32	WOEN2	183.11	14.2	0	29
33	WOEN3	159.26	20.4	0	26
34	WOEN4	102.07	7	0	33
35	WOEN6	194.12	17.2	0	40
36	WOEN7	90.04	11.2	0	29
37	WOENS1	110.28	2.8	0	30
38	ZMD1	11	4.7	0	29

Pipeline and Collector Data

The gathering system consists of several flowlines and manifolds that transport the multiphase mixture of oil, gas, and water from the producing wells to the EPF RAMA-2 facility.

Table 6. Pipeline characteristics

Line name	Start	End	D (in)	L (m)	T (C°)
BEKN1 MFD BEKN	BEKEN1	MFD BEKN	6"	1000	50
BMTG1 MFD BEK2	BMTG1	MFD BEK-M2	6"	3000	50
BRM1 MFD OEN2	BRM-1	MFD RAMA-1	6"	3499	50
ERAA2 MFD RAMA 1	ERAA-2	MFD RAMA-1	6"	2900	50
HAS1 MFD OEN4	HAS-1	MFD OEN-4	6"	14500	50
HMGB1 JCT ERAMA2	HMGB-1	JCT ERAMA-2	6"	7890	50
HMGB2 JCT ZAM	HMGB-2	JCT ZAM	6"	2336	50
NRAA4 JCT NRAA1	NRAA-4	JCT NRAA-1	6"	5500	50
NRAA2 JCT NRAA1 8	NRAA-2	JCT NRAA-1	6"	5000	50
NRAA-1 JCT NRAA-1 6	NRAA-1	JCT NRAA-1	8"	200	50
ERAA-3 NV MFD4	ERAA-3	NVX MFD RAA4	6"	116	50
OEN1 JCT OEN 1	OEN-1	JCT OEN-1	6"	50	50
OEN4 MFD OEN3	OEN-4	MFD OEN-3	6"	3800	50
OEN5 MFD BEKN	OEN-5	MFD BEKN	6"	5400	50
OEN7 MFD OEN M5	OEN-7	MFD OEN-M5	6"	1500	50
OEN8 MFD BEKEN	OEN-8	MFD BEKN	6"	130	50
OEN9 MFD OEN1	OEN-9	MFD OEN-M1	6"	980	50
OEN12 MFD OEN3	OEN-12	MFD OEN-M3	6"	3800	50
OEN 2 MFD OEN3	OEN-2	MFD OEN-M3	6"	6462	50
OEN 3 MFD OEN3	OEN-3	MFD OEN-M5	6"	4460	50
OEN 6 MFD OEN 5	OEN-6	MFD OEN-M5	6"	4300	50
RAA1 MFD RAA2	RAA-1	MFD RAA-M2	4"	8900	50
RAA2 NV MFD RAA 4	RAA-2	NV MFD RAA-4	6"	7200	50
RAA5 NV MFD M4	RAA-5	NV MFD RAA-M	6"	6100	50
WBEK1 POINT BEK 1	WBEK-1	PNT BEK-1	6"	7480	50
WBEK2 MFD BEK2	WBEK-2	MFD BEK-M2	6"	3800	50
WOEN2 MFD OEN 3	WOEN-2	MFD OEN-M3	6"	3400	50
WOEN3 MFD OEN M2	WOEN-3	MFD OEN-M2	6"	3200	50
WOEN4 MFD OEN M2	WOEN-4	MFD OEN-M2	6"	3267	50
WOEN5 MFD BEKEN	WOEN-5	MFD BEKN	6"	4200	50
WOEN6 MFD OEN M2	WOEN-6	MFD OEN-M2	6"	3267	50

Table 7. Collector characteristics

Collector name	Start	End	D (in)	L(m)	T(C°)
JCT NRAA1 MFD RAA5	JCT NRAA-1	MFD RAA-M5	8"	17000	50
JCT OEN1 MFD OEN3	JCT OEN-1	MFD OEN-3	8"	4500	50
MDF RAA (M2 M3)12	MFD RAA-M2	MFD RAA-M3	12"	6426	50
MDF RAA (M2 M3)6	MFD RAA-M2	MFD RAA-M3	6"	6925	50
MDF RAA (M3 M4) A	MFD RAA-M3	MFD RAA-M4	8"	5184	50
MFD (OEN M1 BEKEN)	MFD OEN-M1	MFD BEKEN	8"	9800	50
MFD (OENM3 BEKEN)	MFD OEN-M3	MFD BEKEN	8"	8000	50
MFD (ZMD RAA-M5)	MFD ZMD	MFD RAA-M5	8"	13700	50
MFD BEK (M2 M1)	MFD BEK-M2	MFD BEK-M1	8"	9000	50
MFD BEK 1 PNT BEK 1	MFD BEK-M1	PNT BEK-1	6"	400	50
MFD BEKEN EPF RAMA 2	MFD BEKEN	EPF RAMA-2	12"	12000	50
MFD OEN 5 3	MFD OEN-5	MFD OEN-3	8"	6000	50
MFD OENM4 JCTOEN1	MFD OEN-M4	JCTOEN-1	8"	6500	50
MFD RAMA M1 EPF RAMA 2	MFD RAMA-M1	EPF RAMA-2	10"	17697	50
MFDRAA (M4 M3)	MFD RAA-M4	MFD RAA-M3	6"	6925	50
NV MFD RAA4 EPF RAMA2	NV MFD RAA-M4	EPF RAMA-2	12"	6000	50
PNTBEK1EPFRAMA B	PNT BEK-1	EPF RAMA-2	8"	19976	50
POINT BEK1 EPFRAMA2 A	PNT BEK-1	EPF RAMA-2	8"	16500	50
POINT ERRA-1 MFD RAA-1	PNT ERAA-1	MFD RAA-M1	8"	7200	50

Modeling Procedure

The digital model was constructed in PIPESIM by defining all components from source points (wells) to sinks (EPF RAMA-2). Simulations were performed using the PIPESIM steady-state multiphase flow simulator (Schlumberger, 2022), following an approach similar to that used in recent studies for multiphase flow modeling of wells and gathering networks [16-17]. The network includes wells, flowlines, junctions, and manifolds, with boundary conditions applied at both ends of the system. Fluid properties were defined using four possible methods available in PIPESIM: compositional model by specifying molar composition, PVT file based on laboratory measurements, MFL file (Multi-flash) for multi-phase definition, and black oil model defined by physical parameters (specific gravity API, viscosities. etc.). The model uses empirical correlations to predict pressure drops and flow regimes. The selected methods include the Beggs & Brill correlation [14], which tends to underestimate pressure losses in flowlines containing low points or liquid accumulation zones, and the Dukler-Eaton-Flannigan correlation [18], which tends to overestimate losses in downhill sections without undulations. For each source (well), the following data were entered: oil flow rate, gas-oil ratio (GOR), temperature, and watercut. For each flowline and collector, the outer diameter (OD) and schedule, elevation profile as a function of length, and roughness factor were defined. The roughness factor was set to 0.0018 for

new pipelines and 0.004 for older lines. All simulations were performed in steady-state mode, which is appropriate for evaluating long-term hydraulic behavior and network optimization. The modeling workflow was developed using the PIPESIM multiphase flow simulator (Schlumberger, 2022). The sink node was defined by specifying the pressure at the arrival point (EPF RAMA-2). Heat transfer was considered using standard hydrocarbon parameters: pipe conductivity of 45 w/(m·k), burial depth of 0 inches (air-laid lines) or 31.5 inches (buried lines), and ambient temperature of 50°C (summer) and 5°C (winter). Fluid properties were assigned, including a light oil and gas mixture with density, viscosity, and API gravity defined. The correlation used for Pb (bubble point pressure) and Rs (solution gas ratio) is based on Glaso [19]. For Bo (oil formation volume factor), the Standing correlation is applied. The correlation used for oil viscosity is based on the methods of Petrosky et al. [20] Beal [21], or Pedersen [22], depending on the oil type and reservoir condition. After assembling the network, the model was run iteratively. The simulated values were compared with field measurements (pressure and flow rate). When discrepancies were found, calibration was performed by adjusting input parameters until the simulated and measured data matched satisfactorily. The calibration process ensured accurate prediction of pressure, temperature, and flow distribution across the network.

The final constructed model of the RAMA–RAA field network is shown in Figure 4, which provides a schematic representation of the overall topology of wells, manifolds, and gathering lines leading to the EPF RAMA-2 sink. The simulation results were based on this calibrated configuration.

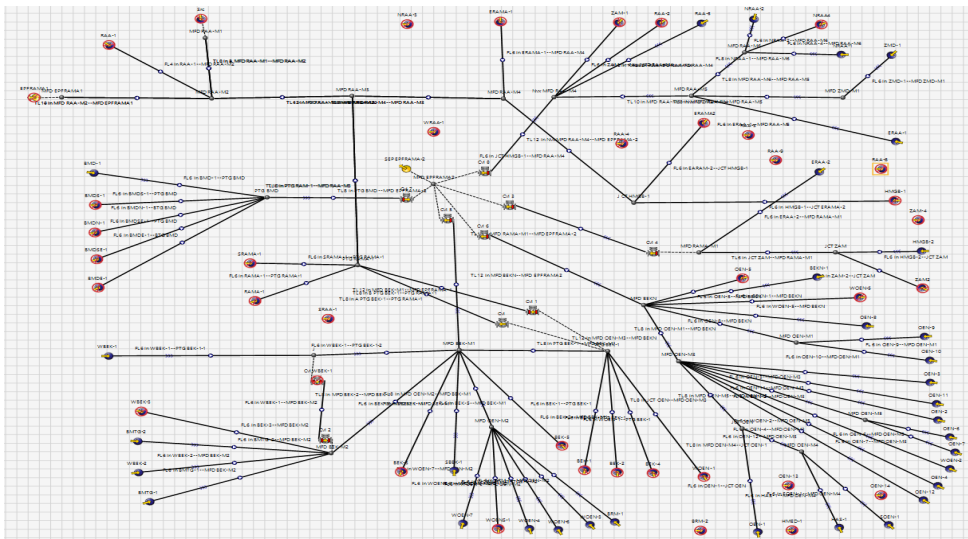


Figure 4. Network schematic of the RAMA–RAA field modeled in PIPESIM

ACKNOWLEDGMENTS

The authors express their sincere gratitude to the entire EP SONATRACH team for their kind support and valuable assistance, with special thanks to Mr. Lemiz Fatih and Mr. Boussandel Abdelaziz.

REFERENCES

1. F. Souas; A. Safri; A. Benmounah; *Pet. Sci. Technol.*, **2020**, 38, 849-857.
2. S. Pattanaik; U. Behera; D. Das; P. K. Misra; *J. Macromol. Sci. B*, **2025**, 64, 586-604.
3. H. A. Abbas; A. D. Manasrah; L. Carbognani; K. O. Sebakhy; M. E. H. E. Nokab; M. Hacini; N. N. Nassar; *Pet. Sci. Technol.*, **2022**, 40, 1279-1301.
4. F. Souas; A. Safri; A. S. E. Meddour; *Studia UBB Chemia.*, **2025**, 70, 221-234.
5. F. Souas; A. Safri; A. Gueciouer; *Studia UBB Chemia.*, **2025**, 70, 177-190.
6. A. S. E. Meddour; F. Souas; *Ovidius Univ. Ann. Chem.*, **2022**, 33, 64-70.
7. R. Kumar; S. Banerjee; A. Banik; T. K. Bandyopadhyay; T. K. Naiya; *Pet. Sci. Technol.*, **2017**, 35, 615-624.
8. S. K. Das; M. N. Biswas; A. K. Mitra; *Chem. Eng. J.*, **1991**, 45, 165-171.
9. J.L. Trallero; *Oil-Water Flow Patterns in Horizontal Pipes*; Ph.D. Dissertation, The University of Tulsa: Tulsa, OK, USA, **1995**.
10. E. W. M. Hansen; *Emerg. Technol. Fluids Struct. Fluid-Struc. Interact.*, **2001**, 431, 23-29.
11. A. C. Bannwart; *J. Pet. Sci. Eng.*, **2001**, 32, 127-143.
12. T. K. Bandyopadhyay; S. K. Das; *J. Pet. Sci. Eng.*, **2007**, 55, 156-166.
13. M. Rudman; H. M. Blackburn; *Appl. Math. Model.*, **2004**, 30, 1229-1248.
14. D. H. Beggs; J. P. Brill; *J. Pet. Technol.*, **1973**, 25, 607-617.
15. F. M. Sani; S. Huizinga; K.A. Esaklul; S. Nesic; *Wear.*, **2019**, 426, 620-636.
16. I. Ahmed; A. P. Iswara; S. Abbas; F. Q. Jamal; I. Ahmad; S. T. H. Shar; A. Naseem; *Heliyon.*, **2024**, 10, e35006.
17. M. Janadeleh; R. Ghamarpoor; N. K. Abbood; S. Hosseini; H. N. Al-Saedi; A. Z. Hezave; *Heliyon.*, **2024**, 10, e36934.
18. A. E. Dukler; M. Wicks III; R. G. Cleveland; *AIChE J.*, **1964**, 10, 44-51.
19. O. Glaso; *J. Pet. Technol.*, **1980**, 32, 785-795.
20. G. E. Petrosky Jr; F. F. Farshad; *SPE Pap.*, **1995**, SPE-29468.
21. C. Beal; *Trans. AIME.*, **1946**, 165, 94-115.
22. K. S. Pedersen; Å. Fredenslund; P. L. Christensen; P. Thomassen; *Chem. Eng. Sci.*, **1984**, 39, 1011-1016.

1-PHOSPHA-2-AZANORBORNENE AS PRECURSOR FOR 1-PHOSPHA-BICYCLO[3.2.1]OCTA-2,5-DIENE*

Peter WONNEBERGER^a , Lydia KEIL^a, Paul SPICKENREUTHER^a,
Peter LÖNNECKE^a , Evamarie HEY-HAWKINS^{b,c*} 

ABSTRACT. 1-Phospha-2-azanorbornenes, the cycloaddition products of 2*H*-phospholes with a sulfonyl imine, can be converted to 1-phospha-bicyclo[3.2.1]octa-2,5-dienes by a reductive rearrangement. This reaction is, however, dependent on the substituent R in a-position. While a clean reaction is observed for R = H or Ph, the 2-pyridyl derivative leads to a complex product mixtures.

Keywords: *P*-heterocycles, phosphanes, reduction, ring expansion, sulfonamides

INTRODUCTION

Phospholes are versatile starting materials for the production of phosphorus heterocycles. The intermediate 2*H*-phospholes, which are accessible *in situ* by sigmatropic rearrangements from 1*H*-phospholes, represent a highly reactive and versatile class of substances with an sp²-hybridised phosphorus atom [1]. In particular, as diene components in Diels-Alder reactions, they provide access to a range of bicyclic phosphorus heterocycles through cycloaddition reaction with a wide variety of dienophiles. In addition to Diels-Alder reactions with carbon dienophiles [2,3,4,5], selected reactions with heteroatom dienophiles such as aldehydes [6] or additional

* See also Supporting information.

^a *Institute of Inorganic Chemistry, Faculty of Chemistry, Leipzig University, Johannisallee 29, 04103 Leipzig, Germany*

^b *Faculty of Chemistry and Chemical Engineering, Babeş-Bolyai University, 11 Arany Janos str., RO-400028, Cluj-Napoca, Romania*

^c *Institute of Bioanalytical Chemistry, Faculty of Chemistry, Leipzig University, Deutscher Platz 5, 04103 Leipzig, Germany*

* Corresponding author: evamarie.hey@ubbcluj.ro

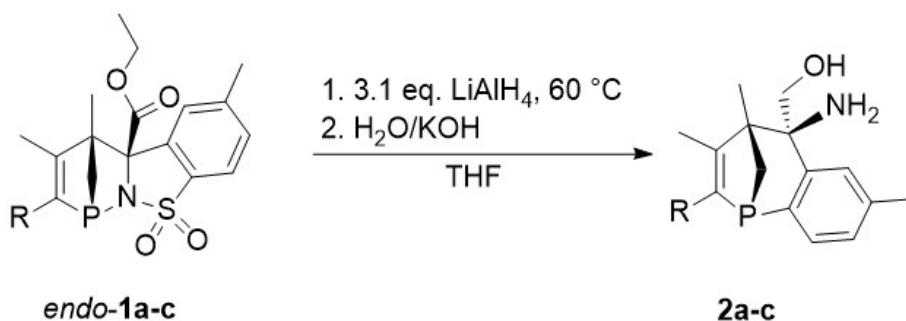


2*H*-phospholes (dimerisation of 2*H*-phospholes) [1] have also been reported. Furthermore, the stereoselective phospho-aza Diels-Alder reaction between 2*H*-phospholes or P-substituted 2*H*-phospholes and *N*-sulfonyl- α -iminoester affords diastereomeric (α -substituted) 1-phospha-2-azanorbornenes (PANs) [7]. The straightforward preparation of PANs and their reactive P–N bond allows numerous derivatisations and therefore access to P-stereogenic compounds with multiple stereocentres [8]. Thus, the P–N bond of PANs can be cleaved by achiral or chiral nucleophiles to give 2,3-dihydrophosphole derivatives as a racemic mixture [7]. Furthermore, we have already shown that reduction of the diastereomerically pure *endo*-5-phenyl-1-phospha-2-azanorbornene (*R_P/S_P*)-*endo*-**1a** with lithium aluminium hydride yielded a seven-membered P-heterocycle, 1-phospha-bicyclo-[3.2.1]octa-2,5-diene, under ring extension (**2a**, Scheme 1) [9]. Only a few synthetic pathways to bridged seven-membered phosphorus heterocycles have been reported until now [10,11,12,13]. We here report our attempts to extend this concept, reductive cleavage of the P–N bond and additional functional groups for the synthesis of 7-membered phosphorus heterocycles, to other (α -substituted) 1-phospha-2-azanorbornenes.

RESULTS AND DISCUSSION

We have investigated the possibility of converting other PAN derivatives into 1-phospha-bicyclo[3.2.1]octa-2,5-dienes. In an analogous reaction employed for the conversion of *endo*-**1a** to **2a** [9], the two PANs *endo*-**1b** and *endo*-**1c** were reacted with an excess of lithium aluminium hydride in THF, followed by aqueous workup (Scheme 1). The compound *endo*-**1b** could be converted to **2b** in a mostly selective reaction, but the isolated yield was only 29% due to losses during recrystallisation. Therefore, the air stable corresponding phosphane sulfide was prepared, but subsequent column chromatographic workup failed and only unspecified decomposition products could be isolated. A potential mechanism for the formation of **2a** was reported previously [9]. Apparently, the ester group has been reduced besides the expected cleavage of the P–N bond via nucleophilic attack of a hydride anion.

Crystals of compound **2b** were obtained from isopropanol at –30 °C. The molecular structure of **2b** is shown in Figure 1 (top). The bonding geometry of the P atom is distorted trigonal pyramidal. In the solid state, dimers are formed via intermolecular OH...N hydrogen donor-acceptor bonds (Figure 1 bottom and Table S6, Supporting Information). Of the nitrogen bonded hydrogen atoms, only H1N is interacting with the π system of an adjacent phenyl ring whereas for the remaining H2N no interactions are detectable at all.



Scheme 1. Reductive ring extension of the PANs *endo-1a-c*.

All chiral compounds presented here are racemic mixtures.

For clarity, always only one enantiomer of each compound is shown.

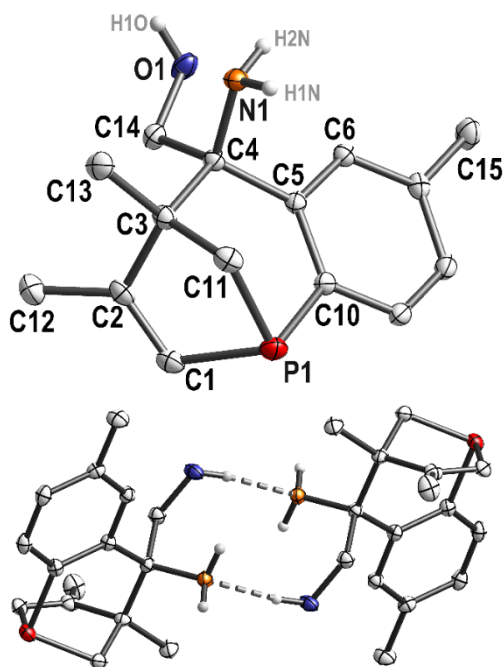


Figure 1. Molecular structure of **2b**. Ellipsoids at 50 % probability, hydrogen atoms other than NH and OH have been omitted for clarity. Selected bond lengths [pm] and angles [°]: P1–C1 182.9(1), P1–C10 182.6(1), P1–C11 183.6(2); C1–P1–C10 98.55(5), C1–P1–C11 88.15(6), C10–P1–C11 95.32(5), P1–C11–C3 105.77(8).

In the case of *endo*-**1c**, the reduction resulted in a complex mixture of P-containing substances in similar ratios. Beside an unsymmetrical diphosphane [$^{31}\text{P}\{^1\text{H}\}$ NMR (CDCl_3) $\delta = 8.8$ (d, $^1J_{\text{P-P}} = 194.6$ Hz), -40.7 (d, $^1J_{\text{P-P}} = 194.6$ Hz) ppm], a primary phosphane [^{31}P NMR (CDCl_3) $\delta = -140.9$ (t, $^1J_{\text{P-H}} = 194.2$ Hz) ppm] and several minor secondary and tertiary phosphanes were observed. In the shift range in which the product **2c** was expected, only a very small singlet [$^{31}\text{P}\{^1\text{H}\}$ NMR (CDCl_3) $\delta = -46.2$ (s) ppm] could be found. No products could be isolated, even after sulfurisation of the mixture followed by chromatography.

Phosphorus-containing cage compounds have also attracted much attention since earlier reports by Regitz and coworkers [14]. A tricyclic compound that is related to **2a,b** featuring a seven-membered diphosphora ring has been previously reported by Tian and Duan in a three-component reaction between different 3,4-dimethyl-1-aryl-phospholes, various ketones ($\text{R}^1\text{R}^2\text{CO}$) and pyrrolidine at 170°C and 5 mol % iron(II) chloride as catalyst (Figure 2) [15].

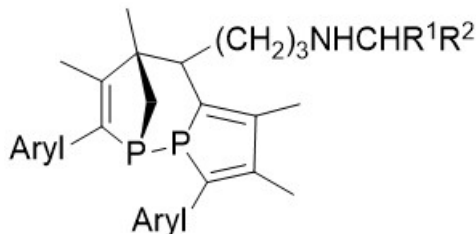


Figure 2. Related seven-membered diphosphora ring obtained in a three-component reaction between different 3,4-dimethyl-1-aryl-phospholes, various ketones ($\text{R}^1\text{R}^2\text{CO}$) and pyrrolidine [15].

CONCLUSIONS

We have shown that the reductive rearrangement of *endo*-6-phenyl-PAN reported by us previously [9] can be partially extended to other *endo*-PAN derivatives. While **2c** was not accessible, **2b** could be obtained and structurally characterised.

The 7-membered phosphorus heterocycle has gained attention for its potential applications, e.g. in optoelectronics [16] or in chiral ligands [17]. Thus, synthetic approaches to these types of compounds are very valuable.

EXPERIMENTAL SECTION

General: All reactions were carried out with standard Schlenk techniques in an atmosphere of dry high purity nitrogen. THF was degassed and distilled from potassium. Hexanes (mixture of isomers) were dried and degassed with the solvent purification system SPS-800 series from MBRAUN. Isopropanol was degassed and used without further drying. The NMR spectra were recorded with a Bruker Avance DRX 400 spectrometer (^1H NMR 400.13 MHz, ^{13}C NMR 100.63 MHz, ^{31}P NMR 161.98 MHz) or a Bruker Ascend 400 spectrometer (^1H NMR 400.16 MHz, ^{13}C NMR 100.63 MHz, ^{31}P NMR 161.99 MHz). For ^1H NMR and ^{13}C NMR spectra, SiMe_4 (TMS) was used as internal standard. The ^{31}P NMR spectra were referenced to TMS using the Ξ scale [18]. Assignment of the configurations and chemical shifts was done using HSQC, HMQC, HMBC, and COSY techniques. The high-resolution mass spectrum (HRMS; ESI) was measured with a Bruker Daltonics APEX II FT-ICR spectrometer. The IR spectrum was recorded on a Thermo Scientific Nicolet iS5 with a diamond ATR (400–4000 cm^{-1}). The melting point was determined in a glass capillary sealed under vacuum using a Gallenkamp apparatus and is uncorrected. LiAlH_4 was commercially available; *endo*-**1b** and *endo*-**1c** were prepared according to literature procedures [7].

1-Phosphabicyclo[3.2.1]octa-2,5-diene (2b): A solution of 2.169 g (5.94 mmol, 1.0 eq.) *endo*-**1b** in 60 mL THF was added to 0.697 g (18.37 mmol, 3.1 eq.) lithium aluminum hydride at 0 °C. After 5 min, the cooling bath was removed, and the suspension was stirred at 60 °C for 21 h. Subsequently, excess hydride species were quenched at 0 °C by adding 1.5 mL of degassed 10% (w/w) aqueous potassium hydroxide solution, resulting in hydrogen evolution. The slurry was heated to 60 °C for 15 min to agglomerate the precipitate. The precipitate was removed using a Schlenk frit and washed four times with 5 mL THF each. The filtrate was concentrated under reduced pressure. The yellowish residue was washed with 20 mL of hexanes and dissolved in 30 mL of boiling isopropanol. The solution was stored at –30 °C overnight and the formed crystals were separated from the mother liquor using a filter cannula and washed with 10 mL of hexanes. Solvent traces were removed under reduced pressure at 60 °C. **2b** was obtained as white crystals (0.447 g, 1.71 mmol, 29%). Mp: 179 °C. ^1H NMR (CDCl_3): δ = 7.50 (s, 1H), 7.33 – 7.23 (m, 1H), 6.96 (d, $^3J_{\text{H-H}} = 7.4$ Hz, 1H), 6.15 (d, $^2J_{\text{H-P}} = 47.4$ Hz, 1H), 3.84 – 3.70 (m, 2H), 2.59 – 2.52 (m, 1H), 2.32 (s, 3H), 2.20 (dd, $^2J_{\text{H-H}} = 13.0$ Hz, $^2J_{\text{H-P}} = 6.6$ Hz, 1H), 1.94 (dd, $^2J_{\text{H-H}} = 13.0$ Hz, $^2J_{\text{H-P}} = 9.1$ Hz, 1H), 1.91 (s, 3H), 1.64 (s, 2H), 1.42 (s, 3H) ppm. $^{13}\text{C}\{^1\text{H}\}$ NMR (CDCl_3) δ = 159.0 (d, $^2J_{\text{C-P}} = 4.1$ Hz), 145.7 (d, $^2J_{\text{C-P}} = 3.8$ Hz), 140.0 (s), 133.8 (d, $^2J_{\text{C-P}} = 42.6$ Hz), 133.4 (d, $^1J_{\text{C-P}} = 12.2$ Hz), 131.3 (d, $^1J_{\text{C-P}} = 13.9$ Hz), 130.2 (s), 127.1 (d, $^3J_{\text{C-P}} =$

13.5 Hz), 68.3 (s), 57.2 (s), 55.0 (d, $^2J_{C-P}$ = 4.0 Hz), 41.8 (s), 22.8 (d, $^3J_{C-P}$ = 3.5 Hz), 21.6 (s), 18.6 (d, $^3J_{C-P}$ = 3.4 Hz) ppm. $^{31}P\{^1H\}$ NMR ($CDCl_3$) δ = -46.2 (s) ppm. ^{31}P NMR ($CDCl_3$) δ = -45.8 to -46.5 (virtual quartet) ppm. HRMS (ESI, THF, pos. mode): m/z calcd. for $C_{15}H_{20}NOP+H^+$: 262.136 $[M+H]^+$; found: 262.138. FT-IR: $\tilde{\nu}$ = 3356 (m), 3294 (m), 3178 (m), 3046 (w), 2957 (w), 2945 (w), 2924 (w), 2870 (w), 1596 (m), 1561 (w), 1469 (m), 1437 (w), 1372 (m), 1262 (m), 1225 (w), 1172 (w), 1154 (w), 1064 (s), 959 (m), 940 (s), 917 (w), 903 (w), 871 (w), 814 (s), 754 (w), 722 (w), 634 (w), 620 (w), 536 (w), 513 (w), 504 (w), 474 (w) cm^{-1} .

X-ray crystallography data

The data for **2b** were collected on a Gemini diffractometer (Rigaku Oxford Diffraction) using Mo-K α radiation (λ = 71.073 pm) and ω -scan rotation. Data reduction was performed with CrysAlis Pro [19], including the program SCALE3 ABSPACK for empirical absorption correction. The structure was solved by dual-space methods with SHELXT-2018 [20] and the refinement was performed with SHELXL-2018 [21]. All non-hydrogen atoms were refined with anisotropic displacement parameters. Detailed structure parameters are given in Tables S1 to S6, Supporting Information. CCDC 2490394 contains the supplementary crystallographic data for this paper. The data is accessible free of charge from the Cambridge Crystallographic Data Centre via: <https://www.ccdc.cam.ac.uk/structures/>

$C_{15}H_{20}NOP$, M = 261.29 g/mol, T = 130(2) K, Triclinic crystal system, space group $P\bar{1}$, a = 812.02(4) pm, b = 995.95(4) pm, c = 1002.79(4) pm, α = 103.699(4)°, β = 111.168(4)°, γ = 108.539(4)°, V = 0.65787(6) nm³, Z = 2, ρ calcd = 1.319 g/cm³, μ = 0.197 mm⁻¹, crystal size = 0.36 x 0.26 x 0.18 mm³, q range for data collection = 2.351 to 32.390°, reflections collected = 13522, independent reflections = 4381 [$R(int)$ = 0.0305], completeness to q : 30.510° = 100.0 %, 243 parameters, 0 restraints, R indices (all data): $R1$ = 0.0525, $wR2$ = 0.1044, Final R indices [$I > 2\sigma(I)$]: $R1$ = 0.0413, $wR2$ = 0.0977. All H atoms were located on difference Fourier maps calculated at the final stage of the structure refinement.

ACKNOWLEDGMENTS

We thank the DFG (HE 1376/46-1) and the Graduate School BuildMoNa for financial support. E.H.-H. acknowledges funding from the European Union – Next Generation EU and the Romanian Government, under National Recovery and Resilience Plan for Romania, through the Romanian Ministry of Research, Innovation and Digitalization, within Component 9, Investment I8 (PNRR-III-C9-2023-I8-CF76, contract nr. 760240/28.12.2023).

REFERENCES

1. F. Mathey, *Acc. Chem. Res.* **2004**, *37*, 954–960.
2. T. Möller, M. B. Sárosi, E. Hey-Hawkins, *Chem. Eur. J.* **2012**, *18*, 16604–16607.
3. P. Le Goff, F. Mathey, L. Ricard, *J. Org. Chem.* **1989**, *54*, 4754–4758.
4. K. Zhang, Q. Zhang, D. Wei, R. Tian, Z. Duan, *Org. Chem. Front.* **2021**, *8*, 3740–3745.
5. F. Mathey, F. Mercier, F. Robin, L. Ricard, *J. Organomet. Chem.* **1998**, *557*, 117–120.
6. P. Toullec, L. Ricard, F. Mathey, *J. Org. Chem.* **2003**, *68*, 2803–2806.
7. P. Wonneberger, N. König, F. B. Kraft, M. B. Sárosi, E. Hey-Hawkins, *Angew. Chem. Int. Ed.* **2019**, *58*, 3208–3211; *Angew. Chem.* **2019**, *131*, 3240–3244.
8. a) K. Ramazanov, P. Lönnecke, E. Hey-Hawkins, *Chem. Eur. J.* **2023**, *29*, e202300790, b) K. Ramazanov, A.K. Müller, P. Lönnecke, O. Hollóczki, B. Kirchner, E. Hey-Hawkins, *Molecules* **2023**, *28*, 7163.
9. P. Wonneberger, N. König, M. B. Sárosi, E. Hey-Hawkins, *Chem. Eur. J.* **2021**, *27*, 7847–7852.
10. J. E. MacDiarmid, L. D. Quin, *J. Org. Chem.* **1981**, *46*, 1451–1456.
11. L. D. Quin, S. C. Spence, *Tetrahedron Lett.* **1982**, *23*, 2529–2532.
12. D. G. Gilheany, B. J. Walker, *Phosphorus Sulfur Relat. Elem.* **1983**, *18*, 183–186.
13. B. Krauss, C. Mügge, B. Ziemer, A. Zschunke, F. Krech, *Z. Anorg. Allg. Chem.* **2001**, *627*, 1542–1552.
14. O. Löber, U. Bergsträßer, M. Regitz, *Synthesis* **1999**, *4*, 644–649.
15. Y. Liu, X. Fan, R. Tian, Z. Duan, *Org. Lett.* **2021**, *23*, 2943–2947.
16. a) X. He, J. Borau-Garcia, A. Y. Y. Woo, S. Trudel, T. Baumgartner, *J. Am. Chem. Soc.* **2013**, *135*, 1137–1147; (b) T. Delouche, R. Mokrai, T. Roisnel, D. Tondelier, B. Geffroy, L. Nyulászi, Z. Benkő, M. Hissler, P.-A. Bouit, *Chem. Eur. J.* **2020**, *26*, 1856–1863; (c) E. Regulska, H. Ruppert, F. Rominger, C. Romero-Nieto, *J. Org. Chem.* **2020**, *85*, 1247–1252.
17. (a) S. Gladiali, A. Dore, D. Fabbri, O. D. Lucchi and M. Massanero, *Tetrahedron: Asym.* **1994**, *5*, 511–514; (b) P. Nareddy, L. Mantilli, L. Guénée, and C. Mazet, *Angew. Chem., Int. Ed.* **2012**, *51*, 3826–3831; (c) R. Mokrai, A. Mocanu, M. P. Duffy, T. Vives, E. Caytan, V. Dorcet, T. Roisnel, L. Nyulászi, Z. Benkő, P.-A. Bouit, M. Hissler, *Chem. Commun.* **2021**, *57*, 7256–7259.
18. R. K. Harris, E. D. Becker, S. M. Cabral De Menezes, R. Goodfellow, P. Granger, *Pure Appl. Chem.* **2001**, *73*, 1795–1818; *Concepts Magn. Reson. Part A* **2002**, *14*, 326–346.
19. CrysAlisPro Software system (1995-2025), Rigaku Oxford Diffraction, Wroclaw, Poland.
20. SHELXT-2018: G. M. Sheldrick, *Acta Cryst.*, **2015**, *A71*, 3–8.
21. SHELXL-2018: G. M. Sheldrick, *Acta Cryst.*, **2015**, *C71*, 3–8.